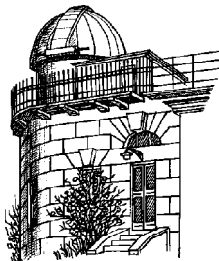


ODESSA ASTRONOMICAL PUBLICATIONS

Volume 26 Issue 1
(2013)



Odessa
«AstroPrint»

CONTENTS

IN COMMEMORATION OF THE 75th BIRTHDAY ANNIVERSARY OF NIKOLAY S. KOMAROV

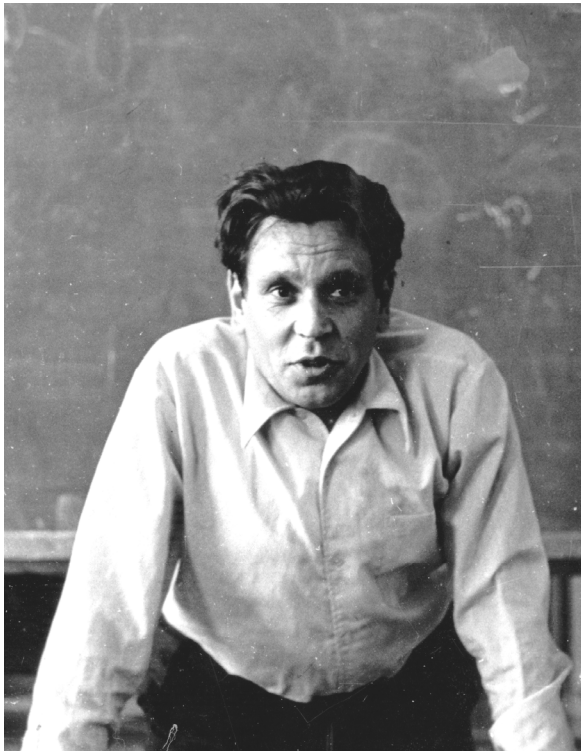
T.V.Mishenina, A.V.Dragunova.....	4
A NEW 800 mm AUTOMATIC TELESCOPE	
S.M.Andrievsky, I.E.Molotov, N.N.Fashchevsky, S.V.Podlesnyak, V.V.Zhukov, V.V.Kouprianov, S.G.Kashuba, V.I.Kashuba, V.F.Mel'nichenko, Yu.M.Gorbanev	6
PROGRAM WWZ: WAVELET ANALYSIS OF ASTRONOMICAL SIGNALS WITH IRREGULARLY SPACED ARGUMENTS	
I.L.Andronov, A.V.Naumova	26
ANALYSIS OF THE PARAMETERS AND ABUNDANCE OF N-CAPTURE ELEMENTS FOR FOUR STARS WITH DIFFERENT METALLICITY	
N.Yu.Basak, T.V.Mishenina.....	30
INTERESTING MOON'S SURFACE FEATURES. OUR STUDY AND SOME INFERENCES	
Yu.N.Bondarenko	31
COMPILATION OF MOMENTS OF SPIN MAXIMA OF THE INTERMEDIATE POLAR EX HYA	
V.V.Breus, I.L.Andronov.....	35
ALL-SKY CAMERAS FOR OBSERVATION AND INVESTIGATION OF VARIABLE STARS AND METEOR SHOWERS	
I.S.Bryukhanov, I.M.Sergey, V.Vatutina, A.Ivchik, M.Pogodina, R.Vatolin, S.Dovnar, V.Osadchaya, A.Tabolich, V.Tabolich, A.Lyubimov, T.Smolenchuk, A.Chernik, M.Chernyavskiy, I.Nazaruk, M.Nazaruk, D.Akulich, E.Zaritskaya.....	38
ABOUT THE GLOBAL MAGNETIC FIELDS OF STARS	
V.D.Bychkov, L.V.Bychkova, J.Madej	43
THE VARIABILITY OF GLOBAL MAGNETIC FIELDS OF STARS. THE NEW OBSERVATIONS DATA	
V.D.Bychkov, L.V.Bychkova, J.Madej	47
THE DETERMINATION OF ABSOLUTE PARAMETERS AND ABUNDANCE OF COMPONENTS BINARY SYSTEMS: THE SPECIFICITY AND PROBLEMS	
L.V.Glazunova	49
THE ABUNDANCES OF HEAVY ELEMENTS IN RED SUPERGIANTS OF MAGELLANIC CLOUDS	
V.Gopka, A.Yushchenko, V.Kovtyukh, A.Shavrina, V.Yushchenko, S.Vasilyeva, Y.Pavlenko, S.Andrievsky	54
MANGANESE ABUNDANCES IN THE ATMOSPHERE OF CLUMP GIANTS	
T.I.Gorbaneva	60
THE MASSES OF THE IONIZED GAS OF PLANETARY NEBULAE ENVELOPES IN LARGE MAGELLANIC CLOUD	
V.Holovatyy, A.Demchyna.....	61
CHEMICAL COMPOSITIONS OF CRAB NEBULA FILAMENTS	
V.V.Holovatyy, B.Ya.Melekh, N.V.Havrylova.....	63
DETERMINATION OF THE EPHEMERIS ACCURACY FOR AJISAI, LAGEOS AND ETALON SATELLITES, OBTAINED WITH A SIMPLIFIED NUMERICAL MOTION MODEL USING THE ILRS COORDINATES	
I.V.Kara.....	66
OBSERVATIONS OF APOPHIS IN NSFCTC (YEVPA TORIA) AND RI NAO (MYKOLAIV)	
A.M.Kozhukhov, N.V.Maigurova, A.V.Pomazan, V.F.Kryuchkovskiy	70
HOMOGENIZED EFFECTIVE TEMPERATURES FOR THE OPEN CLUSTER NGC 188	
V.Malyuto, S.Zubarev.....	73

OPEN CLUSTERS AND FIELD CEPHEIDS IN THE GALACTIC DISK - CONTRADICTIONS IN PROPERTIES	
V.A.Marsakov, B.B.Koval', M.L.Gozha, B.B.Kovtyukh, T.V.Mishenina	74
T CEP, U UMI, Z SCO – MIRA-TYPE VARIABLES WITH CYCLIC PERIOD CHANGES	
V.I.Marsakova.....	78
NON-LTE EFFECTS IN AL I LINES: CHOICE OF ATOMIC DATA	
V.V.Menzhevitski, N.N.Shimanskaya, V.V.Shimansky, D.O.Kudryavtsev, N.A.Sakhbullin...	83
THE NUMERICAL THREE-DIMENSIONAL HYDRODYNAMIC SIMULATION OF THE γ -RAY BURSTERS AND X-RAY BURSTERS	
V.V.Nazarenko, L.V.Glazunova, S.V.Nazarenko	84
THE NUMERICAL THREE-DIMENSIONAL HYDRODYNAMIC SIMULATION OF COLLIDING STELLAR WINDS IN A CLOSE BINARY SYSTEM	
V.V.Nazarenko, L.V.Glazunova, S.V.Nazarenko	87
THE CRITERIA FOR MORPHOLOGICAL CLASSIFICATION OF PF GALAXY CLUSTERS	
E.A.Panko	90
SULFUR ABUNDANCE IN THE GALACTIC DISC STARS	
O.P.Paramonova, T.V.Mishenina, O.Chepizhko	94
DETERMINATION OF THE SATELLITE'S ROTATION USING ITS LIGHT CURVE	
D.Pavlenko	95
NUMERICAL MODELING OF GLOBULAR CLUSTERS TIDAL DISSOLUTION	
M.V.Ryabova, E.G.Senzikas, Yu.A.Shchekinov	99
DETERMINATION OF PARAMETERS OF WHITE DWARF BY THE HYDROGEN SPECTRUM IN THE MODEL WITH LINEAR EQUATION OF STATE	
Ch.Scherbakov	102
BELARUSIAN PROJECT "ASTROBLOKNOT" (ASTRONOMICAL NOTEBOOK) AND DATA MINING: RESULTS OBTAINED IN THE CONSTELLATION OF EQUULEUS	
I.Sergey, S.Dubrouski, I.Baluk, A.Pobiacha.....	105
INCREASE IN THE ARRAY TELEVISION CAMERA SENSITIVITY	
O.Sh.Shakhrukhanov	107
DETERMINATION OF THE STELLAR SCINTILLATION PROPERTIES WITH THE FAST-PHOTOMETRIC CAMERA	
O.Sh.Shakhrukhanov	108
ESTIMATIONS OF DYNAMIC PARAMETERS AND POSSIBLE HABITABLE ZONES FOR SELECTED STARS OF PULKOVO PROGRAM	
N.A.Shakht, L.G.Romanenko	109
LI I 6708A BLEND IN THE SPECTRA OF STRONGLY MAGNETIC STAR HD166473	
A.V.Shavrina, V.Khalack, Y.Glagolevskij, D.Lyashko, J.Landstreet, F.Leone, N.S.Polosukhina, M.Giarrusso.....	112
TOWARDS A DETERMINATION OF DEFINITIVE PARAMETERS FOR THE LONG PERIOD CEPHEID S VULPECULAE	
D.G.Turner.....	115
HQ CAR IS A NEW W VIR TYPE STAR	
S.N.Udovichenko, V.V.Kovtyukh, I.A.Egorova, S.I.Belik	120
MULTIPHASE SPECTROSCOPIC OBSERVATIONS OF THE LONG-PERIOD CEPHEIDS / CARINAE	
I.A.Usenko, V.V.Kravtsov, V.V.Kovtyukh, L.N.Berdnikov, A.Yu.Knyazev, R.Chini, A.B.Fokin.....	123
CHEMICAL COMPOSITION AND ATMOSPHERE PARAMETERS OF THE DOUBLE-MODE CEPHEID U TRA	
I.A.Usenko, A.Yu.Knyazev, L.N.Berdnikov, V.V.Kravtsov.....	127
THE PLANETARY HOST RED GIANT HD47536 – CHEMICAL COMPOSITION AND SIGNS OF ACCRETION	
A.V.Yushchenko, P.Rittpruk, V.A.Yushchenko, Y.-W.Kang.....	131

IN COMMEMORATION OF THE 75TH BIRTHDAY ANNIVERSARY OF NIKOLAY S. KOMAROV

T.V.Mishenina, A.V.Dragunova

Astronomical Observatory of the Mechnikov Odessa National University



Nikolay Sergeyevich Komarov (16.06.1938–03.08.2003) was born in Sestroretsk town in Leningrad region (USSR) in the family of a naval officer. After the World War II his family moved to Odessa. In 1955, Nikolay graduated from a high school and entered the Department of Mathematics of the Faculty of Mathematical and Physical Sciences at Odessa State University. The launch of the first artificial Earth's satellite aroused his interest in outer space, and he transferred to the Department of Physics of the faculty to specialise in astronomy. During 1955-1960, Nikolay Komarov was a leader among other students in Odessa as he had the largest number of artificial satellite observations. He was very enthusiastic about spectroscopy as far back as he was a student and made the meteor spectra the subject of his graduation Master's paper.

On having graduated from the University in 1960, Nikolay was employed at the Odessa Astronomical Observa-

tory and spent the first year of employment at the observational station in Mayaki village, being engaged in the visual observations of variable stars using the 19" telescope installed outdoors and not equipped with the clock drive for automatic tracking. In 1961, Nikolay Komarov entered the PhD programme, and Vladimir Tsesevich was assigned to be his academic advisor.

The future academic career of Nikolay Komarov, including selection of the focus area and line of his research, was significantly influenced by Sergey V. Rublyov and Ivan M. Kopylov. Sergey Rublyov who was the Chief of the Mayaki Observational Station, sent Komarov on mission to the Crimean Astrophysical Observatory (CrAO) to collect the observational material for his PhD thesis; and there Komarov got into the spectral observations with the 50" reflector. And I. Kopylov provoked the interest in the spectroscopic studies and phenomenon of the so-called 'metallic' (metal-line) stars. The PhD thesis "Kinematic and Morphological Properties of Stars with Enhanced Metal Lines" was successfully defended by N. Komarov in 1968. The spectrograms of 29 stars, obtained with the quartz spectrograph of the 122 cm reflector at the CrAO of the Academy of Sciences of the USSR, provided by I. Kopylov, were used in that PhD study; besides, within the framework of that study the stellar atmosphere models were built within the spectral range A0-F0 near the Main sequence under the local thermodynamic equilibrium (LTE), plane-parallel, radiation and hydrodynamic equilibrium approximations. The temperature distribution was determined under the grey approximation and using the Chandrasekhar method of averaging the intensity by direction; the absorption by metals was assigned as an opacity source. Later on the temperature distribution was corrected for the non-greyness of the atmosphere by the Swihart method. The model grid at different ratios of hydrogen relative to metals for T_{eff} 9000, 8000, 7000, 6000K and $\log g = 4, 3$ was computed by the Universal Electronic Digital Machine (URAL-2) of the Computation Centre of Odessa State University. The calculation of the star envelope, i.e. that part of it where it is possible to neglect the energy distribution, was performed; the catalogue of 380 metal-line stars was compiled; and a set of very weighty conclusions on the parameters, kinematic properties and

velocities of axial rotation of the metal-line stars were made.

After the PhD thesis defence Nikolay was appointed as the Chief of the Department of Astrophysics, which was the largest unit of the observatory at that time. During the years of follow-up the observatory underwent a series of changes, and after reorganisation Nikolay headed first the Section and later the Department of Spectroscopy, and during the last years of his work he was the Chief of the Department of Physics of Stars and Galaxies, which was the new largest unit of the observatory with consolidated Departments of Variable Stars and Astrospectroscopy.

Having a good grounding in mathematics, being a natural leader with keen mind, Nikolay always demonstrated the intuitive ability to perceive an interesting and promising line of research. Along with V. A. Pozigun, he pioneered the near-infrared star observations and investigations in the Soviet Union. The electrospectrophotometer, designed by Komarov, had been in operation at the Mayaki Observational Station from 1966 to 1970; and then, being attached to the 17" telescope, it was removed to Turkmenistan and installed in Vannovskiy village where acted till 1975. On the initiative and with the participation of Nikolay Komarov several more electronic photometers and electrospectrophotometers, covering a wide range of wavelengths, were constructed and put into operation (more details can be found in the authors' paper in *Odessa Astronomical Publications*, vol. 21, 2008, pp. 5–8). Different instruments, designed to record spectra and measure brightness of stars were developed under scientific supervision of N. Komarov, namely broadband amplifiers, recorders and memory devices, computer communication and control interfaces. All activities concerned with the automation of the observation processes were initiated, developed and controlled with the direct involvement of N. Komarov. The equipment was installed in different regions of the former USSR at sites with good astronomical climate conditions, such as in Turkmenistan (Mt. Dushak-Erekdag), in Georgia (Abastumani village), Armenia (Pass Bezymyanny), in the vicinity of Mt. Elbrus in the North Caucasus (Terskol Peak), in the Sayan Mountains (Mondy village) and in the Pamir Mountains (Murgab village).

Tens of young Odessa astronomers got systematic training in the high-mountain research expeditions. Nikolay himself participated not only in the observations at the stations, established by him, but also in observations of solar eclipses and zodiacal light (in Chukotka, Kamchatka, Sakhalin in 1981, as well as in the Hindu Kush). The obtained observations were included into several published catalogues of spectral energy distribution and broadband photometric data. The observatory's computerization was launched on the initiative of N. Komarov and at the ex-

pense of the funds raised from executing of commercial contracts he agreed upon.

The spectroscopic studies by Nikolay Komarov were not limited to the determination of the spectral energy distribution. The stellar fundamental parameter study, spectroscopic analysis of stellar atmospheres, determination of the chemical composition and calculations of the synthetic spectra were carried out in the Department of Astrospectroscopy since the late 1960s. The formation of the study group "Stellar Atmospheres" by N. Komarov together with N.A. Sahibullin, A. Sapar and Y. Straume was good first start to coordinate the activities on the high-dispersion spectra observation, interpretation and simulation of the stellar atmospheres in the USSR. Then Komarov initiated the coordinated efforts of the researchers of the stellar atmospheres and evolution theories; and in 2002, he arranged International conference "Chemical and Dynamic Evolution of Stars and Galaxies" within the framework of the study group "Stellar Atmospheres". The established group has been continuing its activities, having an international status nowadays. Nikolay Komarov was also one of the organisers of the All-Union Workshop on the Spectrophotometric and Photometric Standards.

In 1989, N. Komarov defended the ScD thesis "Atmospheric Structure of Giant Stars" and soon after became a full professor. He published 160 scientific studies, 3 monographs and many catalogues and drafted 56 reports on the agreed-upon topics.

In his monograph "Cold Giant Stars" that was dedicated to Sergey Rublyov, Nikolay Komarov summarized the results obtained by himself and those received under the supervision of Rublyov. The following activities were performed under the supervision of Nikolay Komarov: the non-LTE spectral analysis, determination of the metallicity gradient of the galactic disc by calibrations of $[Fe/H] - CN$ for the open clusters, determination of abundances of isotopes and the n-capture elements, investigation of formation of dust grains in the upper atmospheres of giants, etc.

Nikolay Komarov paid great attention to the educational, scientific and organisational activities. There were more than ten PhD theses written and defended under his supervision.

Nikolay Komarov headed a large team that mainly consisted of young people and he helped many of them in finding their calling in science; he also fostered improved scientific communications of Odessa Astronomical Observatory with different astronomical and other organisations and enhanced the observatory facilities. He was a really committed person with multifaced interests and got others involved by his enthusiasm. Eternal memory of him shall live in the hearts of his like-minded colleagues and associates and shall be embedded in the environment of his home observatory. And what is the most important, his cause lives on!

A NEW 800 mm AUTOMATIC TELESCOPE

S. M. Andrievsky¹, I. E. Molotov², N. N. Fashchevsky¹, S. V. Podlesnyak¹, V. V. Zhukov³,
V. V. Kouprianov⁴, S. G. Kashuba¹, V. I. Kashuba¹, V. F. Mel'nichenko¹, Yu. M. Gorbanev¹

¹ Astronomical Observatory of Odessa National University, Odessa, Ukraine
scan@deneb1.odessa.ua

² Keldysh Institute of Applied Mathematics, Moscow, Russia, im62@mail.ru

³ Skyline Electronics Ltd. Co., Odessa, Ukraine, vadim@skyline.od.ua

⁴ Central (Pulkovo) Astronomical Observatory of the Russian Academy of Sciences
Saint Petersburg, Russia, v.kouprianov@gmail.com

ABSTRACT. A new automatic telescope, a 800-millimeter main mirror catadioptric anastigmatic aplanat, was constructed by specialists of Odessa National University Astronomical observatory (Ukraine) in cooperation with their colleagues from the ISON project (Russia), and was recently put into operation. The telescope is mounted at Mayaki station in suburb of Odessa. It is equipped with a focal corrector and a professional CCD camera. The telescope is used now for observations of geostationary objects, asteroids, and comets. In addition, this telescope can be used for the high precision photometric observations of faint objects up to 20^m.

Key words: small telescope construction, telescope design.

1. Introduction

By the 1980–90th the space telescope projects had started to play an increasingly important role, and they seemed to be the undoubted thing of the future (e. g. see the article of that time by member of Armenian National Academy of Sciences Grigor Gurzadyan, issued in the Literary Newspaper (*Literaturnaya Gazeta*) No. 18, the 4th of May 1988).

Nevertheless, in the mid of 90-s the IAU have registered all telescopes with primary mirror diameters of more than 6 m as a separate class of large telescopes. The construction and putting in operation large and very large telescopes enabled the ground-based astronomy to maintain its position and obtain a large amount of high-quality observational material. Keen competitiveness of large telescopes resulted in discontinuation of use of some telescopes with 1–2 m mirror diameter.

With a tremendous up-growth of the ground-based and space astronomy, small telescopes (conditionally those with primary mirrors of less than 1 m diameter) definitely succeeded in taking their niche. The absence

of competition between different observational programmes, practically unlimited possibility to use the periods available for observations and low power inputs associated with operation of such instruments, made existing small telescopes irreplaceable in discovery and photometry of variable stars, discovery and astrometry of asteroids and cometary nuclei, observation of artificial satellites, and it is extremely important that with such telescopes regular monitoring of active satellites and passive orbiting fragments (space debris) in the geostationary orbit has been conducted.

The concept of a reflecting telescope with primary mirror diameter of 800 mm (OMT-800, i. e. Odessa Multifunctional Telescope) occurred to two co-authors of this paper while their participating in the KOLOS conference in Slovakia (at Vihorlat observatory) in the end of 2006. It took them several years to implement that concept – to design the telescope and its infrastructure, necessary for its operation. Despite huge problems associated with the construction of that instrument, we succeeded in building the telescope and putting it in operation at the end of 2012. That became feasible, primary, due to enthusiasm and self-sacrifice of some observatory staff members, who formed the so-called “gruppa vosmidesyatki”, i. e. the 80-cm telescope group.

2. New OMT-800 in the International Scientific Optical Network (ISON)

In Russia, the ISON project (Scientific network of optical instruments for astrometric and photometric observations) is one of the main sources of information on the near-Earth space. There are 33 observatories in 14 countries in the world that are involved in observations of satellites, space debris objects and asteroids. Based on the data of the ISON, the problems of the near-Earth space hazards prediction are being solved within the framework of the Automated System on the near-Earth Space

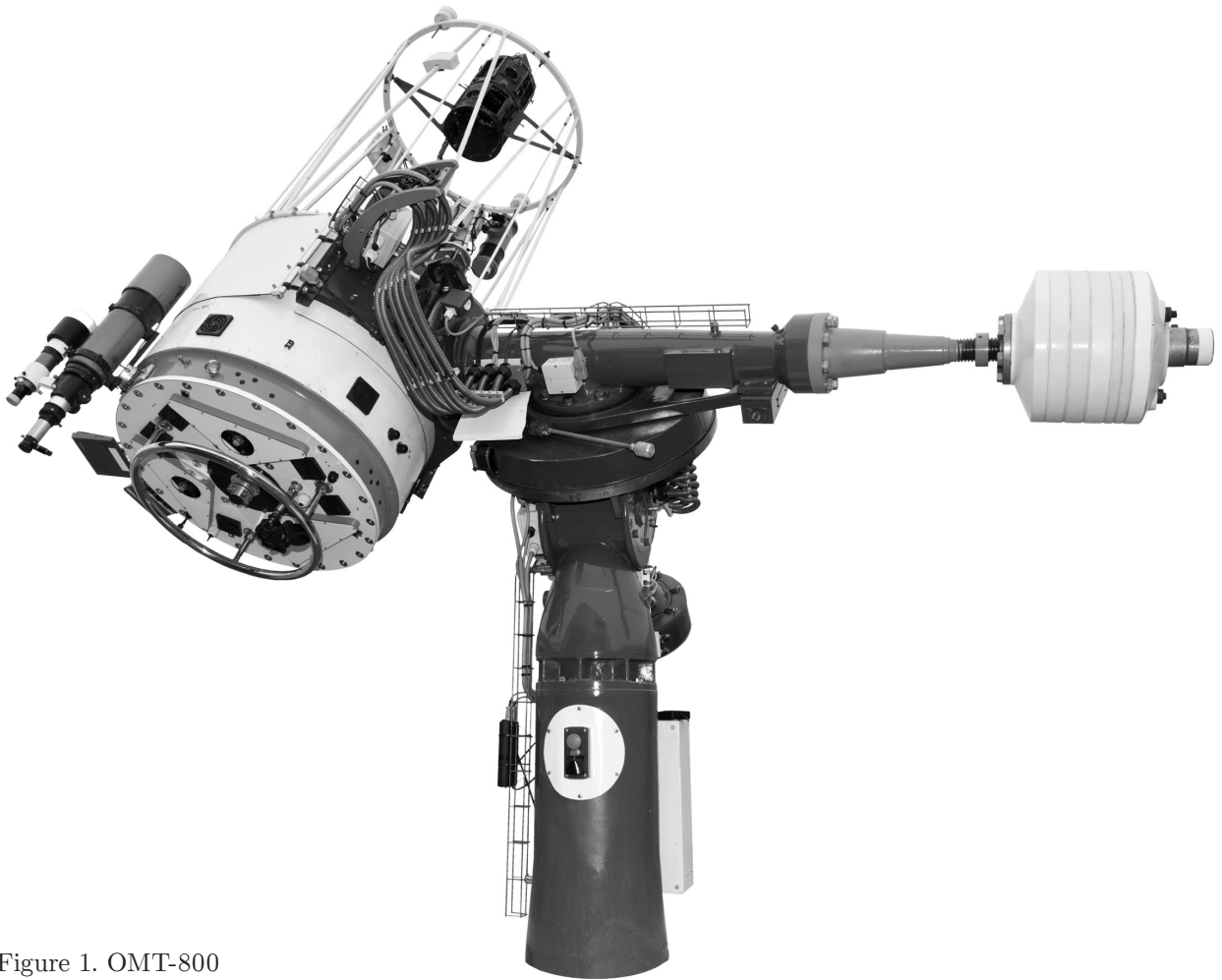


Figure 1. OMT-800

Hazards Warning. As of today, the ISON measurements make up 97% of the total local data on high-orbit space objects and 85% of the data on asteroids. In 2012, more than 5.8 millions measurements were obtained for space objects (more than 15 million measurements have been collected over 6 years) and more than 140 thousands for asteroids (more than 300 thousands of measurements have been gathered since 2010).

The ISON surpasses the capability of the USA space control system by its parameters of geostationary orbit space monitoring as a larger number of objects are tracked with greater accuracy. The project is coordinated by the Keldysh Institute of Applied Mathematics of the Russian Academy of Science where the Centre for Man-made Space Debris Information Collection, Processing and Analysis was established, as well as the division of the ASSHW on the hazard monitoring of objects in the geostationary (GEO), highly elliptical (HEO) and medium-high Earth near-circular orbits.

New telescopes have been developed and manufactured (30 telescopes are installed at the involved observatories); the reconditioning and retrofitting of the outmoded facilities have been carried out, and more

than 50 CCD cameras have been purchased to equip to working telescopes. The unified software systems for the telescope control and automatic processing of the CCD-frames of satellite and asteroid observations were developed, and they have been used at all the ISON observatories.

70 telescopes of the ISON are combined in five sub-systems:

1. The search and survey subsystem of explorer telescopes (with apertures of 19.2–25 cm).
2. The subsystem of telescopes to monitor faint space debris fragments (with apertures of 40–80 cm).
3. The subsystem of telescopes to monitor the bright target satellites in the designated orbit (with apertures of 25–36 cm).
4. The subsystem of telescopes to detect asteroids and comets (with apertures of 40, 60 and 65 cm).
5. The subsystem of telescopes (with apertures from 40 cm to 2.6 m) for the photometric observations of the near-Earth approaching asteroids.

The ISON monitors about 1800 GEO objects, including 300 small-size space debris fragments and around 500 objects in the highly elliptical orbits. Unexpectedly,

a significant number of GEO objects of a new class have been detected, such as those with high area-to-mass ratio that with time are to traverse highly elliptical and even lower Earth orbits. Due to the ISON activities six near-Earth approaching asteroids, three comets and more than 1500 asteroids of different types were discovered; the rotation periods of 14 asteroids were measured; two binary asteroids were discovered; the YORP-effect (Yarkovsky–O’Keefe–Radzievskii–Paddack effect) was successfully detected for three asteroids.

New telescope OMT-800 will be used in the ISON for the GEO monitoring, new asteroid search, as well as to provide useful astrometrical information about known asteroids and comets.

3. The optical layout

The main optical instruments and devices of the described telescope are manufactured in the optical workshop of the Astronomical Observatory of Odessa National University. The workshop is situated at the Observatory suburb station in Mayaki at the distance of about 40 km from the Odessa city. It was established as early as in 1971 for the planned at that time building a telescope with 1.5-meter mirror diameter according to the P. P. Argunov design. Unfortunately, it did not ever proceed to the construction of that telescope, but later a telescope with 1 meter mirror diameter was built under the mentioned design and installed in Slovakia in 2001 (Vihorlat observatory), and it has been still in operation.

There are three rooms with equipment in the above-mentioned workshop, a corridor for the knife-edge tests of optical instruments, as well as a separate room for the vacuum aluminizing of mirrors. There are ten optical machines, most of them were commercial non-sellers and were subsequently partly repaired and upgraded.

The edge-trimming and grinding-and-polishing machines KOS-750 and SP-700 can be used for large mirrors. The latter was considerably reworked so that it became possible to make mirrors with diameters larger than 700 mm and, what is crucial, to control the mirror shape just by placing mirrors into vertical position not taking them away from the machine.

The sital mirror blanks were purchased as early as the Soviet times, generally, from the Lytkarino Optical Glass Factory (Russia). In the late 70’s our Astronomical observatory managed to purchase three off-the shelf mirror discs of 0.8-m diameter. That mirror size was in very short supply. Those mirror blanks were used to make mirrors for our telescopes mounted at Terskol peak, Northern Caucasus (the Cassegrain telescope), in Turkmenistan (the Ritchey–Chrétien telescope), and also a mirror for the telescope described in the present article.

We started to make the mirror for the described telescope (of the Ritchey–Chrétien design) in late 80’s (for the other purposes at that time), but shortly after, the work was stopped. It was resumed only about twenty five years

later under another programme, and for another optical layout, namely for prime focus with corrector.

The optical layout of the new telescope that was put in operation with a mirror diameter of 800 mm can be called a catadioptric plan anastigmat. When developing the layout, it was intended to have as wide angular field of view as possible with 2-inch CCD with a good relative aperture. A rather high image quality across the whole field of view was implied. We also made some additional requirements to ourselves.

The known arrangement of hyperbolic mirror with four-lens Wynne corrector (Wynne, 1949) was chosen as a prototype. The corrector with four lenses of the most common types of glass, which are easily available, showed quite good results only provided that the last element of length is small. That is why we had to secure that a camera with extremely small distance between the cover glass and the light-sensitive chip had to be used as a light sensor.

The layout with aspherical primary mirror and four-lens corrector has a rather adequate number of corrector parameters both to compensate most aberrations and to gain a series of extra properties. We managed to get not only a working value of aberration spot with the flat field of view of 1.3°, but also the following: 1) two of four lenses can be stuck together with optical balsam; 2) the rearmost surface of the corrector is flat; 3) the curvature of non-adjacent surfaces of two lenses is the same. Extra properties were necessary, in particular, to reduce the number of trial lenses to control the surface shape. Those lenses were manufactured at the factory of special instrumentation “Arsenal” (Kiev, Ukraine).

When checking each next manufactured lens, the inevitable inaccuracy of the lens thickness was obtained. The layout was optimised according to the actual situation with thickness of unmanufactured lenses and air gaps varying. Though a slight deterioration of the result ensued from each variation, the final set of the telescope design values remained quite good. Such methods are called “optical maintenance”, they promptly facilitate the manufacturing of unique optical sets.

At first, we intended to install a flat mirror next to the primary one to shorten the tube, and such mirror was manufactured. But due to the reasons of minimization of optical surfaces number we refused to use this flat mirror afterwards.

In accordance with the new decision, it was necessary to lighten the telescope tube as the supporting mounting APT-6 (astronomical parallactic tripod of type 6) operates at the breaking point.

The basic parameters of the telescope are as follows: the entrance pupil, focal ratio, total length of the telescope optic layout, field of view and spectral range. The design values are surface curvature, air gaps and lens thickness, refractive and asphericity indices. The image quality for large- and medium-size non-visual telescopes can be adequately represented by dot charts.

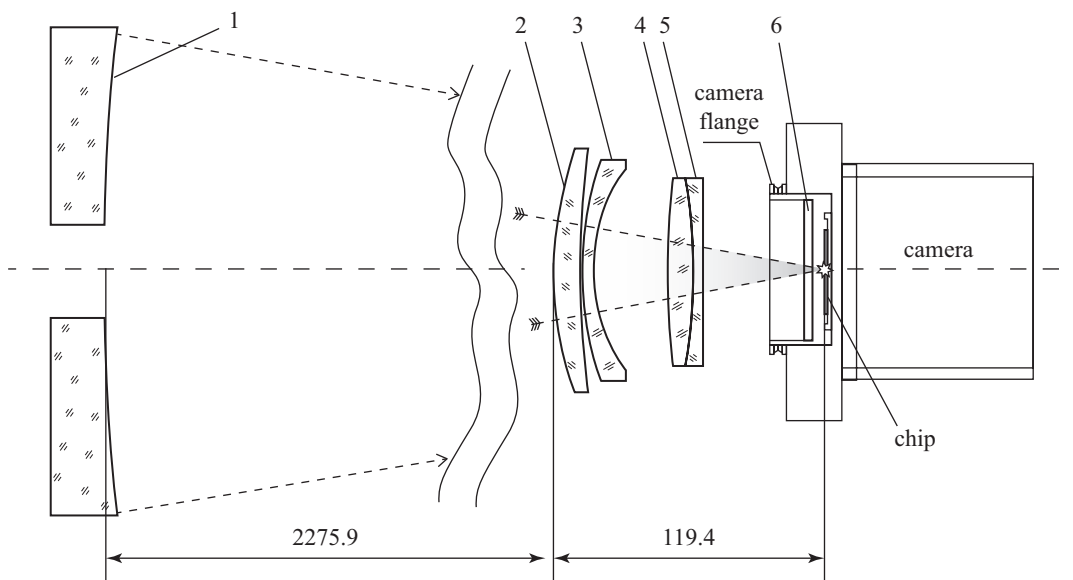


Figure 3.1. Catadioptric scheme with corrector (see numeration in Table 3.1).

Table 3.1. Optical characteristics of the constructive elements of OMT-800.

#	detail	surface curvature radius	next surface distance	eccentricity square	type of glass	diameter of detail
1	main mirror	-4796.35	-2275.90	+1.1986	LK5	800
2	first lens	-135.52	-11.54	0.0	K8	98.4
		-498.90	-0.10	0.0		
3	second lens	-135.52	-7.29	0.0	K8	90.2
		-66.76	-30.20	0.0		
4	third lens	-219.95	-10.00	0.0	K8	74.8
		+219.95	0.0 (glued surfaces)	0.0		
5	fourth lens	+219.95	-3.00	0.0	F1	74.8
		∞	-48.70	0.0		
6	protective glass of the CCD		-3.20	0.0	quartz	60
7			$S' = -5.334$	0.0		

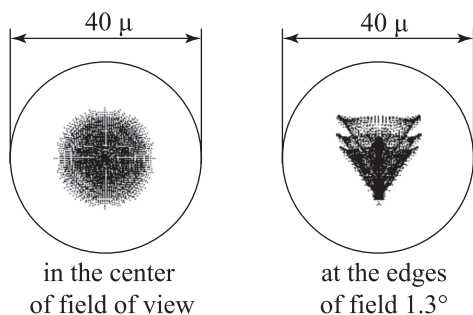


Figure 3.2. Estimated image quality for catadioptric scheme with corrector.

We provide the optical layout, measured design values, as well as estimated dot charts of our telescope optics (Fig. 3.1, Fig. 3.2 and Table 3.1).

As is seen, the stellar images corresponding to one pixel of the astronomical camera might be expected across the whole field of view.

Actual image quality as for all other telescopes, by the way, will yield to the estimated quality due to deflections, manufacture inaccuracy, alignment, focusing, sidereal tracking, as well as the limb effect, atmospheric turbulence, etc. The focal surface of the telescope is flat. The distortion is the only essential aberration. It reaches 7.25% at the edges of the field of view.

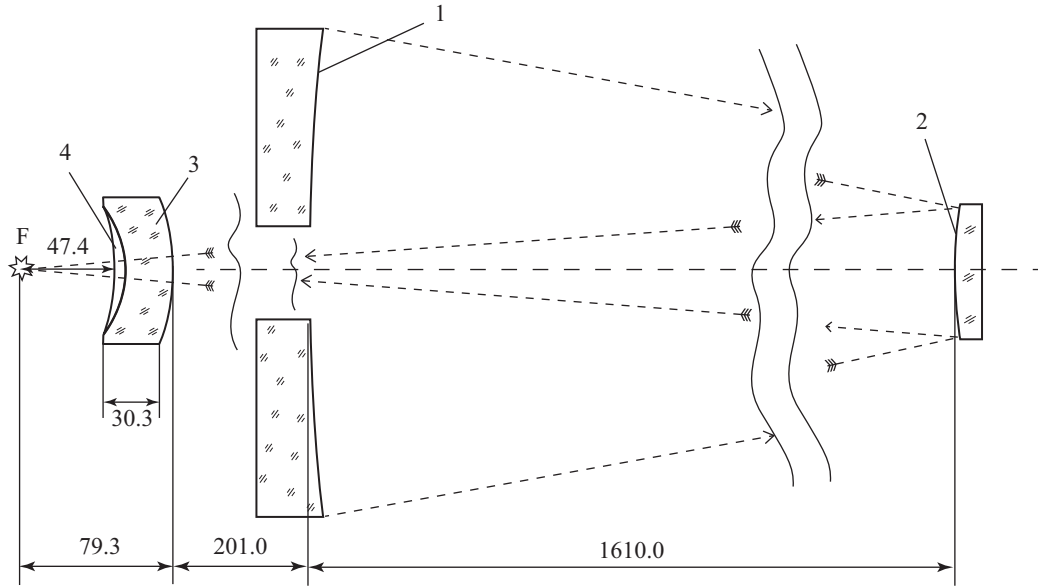


Figure 3.3. Optical layout for alternative two-mirror scheme (see numeration in Table 3.2).

Table 3.2. Optical characteristics of the constructive elements for the alternative scheme.

#	detail	surface curvature radius	next surface distance	eccentricity square	type of glass	diameter of detail
1	main mirror	-4796.35	-1610.00	+1.1986	LK5	800
2	secondary mirror	-2700.00	+1811.00	+8.8980	LK5	270
3	first lens	+103.60	+25.00	0.0	F1	80
		+58.37	0.0 (glued surfaces)	0.0		
4	second lens	+58.37	-7.00	0.0	K8	80
5		+103.60	S'+47.50	0.0		

As the primary mirror of our telescope is a hyperboloid, and moreover, it has a central opening, we manufactured additional second convex mirror to have an alternative optical layout similar to the Ritchey–Chrétien design in case of any possible future changes in the observation programme. The alternative optical layout expanded with special field-flattener lens that also corrects astigmatism, and scarcely causes chromatic aberrations, (according to the estimated dot charts) will allow to obtain very high-quality image, higher relative aperture (for such type of layouts) $A = 1:6.4$ and relatively wide field of view $2w = 0.66^\circ$ deg or 58.9 mm in diameter. The total length of the telescope optic layout $L = 1890.5$ mm (see Fig. 3.3). The spectral range of achromatisation is still the same, i. e. $\lambda = 0.486 \div 0.820 \mu\text{m}$. Fig. 3.3, Fig. 3.4 and Table 3.2 explain alternative scheme.

As is seen, the estimated aberration images do not exceed 10 micrometers. The distortion at the edges of the field of view is just 0.23%.

While polishing the primary mirror, its shape was controlled by the Maksutov compensation scheme

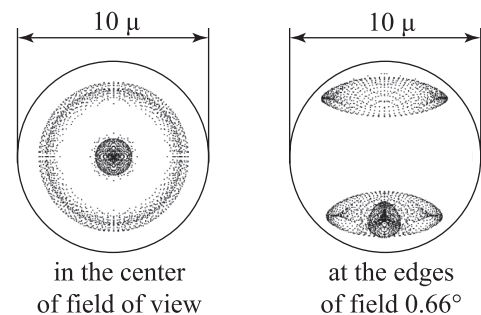


Figure 3.4. Expected image quality for alternative two-mirror scheme.

(Maksutov, 1948) with a spherical auxiliary mirror of 320 mm diameter and a flat diagonal mirror to shift the auto-collimation point to the Foucault knife. The aspherization was executed by the method of almost critical overhanging of the polisher sideways at minimum crank velocity and relatively high spindle velocity. It took almost six months to manufacture the mirror.

Table 3.3. The main characteristics of OMT-800

Main mirror diameter, <i>mm</i>	800
Telescope effective diameter, <i>mm</i>	755
Telescope total optical length, <i>mm</i>	2395.3
Telescope effective focal length, <i>mm</i>	2134.3
Focal ratio	1:2.67
Mass of main mirror, <i>kg</i>	75
Focal length of main mirror at apex, <i>mm</i>	2398.2
Main mirror eccentricity square	1.1986
Max deviation of main mirror from the ideal surface, <i>nm</i>	60
Linear diameter of the field, <i>mm</i>	49.14
Angular diameter of the field, <i>arc min</i>	78
Spectral range of achromatization, <i>nm</i>	486–820

While manufacturing lenses, the most intricate problem was to adjust radii without sagging of the lens thickness as such adjustment was made with glass grinders that do not keep their curvature. The first results, obtained with our telescope, show an expected image quality.

The main characteristics of OMT-800 are listed in Table 3.3. More detailed information about optical layout can be found in Fashchevsky (2011) and Michelson (1976).

4. Telescope mechanics

A modern telescope is an integrated complex that contains optical components, mechanical assemblies, systems for their control and monitoring, as well as system of recording and pre-processing of optical data.

Correct operation and interaction between any component and all the others are crucial for the whole system performance and successful resolving of the set observation tasks.

Generally, when commencing the telescope design work, the tasks that should be solved with this instrument and relative requirements for all system components are defined. However, it is not always the case. When building OMT-800, we had to proceed, first of all, from our technological capabilities and financial resources.

Though the concept of such an instrument with the primary mirror diameter of about 1 meter was discussed by Odessa engineers several decades ago (and there was a considerable background for that, since comprehensive experience in manufacturing of rather large-size astronomical optics existed as the whole department for instrument making, headed at that time by L. S. Paulin; and there was an availability of suitable optical blanks,

required equipment, instruments and materials), only 4 such instruments were manufactured for the whole period. Two reflectors with a 0.8 m primary mirror diameter were installed in Turkmenistan (on the Mt. Dushak-Erekdag) and in the Caucasian mountains (Terskol Peak); one reflector with the primary mirror diameter of 1 m was installed in Slovakia, and one reflecting telescope with a 0.6 m primary mirror diameter – at the observation station in Mayaki. It should be noted that the control of those reflectors demanded great efforts and that rendered the work of observers hard.

One of the basic features that could distinguish OMT-800 from all previous telescopes with mirrors of similar diameters was to manufacture a modern automatic telescope that could make observations not only useful from the astronomical standpoint, but a pleasant occupation. Such reflector was aimed to solve the set of tasks at a qualitatively new level. It was those conditions that determined basic requirements for mechanics and control system.

First, several alternate solutions of the task were suggested. But we proceeded primarily from our capabilities. There was a factory-made telescope mount APT-6 (astronomical parallactic tripod, manufactured by Leningrad Optical Mechanical Association) available; it remained after disassembly of the time-expired Seven-camera astrograph at Mayaki observation station, which should be thoroughly remodelled to become a basis for building an automatic telescope. The operational experience of our reflecting telescope with 800 mm diameter of the mirror with such mount, installed in Turkmenistan, showed that such a combination enabled to solve some observation tasks, but the load of the telescope mount was provided to be limit in so doing. The telescope automation inevitably demands large reworking of APT-6 as the stiffness, accuracy and the limit torque requirements are much tighter in that case. APT-6 has a 360 tooth precision worm gear pair in the polar axle for the sidereal tracking. That worm gear pair was retained after rework and has been used to control telescope's motion relative to that axle. The axle itself is in a rather strong mount, and it required relatively small reworks. Nevertheless, for many years of the previous exploitation of APT-6 its bearings and some components were notably threadbare and needed replacing or reworking. We removed all unnecessary components related to the manual control and provided for the possibility of obligatory installation of the angular displacement sensor. We made necessary adjustment, repaired the angle of altitude and azimuth control mechanisms.

But the key work that had to be done was the modernization of the declination axle. First of all, the existing axle did not provide the required stiffness. Careful examination of the design let find reserves for an increase in rigidity. Besides, it was necessary to design, manufacture and install a worm gear pair in the axle not decreasing the stiffness that is already limit enough,

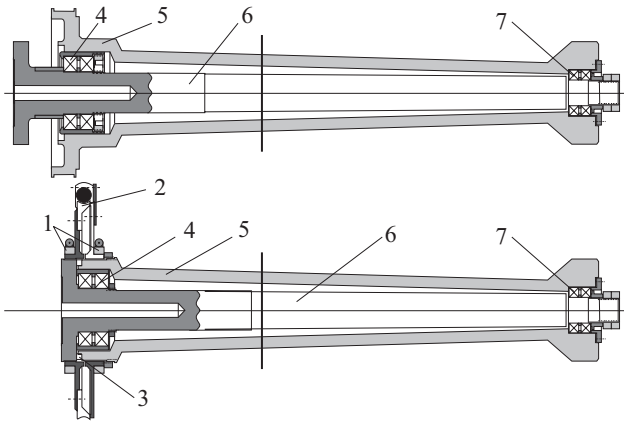


Figure 4.1. The declination axle arrangement before (upper figure) and after (lower figure) reconstruction.

1 – friction clutch couplings, 2 – the worm gear pair, 3 – the front thrust bearing, 4 – the front radial bearing assembly, 5 – the axle housing, 6 – the declination axle, 7 – the rear radial thrust bearing assembly.

to find place for the declination motor and angular displacement sensor, as well as to provide for proper and reliable joint between the telescope mount and tube; and also to manufacture a new precision friction brake and provide necessary alignment of the worm-gear.

The declination axle arrangement before reconstruction is shown in the upper part of Fig. 4.1, and the result of modernization is shown in its bottom part. It is seen how the design changed and due to what its stiffness increased. The axle became shorter, its overhang from the support bearings became minimum, and at that the flexure deformations are immediately transmitted through the front thrust bearing to the axle body and due to that they are decreased considerably. Being modernised, the centre of mass of the telescope tube can be brought much closer to the axle body that will undoubtedly improve the operating conditions for the mount and considerably decrease quantity and mass of the counterweights and, therefore, the total load and the moment of inertia. The friction gears enable to disconnect the worm gear pair from the axle if necessary and to install it in any convenient position, and due to their specific design they provide additional stiffness. A 300 tooth worm-wheel and worm gear with the same module as that one in the declination axle were available, but required some improvement. After manufacture and assembly that pair was aligned and seated. That procedure shall be regularly repeated to ensure the final adjustment of the worm gear pair.

Using specific couplings in the worm gear drive we installed stepper motors with 200 steps per revolution and 64 microsteps per full step operating at up to 2.8 A, which provide maximum pointing speed of up to 1 degree per second. That ensures the required drive rate, as well as fair accuracy of telescope's pointing to an object. As a result, we obtain a German type paral-

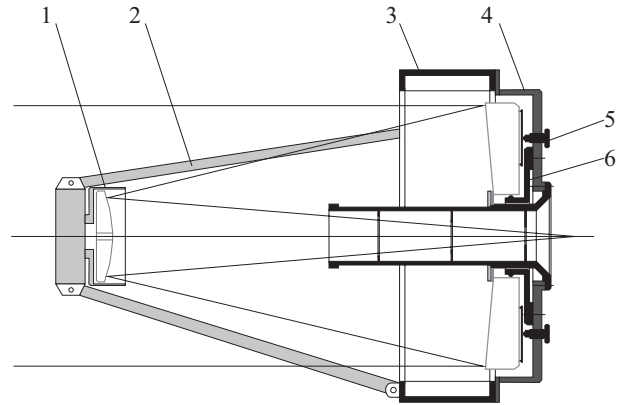


Figure 4.2. The design of the first version of the telescope tube.

1 – the secondary mirror assembly, 2 – support fork arms, 3 – hexagon declination-box frame, 4 – the primary mirror support cell, 5 – support mechanisms, 6 – the central pivot.

lactic mount with new capabilities, which enables to arrange observations more effectively and to improve the telescope efficiency considerably.

It should be noted that all that hard work on modernization of the mount was done with the only available 1K62 lathe that was far from being new, and for which the machining of components with such dimensions was virtually beyond its capabilities. However, some ingenuity, as well as manufacture of necessary additional auxiliaries eventually let machine the axle, mount body, worm-wheel and friction gears with required accuracy.

The next essential component of the reflector mechanics is the tube. There are a lot of requirements imposed upon it, and those are sometimes mutually exclusive. The tube must secure proper and stable mutual arrangement of optical elements, minimise their inevitable deformations or, if possible, compensate them, enable to perform accurate alignment and focusing of optics within the required limits, and provide specified temperature and humidity conditions. The tube is also aimed to compensate adverse temperature effects, to protect optics against extrinsic interference, polluting light that interferes with the telescope viewing. When manufacturing the tube, it is necessary to provide the possibility to mount accessories on it, as well as to ensure the feasibility of balancing with minimum additional counterweights. And in spite of all that, the tube must be lightweight, high-strength and rigid. And that is far from being a complete list of requirements.

When manufacturing the tube in accordance with the above-indicated requirements, some errors are likely to occur. The first version of the tube design for the described instrument turned out to be faulty, though it was that variant (see Fig. 4.2), which was implemented in manufacturing of our telescope, installed in Turkmenistan.

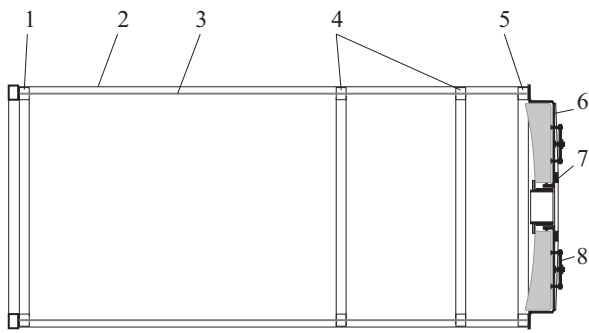


Figure 4.3. The design of the second version of the telescope tube.

1 – the front mounting ring, 2 – the covering shroud, 3 – longitudinal braces, 4 – the declination-box frame, 5 – the rear mounting ring, 6 – the mirror support cell, 7 – the central ball-bearing support, 8 – the support and collimation mechanisms.

Such design includes three fork (three-“feather”) arms that must support the secondary mirror assembly, a hexagon girder declination-box frame, welded dish-shaped primary mirror support cell with load bearings support mechanisms, the central pivot and the light detector mounting assembly at the rear. It was expected that when using corrector instead of secondary hyperbolic mirror, a flat mirror will be installed in its place to let the light passed through the corrector to reach the CCD camera inside the tube. Later, it turned out that despite apparent simplicity and usability of such an arrangement it has a lot of grave disadvantages. The main objections are excessive weight due to ineffective masses of metal and relatively far distance between the optical axis and the mount body that causes a considerable increase in counterweight, the moment of inertia, total load of the mount and control system.

Instead of that a design of solid tube containing thin (of 1 mm thickness) steel shroud with two mounting rings and distance pieces between them in the middle section of the tube and the similar rings at its ends. A holder, where the alignment and focusing mechanism, corrector and the CCD camera are installed, is attached to the front ring with support vanes. The mirror support cell is fixed on the rear ring. The whole construction is tightened with six longitudinal braces and is prestressed, and that considerably decreases the flexure deformation and improves the overall strength. Such a design has been used in telescopes, manufactured by our observatory specialists, more than once and proved to perform well. The primary mirror cell remained the same, but it was machined on a large lathe with ineffective excess metal removed. In accordance with the new design the support and collimation mechanisms were made. The central ball-bearing support was installed. To attach the tube to the declination axle, a special cradle and a thin-walled band clamp were manufactured from a part of remained hexagon declination-box frame. The tube proved to be very strong, light with reliable protection of optics and compliant with main requirements (see Fig. 4.3).

Nevertheless, when manufacturing the tube of the second design we did not take into account the fact that the tube of such design should have a significant windage, which will have significant impact on the observations because of absence of the dome. That is why it was decided to leave the middle and rear sections of the tube unmodified, and to rework the front section (approximately 2/3 of tube length), to the lattice truss made from concurrently as thin as possible and durable bars strengthened with braces. That is how the final design of the tube eventually was worked out (see Fig. 4.4).

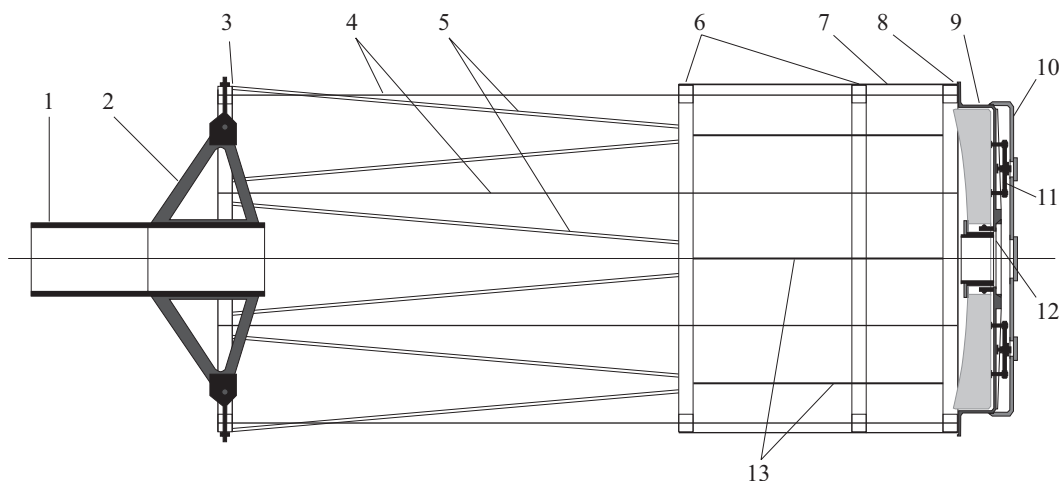


Figure 4.4. The design of the final version of the telescope tube.

1 – the central holder, 2 – support vanes, 3 – the front mounting ring, 4 – longitudinal braces, 5 – components of the front truss, 6 – the declination-box frame, 7 – the covering shroud, 8 – the rear mounting ring, 9 – the primary mirror support cell, 10 – the protective cap, 11 – the support and collimation mechanisms, 12 – the central ball-bearing support, 13 – inner distance pieces.

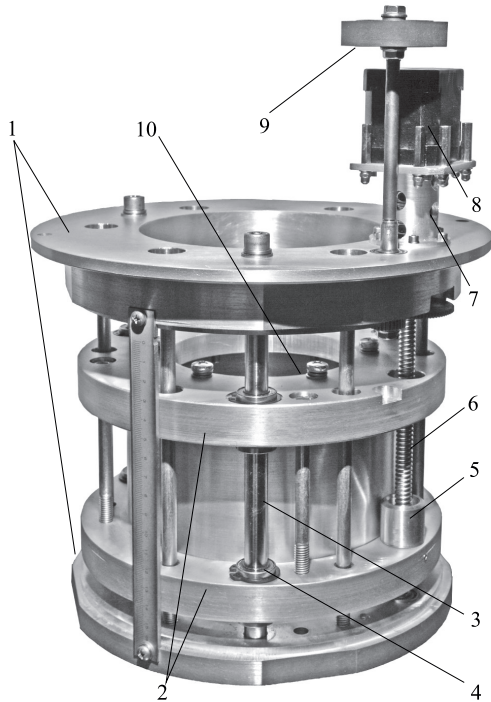


Figure 4.5. Focusing mechanism.

The large-aperture telescope requires quite frequent and precise focusing procedure. For this aim we developed and manufactured the focuser of our own original design. A general view of this focuser is shown in Fig. 4.5. For the better visibility of details we give its image as it looked before painting. Focuser provides very precise linear movement of its movable part 2 relatively to its fixed part 1. Movement is provided by three pairs of linear motion bearings 4, rigidly coupled to the moving part on the three precisely fixed guides 3, which in turn are rigidly coupled to the fixed part 1. The motion can be achieved either by the rotation of the handle 9, or the by the stepper motor 8 related to the screw drive via zero-backlash flexible coupling 7. Screw 6 is mounted on the fixed part of the focuser between the two angular contact ball bearings with adjustable buttress screw. Ball screw nut 5 is mounted on the moving part of the focuser. Both together screw and nut form precise ball-screw pair (made by Hiwin, <http://hiwin.com>) with a step of 2.5 mm per turn. Flange 10 of the moving part is used to attach corrector to the camera FLI ML9000.

Remotely operated focusing mechanism, including the lens corrector, adapter flange of the CCD camera and the CCD camera itself, is installed in the central holder. The alignment mechanisms are placed on the outer surface. The arrangement allows for temperature regulation and drying-out when the humidity is excessive. The holder being two-point fixed to the support vanes is four-point attached to the front mounting ring with four support vanes. Such an arrangement distinctly stabilises its centred position, although slightly worsens the diffraction

pattern. Thin (15x15 mm) standard hollow bars that form a truss similar to the Serrurier truss are welded in six points to the front mounting ring and to the first ring of the central section of the tube. The central section of the tube is clamped with a thin (1 mm) band and special cradle that secure the tube's attachment to the declination axle with very slight deformations, as well as provide for adjustment of the position of its centre of gravity relative to the axle that is useful when the preliminary balancing is performed. The end rear ring holds the primary mirror cell, which is bolted on the inside of the tube. The mirror held in support cell is mounted on the central ball-bearing support that provides the lateral support and the mirror's tilting not changing the required centred position. To provide the longitudinal support, the Grebb classical nine-point support system is used with arrangement of mechanisms, which also allow for adjustment to the collimation, on the outer side of the cell. The support cell is equipped with the mirror temperature offset and ventilation system. A light rear cap protects the supports and the mirror and makes the manual control of the telescope easier that is crucial in case of emergency.

The complete telescope general arrangement is presented in Fig. 1.

5. Electric and electronics of OMT-800

The power supply for all telescope systems is provided by four switching power supply units, placed in the IP54 damp-proof and dustproof power distribution electroassembly box, mounted on the telescope column. All cables enter the power distribution box through the cable glands not damaging its leak-tightness. To maintain the temperatures permissible by manufacturers of the power supply units and the telescope control system, as well as to avoid condensation, a 50 W heating element and the regulation relay that automatically switches it on at temperature below +10°C are installed in the power distribution box.

A&I GoTo System controller (<http://gotosystem.xm4.ru>) is selected as the telescope control system. That controller uses common control protocol compatible with the Synta EQ-6 mount control protocol. The controller software is compatible with the ASCOM standard; hence, the telescope control can be carried out by any ASCOM-compatible software.

Further to our request, the following modifications of the off-the-shelf controller were designed:

1. Heavy-duty control switches for the stepper motor windings were installed.

2. The Trimble Copernicus II GPS receiver module that differs from the standard one in availability of two serial ports and the high-accuracy pulse per second output was installed. One serial port of the GPS module is connected to the telescope control processor to assign the observation point position and accurate time; the

second serial port is connected to the control workstation to provide the NTP-server functioning. The pulse per second is used to the precise synchronization of the CCD-camera shutter.

3. The controller is equipped with emergency contacts allowing of development of the system of telescope emergency stop on the occurrence of different events associated with the tube orientation or dangerous proximity of the camera to various objects without losing orientation of the tube axes. Such a system is currently being developed on the basis of ultrasonic sensors.

4. Taking into account the great weight of the telescope, the controller firmware has been modified to provide a smoother acceleration and deceleration of axial motors.

The telescope management controller operates two Trinamic QSH6018-86-28-310 two-phase hybrid motors. Those stepper motors were optimized to achieve the microstepping mode. The step angle of the motor is 1.8°. The maximum torque is 3.1 nm. The motors have standard NEMA23 flange that enables to easily replace the telescope control system with another one, for instance, with the DC motor control system, just by changing the stepper motors and telescope controller.

The focusing mechanism is controlled by the AS-COM-compatible Colibri focus controller (http://gotosystem.xml4.ru/astrokinetic_fokuser_kolibri) that was modified just by repacking in the IP54 case. The controller operates Trinamic QSH4218-51-10-049 focusing stepper motor (with the step angle of 1.8°, the torque of 0.49 nm and NEMA17 flange). The stepper motor functions in the microstepping mode at 1/16 stepping and rotates the screw of the ball screw assembly with the thread pitch of 2.5 mm. Thus, one microstep of the focuser stepper motor corresponds to the linear displacement of 0.781 μm. The temperature sensor is connected to the focuser controller, and on having correspondingly configured the focus controller, it allows of automatically readjusting the focus when the tube temperature changes. The parameters of the automatic thermal tuning of the focus are empirically

determined following several estimations of the focuser best position at different temperatures.

The power supply for all telescope systems is provided by four power supply units, installed in the power distribution box. The functionality, marking and peak current for each power supply unit are given in Table 5.1. It should be noted that the peak voltage available on the telescope tube is 12 V. Therefore, the telescope is accident-proof in terms of electrical safety.

There are three emergency buttons mounted on the telescope column, beside the outer door of the pavilion, and on the operator workplace. Pressing of any of those buttons, results in immediate breaking power supply to the power distribution box of the telescope. Therefore, in case when immediate emergency stop of the motion of the telescope or any other device is needed, the observer can promptly perform such a stop staying in the control room or in the pavilion.

The IP video camera Axis 206, whose image is displayed on one of the operator's monitors, is installed in the pavilion with the aim to visually survey the telescope motion when pointing. While pointing, switching on the spotlight in the pavilion from the control room is provided.

On the assumption that most telescope movements are to be not controlled by an operator, we pay particular attention to the cable that is laying from the fixed column to the tube of the telescope and to the further cable routing through the telescope tube, so that the snagging and damage of the cables are avoided (Fig. 5.1). To ensure safety of the cables, the declination axes and two cable masts were manufactured and installed on the declination axis body and on the telescope tube mounting assembly, respectively. Six Lapp SILVYN FD-PU flexible tubings, that are resistant to mechanical damage and keep flexibility within a wide temperature range, were laid between the cable mast of the declination axis body and the column, as well as between the telescope tube cable mast and the declination axis body. Those tubings are connected to each other by the line connectors that integrate them in the united flexible flat cable trunk. It

Table 5.1. Power supply characteristics.

Marking	Power supply unit, current, type	Using equipment
24V	24V, 12A, switching	A&I GoTo System telescope management controller.
12V-S	12V, 12.5A, switching	Camera FLI ML09000, meteor camera, Colibri focusing controller.
12V-U	12V, 20A, switching	Devices for heating the tube, focuser, telescope finder and guiding telescope, as well as for the primary mirror cooling.
5V	5V, 10A, switching	USB concentrators, lighting of the filed of view of finderscopes.

Table 5.2. Cable characteristics.

Cable line	Functionality	Cable type	Quantity
1	Power supplies	Lapp Ölflex FD 855 P 7G2.5	1
2	Signal lines	Lapp Ölflex FD 855 P 25G0.5	1
3	Operation of the declination motor	Lapp Ölflex FD 855 CP 4G1	1
4	Coaxial video cables	TASKER RG58PUR	6
5	Ethernet cables	Molex PCD-00183-0E	6
6	USB 2.0 cables	Belkin F3U154CP4.8M	2

is possible to replace any group of cables without disconnection or disassembling of other cables. The functionality and quantity of cables in each tubing are given in Table 5.2.

Continuous-flex cables, designed for moving applications down to -25°C , are used for flexible cable trunks. Power cables, signal line cables, as well as shielded cables for declination motor control on the side of the column, and on the side of the tube are terminated with high-quality industrial EPIC® connectors, produced by Lapp Group. The coaxial cables on the side of the column and on the side of the tube are terminated with BNC connectors. The Ethernet cable lines are terminated with RJ-45 connection modules.

Two plastic tubes with junction boxes in the middle and at their heads are laid along the telescope tube for cabling. Cable glands are fitted in those boxes to feed the cables through to connect to the devices as required. Therefore, the cable trunks have a level of dust and humidity protection not less than IP54.

The larger the telescope size is, the oftener the limitation of the USB cable length, which can not exceed 5 m as per specification limits, causes inconvenience at the designing stage. There are USB active extension cables available in the market, but, generally, most of them are of poor quality, and their lengths do not exceed 10 meters. Hence, it was decided to omit USB active extension cables, and to use USB concentrators with cables not longer than 5 meters between them. We also considered the limit for the number of USB concentrators to be not more than 5 units per chain. The USB concentrators' layout and the lengths of cables between them are given in Fig. 5.2. As a result, we are enabled to connect the USB 2.0 devices to the telescope wherever possible using short cables.

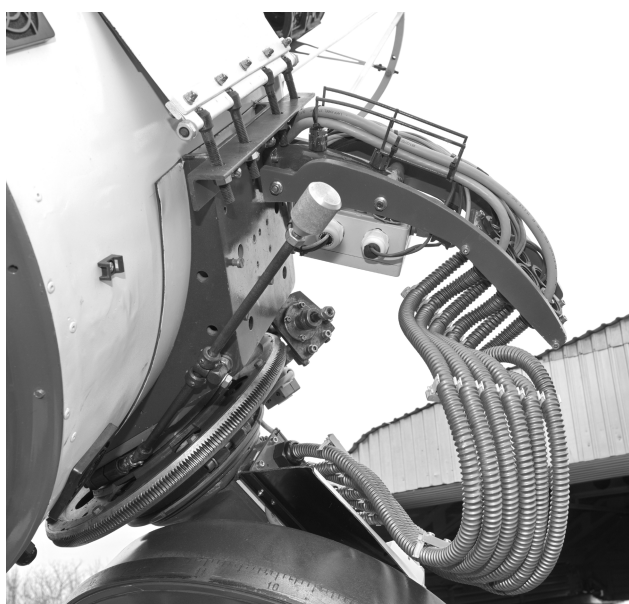


Figure 5.1. Cable-main at the telescope mounting.

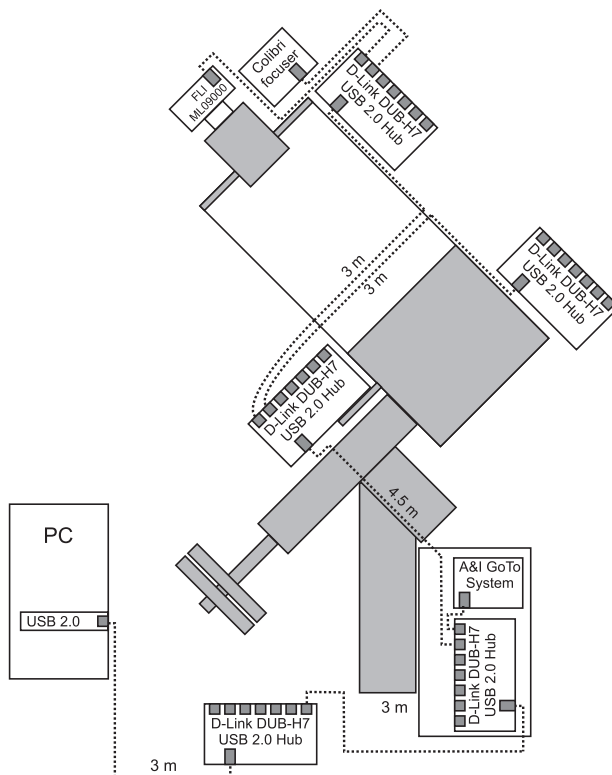


Figure 5.2. Architecture of the USB network of OMT-800.

When designing our telescope, we paid an attention to the heating-up of the optics to prevent condensation and freezing problems. The 18W self-adhesive film heating elements connected to 12V power supply were used for optics heating. There are six heating elements mounted inside the tube near the mirror cell: two of them were mounted inside the outer housing of the focusing sleeve, and one each — on the dew caps of the guiding telescope and finders.

Taking into account a considerable mass of the telescope primary mirror, to equalise the primary mirror temperature to ambient temperature, six fans were mounted on the rear cover of the mirror cell and six fans were placed within the lateral surface of the pipe for blower cooling of the primary mirror. The fans of 80 mm in diameter have replaceable filters that prevent ingress of dust to the telescope tube. The blowing and heating are controlled by the blowing and heating control console mounted on the mirror cell of the telescope.

Telescope is operated from the control room, which is located next to the pavilion of telescope. USB network of telescope is connected to the only one USB 2.0 port of managing workstation HP Compaq 6000Pro. There is also output of GPS receiver connected to RS-232 port of this workstation providing operation of the NTP server.

6. Optical adjustment procedure of OMT-800

Telescopes rarely achieve the image quality that is accomplished “on paper”. When computing, it is assumed by default that all optical components are coaxial and mutually distant in a quite definite manner. However, in fact, the main optical axes are rather speculative, and their actual adjustment is not controlled; meanwhile, long typical length of a telescope’s body tube makes it difficult to align the optical components with adequate accuracy.

There are certain methods to optimise the image quality, which depends on optical adjustment of a telescope. The procedure consists of such shifts and tilts of the components that must result in the image enhancement. The sequence of operations depends on the specific optical circuit and methods applied by a technician.

Theoretically, each optical component of the axisymmetric telescope optics should be five-degrees-of-freedom aligned. Our telescope consists of six components: the primary mirror, four internal lenses, assembled in the corrector’s body and CCD camera. There is a good reason to suppose that this body was likely to be constructed rather efficiently, providing proper mutual arrangement of lenses, therefore it can be suggested to assemble them as an integral block. Besides, the mirror, which is fixed by axial and lateral supports, is generally not allowed of any linear shift. Hence, the number of possible angular and axial adjustments can be rather small, i.e. the adjustment (centring and focusing) of our telescope should not be technically intricate to perform.

Though the above-mentioned corrector lenses assembly is placed very near to the telescope’s focus, the angular and lateral misalignment of the components manifests itself mainly as the decentring coma, i.e. comatic aberration that seriously damages the quality of images. On the sky snapshots, obtained under these conditions, the stellar images are blurred and wedge-shaped, even in the centre of the field.

Just a 10 mm parallel shift of any component relative to another one across the principal optical axis results in inadmissible aberration spot expansion up to 0.2 mm. A shift up to 1 mm can be considered not hazardous as such the aberration spot does not yet exceed the dimensions of one pixel.

Parallel misalignment of the mirror and the corrector axes also adds to a certain lateral shift, by so doing summing up the damage from both types of decentring. Mutual tilting of axes of our telescope is not critical unless the tilt exceeds 1.5 arc minutes. It is difficult to provide such order of accuracy of centring.

The situation can be saved by counterdecentring, i.e. by counterbalancing the mutual tilted axes with lateral shift of components in the opposite direction. In that case, both decentring comas are differently directed, and they compensate each other to a great extent. For instance, with the tilt of axes of a quarter of a degree,

the counterdecentring lateral shift by 10 mm results in a quite adequate aberration spot of average diameter of about 0.015 mm. Although, in so doing, the centre of the field and the centre of the best images diverge by about the same 10 mm as mentioned above, the radial symmetry of the spots dimensions relative to those centres is broken, and there is some inclination of the focal surface to the light detector plane occurred. All that could be neglected, but it should be taken into account. Thus, examining the shape and size of the star image on the monitor allows of possible more or less adequate centring the telescope.

However, at the very beginning of adjustment procedure, the instrument tends to be poorly adjusted and its star-image-wise centring is not efficient due to very strong coma. That is why the first-approximation centring is carried out by indirect methods, which are described below.

Other considerations on the tolerances are as follows:

1. Inaccuracy in the distance between the lenses, as well as in the distance between the lens assembly and the mirror and (or) light detector generally results in the increase of spherical aberration – the star images enlarge, and fringes around bright stars’ images or the ring-shaped images of dim stars on the monitor screen are clear evidences of such aberration.

2. Inaccuracy in measuring the thickness of lenses increases the chromatic aberration substantially. Such aberration is clearly seen on the RGB monitor, and on the monochrome monitor the edges of starspots are blurred with fringes noticeable around. At the periphery of the field starspots are oblong in the radial direction due to the lateral chromatic aberration.

As the lens thicknesses and distances between them in the assembled corrector do not vary, all such failures are on the manufacturers’ conscience. In our telescope the rear element of length, i.e. the distance between the rearmost surface of the fourth lens and the camera, is fixed. It is only the air gap between the mirror and the first lens, which is still within a technician’s power to fix. The focusing is carried out by adjusting that distance.

To make the initial centring of corrector accurate and reliable, it is possible to use the concave mirror attached and clamped to the corrector’s body (Fig. 6.1). The wedge angle of that mirror should be corrected during the manufacturing process, and the mirror’s curvature should be such as with ideal telescope focusing and centring its centre coincides the centre of curvature of the primary mirror.

Let us fix our light source in the point of convergence, i. e. the centre of curvature C of the primary mirror 2. If the mirror and corrector axes are not parallel to each other, then the adjustment mirror will reflect that light source in some point 4 as another spot of light on the screen. Should our corrector be turned around using the adjustment devices so that the spot of light 4 would also converge to point C , then the corrector is to be equally

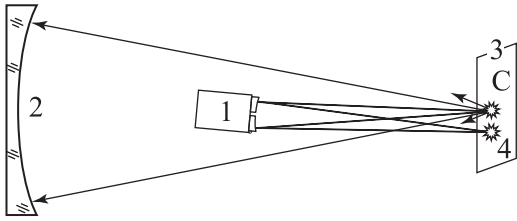


Fig. 6.1. Explanation of the procedure of initial centring of the corrector.

1 – corrector and temporarily attached adjustment mirror assembly; 2 – primary mirror of the telescope; C – centre of curvature of the primary mirror, which can be found by the Foucault knife-edge test or by convergence of some light source with the spot of light reflected by that mirror. The light either a knife source per se is edge or a torch bulb or at least a light-emitting diode or even a laser pointer. The reflected spot of light can be observed on screen 3.

centred (but only in the first approximation). Using the Foucault knife edge as a light source, the telescope can be also focused and rather accurately at that.

As the centre of curvature of the primary mirror is at a distance equal to two focal lengths from the latter, then point C can be inaccessible in the small-size observation pavilion. In that case, the adjustment reflecting surface can be figured in the centre of the convex lens 1 (Fig. 6.2), clamped to the corrector's body. The lens will make the virtual image of the centre of curvature C appear closer to the corrector, and the above-described procedure can be carried out using near point C' to place a light source.

However, in this case, it is impossible to focus the telescope adequately by the Foucault knife-edge as the light beam from the light source on having passed through the adjustment lens and the block of corrector lenses, being reflected back by the primary mirror and then again passing through the same lenses, will acquire severe spherical aberration.

The primary mirror of our telescope has an axial hole that is absolutely unnecessary for the prime focus design, but it can be used in the alternative optical system of the two-mirror Ritchey–Chrétien design. It is not assured that the hole's axis coincides with the principal axis of the aspherical reflecting surface, and that to some extent deprives reasonableness of the above-mentioned initial adjustment methods.

If the mirror was monolithic, its geometric centre should be marked (supposing that centre coincides with the pole of the aspherical surface C, it can not be otherwise when manufactured competently). It is possible to do as early as on the machine tool, for example, in the form of the ring flute of a tubular drill.

The centring is carried out with a narrow bunch of beams from the laser collimator 1 (Fig. 6.3). Covers 3 and 4 with narrow openings in their centres are clamped to open ends of the corrector's body 2 (with all its integral parts). It is not difficult to mechanically achieve

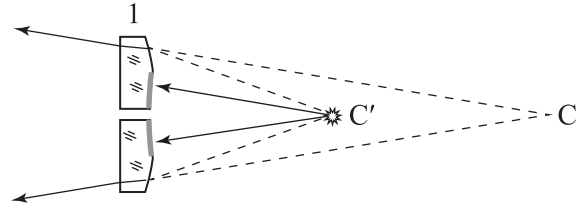


Fig. 6.2. Virtual image of the centre of curvature C.

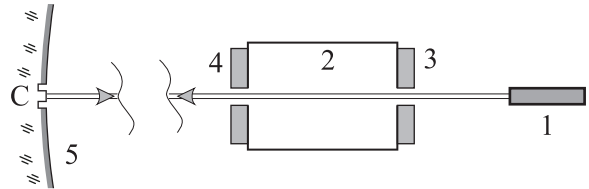


Figure 6.3. Adjustment procedure.

1 – laser collimator; 2 – corrector's body; 3, 4 – covers; 5 – primary mirror.

that the openings are aligned exactly along the body axis. By admitting the light beam through those openings, the corrector is oriented so that the light rays arrive to the geometric centre C of the primary mirror 5 marked with a groove. By tilting the primary mirror, it is provided that the reflected light beam passes the same openings on its way back. Such adjustment is more rigorous, although it is likely to be less accurate.

7. OMT-800 control system software and image analysis pipeline

The present OMT-800 *telescope control system* (TCS) software is built around the CHAOS package. CHAOS is an integrated framework for controlling the various astronomical instrumentation, including robotic mounts and domes, charge-coupled device (CCD) cameras, and filter wheels. Its major focus is on accurate timing which is essential for observations of fast-moving objects like near-Earth asteroids (NEAs), space debris, and other rapid transient phenomena like gamma-ray burst (GRB) afterglows or exoplanet transits. CHAOS is designed for maximum flexibility in working with different types of objects and observation modes and for a reasonable degree of automation combined with the possibility of manual operator's intervention and fine-grained control of the observation flow. The package is being developed and maintained at Pulkovo observatory (Devyatkin et al., 2009) since 2000, and within the ISON project (Molotov et al., 2008) since 2005. Currently, its development is mostly frozen, and it is superseded now by a newer TCS platform FORTE (Kouprianov, 2012); however, CHAOS is still responsible for routine operation of almost all optical sensors of ISON.

CHAOS is a modular (mostly Windows-based) package; its basic components include: accurate timing subsystem disciplined from an atomic clock or a GPS receiver, datalogging facility, hardware abstraction modules, networking and remote control, ephemeris engine, scheduler, data storage, and graphical user interfaces (GUIs). Separate modules are written in different programming languages and frameworks (C, Python, Delphi, Ada'95, Fortran) and are connected via dynamic linking using the appropriate C application programming interfaces (APIs) and via sockets with a set of dedicated networking protocols. CCD camera control subsystem may also serve as a standalone application for interactive image acquisition and examination.

A special hardware abstraction layer separates the high-level part of the package (GUIs and scheduler) from hardware protocols and device drivers. It consists of a set of mutually interchangeable modules each of which controls the particular type and model of hardware and provides a generic API with functions common to all hardware devices of this type. This kind of design is characteristic to most of the general-purpose TCS platforms like RTS2 (<http://www.rts2.org>) and Indi (<http://www.indilib.org>), as well as to many freeware and proprietary planetarium and observatory control packages. The specific set of hardware abstraction layer components used in the OMT-800 setting is quite basic and includes modules for A&I Goto System stepper motor controller (gotosystem.xm4.ru/a_i_goto_system_2), and Finger Lakes Instrumentation (FLI) (<http://www.flicamera.com>) CCD cameras with the Universal Serial Bus ver. 2.0 (USB 2.0) interface.

System time is provided by a dedicated stratum 1 Network Time Protocol (NTP) server driven by a Trimble Copernicus II GPS receiver. Accurate exposure timing is guaranteed by hardware triggering from the pulse-per-second (PPS) signal generated by the GPS receiver connected to the corresponding port of the camera. The formal accuracy of hardware triggering of this kind is better than a microsecond, and hence is far beyond any practical demands. However, the real timing accuracy is limited by the finite speed and instability of the mechanical CCD shutter, as well as by its poor reliability at low temperatures and high air humidity. The ISON's broad experience with Uniblitz shutters over the years allows us to estimate the average timing accuracy achievable with these shutters as several hundredths of a second, and it may easily drop to several tenths in the less favorable conditions without special precautions.

The integrated CHAOS *scheduler* can work with the following types of objects:

1. Deep-sky objects with fixed right ascension (α) and declination (δ); arbitrary tracking rates (v_α, v_δ) can be also applied.

2. Geostationary-like objects with fixed hour angle (t) and declination (δ); arbitrary tracking rates (v_t, v_δ) can be also applied.

3. Major planets of the Solar system, asteroids, comets, and Earth-orbiting objects; their ephemerides are given in the tabular form in text files, and CHAOS can track them in real time according to the ephemeris.

4. Satellites of major planets — same as other moving objects, but CHAOS can apply an offset to move the central planet away from the field of view.

For each type of object, one can specify the desired priority, constraints, and mode of observation, including the number of exposures, their duration, time step, and sequence of optical filters (unused in the OMT-800 setting, since at present it has no filter wheel). The optional exposure constraints and scheduling hints include constraints on the time of observation, apparent magnitude of the object, zenith angle or airmass, and hour angle. The actual scheduling algorithm depends on the objects observed; for instance, for deep-sky and slow-moving Solar system objects (asteroids, comets, etc.) it is as follows: descending objects are observed first, by decreasing zenith angle; these are followed by objects near culmination, sorted by decreasing hour angle; finally, ascending objects at sufficiently high altitudes, or sufficiently close to culmination are observed, as well as lower-priority objects, in the same order. CHAOS also accepts observation plans from external schedulers — for example, OMT-800 can do follow-up observations of faint space debris according to the optimal strategy calculated by the ISON planning and analysis center in Keldysh Institute for Applied Mathematics, Moscow. Although scheduling is generally targeted at fully automatic operation over the whole night, the telescope operator can manually pause, resume, restart, and edit the schedule when necessary, as well as initiate any manual observations or maintenance operations, like capturing calibration images or re-alignment. Figure 7.1 shows the main TCS components in action.

The OMT-800 data processing pipeline is based on the Apex II image analysis platform (Kouprianov, 2008; Devyatkin et al., 2010). Apex II project started in 2004 at Pulkovo as an effort to create a modern open software platform for general astronomical image analysis and, in particular, to fill the gap of non-specialized and all-purpose, but still highly reliable software for accurate automatic positional astronomy. The first application of the package was massive everyday data reduction in the continuous NEA follow-up campaign conducted by Pulkovo observatory and its mountain site near Kislovodsk (Devyatkin et al., 2009). Since 2005, Apex II is supported by the ISON project, where its major goal is the initial data reduction of survey and follow-up observations of artificial Earth's satellites and space debris on almost all ISON sensors, including OMT-800. Other current applications include double and multiple asteroid photometry, GRB astrometry, and search for exoplanets. Although the Apex II core and library remains open-source for the scientific community, the satellite/space debris package and its key

CHAOS TCS 2.3.1 (Manual Mode) - V. V. Kouprianov

#	Exp	T	Target	α	δ	$\dot{\alpha}$ ["/min]	$\dot{\delta}$ ["/min]	$\Delta\alpha'$	$\Delta\delta'$	m	Exposure [s]	Filter
63	GEO 95462			19 ^h 53 ^m 32 ^s .13	-17° 21' 55".7	1.1	2.5			15.7	8 x 7:15	
64	GEO 95465			19 ^h 00 ^m 19 ^s .60	-22° 49' 17".7	0.5	-0.2			17.2	8 x 7:15	
65	GEO 95479										8 x 7:15	
66	GEO 95480			15 ^h 56 ^m 16 ^s .67	-05° 13' 27".2	1.6	-0.4			17.2	8 x 7:15	
67	GEO 95490			19 ^h 23 ^m 49 ^s .77	-03° 57' 26".4	-1.3	-0.3			15.8	8 x 7:15	
68	GEO 95509			18 ^h 31 ^m 38 ^s .29	-16° 44' 09".0	3.3	1.2			16.6	8 x 7:15	
69	GEO 95514										8 x 7:15	
70	GEO 95522			21 ^h 35 ^m 27 ^s .73	-14° 07' 21".1	0.2	3.5			18.1	8 x 7:15	
71	GEO 95525			18 ^h 08 ^m 29 ^s .66	-05° 07' 54".0	1.7	0.4			15.4	8 x 7:15	
72	GEO 95531										8 x 7:15	

Control

V. V. Kouprianov

Mode:

Imaging

Camera:

Exposure: x s

Prefix:

Interv: s #:

Frame:

Target Correct

Name:

α :

δ :

t :

Pointing:

Tracking

Sidereal:

t : "/s

δ : "/s

Filter:

Observation conditions

Temperature: °C Humidity: %

Air pressure: hPa

Moon

α = 04^h 37^m 33^s.29 Rise: 02:09

δ = +19° 28' 08".6 Transit: 09:47

t = 14^h 46^m 02^s.25 Set: 17:25

A = +40° 08' 04".5 Phase: 172.7° (0.4%)

z = 104° 12' 55".1 Separation: 53.4°

Tube position (obs.)

α = 08^h 28^m 13^s.97

δ = +42° 59' 14".3

t = 10^h 55^m 21^s.58

A = -11° 44' 51".8

z = 89° 28' 24".9

Time

Date:

UTC:

LST:

Figure 7.1. Screenshot of a working session of CHAOS TCS on the OMT-800 control workstation.

algorithms are the property of ISON and available to ISON members only.

Apex II is designed along the guidelines similar to those of such well-known proprietary packages as MATLAB® (<http://www.mathworks.com>) and IDL® (<http://www.exelisvis.com/idl>). Namely, the platform is based on a high-level scripting language convenient for vector and matrix operations, includes a large library of relevant algorithms (mostly implemented in the same language, but with bindings to high-performance and mature libraries in “classical” languages like C and Fortran); the library is accessed by user-level batch-mode or interactive GUI applications doing some specific data analysis tasks. Moreover, for those, who learn the language and library, interactive console mode is also available for the data analysis beyond the existing applications and for rapid prototyping of new algorithms. However, unlike the packages mentioned, Apex II makes extensive use of the existing open-source infrastructure for scientific computing which is built around the modern high-level programming language Python (<http://www.python.org>) and includes the following packages: NumPy (<http://www.numpy.org>) for basic array operations, vectorial notation, and numerics; SciPy (<http://www.scipy.org>), a huge collection of advanced numerical methods, including optimization, computer vision, and many others; matplotlib (matplotlib.org) for scientific plotting; PyFITS (http://www.stsci.edu/institute/software_hardware/pyfits) for Flexible Image Transport System (FITS) format input/output; PyWCS (<http://www.astropy.org>) for coordinate system transformations; wxPython (<http://www.wxpython.org>) for building GUIs, and several others. In recent years, these packages gained a growing popularity among the scientific community.

The basic automatic data processing pipeline in Apex II is a console-mode Python script that works in batch mode without any user intervention. Its details depend on the problem it is intended for (e. g. the details of object extraction for asteroids and space debris are different), but almost any complete data reduction pipeline always contains the following large blocks:

1. Calibration.
2. Source extraction.
3. Source measurement.
4. Differential astrometry.
5. Differential photometry.
6. Post-processing.
7. Reporting.

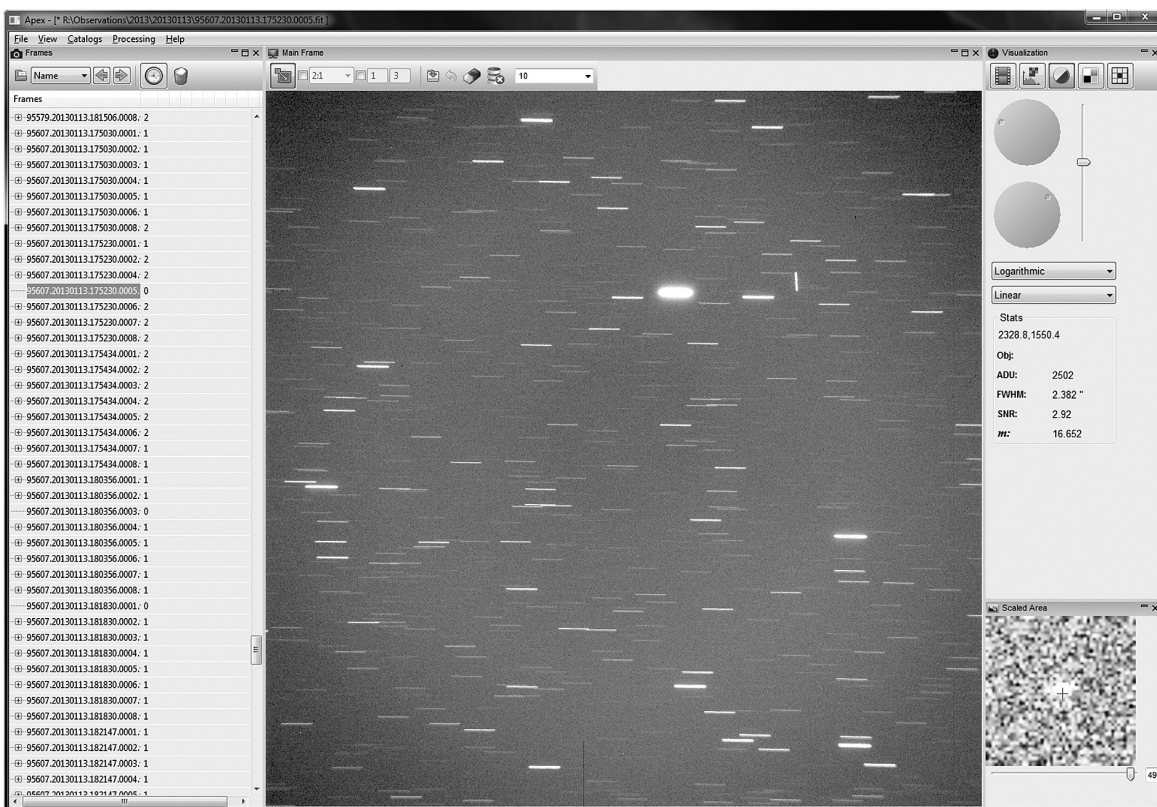
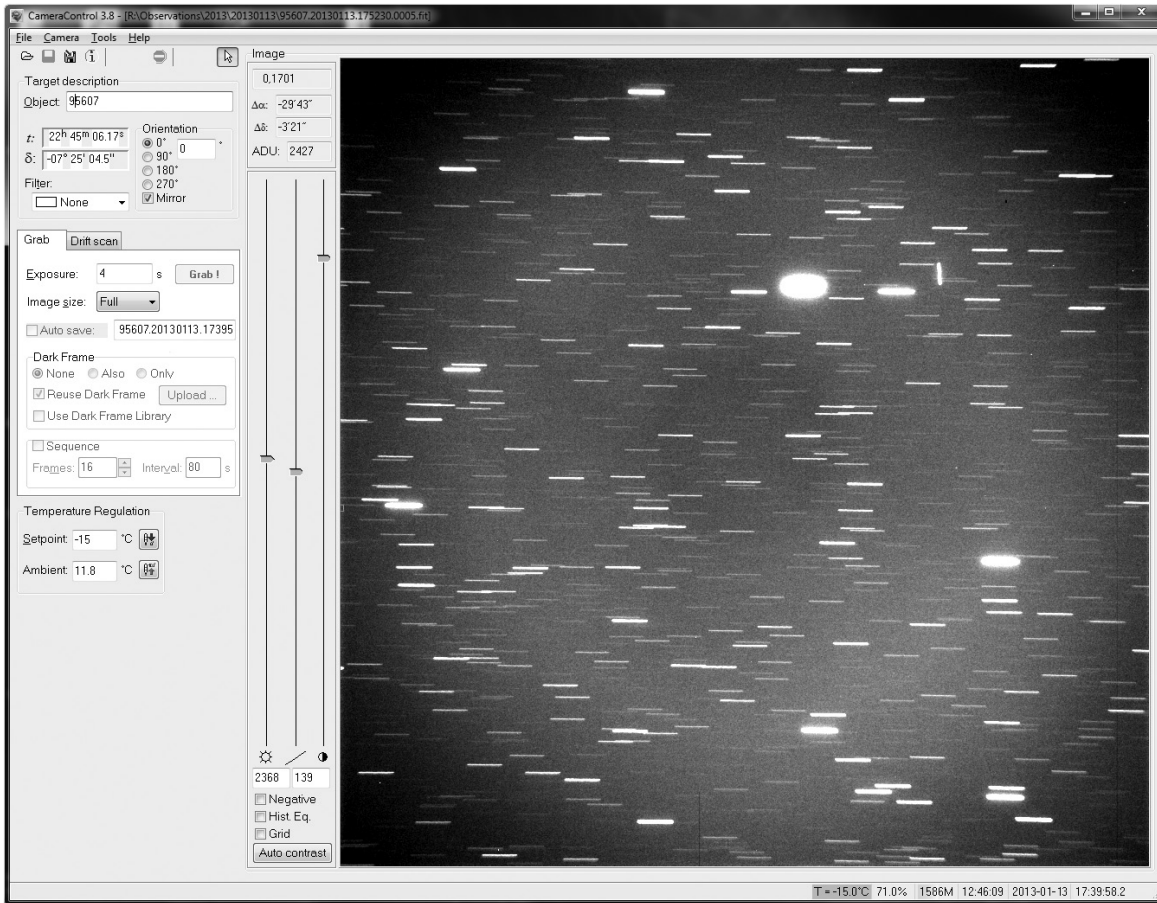


Figure 7.2. The screenshots of CameraControl panel (up) and Apex GUI panel (below). The figure shows a typical image of the sky with the object being tracked (telescope tracking switched off).

As an example, let us consider the data reduction pipeline for faint space debris follow-up. In general, image *calibration* includes cosmetic, dark, and flat correction; however, the main goal of this kind of observations is obtaining the accurate orbital data, and since positional measurements are practically not affected by dark and flat calibration, these steps are optional and are applied only when better characterization of a space debris fragment by means of photometry is required. As described in (Kouprianov, 2008), *source extraction* includes flattening the sky background, segmentation by global threshold, accompanied by binary morphological filtering to better detect faint star trails, and isophotal analysis. A separate source extraction pass is required to detect space debris, since their morphological properties are completely different from those of the field stars, which is actively exploited by the pipeline to eliminate the latter and thus substantially reduce the number of false detections at the very early stage of the pipeline. However, this pass only results in the list of *candidate* detections that still contains false positives; the final decision is made later by correlation of detections from several frames (see below). *Source measurement* is intended to obtain a set of more accurate parameters of each object, including its position, shape, and flux, than those provided by isophotal analysis; this is done by point-spread function (PSF) fitting, both for point-like and for trailed sources. This also helps to identify most of the initial false detections (including cosmic ray hits and background noise due to a low detection threshold value): since the real objects' full widths at half-maximum (FWHM) after PSF fitting usually lie within a rather small range of values, posing constraints on the post-fit FWHM serves as a very efficient method of identifying false positives. Differential astrometry implies matching centroid positions of the field stars detected to the appropriate catalog (since the OMT-800 field of view is large, Tycho-2 catalogue (Høg et al., 2000) is the best choice; UCAC4 (Zacharias et al., 2011) can also be used when appropriate), calculating plate model parameters, including non-linear terms in coordinates to account for the residual optical distortions, and applying them to candidate space object detections; the resulting nominal frame-to-frame root-mean-square (RMS) error of positional measurements of space debris is of the order of 0.1"-0.2" for an average object, and down to several hundredths of arcseconds for the bright objects with signal-to-noise ratio (SNR) of 100 and more; this is usually several times worse than the values achieved for point source-only images that do not involve any trailed sources, but is still fully acceptable in terms of the required orbital data accuracy. Differential photometry is done by matching the field stars to the reference catalog (UCAC4 is the better choice here, since its magnitude range better matches that of the target objects, and its own instrumental system is close enough to the integral

band of OMT-800), calculating reduction model parameters with optional correction for differential extinction, which is essential at high airmass values for the large fields of view, and applying them to the measured fluxes of candidate space object detections. For the OMT-800 space debris astrometry pipeline, the purpose of *post-processing* is to correlate candidate space object detections from several images comprising a single cadence in order to identify tracklets of separate space objects and eliminate false detections that do not belong to any tracklet; the *k*-d tree-based moving object detection algorithm behind this is similar to the one used at PanSTARRS (Kubica et al., 2007) for intra-night correlation. Finally, all tracklets found are validated by initial orbit determination and *reported* in the format appropriate for further analysis at the Keldysh Institute for Applied Mathematics planning and analysis center.

As it was mentioned above, this pipeline runs fully unattended. However, visual inspection of images and detections found by the pipeline is still possible by means of a special integrated Apex GUI application (see Fig. 7.2, bottom panel). This application is, first of all, an advanced FITS image viewer written in wxPython and based on the OpenGL (<http://www.opengl.org>) shader technology which allows for smooth real-time image enhancement aimed at visual detection of the faintest objects possible. In particular, manual operator's control is required in an extremely rare case of false detections that may still survive all validity checks of the automatic pipeline with non-vanishing probability, mostly due to a very low detection threshold of about 2.5σ ; then Apex GUI allows to quickly identify a suspicious uncorrelated detection as either real or spurious. Apex GUI currently evolves to a full-featured general-purpose astronomical data reduction application for both controlling the high-level automatic pipeline operation and for low-level interactive image analysis.

Whenever possible, all pipelines are accelerated by the Apex II parallel subsystem which is designed to utilize the full central processing unit (CPU) power of the data processing workstation. With its help, data analysis achieves the realtime performance (i. e. it is faster than the image acquisition rate) without sacrificing the capability to detect the faintest objects. Currently, the parallel subsystem is being gradually transferred to the OpenCL framework (<http://www.khronos.org/opencl>) to further increase performance by utilizing the computing capabilities of general-purpose graphics processing units (GPGPUs).

Thus we may conclude that the software currently installed at the OMT-800 control and processing workstation is capable of doing the full cycle of image acquisition and initial data reduction, and is sufficiently flexible to suite the needs of a broad range of observation campaigns.

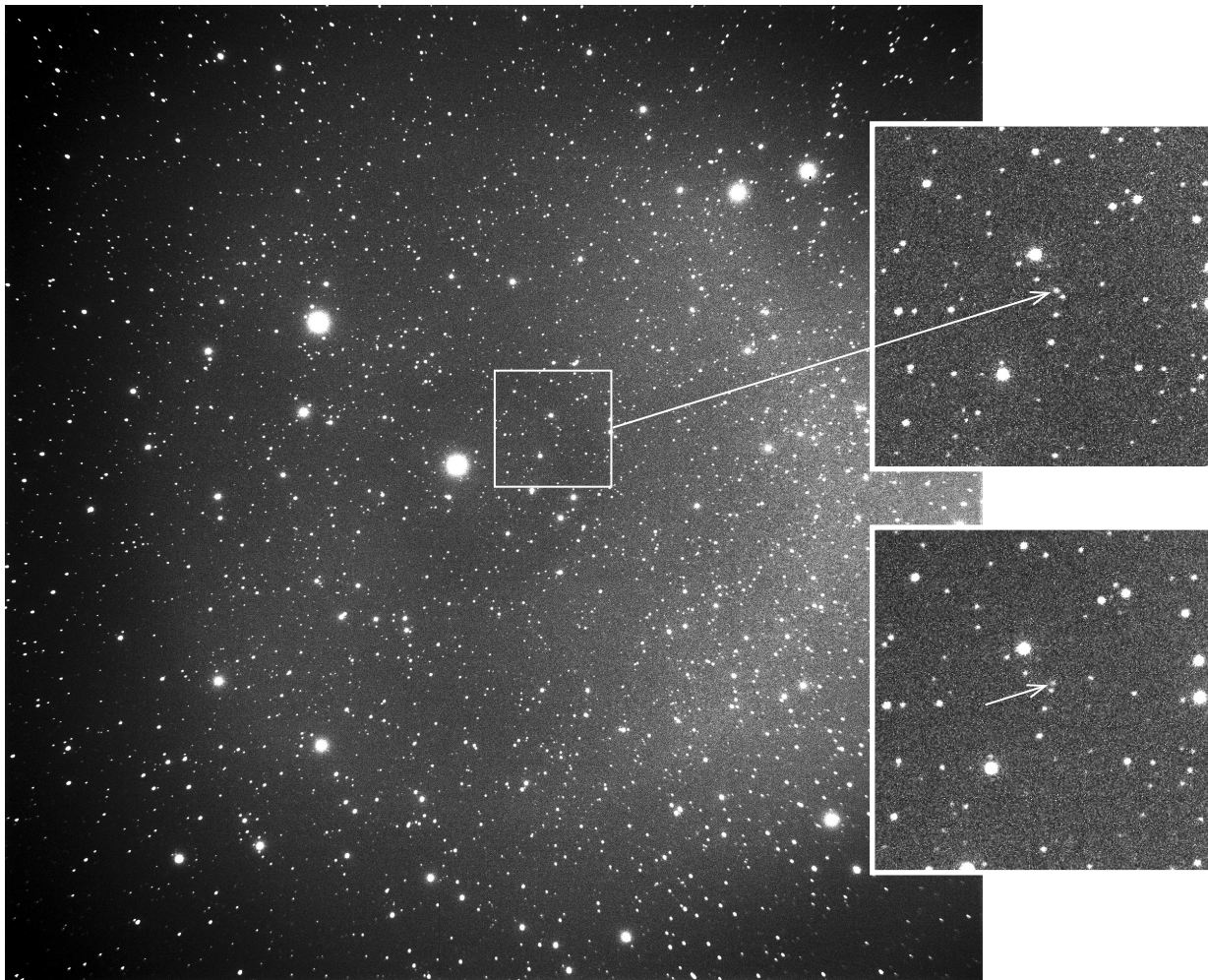


Figure 8.1. The shot is made with OMT-800 March 3, 2013, 0:00UT with exposure time of 10 sec. The arrow shows the image of comet C/2012 S1 ISON. The next fragment of the shot made 25 minutes later is shown at the bottom right.

8. Aims and objectives of the OMT-800

Within a wide range of the astrophysical objectives, the systematic observations using OMT-800 are defined by its characteristics, such as the limiting magnitude,

field of view, telescope control system and astronomical seeing conditions at the telescope's location.

At the observation point in Mayaki the number of the nights available for optical observations per year averages about 170 (Fig. 8.2). The absence of any significant

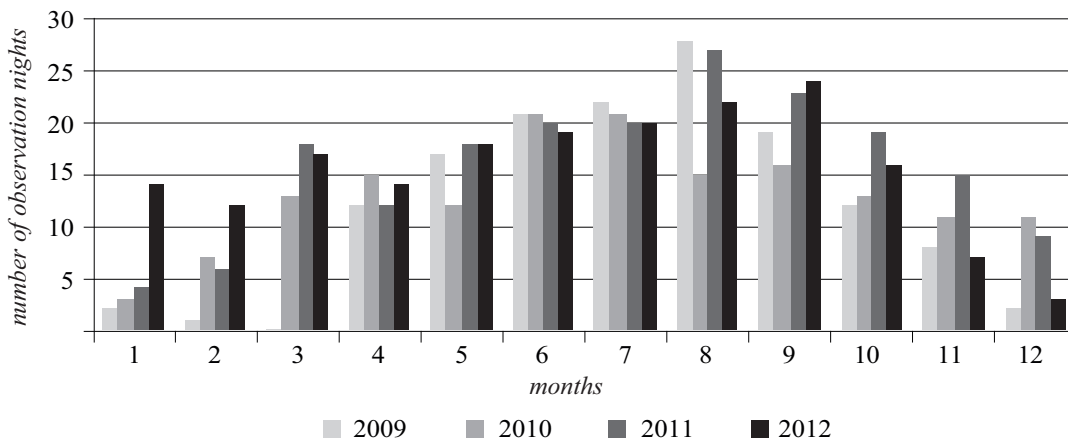


Figure 8.2. Statistics of the clear sky nights at Mayaki station.

artificial light pollution improves the limiting magnitude of the equipment. Nevertheless, the proximity of the observation station to the Dniester river often worsens quality of the images due to the large amount of a water vapor in the surface layer of atmosphere.

Currently, the following observational programs are carried out with OMT-800:

1. Positional observations of artificial satellites in the geostationary orbits (Molotov et al., 2008).
2. Observations of the near-Earth approaching objects.
3. Observations of the Solar system small bodies (Fig. 8.1, as an example; Wibe, Y. et al. 2013).

9. Auxiliary equipment at the OMT-800

The meteor patrol method is applied in meteor studies to determine kinematic and physical characteristics of the meteor events and interplanetary dust particles that cause such events. For this purpose simultaneous operation of at least two base stations is realised. Normally, high-speed cameras with wide-angle lenses are used, and the pre-processing is carried out after each night of patrolling.

The television meteor patrol has been constructed in Odessa in 2003. Television cameras Watec LCL-902K, Watec LCL-902H and Watec LCL-902H2 with a time resolution of 20 ms are used to record meteor events.

The meteor patrol equipped with cameras with fields of view and magnitude limits from 36×49 arc degrees and 7.0^m for the most wide-angle camera to 0.6×0.8 arc degrees and 13.5^m for Schmidt telescope

Synchronous observations, i.e. observations with a few polytypic instruments on the same parallactic mounting, proved themselves to be particularly efficient. The application of the synchronous method of observations enables to maximize the benefits of different optical systems. Depending on the observation task, it is feasible to enlarge the field of view or to record a meteor event with high resolution using different systems.

When designing and building the television meteor patrol on the base of the telescope with the mirror diameter of 800 mm, it was intended to make it possible to mount several cameras for the meteor patrol. One of the cameras (with KO-140 lens), fixed on the OMT-800 tube, is shown in the Fig. 9.1. It is possible to combine different astronomical cameras depending on the posed research tasks.

The following algorithm of work of base meteor stations is suggested. One of the stations (the master telescope at Mayaki station) conducts its planned observations under any non-meteor program at any point on the celestial sphere; and the second station (the slave telescope at Kryzhanovka station), equipped with the Schmidt telescope and several cameras, performs calculations of the point of observation that corresponds to the guidance sector where the first station telescope

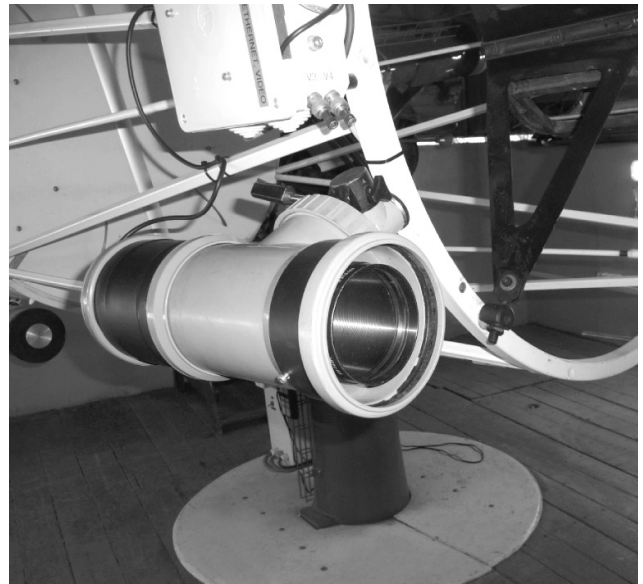


Figure 9.1. Meteor camera attached to OMT-800 tube.

is pointed at. Thus, both stations, which are at 45 km distance from each other, carry out the meteor patrol session in such a way that instruments on both stations are pointed at the same space area. Whenever the point of observation of the master telescope is changed, the corresponding procedure of recalculation and re-pointing of the slave telescope takes place.

Coordination of observations is realized with specific software “Meteor Explorer software” that was developed by one of the authors of this paper. Every minute, while the master telescope is in operation, the program sends the file with equatorial coordinates of the point of observation to the remote server.

The program enables one to conduct calculations for different meteor showers at different heights of the meteor events (80-100 km), that allows one to increase the number of meteors detected at both stations.

The software also contains program for real time record of meteor events, or record of video streams from meteor cameras, and the subsequent pre-processing of the data.

The methods of the base telescopic observations has been tested during 2009-2012 expeditionary studies on Zmeinii Island in the Black Sea with the 150 km base line between the observation sites (Zmeinii Island – Kryzhanovka station).

It should be noted that a meteor event can be also captured within the master telescope filed of view as the meteor track image, and in that case we can obtain the meteor image with a high spatial resolution across the meteor trajectory.

Reconfiguration of auxiliary equipment will allow carrying out the meteor patrol for various tasks of meteor researches.

10. Conclusion

New automatic Odessa multifunctional telescope (OMT-800) was created by the specialists of Astronomical Observatory of Odessa I. I. Mechnikov National University in cooperation with colleagues from ISON project. This telescope will be used for astrometric and (in the future) photometric observations of the near-to-Earth celestial bodies: high-elliptical orbit artificial satellites, geostationary satellites, asteroids and comets.

Acknowledgements

The authors are bound in honour to express their gratitude to everybody, who to some extent contributed to creation of this telescope and its infrastructure. First of all, we are deeply grateful to untimely deceased in 2009 staff member of the Astronomical Observatory Eugeny Gubin for his self-denying work devoted to the realization of this project. Among those, who also participated in the work at different stages, there are: I. Aslamov, V. P. Bezdenezhnyi, A. Biryulin, V. N. Bondarenko, Yu. N. Bondarenko, L. Borodina, O. Chekalin, A. Chkourdiouk, N. I. Dorokhov, N. F. Golovan', N. I. Koshkin, A. I. Movchan, Yu. S. Romanov, Yu. D. Russo, D. G. Serebryanskiy, I. Shepelenko, R. Shepelenko, A. V. Skutareno, V. P. Sotnikov, L. Tsybizova, O. Tsybizov, A. Yudin.

We also thank all the people, who started building the pavilion (which was originally intended for another telescope) under the supervisory of Yu. D. Russo and Yu. S. Romanov in 80-s.

SMA thanks the Ministry of Education and Science of Ukraine for financial support that facilitated the preparation of this paper.

References

- Afanasiev, V. L.; Kalenichenko, V. V.; Karachentsev, I. D. Detection of an intergalactic meteor particle with the 6-m telescope. *Astrophysical Bulletin*, 2007, Vol. 62, Issue 4, pp. 301-310.
- Ascom. Standards for astronomy. <http://ascom-standards.org> QMOT QSH6018 MANUAL. c 2011. TRINAMIC
- Devyatkin, A. V.; Gorshanov, D. L.; Kouprianov, V. V.; Vereshchagina, I. A.; Bekhteva, A. S.; Ibragimov, F. M. "Astrometric and photometric observations of solar system bodies with Pulkovo Observatory's automatic mirror astrograph ZA-320M" // *Sol. Sys. Res.*, 2009, 43(3) 229-239
- Devyatkin, A. V.; Gorshanov, D. L.; Kouprianov, V. V.; Verestchagina, I. A. "Apex I and Apex II software packages for the reduction of astronomical CCD observations" // *Sol. Sys. Res.*, 2010, 44(1), 68-80
- Fashchevsky, N. N. Optical telescopes and astronomical optics. Odessa, "Astroprint", 2011
- Gorbanev, Yu. M.; Golubaev, A. V.; Zhukov, V. V.; Knyaz'kova, E. F.; Kimakovskii, S. R.; Kimakovskaya, I. I.; Podlesnyak, S. V.; Sarest, L. A.; Stogneeveva, I. A.; Shestopalov, V. A. Methods and statistics of TV observations of telescopic meteors. *Solar System Research*, 2006, Vol. 40, Issue 5, pp. 412-426.
- Gorbanev Yu. M., Shestopalov V. A., Sarest L. A., Golubaev A. V. Zmiinyi island Scientific project Abiotic Characteristics Monographs Part 6 Astronomical studies p.138-154.
- Høg, E.; Fabricius, C.; Makarov, V.V.; Urban, S.; Corbin, T.; Wycoff, G.; Bastian, U.; Schwekendiek, P. et al. "The Tycho-2 Catalogue of the 2.5 million brightest stars" // *Astron. Astrophys.*, 2000, 355, L27-L30
- Kouprianov, V. "Distinguishing features of CCD astrometry of faint GEO objects" // *Adv. Space Res.*, 2008, 41(7), 1029-1038
- Kouprianov, V. "Apex II + FORTE: Data Acquisition Software for Space Surveillance" // *Abstracts of the 39th COSPAR Scientific Assembly 2012*, July 14-22, Mysore, India, ISSN-1815-2619, PEDAS.1-0004-12
- Kubica, J.; Denneau, L.; Grav, T.; Heasley, J.; Jedicke, R.; Masiero, J.; Milani, A.; Moore, A.; Tholen, D.; Wainscoat, R. J. "Efficient intra- and inter-night linking of asteroid detections using kd-trees" // *Icarus*, 2007, 189, 151-168
- Maksutov D. D. Fabrication and study of astronomical optics. Leningrad — Moscow: Gostekhizdat. 1948. p. 237-242
- Michelson, N. N., Optical telescopes. Theory and construction. Moscow, "Nauka", 1976.
- Molotov, I.; Agapov, V.; Titenko, V.; Khutorovsky, Z.; Burtsev, Yu.; Guseva, I.; Rumyantsev, V.; Ibrahimov, M.; Kornienko, G.; Erofeeva, A.; Biryukov, V.; Vlasjuk, V.; Kiladze, R.; Zalles, R.; Sukhov, P.; Inasaridze, R.; Abdullaeva, G.; Rychalsky, V.; Kouprianov, V.; Rusakov, O.; Litvinenko, E.; Filippov, E. "International scientific optical network for space debris research" // *Adv. Space Res.*, 2008, 41(7), 1022-1028
- Motion Control GmbH & Co. KG. http://www.trinamic.com/tmctechlibcd/QMot_motors/QSH6018/QSH6018_manual.pdf
- Universal Serial Bus Specification Revision 2.0 c 2000, Compaq Computer Corporation, Hewlett-Packard Company, Intel Corporation, Lucent Technologies Inc, Microsoft Corporation, NEC Corporation, Koninklijke Philips Electronics N.V.
- Wibe, Y. et al. Observations and Orbits of Comets. *Minor Planet Electronic Circ.*, 2013-G31 (2013)
- Wynne, C.G., 1949, *Proc. Phys. Soc.*, B62, 772
- Zacharias, N.; Finch, C.; Zacharias, M. I.; Girard, T. "UCAC4 status" // Poster paper presented at the AAS 218, 2011, Boston, MA

PROGRAM WWZ: WAVELET ANALYSIS OF ASTRONOMICAL SIGNALS WITH IRREGULARLY SPACED ARGUMENTS

I.L.Andronov¹, A.V.Naumova²

Department "High and Applied Mathematics", Odessa National Maritime University
Odessa, Ukraine

¹ *il-a@mail.ru*, ² *lusik93@list.ru*

ABSTRACT. A program WWZ is introduced, which realizes the wavelet analysis using an improved modification of the algorithm of the Morlet wavelet for a general case of irregularly spaced data, which is typical for the databases available in virtual observatories. Contrary to the well-known analogs, working with regularly spaced (equidistant in time) arguments, we have implemented an improved algorithm presented by Andronov, (1998KFNT...14..490A, 1999sss.conf...57A), which significantly increases the signal-to-noise ratio. The program has been used to study semi-regular pulsating variable stars (U Del et al.), but can be used for the analysis of signals of any nature.

Key words: variable stars, quasi-periodic and cyclic oscillations, long-period pulsating variables, data analysis, wavelet analysis, U Del.

One of the main directions of modern astrophysics is the study of variable stars. Specificity of astronomical observation is that in many cases the times at which the observation are obtained, are irregularly spaced. This is characteristic to collections of photographic negatives "Sky Patrol", available in a variety of observatories, as well as to more modern CCD sky surveys. Such observations are sometimes available through the Internet and included in national and international projects "Virtual Observatory". In Ukraine there are programs VIRGO (Virtual X-ray and gamma-ray observatory) and UkrVO (Ukrainian Virtual Observatory (Vavilova et al. 2012)).

Wavelet analysis is a method of investigating changes in the period of signals that are not strong periodic, but it is has sense to introduce "instantaneous" values of the "period" or "cycle length". In astronomy, such signals are called "quasi-periodic oscillations" (QPO) and are common to many types of variable stars – low-mass X-ray binaries, cataclysmic and symbiotic systems, semi-regular pulsating stars etc.

Mathematical foundations of the theory of wavelets are presented e.g. in the monographs by Daubechies (1992) and Vitjazev (2001) and reviews (e.g. Astafieva 1996). For the time series analysis, often is used the Morlet wavelet, which is based on a combination of the Fourier transform with the weight function being proportional to the Gaussian function. This conversion is included in the popular software, e.g. MatLab, SciLab. This algorithm allows to analyze only the signals, which are equally spaced in time, i.e. $t_k=t_i+(k-i)\Delta t$,

where is t_k is argument (typically time) of the k^{th} observational point and Δt is step (discretization in time). So for astronomical time series, Szatmary et al. (1994) have proposed to used simplified formulae, just changing integrals to sums on all observations.

As for the irregularly spaced time series, the basic functions do not satisfy conditions of orthogonality, the simplified formulas lead to a dependence of the 2D test function on the origin of the signal (i.e., its mean value), thus depriving the analysis of the physical meaning. Foster (1996) proposed to use the method of least squares with additional weights, and has introduced the test function «WWZ». A detailed analysis of the statistical properties of this and three other test functions was given by Andronov (1998, 1999), which is a special particular case of using arbitrary basic functions $f_\alpha(z)$ and the weight (filter) functions $w(z)$ (Andronov 1997).

The approximation may be written in a form:

$$x_c(t, t_0, P) = \sum_{\alpha=1}^m C_\alpha f_\alpha(z) \quad (1)$$

Here x_c is a smoothed value of a function which depends on the trial time t , on a "shift" t_0 and a "scale" (period) P ; $z = (t-t_0)/P$, $C_\alpha(t_0, P)$ – the coefficients of expansion of the local signal on basic functions $f_\alpha(z)$, and m – the order of the model.

For the „least squares extension” of the Morlet wavelet, $f_1(z)=1, f_2(z)=\cos(2\pi z), f_3(z)=\sin(2\pi z), m=3$. The weight function $w(z) = \exp(-cz^2)$ is the Gaussian function, where c characterizes the width of the smoothing filter. When $c=0$, $w(z)=1$, and we have a global approximation of the sine wave. When $c \rightarrow \infty$, the filter function decays very quickly, and one obtains an asymptotic approximation of the local polynomial of degree 2, which corresponds to the method of running parabolae (Andronov, 1990, 1997). For applications, the most commonly used is an intermediate value $c=1/80 \approx 1/8\pi^2$. In the case of insufficient data, the values of c may be decreased by a factor of 4 (corresponding to twice larger time resolution and twice smaller period resolution). A comparison of results of the wavelet analysis for different values of c was presented also by Chinarova (2010) for the semi-regular variable RU And. Also, as a weighting function, one may use a local function $w(z)=(1-z^2)^2$ for $|z|<1$ (Andronov, 1990, 1997).

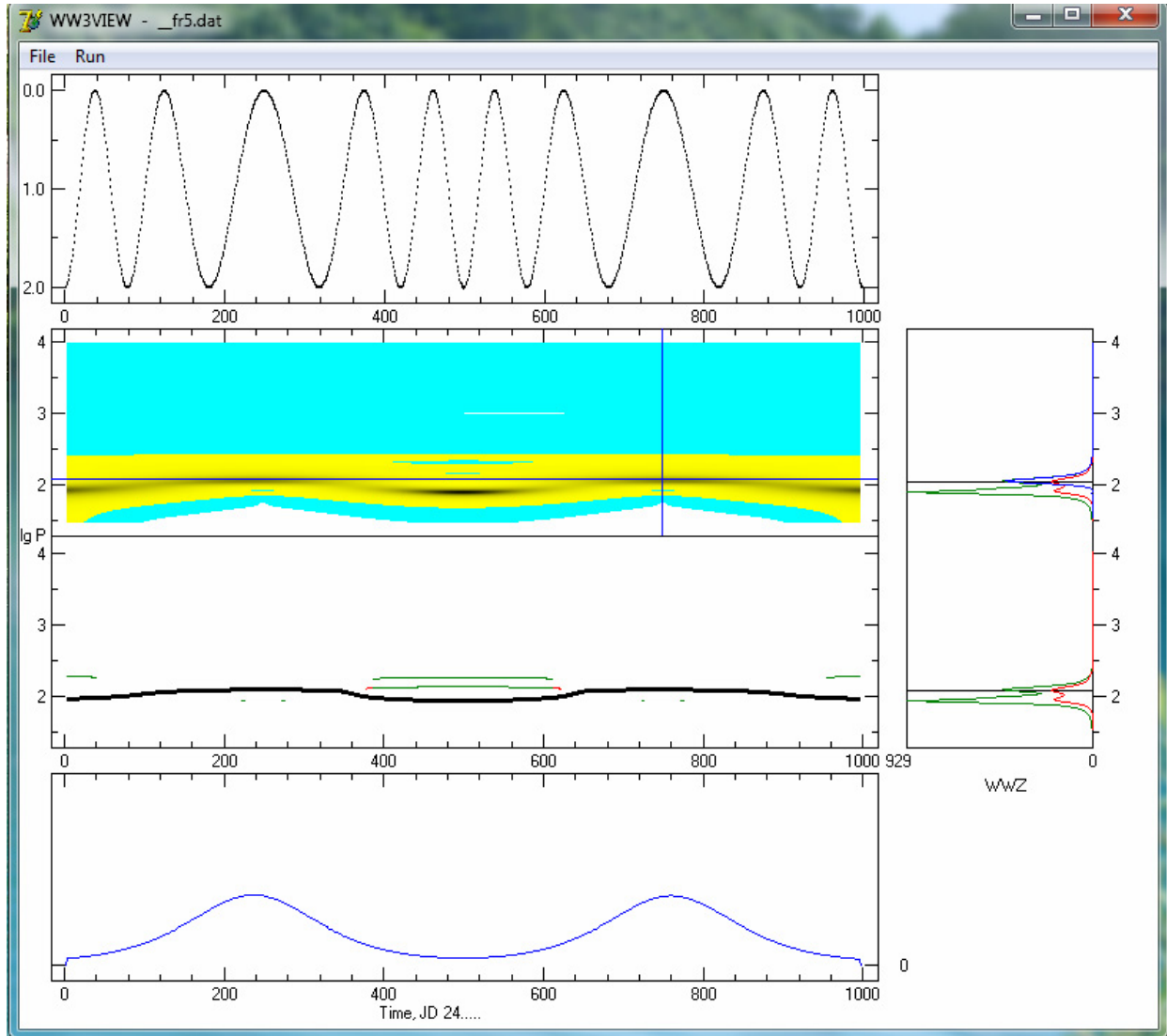


Figure 1: Screenshot of the program WWZ. From top to bottom: light curve of the model signal with rapidly changing period; the wavelet map (the dependence of the test function of time and of the logarithm of the period); the skeleton of the wavelet map (time dependence of the values of the period, the corresponding local peaks are highlighted in red peaks above a critical value equal to half of the maximum, and green – above the "threshold of detection", adopted at 3; thick black line indicates the position of the maximum for this shift); the cross-section of the wavelet map in time for a fixed period. Right: blue marks a cross-section of the wavelet map at a fixed time (local periodogram), red shows the averaged periodogram, and green – the maximum value of the periodogram for a fixed period ant different shift.

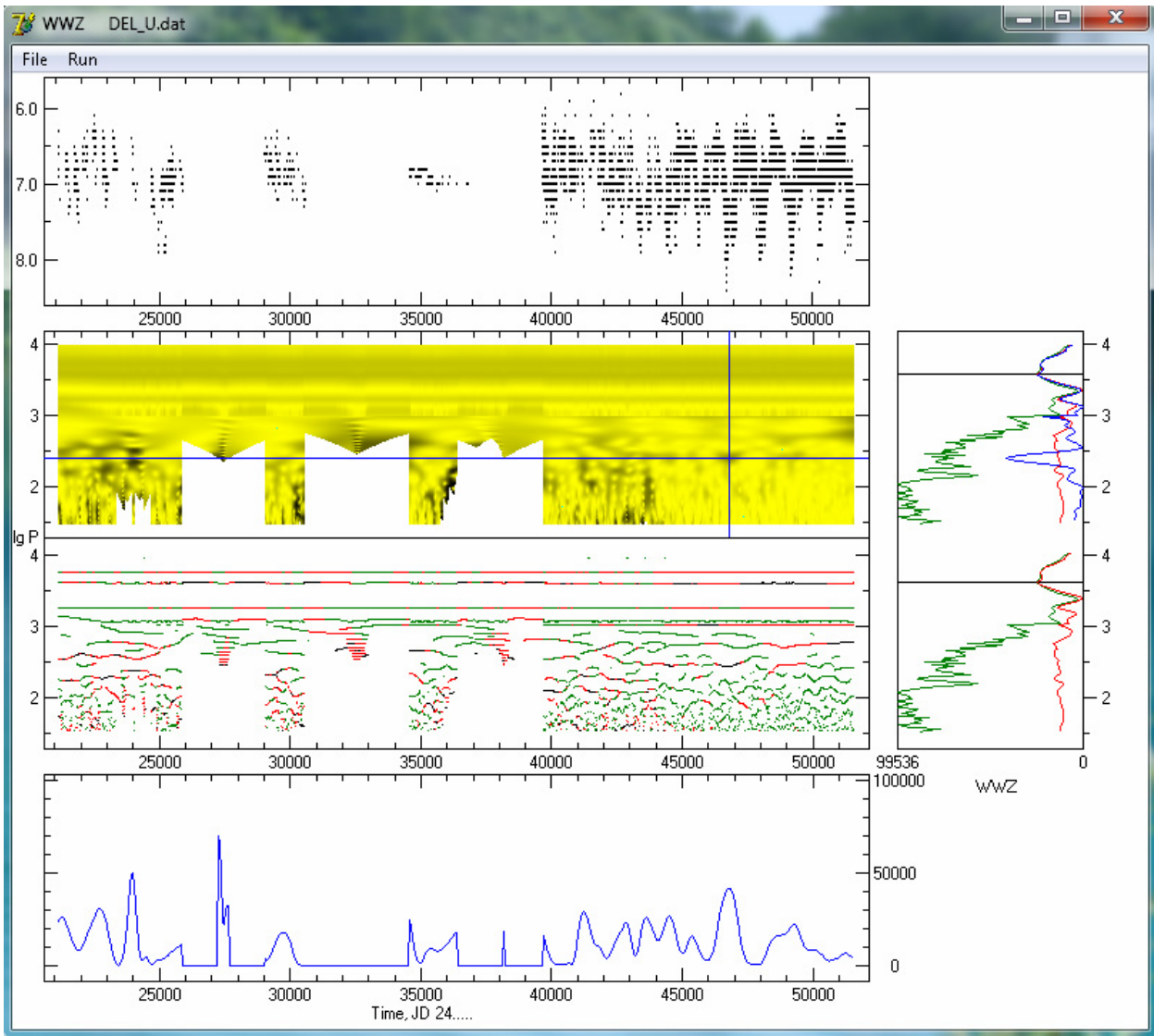


Figure 2: Screenshot WWZ for semiregular pulsating star U Delphini (similar to Fig.1). From top to bottom : light curve (the dependence of magnitude on the time in the Julian dates); the wavelet map; the skeleton of the wavelet map; the cross-section of the wavelet map in time for a fixed period. Right: blue marks a cross-section of the wavelet map at a fixed time (local periodogram) , red shows the averaged periodogram, and green – the maximum value of the periodogram for a fixed period.

We had developed a program to evaluate few test functions: r – semi-amplitude of oscillations, S – the ratio of the weighted signal variance to the total variance (often denoted in other mathematical packages through r^2 – the square of the correlation coefficient between the observed and smoothed values, i.e. the same letter r has another meaning), and WWZ – the "signal/noise" ratio.

As an illustration, we present the results obtained using our program for one of the semi-regular pulsating stars – U Delphini. A separate study of this star using various methods was presented by Andronov and Chinarova (2012). The original observations were published in the database of the French Association of Variable Star Observers "AFOEV", which is the precursor of modern databases of virtual observatories. The diagrams are shown in Fig. 1 for the model signal with a periodic modulation of the fundamental period and in Fig. 2 for U Delphini.

The program has been named WWZ, as one of the calculated test functions. Unlike previously worked analog (in the computer language Fortran, in text mode), the program WWZ was written in Object Pascal, and has a graphical interface and the ability to visualize both the original light curve and the test functions $F(t_0, P)$ (WWZ, S and r), which depend on time (shift) t_0 and period (scale) P .

The graphic representation of the 2D dependence of the test function $F(t_0, P)$ is called "a wavelet map".

In addition, the program displays a "skeleton" – the time (t_0) dependence of the values of the periods corresponding to the local peaks at the wavelet map for a fixed t_0 . Different colors show the peaks above and below the limit value $F_{\max}(t_0) = \max_P(F(t_0, P))$, to facilitate the visual perception of the "skeleton". In the case of a constant period(s) "skeleton" should appear as a horizontal line(s). However, due to irregular spacing in time of the observations, the lines at the

"skeleton" are apparently short or inclined. It also demonstrates the falsity of the respective peaks.

For convenience of the study of changes of the significance of different periods, we introduce a "cut mode": the horizontal (time cross-section, $P=\text{const}$) and vertical (period cross-section, $t_0=\text{const}$), where the point (t_0, P) is chosen by a mouse click. Corresponding two images are displayed below the "skeleton" and right from the wavelet map. For comparison, the two "wavelet periodograms" (also called "wavelet scalegrams") are shown – an average (shown in red) and "maximum" (for all time points within a "cut"). It should be noted, that, for small periods, the "maximum" value is many times greater than the average. This is due to the effective reduction of the number of points used for smoothing in the formula (1) and a corresponding increase in the scatter of the test function. Detailed mathematical description of the statistical properties was presented by Andronov (1998).

Because the relative widths of peaks at the scalegrams used in the wavelet analysis is substantially constant (in contrast to a classical periodogram, where the width of peaks is constant in frequency), instead of the period it is reasonable to use the logarithm of the period.

The range of periods is selected in accordance with a time variability of stars of corresponding types. For semiregular stars (including U Delphini), we used a range of $1.5 \leq \lg P \leq 4$. For stars with more rapid changes of brightness, the range is moved from seconds to about an hour.

The format of the input files for the described program: the light curve presented in two columns (t_i, x_i) , where $t_i = \text{HJD} - 2400000$ – the time in Julian days and x_i – stellar magnitude (or, alternatively, the intensity) of the object. Output file format used by 2. In the "full" format, the output is: the period P , the shift t_0 and test functions WWZ, S , r .

In the program, there are few restrictions for a case of "bad coverage" of the interval of smoothing by observations. E.g. there must be points after and before the shift t_0 and the effective number of observations should exceed 3. Otherwise the values of all the functions are set to zero. In this case, the wavelet map displays the white field.

For example, Fig. 2 shows that in the intervals, where there are no observations, the values are displayed only for large values of the period. That is, where the smoothing function is determined by the "distant" observations (before and after t_0). Obviously, such missing dots are not used in the weighted averaged wavelet map to obtain the corresponding periodogram.

In the short format, a special "variable length" algorithm: for each shift t_0 is determined the number n_p of trial periods P , for which the value of the test function is non-

zero. Then in the file are written t_0, n_p and an array of values of the remaining test function. For sparing file size, only one of the test functions is chosen (namely WWZ).

The second output file contains the characteristics of the skeleton, and the third one – the mean weighted wavelet periodogram ($\lg P, \langle WWZ \rangle, \langle S \rangle, \langle r \rangle$).

Conclusions

The program for the wavelet analysis of the modified method of Morlet is introduced. The algorithm generalized to the general case of irregularly spaced (in time) observations was proposed by Andronov (1998). The program enables to calculate three different test functions with a meaning of: a) the "signal/noise" ration (WWZ); b) the square of the correlation ratio for the observed and smoothed values of the signal (S); c) the semi-amplitude r of the smoothing sine function,

The program has the graphical interface and the ability to visualize the light curve and wavelet maps, cross-sections on both coordinates and the skeletons.

We developed the software used for the study of variable stars, and the results of this study will be used in the frame of the projects "Ukrainian Virtual Observatory" (UkrVO) (Vavilova et al., 2012) and "Inter-Longitude Astronomy" (Andronov et al., 2010).

References

- Andronov I.L.: 1990, *Kinem. Phys. Celest. Bodies*, **7**, 70, 1991KPCB...7...70A
- Andronov I.L.: 1998, *Kinem. Phys. Celest. Bodies*, **14**, 374, 1998KPCB...14..374A
- Andronov I.L.: 2010, *Odessa Astron. Publ.*, **23**, 8.
- Andronov I.L., Chinarova L.L.: 2012, *Odessa Astron. Publ.*, **25**, 148.
- Andronov I.L.: 1997, *Astron. Astrophys. Suppl.*, **125**, 207.
- Andronov I.L.: 1999, in: *Priezzhev VB, Spiridonov VP (eds.) Self-Similar Systems*// Dubna: JINR, 57.
- Astafieva N.M.: 1998, *UFN (Advances in Physical Sciences)*, **166**, 1145.
- Chinarova L.L.: 2010, *Odessa Astron. Publ.*, **23**, 25.
- Daubechies I.: 1992, *Ten Lectures on Wavelets*, SIAM.
- Foster G.: 1996, *Astron. J.*, **112**, 1709.
- Szatmary K., Vinko J., Gal J.: 1994, *Astron. Astrophys. Suppl.*, **108**, 377.
- Vavilova I.B.: 2012, *Kinem. Phys. Celest. Bodies*, **28**, 85, 2012KPCB...28...85V
- Vitjazev V.V.: 2001, *Wavelet Analysis of Time Series* (in Russian), St-Petersburg Univ.

ANALYSIS OF THE PARAMETERS AND ABUNDANCE OF N-CAPTURE ELEMENTS FOR FOUR STARS WITH DIFFERENT METALLICITY

N.Yu.Basak, T.V.Mishenina
Astronomical Observatory, Odessa National University
T.G.Shevchenko Park, Odessa 65014 Ukraine
astro@paco.odessa.ua

ABSTRACT. Based on the spectra obtained with echelle spectrograph SOPHIE (1.93 m telescope, OHP, France) and the selection of lines (Basak & Mishenina, 2012). we have redefined the parameters and have determined the abundances of the elements produced in the process of neutron captures for stars HD 6582, HD19445, HD 84937, HD170153. Obtained abundance of Y, Zr, La, Ce, P, Nd, Sm, and Gd, shows the solar scaled abundance distribution.

Key words: Stars: abundance – Stars: late-type

To analyze the stars in a wide range of metallicity ($-3 \leq [\text{Fe}/\text{H}] \leq -0.7$) based on the spectra obtained with high resolution and signal to noise ratio (S/N) allow us to precise the sources of its production at different metallicities.

The spectra for the four stars were selected from the archives of the spectrograph SOPHIE (Perruchot et al. 2008) at 1.93 m telescope (OHP, France) (<http://www.obs-hp.fr/www/guide/sophie/sophie-info.html>). Processing of the spectra was performed using the new version of the DECH20 software by Galazutdinov (1992).

In this work we have redefined the parameters for four stars HD 6582, HD19445, HD 84937, HD170153 and focused our attention on the elements produced in the process of neutron captures. The effective temperature T_{eff} were redefined upon the independence of iron abundance, obtained with the lines of Fe I, from the potential of the lower level of the line. The gravity $\log g$ was determined using ionization balance for Fe I and Fe II. The microturbulent velocities ξ were determined using the independence of the iron abundance on the individual equivalent width of Fe I lines. The main parameters of the stars are in Tabl. 1.

Table 1. Parameters of studied stars

HD	V	Sp	T_{eff} (K)	$\log g$	ξ (km s ⁻¹)	[Fe/H]
6582	5.1	G5Vb	5330	4.35	0.4	-0.86
19445	8.1	A4p	5950	4.1	1.3	-1.99
84937	8.3	sdF5	6200	3.8	1.6	-2.15
170153	3.6	F7V	6160	4.0	0.9	-0.57

To determine the abundance we used the Kurucz's models and the line list (Basak & Mishenina, 2012). The atomic parameters of this line list were taken from the

database VALD (Kupka et al., 1999), for Ce II lines from Lawler et al. 2009. The Fe, Y, Zr, La, Ce, Pr, Nd, Sm, and GdII abundances in the atmospheres of studied stars were computed under the WIDTH program by Kurucz (1993).

The results are given at Fig.1. As solar abundance we used the data from Grevesse et al (2010).

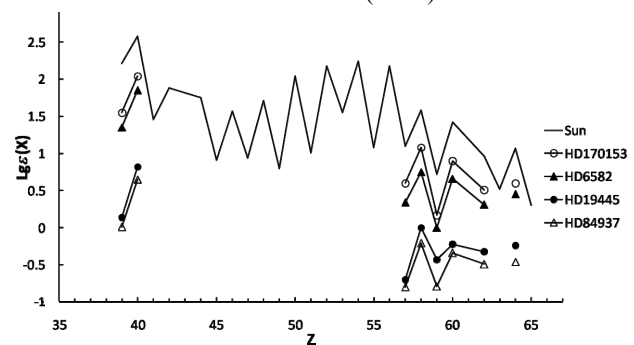


Fig. 1. Behaviour of the element abundances in the atmospheres of the Sun and of investigated stars.

Results and conclusions

1. We determined the abundance of Fe (using from 475 to 876 lines), Y (from 11 to 23), Zr (from 9 to 23), La (from 7 to 25), Ce (from 5 to 57), Pr (from 4 to 22), Nd (from 11 to 73), Sm (from 5 to 46), and Gd (from 1 to 12).

2. We found that distribution of n-capture element's abundance in studied stars are corresponding to solar scaled abundance distribution. This suggests that the sources of enrichment by these elements with pre-stellar medium are the same as for the Sun.

Acknowledgments. This work was supported by the Swiss National Science Foundation (SCOPES project No.~IZ73Z0-128180/1).

References

- Basak N.I., Mishenina T.V.: 2012, *Odessa Astron. Publ.*, **25**, 159.
Galazutdinov G.A.: 1992, Prepr.SAO RAS, **92**, 28.
Grevesse N. et al.: 2010, *Astrophys. Space Sci*, **328**, 179.
Kupka F. et al.: 1999, *Astron. and Astrophys. Suppl. Ser.*, **138**, 119.
Kurucz R.L.: 1993, CD ROM n13.
Lawler et al.: 2009, *Astrophys. J. Suppl.*, **182**, 51.
Perruchot et al.: 2008, "The SOPHIE spectrograph Proceedings of the SPIE, 7014.

INTERESTING MOON'S SURFACE FEATURES. OUR STUDY AND SOME INFERENCES

Yu. N. Bondarenko

Astronomical observatory, Odessa National University,
Shevchenko Park, Odessa, Ukraine, 65014

ABSTRACT. In this article the results of the long-term CCD observations of the Moon are presented. We describe some unusual features existing on the Moon's surface and discuss their possible origin.

Observations of the Moon's surface even with the small-size telescopes appear to be quite promising. It could be that the author of the present study succeeded in discovering peculiar circular structures in some places on the Moon's surface, extraordinarily round shape of some dark patches of the lunar maria and the dark stripe of unclear origin on the shore of Mare Humorum.

It is likely that peculiar craters of unknown origin, which are localized on the fissures, are the centre of activity in the crater Alphonsus, rather than the crater's central peak as it was suggested by N.A. Kozyrev (Fig.1,2). The mechanism of their formation and dark material ejecting can be hardly explained by the known processes.

To clarify the issue on the transient lunar phenomena (TLP), the author of this paper has been conducting observations of the Moon at the Mayaki observational site for several years already. For that purpose, the Cassegrain reflector with the primary mirror diameter of 40 cm and the 3 m equivalent focus length was used. It was mounted on the astronomical parallactic tripod (APSh-6) and equipped with the VAC-135 video camera with the 8x10 mm black-and-white CMOS sensor of the progressive scanning type. The tripod redesign was narrowed down to the replacement of the gravity-powered clock drive by the equivalent electric-motor drive with mounting of electric motors instead of mechanical alignment devices. That reflector is also used for the photographic meteor observations.

It is mainly those lunar regions were photographed, which were reported to be the most active by the literary sources. The video footages made up of several hundred frames are processed in VirtualDab and RegiStax4. Our device allows of conducting observations in 4 optical light filters: 420 nm, 550 nm, 700 nm and 1000 nm. The best spectral resolution is obtained in the red and yellow-green regions of the spectra. Composing of two or three images, which were recorded with a time interval, allowed of implementing a specific comparator as any visible changes in the image that occurred within that interval will be highlighted in colour. Besides, the colour image

appears to be visually sharper than the black-and-white one.

Unfortunately, we did not manage to apply such a method of composing of different colour images to the full extent due to problems with the software available. Therefore, the colour images were recorded mainly at the large Moon's phases when it was possible to detect weak colour variations in albedo.

The procedure of observations contains initial recording of observations, their viewing and further processing. 20-30 sharp final images can be made during one night of observations. Between recording images, the Moon is real-time displayed on the screen. Predominantly, the bright side of the Moon was observed. Meanwhile, the possibility of the Moon's surface observation in the Earthshine has been considered.

High turbulence in the Earth's atmosphere makes the image processing more difficult; however, we succeeded in obtaining images of the Moon's surface with the ground resolution of several kilometres with the reflector available. A large amount of interesting images are gathered, and they are available for all interested in their processing.

The issue on the transient lunar phenomena was managed to be solved just partially. The major part of the corresponding reports on those phenomena is evidently associated with ambiguities and inaccuracies in observations. Some information on the mentioned phenomena can be found at <http://www.ufo.obninsk.ru/moon5.htm>.

The issue regarding the crater Eratosthenes, at the bottom of which the dark patches that vary over a lunar day were observed, was slightly clarified. As the pattern of such variations recurs every lunar day, it was concluded that it could be just due to the light effects. The same is fair for the so-called 'champion' of such phenomena - the crater Aristarchus; its appearance changes in a regular manner over each lunar day.

It should be noted that the same Moon's surface features appear in very different manner relative to the lighting conditions, and that can be one of the factors causing misinterpretations of the detected phenomena.

The occurrence of the transient lunar phenomena was neither confirmed nor disproved during our observations. Moreover, peculiar circular features were detected on the Moon's visible surface. Those are apparently the albedo features, and they appear regularly at the near full Moon

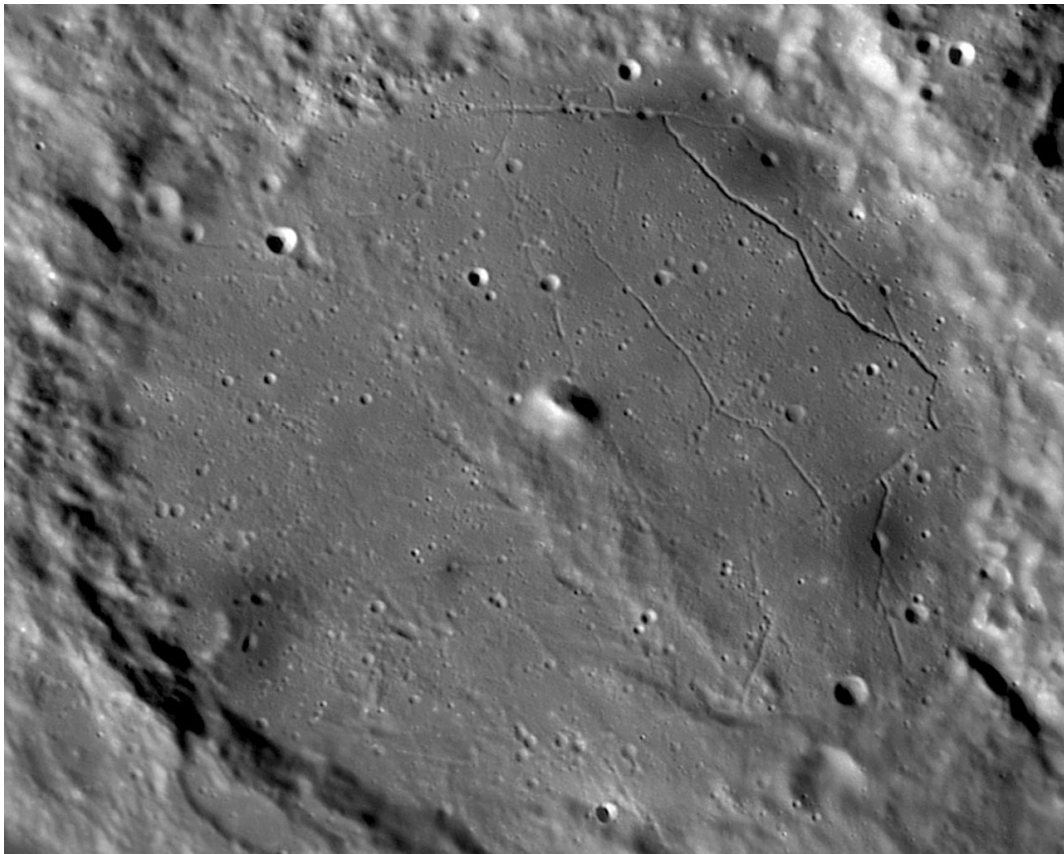


Figure 1: Crater Alphonsus

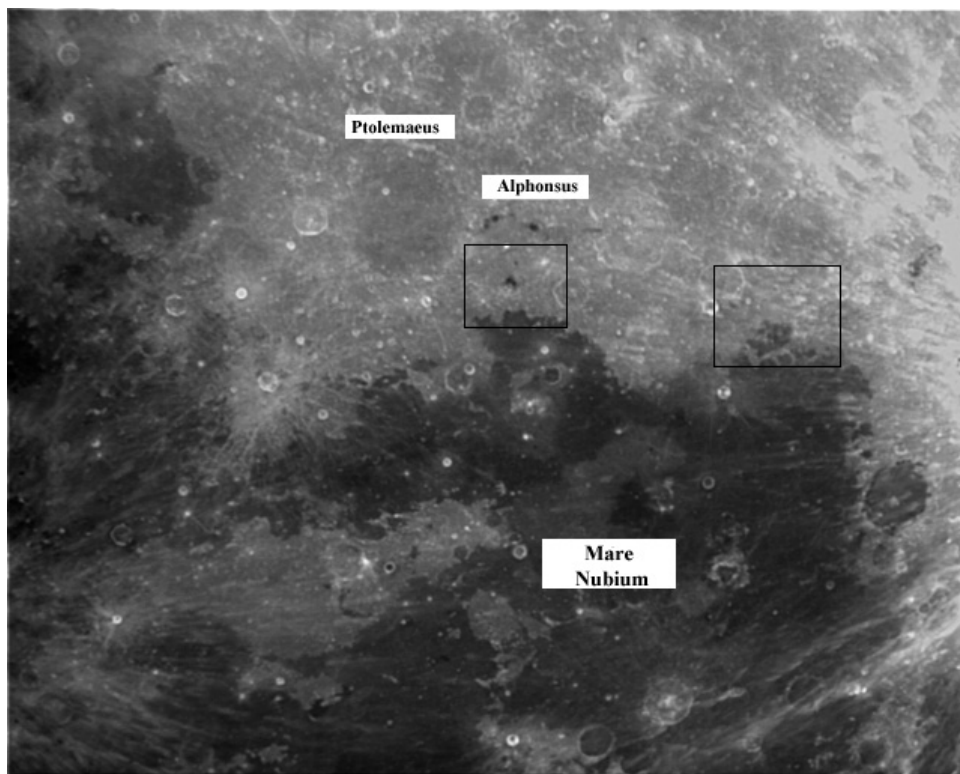


Figure 2: Mare Nubium and crater Alphonsus

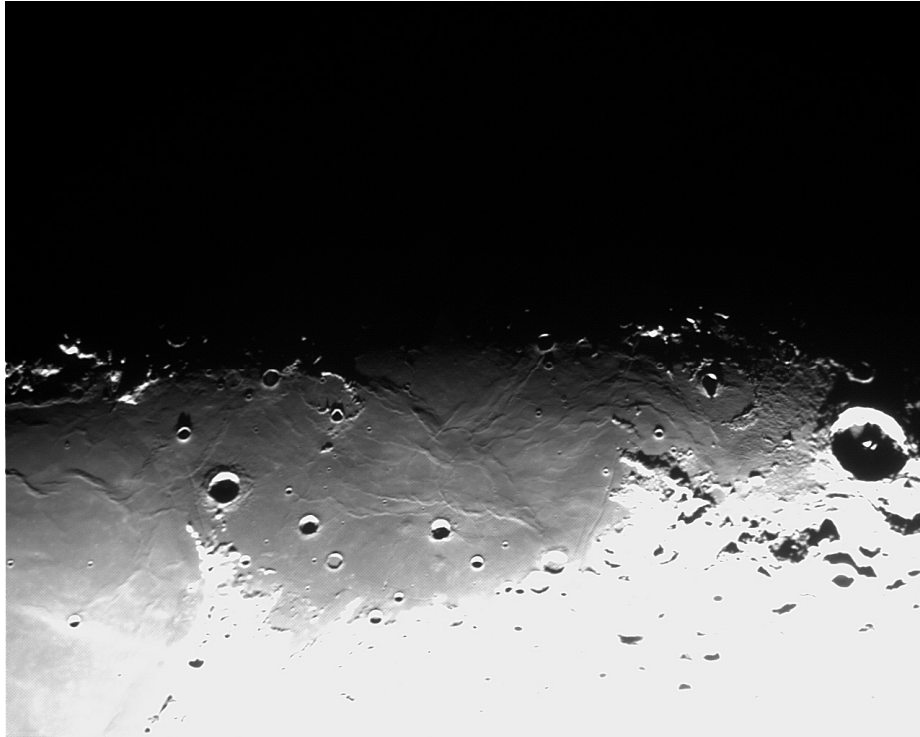


Figure 3: Local evening in Mare Tranquillitatis ("Dream valley", the photo is taken by the author). It is possible to distinguish some ring ridges that can be craters filled in with lava when the mare was formed. They are not similar to the circular features, which are best seen at the local noon.

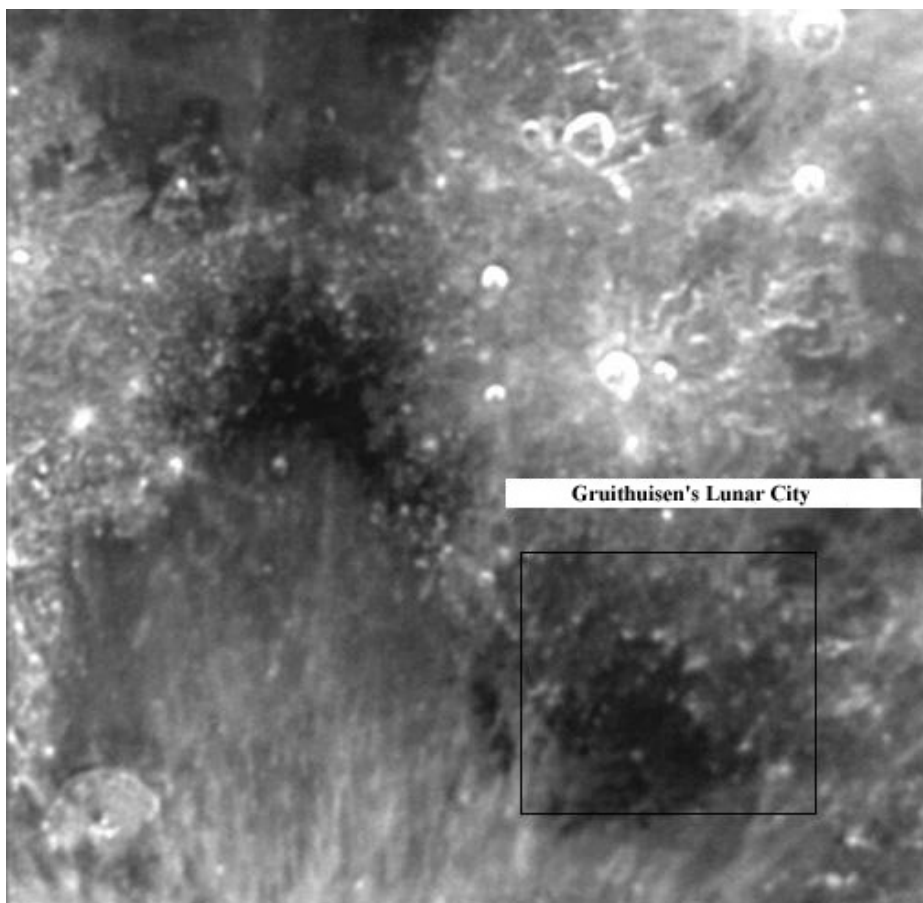


Figure 4: A ring feature against the Gruithuisen's Lunar City background.

phase. They have the regular shape of narrow discrete rings, and almost all of them can not be explained within the framework of the current hypotheses of the lunar circular structure formation. Those features are best seen at the local noon. With the oblique incidence of sunlight on that region of the Moon's surface, a streak of smoother surface can be sometimes (but not always) observed in the places of the ring localisation.

It should be noted that the mentioned circular features can not be explained by the ringing artefacts of the image processing as they become apparent on the initial observation records that had not yet been processed (Figs. 3, 4). They can also be traced on the images from various sources (e.g. images taken during the Clementine spacecraft mission or images available at the Astronominsk web-site: <http://www.astronominsk.org>).

The period of visibility of those circular features is about 4-6 days. They do not flare up near the full Moon, and hence, can hardly be explained by the absence of the retro-reflective (cataphot) glass beads. It is obvious that neither they could be old partially erased craters. That is especially true with regard to the sharpest and most contrasty ring located against the background of the crater Alphonsus and adjacent highlands. That ring when it is best seen can be identified even better than Alphonsus, the location of which can be determined only by its inner dark patches.

It should be noted that subsurface circular structures were also discovered in Mars by the Mars Express mission. But it is not clear whether those features are of similar origin with the lunar ones as the history and crustal structure of the Moon and Mars are different a priori.

We discovered six such circular structures. And there is one more interesting feature found on the shore of Mare Humorum. There is a cut across one of the lunar craters from where a straight dark stripe stretches till the Mare Humorum plain. That stripe does not become apparent in the relief features. It does not appear as a tectonic fault or fissure, which are typically brighter at the full Moon. But it is similar to the mentioned peculiar circular features though. It is not resulted from the ringing artefact due to the CCD television camera structure. When rotating the CCD camera that stripe does not disappear.

Besides, it is worth of paying attention to the S-shaped boundary between the dark and bright surface of the Mare Nubium near the crater Gassendi. The origin of that boundary can not be explained. It should be noted that dark patches on the lunar plains often appear like they are result from some self-propagating process kind of the steppe fire. It can be indicative of the fact that the material of the superficial regolith layer is sorted in the course of a certain process (e.g. electrostatic one).

Some images showing those peculiar features are available for downloading and discussing at <http://www.astronomy.ru/forum/index.php/topic,89610.new.html#new>.

While observing the Moon, the crater Alphonsus has been paid our special attention. The obscuration in the centre of that crater, observed by Kozyrev, as well as the obtained spectra have been actively discussed (see "The near-Earth space environment exploratory research", 1961). Although no activity was registered in that region, some interesting suggestions can be retrieved from the archive images, obtained in the Pic du Midi Observatory, France, with the ground resolution of about 100 meters. Several irregularly shaped dark patches can be observed in the mentioned images of the crater Alphonsus. The centres of distribution of those dark patches are peculiar craters that are localised at the fissures of cooling, formed during the solidification of lava that filled up hollows and cavities of the crater billion years ago. Those craters are not circular, they are assignably located exactly on the fissures and evidently are not impact craters or those resulted from volcanic eruptions. One of the craters exhibits a peculiar 'tail' that stretches towards the East and could be the dust tail. That tail can be traced throughout the whole series of our images. The craters look like the material has been ejected from them. When correlating the patch sizes and the possible rate of the material spreading, the latter is supposed to be about 100 meters per second. It should also be taken into consideration that by all indications the ejected material should have spalled from a massive basalt plate, but that is peculiar per se. Such peculiarities of those craters and patches allow of assuming that it is those craters located on the fissures that are the sources of activity in Alphonsus rather than its central peak, which can not be distinguished in our images.

In some cases the dark patches that are visible within the mare regions, in particular within the region of Mare Nubium adjacent to the Alphonsus, have peculiar circular shape, which can be just partially traced along the patch contour. Such a pattern could be explained by the filling of the impact crater with the dark-coloured lava, but no evidences of impact feature presence were detected along the contours of those patches.

The image catalogue of the described peculiar Moon's surface feature images is available at <http://www.astronomy.ru/forum/index.php/topic,89610.new.html#new>.

The following conclusion can be made: at present the Moon as a cosmic object is of great interest for observations with the small-size telescopes.

I would like to express my sincere gratitude to all those who helped me to obtain data for this paper.

References

The near-Earth space environment exploratory research. The Foreign Literature Publishing House, Moscow, 1961 (in Russian).

COMPILATION OF MOMENTS OF SPIN MAXIMA OF THE INTERMEDIATE POLAR EX HYA

V.V. Breus¹, I.L. Andronov²

Department “High and Applied Mathematics”, Odessa National Maritime University,
Odessa, Ukraine, ¹ *bvv_2004@ua.fm*, ² *tt_ari@ukr.net*

ABSTRACT. We present a compilation of the spin maxima of the intermediate polar EX Hya determined using the same methods for our own observations from the Tzec Maun observatory, published observations from the SuperWASP, ASAS and AAVSO databases. For completeness, published data published by other authors are used. We obtained the ephemeris of the spin maxima $T_{\max} = 2437699.89079(59) + 0.0465464808(69)E - 6.3(2) \cdot 10^{-13}E^2$, which corresponds to the characteristic time of acceleration of rotation (spin-up) of $4.67(14) \cdot 10^6$ years.

Key words: Stars: binaries: close - stars: novae, cataclysmic variables - stars: individual (EX Hya)

EX Hya is a magnetic cataclysmic variable. Such binary systems consist of a red dwarf filling its Roche lobe and a magnetic white dwarf. The sub-class of intermediate polars is characterized by a spin period of the white dwarf, which is shorter than the orbital period (cf. Warner 1996, Hellier 2001). Typically, the spin periods of white dwarfs are close to an “equilibrium value”, i.e. to the period of the Kepler rotation of the inner part of the accretion disk around the white dwarf at a distance equal to the radius of magnetosphere. However, this “classical” model corresponds not to all intermediate polars. Detailed analysis shows that, in some systems, the magnetosphere is large enough to prevent formation of the accretion disk, similarly to “asynchronous polars” (Andronov 1987). Norton et al. (2004) split intermediate polars into “disk-fed” and “stream-fed” and suggested EX Hya as a “stream-fed” system. Andronov and Breus (2013) presented a detailed discussion of the parameters of period variations of this system and made estimates of the system parameters which are self-consistent. Breus et al. (2012) discussed a group of intermediate polars.

In this paper, we present a complete list of the spin maxima determined using a multi-periodic (spin+orbital) fit using the software MCV (Andronov and Baklanov 2004). The accuracy estimates for a single timing for the AAVSO data range from 0.00014^d to 0.00152^d (mean 0.00059^d), for the Tzec Maun data – close to 0.003^d . The

statistically optimal fit is a parabola. Its parameters are listed in the abstract.

Table 1. Moments of the spin maxima of EX Hya in BJD-2400000 and corresponding reference

Time	Ref.	Time	Ref.
37699.89200	1	43970.48200	3
37699.93700	1	43971.50700	3
37736.94000	1	43972.43100	3
37737.92000	1	45404.06400	4
37755.74600	1	45404.11000	4
37755.80100	1	45404.15400	4
37755.83800	1	45433.05800	4
37755.88300	1	45433.10400	4
37755.92900	1	45433.14800	4
37786.74200	1	45433.19900	4
37786.79300	1	45443.02100	4
37789.71900	1	45443.06800	4
37789.77600	1	45443.11500	4
37791.73100	1	45443.16400	4
37791.77200	1	45445.15500	4
37793.77400	1	45473.09200	4
37813.69700	1	44653.73960	5
37813.74000	1	44662.67250	5
37816.72600	1	44662.72020	5
37821.70500	1	44663.69980	5
37821.74800	1	44665.65370	5
37822.72900	1	44665.69680	5
38083.10200	1	44675.60960	5
38083.15600	1	44675.70510	5
38083.20100	1	44686.63200	5
38084.03600	1	44686.64440	5
38084.08100	1	44686.73300	5
38084.12500	1	45032.71110	5
38084.17700	1	45032.76250	5
38084.22000	1	45104.44180	5
38087.06800	1	45104.48980	5
38174.66500	1	45104.53360	5
38174.70600	1	45104.58600	5
38410.00100	1	45105.51510	5
38493.83400	1	45105.55700	5

38496.81400	1	45121.47750	5	42126.73400	1	46564.91990	6
38497.79200	1	45121.52400	5	42126.73900	1	46564.97180	6
39147.02500	1	45122.45920	5	42126.78700	1	46565.01570	6
39175.92700	1	45122.50080	5	42126.82800	1	46565.06060	6
39175.97400	1	45122.54960	5	42126.87200	1	46565.85090	6
39176.01500	1	45433.61860	5	42127.62000	1	46565.90280	6
39176.94800	1	45434.50290	5	42127.67100	1	46565.94960	6
39176.98800	1	45455.49410	5	42127.71500	1	46565.99630	6
39229.73300	1	45455.53800	5	42127.76100	1	46566.04100	6
39533.92000	1	45455.58240	5	42127.80900	1	46592.85450	6
39625.70200	1	45455.63250	5	42127.85700	1	46597.88570	6
40009.67200	1	45456.47410	5	42128.65000	1	46597.92800	6
40035.87500	1	45456.51900	5	42128.68900	1	46597.97120	6
40035.91500	1	45456.57020	5	42128.78900	1	48267.58240	7
40049.88100	1	45456.61680	5	42128.83800	1	48268.56290	7
40049.92800	1	45538.43840	5	42128.87500	1	48268.61000	7
41333.63100	1	45538.48720	5	42129.62800	1	48269.54300	7
41361.87800	1	45732.67780	5	42129.66800	1	48269.58070	7
41362.91400	1	45732.77260	5	42129.71200	1	48272.51230	7
41368.86900	1	45733.73200	5	42129.76100	1	48272.56350	7
41369.79700	1	45734.68520	5	42129.81000	1	48272.60850	7
41369.84600	1	45734.73050	5	42776.80300	1	48273.58610	7
41370.86600	1	45734.77390	5	42870.87100	1	48274.56870	7
41371.85100	1	45752.74410	5	42872.73600	1	48274.60960	7
41372.81900	1	45753.76120	5	42872.78100	1	48275.54160	7
41372.87100	1	45754.73920	5	42873.57400	1	48275.58940	7
41392.78800	1	45754.78610	5	42873.61900	1	48276.57300	7
41392.83800	1	45771.54110	5	42872.36100	2	48276.60810	7
41392.88200	1	45771.58890	5	42872.40300	2	48278.56230	7
41393.68100	1	45771.63790	5	42872.45700	2	48278.60980	7
41393.72200	1	45812.50210	5	42872.49800	2	45546.44500	8
41393.77100	1	45812.55170	5	42872.54800	2	46261.30440	8
41393.81700	1	45848.43410	5	42872.59800	2	46261.34710	8
41393.86600	1	45848.52760	5	44320.83200	2	46261.39280	8
41394.84100	1	45887.44100	5	44322.64700	2	46261.44500	8
41394.88800	1	46313.07100	6	44322.70000	2	46261.49050	8
41397.72900	1	46317.95920	6	44322.74500	2	46261.53530	8
41397.77600	1	46321.07300	6	44322.79000	2	46261.57890	8
41397.82400	1	46499.94810	6	44322.83800	2	46261.62390	8
41397.86700	1	46499.99600	6	44324.70000	2	46261.67300	8
41399.77500	1	46500.04570	6	44324.74500	2	46261.72180	8
41399.81600	1	46500.08430	6	44324.79200	2	46261.76360	8
41399.86900	1	46500.12550	6	44324.84000	2	46261.81480	8
41441.52600	1	46506.04400	6	43960.04800	3	46262.37070	8
41441.57300	1	46506.96970	6	43960.70100	3	46262.42270	8
41442.59400	1	46507.02500	6	43960.75500	3	46262.46680	8
41444.55500	1	46507.07050	6	43960.79600	3	46262.51300	8
41444.59900	1	46507.10730	6	43961.35600	3	46262.55520	8
41447.52800	1	46507.15340	6	43961.40900	3	47328.79044	8
41449.53000	1	46513.02930	6	43961.45500	3	47328.88757	8
41860.99600	1	46521.12270	6	43961.68300	3	47328.98132	8
41865.89000	1	46521.17060	6	43961.89400	3	47329.02481	8
41865.94100	1	46534.10910	6	43962.42700	3	47329.16375	8
42125.57400	1	46534.16020	6	43962.47600	3	47329.30569	8
42125.61500	1	46536.07300	6	43962.51900	3	49185.47425	8
42125.66600	1	46536.11140	6	43962.57000	3	49502.17402	8
42125.71100	1	46536.15620	6	43963.07000	3	50193.99031	8
42125.76600	1	46558.92470	6	43963.59200	3	51683.27876	8
42125.80700	1	46558.97440	6	43963.64100	3	51687.51537	8
42125.85000	1	46561.94120	6	43963.73100	3	52364.81020	8
42126.64600	1	46561.98590	6	43963.78500	3	52364.86080	8
42126.69000	1	46564.87830	6	43963.82600	3	52366.72760	8

43963.87000	3	52366.77590	8	43970.15500	3	55343.70633	12
43963.89800	3	53027.76780	8	43970.20100	3	55345.74814	12
43963.91700	3	53027.81170	8	43970.28600	3	55346.54597	12
43963.96800	3	53030.83890	8	43970.34400	3	55353.41999	12
43964.10000	3	53922.24075	9	43970.43200	3	55602.64567	12
43964.14900	3	53924.23738	9				
43964.19900	3	54235.21476	8				
43964.38100	3	54237.96000	8				
43964.42900	3	54240.38080	8				
43964.61300	3	54243.03427	8				
43964.66600	3	54301.68235	8				
43964.71100	3	55242.04153	10				
43964.75400	3	55243.86350	10				
43964.85100	3	55245.96115	10				
43964.94300	3	55266.16346	10				
43964.99200	3	55278.96482	10				
43965.03000	3	55720.03332	10				
43965.08000	3	53517.19677	11				
43965.12700	3	51979.68379	11				
43965.36800	3	52724.98354	11				
43965.40200	3	53086.64265	11				
43965.45400	3	53477.91196	11				
43965.50400	3	53517.19677	11				
43965.54200	3	53807.97021	11				
43965.58800	3	54230.51766	11				
43965.63900	3	54566.29857	11				
43965.68900	3	54920.42192	11				
43965.73200	3	54306.05891	9				
43965.78000	3	52739.27160	12				
43965.82700	3	52741.27171	12				
43965.87700	3	52746.43884	12				
43965.91400	3	52747.46381	12				
43965.97200	3	52758.95966	12				
43966.01100	3	52761.84613	12				
43966.05200	3	53020.13009	12				
43966.43300	3	53066.16300	12				
43966.48400	3	53149.43193	12				
43966.52700	3	53150.41352	12				
43966.57300	3	53839.43331	12				
43966.95400	3	53842.41170	12				
43966.99400	3	53863.35822	12				
43967.03500	3	54191.04295	12				
43967.45600	3	54192.01924	12				
43967.50000	3	54192.01953	12				
43967.55000	3	54192.01953	12				
43968.94600	3	54192.01971	12				
43968.98600	3	54217.99108	12				
43969.04000	3	54218.96889	12				
43969.08800	3	54219.94688	12				
43969.12700	3	54225.95095	12				
43969.18300	3	54226.97509	12				
43969.28000	3	54227.95194	12				
43969.36800	3	54949.97649	12				
43969.41300	3	54955.00266	12				
43969.45800	3	54970.36511	12				
43969.49500	3	54976.32200	12				
43969.55100	3	55061.92956	12				
43969.59600	3	55278.97585	12				
43969.96400	3	55313.03434	12				
43970.01600	3	55340.12068	12				
43970.05500	3	55341.70967	12				
43970.10900	3	55342.73235	12				

The data sources:

- 1 Vogt et al, 1980
- 2 Gilliland, 1982
- 3 Sterken et al, 1983
- 4 Hill et al, 1984
- 5 Jablonski et al, 1985
- 6 Bond et al, 1988
- 7 Hellier et al, 1992
- 8 Mauche et al, 2009
- 9 Observations from SuperWASP public archive
- 10 Observations obtained using telescopes of the TzecMaun Observatory
- 11 Observations from The All Sky Automated Survey (ASAS) data archive
- 12 Observations from AAVSO database

Acknowledgements. We thank Dr. L.Hric for helpful discussions and hospitality during the stellar conference in Bezovec, to the Tzec Maun Foundation for allowing to get observations at the remotely controlled robotic telescope. The SuperWASP, ASAS and AAVSO databases were analyzed. The study was made in a course of the projects "Inter-Longitude Astronomy" (Andronov et al. 2010) and "Ukrainian Virtual Observatory" (Vavilova et al. 2012).

References

- Andronov I. L.:1987, *Ap&SS*, **131**, 557
 Andronov I.L., Baklanov A.V.: 2004, *Astronomy School Reports*, **5**, 264, <http://uavso.pochta.ru/mcv>
 Andronov I.L, Breus V.V.: 2013, *Astrophysics*, **56**, 518.
 Andronov I.L. et al.: 2010., *Odessa Astron. Publ.*, **23**, 8
 Bond I.A., Bond I.A., Freeth R.V., 1988, *MNRAS*, **232**, 753
 Breus V.V. et. al.: 2012, *Częstochowski Kalendarz Astronomiczny 2013*, 153, 2012arXiv1212.6712B
 Gilliland R. L.: 1982, *Astrophysical Journal*, **258**, 576
 Hellier C.: 2001, *Cataclysmic Variable Stars. How and why they vary?* Springer. 210 pp.
 Hellier C.; Sproats L.N.: 1992, *IBVS*, **3724**, 1
 Hill K.M., Watson R.D.: 1984, *Astronomical Society of Australia, Proceedings*, **5**, 4, 532
 Jablonski F., Busko I.C.: 1985, *MNRAS*, **214**, 219
 Mauche, C. W.; Brickhouse, N. S.; Hoogerwerf, R.; Luna, G. J. M.; Mukai, K.; Sterken, C.: 2009, *IBVS*, **5876**, 1
 Norton A.J., Wynn G.A., Somerscales R.V.: 2004, *Astrophys. J.*, **614**, 349.
 Sterken C., Vogt N., Freeth R., Kennedy H.D., Page A.A., Marino B.F., Walker W.S.G., 1983, *Astronomy and Astrophysics*, **118**, 325
 Vavilova I.B. et al.: 2012, *Kinem.Phys.Cel.Bodies*, **28**, 8
 Vogt N., Krzeminski W., Sterken C.: 1980, *Astronomy and Astrophysics*, **85**, 106
 Warner B.: 1995, *Cataclysmic Variables Stars*, Cambridge University Press, 562pp.

ALL-SKY CAMERAS FOR OBSERVATION AND INVESTIGATION OF VARIABLE STARS AND METEOR SHOWERS

I.S.Bryukhanov, I.M.Sergey, V.Vatutina, A.Ivchik, M.Pogodina, R.Vatolin, S.Dovnar,
V.Osadchaya, A.Tabolich, V.Tabolich, A.Lyubimov, T.Smolenchuk, A.Chernik, M.Chernyavskiy,
I.Nazaruk, M.Nazaruk, D.Akulich, E.Zaritskaya

The Republic Centre of Technical Creativity, 12, Makayonka, Minsk 220033, Belarus
betelgeize_astro@mail.ru

ABSTRACT. This paper studies the capabilities of the all-sky weather (meteorological) cameras in investigation of bright variable stars and determination of apparent radiants of meteor showers.

1. Introduction

The elaboration of this experimental study within the framework of the “Astrobloknot” (Astronomical notebook) project using the meteorological all-sky camera images has been conducted in several steps and for several reasons:

– I. Sergey suggested carrying out observation of the Geminids meteor shower maximum activity using the all-sky cameras of the Tzec Maun project in Australia and in the USA.

– On having conducted the above-mentioned observation, I. Bryukhanov found that such images could be also used to determine extreme points of bright variable stars for the O–C research works as the limiting magnitude of those images was 6.5 m in good weather conditions; besides, the number of shots taken per day with certain cameras varied between 400 and 950.

– N. Samus and L. Berdnikov suggested continuing of such studies for eclipsing and the Cepheid variables, respectively, as there have been precious few extreme points of bright variable stars actually observed for the last 30 years.

So that is how the **All-Sky Beobachter** (‘beobachter’ means an observer in German) project for electronic surveillance of the meteor shower maxima and bursts of activity, as well as the bright variable extrema arose. That

is a small supplement to the “Astrobloknot” project regarding bright stars.

Images from three all-sky cameras in the Southern Hemisphere and seven all-sky cameras in the Northern Hemisphere are currently available online to be downloaded free of charge.

New software to conduct such continuous sky monitoring, developed by D. Akulich, is available since July 2010.

2. Variable stars

I.Sergey carried out experiment focused on rapid processing of all-sky camera images with MaximDL programme. The results showed that the indicated programme enabled to more or less reliable measuring of brightness of only those stars, which are brighter than 3 m.

Due to a large number of all-sky camera shots per day (from 400 to 950 shots), the target star brightness and time of the average value were averaged over several images. The average value provides the measurement accuracy ~ 0.1 m; and the instant of time can be determined with accuracy to 7-10 minutes.

Eye-estimates of the investigated stars’ brightness using the all-sky camera images displayed on the screen allow of measuring the brightness of stars of up to 6.5 m with normal accuracy.

The results of brightness measurements of faint stars have still been processed so far. The light curves of famous periodic classical variable stars, obtained by the methods described above, are presented here below (see Figs. 1-4).

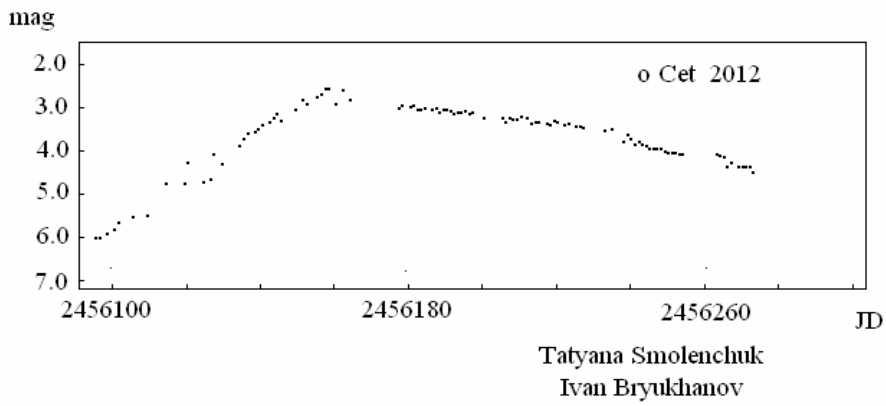


Figure 1

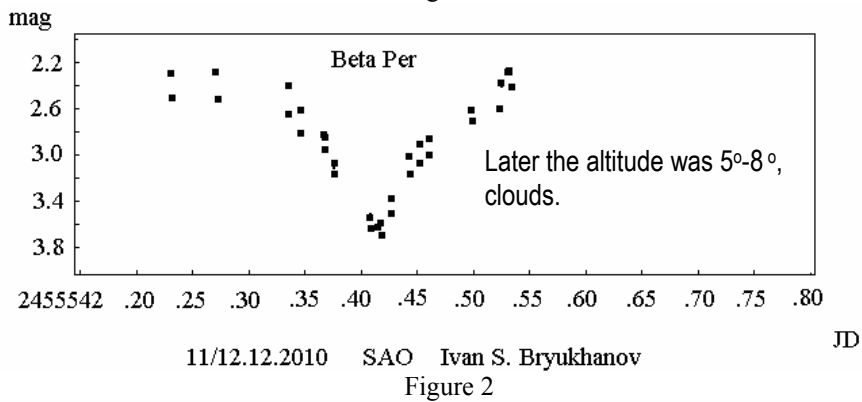


Figure 2

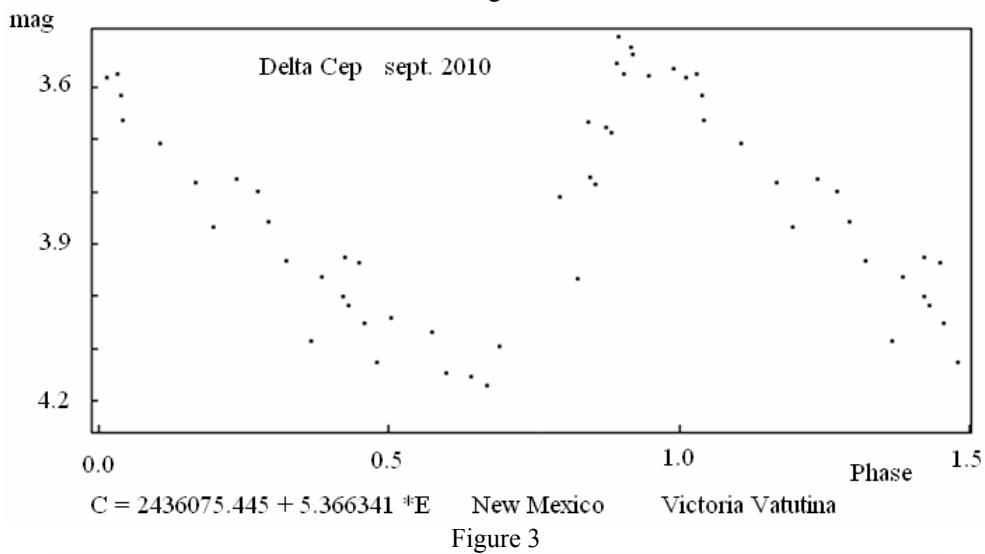


Figure 3

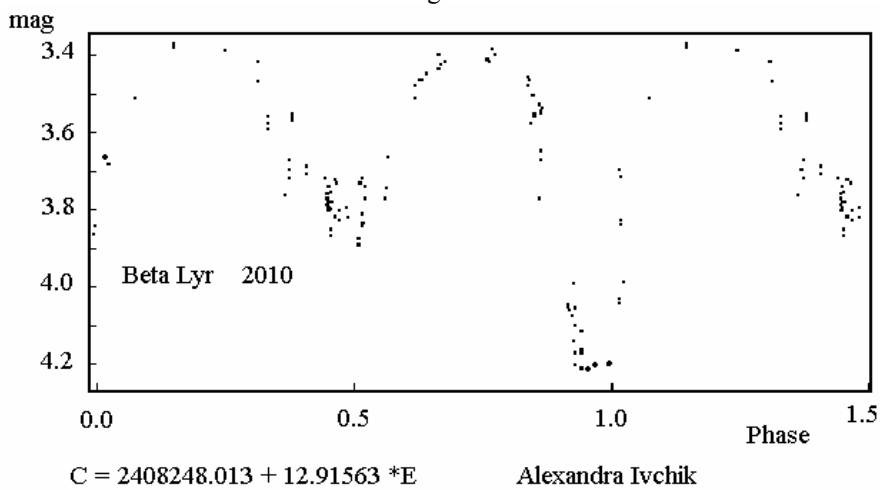


Figure 4

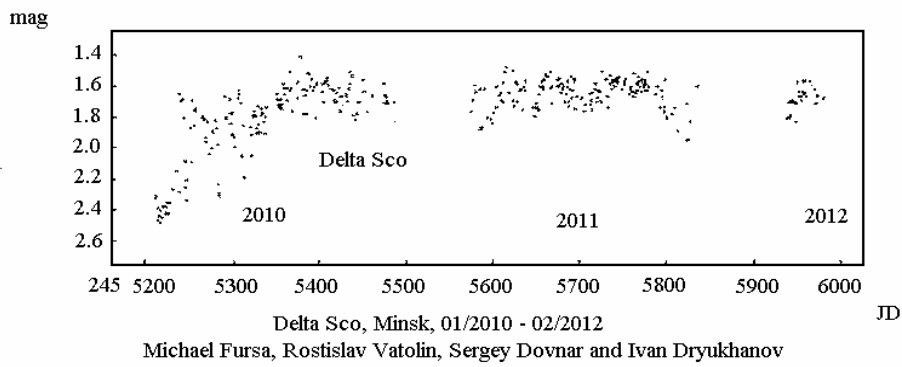
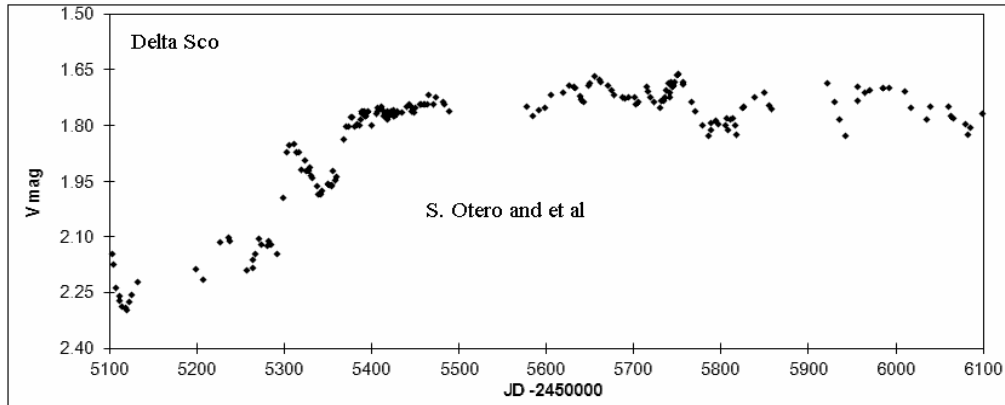
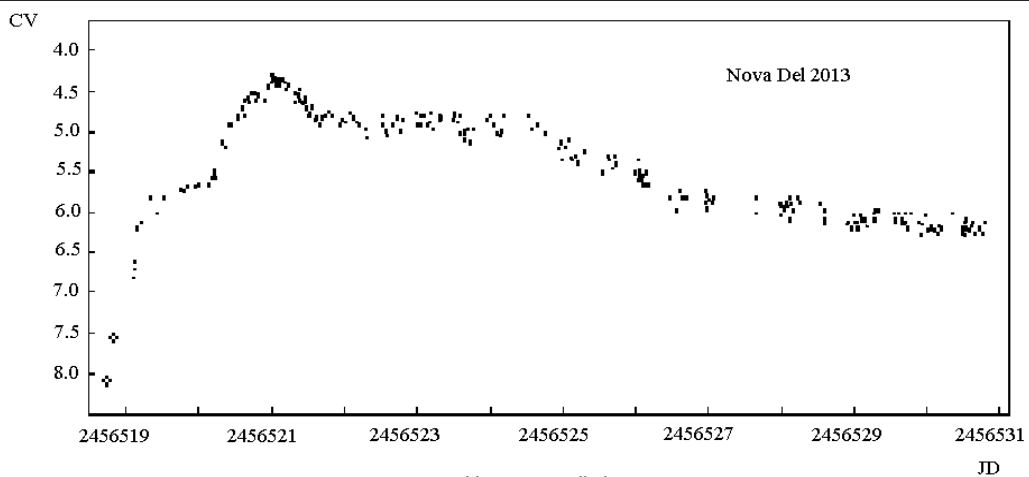
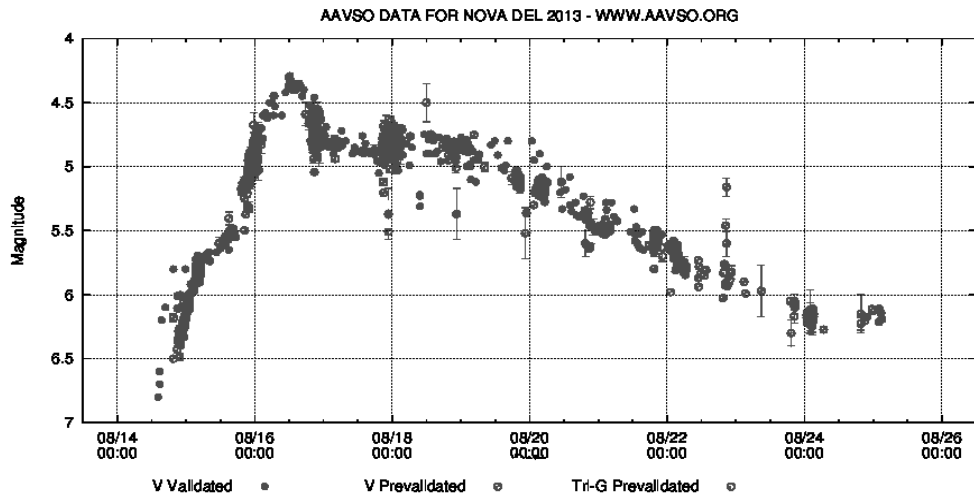
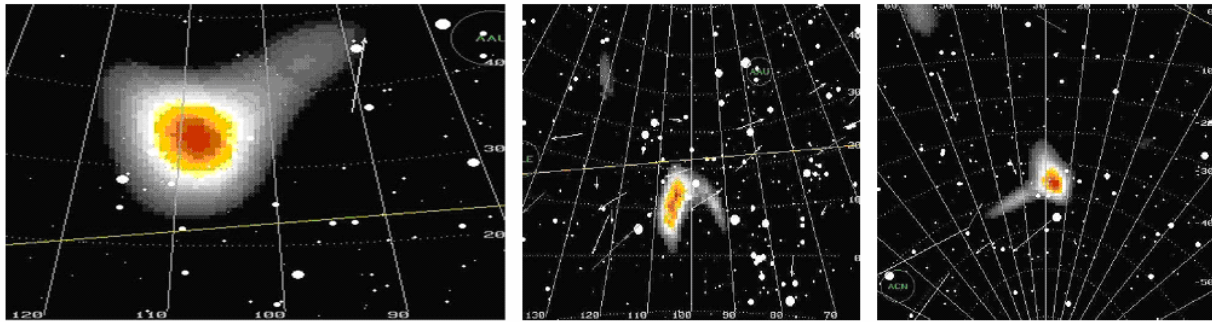


Figure 5



Ivan S. Bryukhanov 3 all-sky camera's

Figure 6



Left: The Geminids' radiant on 2009 December 13–14 at $\alpha = 108^\circ$ and $\delta = +34^\circ$ (all-sky camera in New-Mexico, United States). *Center:* The Monocerotids' radiant on 2009 December 6–8 at $\alpha = 105^\circ$ and $\delta = +13^\circ$ (all-sky camera in Pingelly, Australia). *Right:* The Phoenicids' radiant in 2009 at $\alpha = +28^\circ$ and $\delta = -47^\circ$ (all-sky camera in Pingelly, Australia).

Figure 7

The measurements of brightness were conducted in the CV rays (and in more practical classical degrees of brightness) as the main goal of such surveillances is to determine the extreme points.

The measurements of unique blue flaring variable Delta Scorpii were performed as an experiment, and the periastron passage fell on July 2011 and could be controlled. By assent of Sebastian Otero, the multi-observer diagram by foreign observers and those in Minsk is presented in Figure 5; as is shown, it is possible to obtain normal qualitative photometric data for bright variables with amplitude of more than 0.5 m using even the simplest meteorological all-sky cameras.

By the time of this article preparation, on the night of 14/15 of August 2013 a possible Nova burst in Delphinus was discovered by Japanese amateur astronomer Koichi Itagaki with 60-cm reflector and the CCD-camera without filters.

Ivan Bryukhanov carried out almost 24-hour measurements of brightness using the images from all-sky cameras in Chile, Australia and SAO RAS purposely to settle the issue how it is possible for a single observer to accurately and reliably determine the variable brightness using several cameras and plot a diagram of the nova outburst. The results were just as well as those of 381 AAVSO observers (Fig. 6).

3. Meteor showers

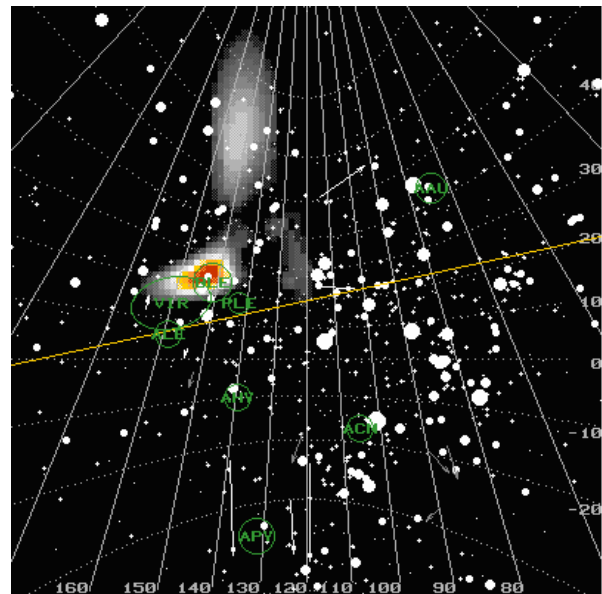
The astrometry data for meteors were processed with the programme "RADIANT-1.42" developed by the IMO Visual Commission Director Rainer Arlt.

The first data as such the results of comparison between the photographic visual estimation of the radiant for the Geminids meteor shower and the 2009-2010 all-sky camera images were applied into print during the IMC-2011 conference in Sibiu in Romania.

At that time the Geminids activity was rather high and allowed of detecting many meteors in the all-sky camera images and consequently finding real radiant for each year. The Monocerotids and Phoenicids radiants in 2009 were also accidentally detected and estimated using those images (Fig. 7).

As an experiment the surveillance of the 2010-2012 all-sky camera images of the Leonids, the peak activity of which was rather low – not more than 15-17 meteors per hour (and the

Moon was shining near the radiant in 2011), was conducted. The Leonids radiant was estimated (Figures 8-10).



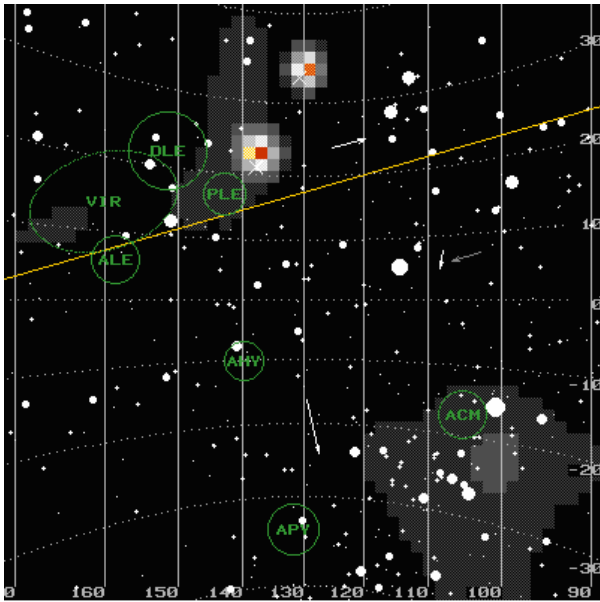
The Leonids radiant on 2010 November 15-18 (RA = 154° and Dec = $+21^\circ$ (all-sky camera in New-Mexico, United States)

Figure 8

In 2011 there was a burst of the October Draconids with one peculiarity that the event occurred at nearly full Moon. In fact, all images by the all-sky cameras were light-struck. However, the third auxiliary camera in SAO enabled to determine the meteor shower radiant. Meanwhile, a weak all-sky camera in Kiruna properly recorded bright red meteors of the Draconids, and the result of the radiant estimation using that camera images turned out to be the most reliable one (Fig. 11, 12).

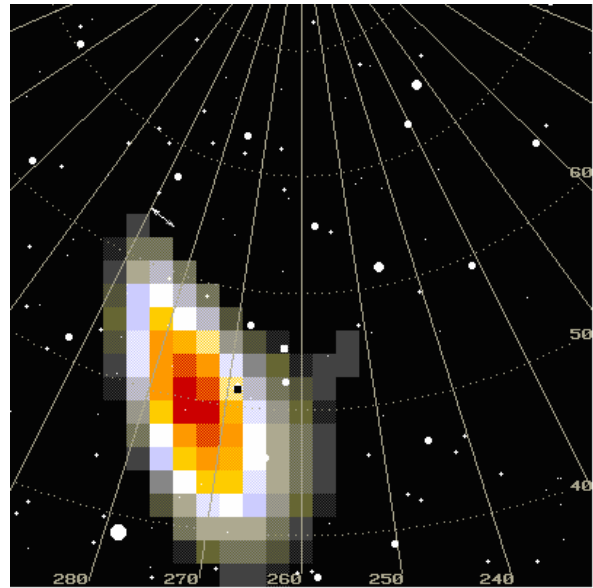
Our colleagues from the IMO suggest fixing just upon the radiant estimation and using of the all-sky camera images to confirm high activity and outbursts of meteor showers, including unlabelled ones.

The brightness estimations for bright variables using the all-sky camera images can be combined with measurements using photographic plates from Odessa photographic glass plate archive in the V band for stars of magnitude 5 and fainter ones.



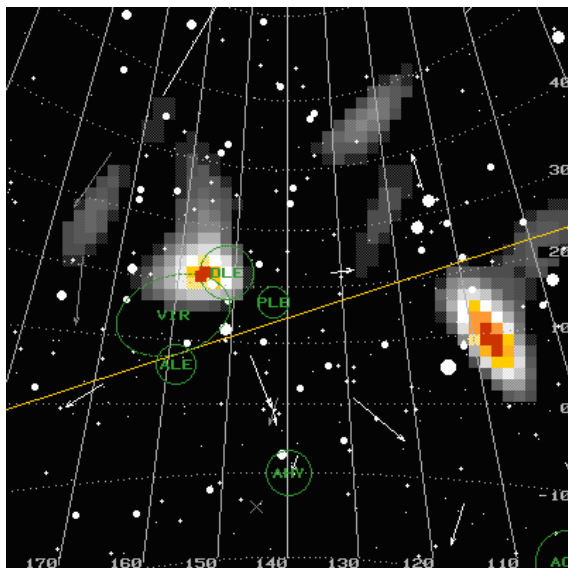
The Leonids radiant on 2011 November 17-18
(RA $\sim 138^\circ$ and Dec = $+22^\circ$) (all-sky camera Special
Astrophysical Observatory, Russia)

Figure 9



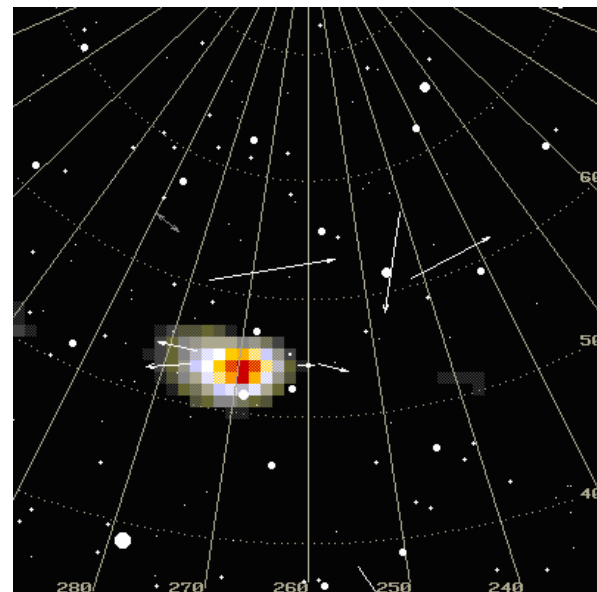
The Draconids radiant on 2011 Oktober 08-09
(RA = 275° and Dec = $+49^\circ$) (all-sky camera Special
Astrophysical Observatory, Russia)

Figure 11



The Leonids radiant (RA = 156° and Dec = $+21^\circ$)
and Alpha-Monocerotids radiant
(RA = 108° and Dec = $+10^\circ$) on 2012 November
16-19 (all-sky camera in New-Mexico, United States)

Figure 10



The Draconids radiant on 2011 Oktober 08-09
(RA = 269° and Dec = $+54^\circ$) (all-sky camera The
Swedish Institute of Space Physics, Kiruna)

Figure 12

Acknowledgements. We express our gratitude to Sergey Andrievskiy, Sara Beck, Sergey Schmalz and Rainer Arlt for their contribution to the project.

References

Pereira W.E.: 2003, The CONCAM global sky monitoring network: Its evolution and creation of a performance model? - PhD thesis.

Smith R., Walker D., Schwarz H.E.: 2004, The Tololo All Sky Camera, Scientific detectors for Astronomy, The Beginning of a new era, (eds.), 379-384.

Martinez P., Klotz A., Demers A.: 1998, Introduction to CCD Astronomy, Cambridge University Press.

Verma S., Gorka S., Prabhu T.: 2012, Image acquisition from All Sky Camera and its applications. Dept. of Instrumentation, Cochin Univ. of Science and Techn., Kochi, India.

Bryukhanov I.S., Korotkiy S.A. et al.: 2011, Proceedings of the IMC, Sibiu (Romania).

ABOUT THE GLOBAL MAGNETIC FIELDS OF STARS

V.D. Bychkov¹, L.V. Bychkova¹, J. Madej²

¹ Special Astronomical Observatory of RAS,
Nizhnij Arkhyz, Russia, *vbych@sao.ru*

² Warsaw University Observatory, Warsaw, Poland *jm@astroww.edu.pl*

ABSTRACT. We present a review of observations of the stellar longitudinal (effective) magnetic field (B_e) and its properties. This paper also discusses contemporary views on the origin, evolution and structure of B_e .

Key words: Stars: magnetic field

1. Introduction

At present there are collected direct measurements of the longitudinal (effective) magnetic fields in 1873 stars of various spectral types. The total number of the magnetic field B_e measurements amounts to 24124. In the following text we shall refer to B_e as the magnetic field for brevity.

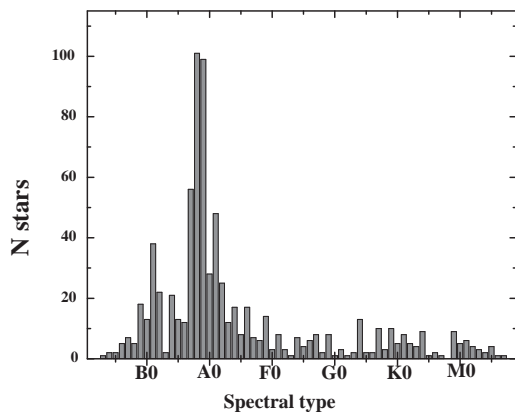


Figure 1: Number distribution of stars with measured longitudinal magnetic fields B_e vs. spectral type.

The dominant part of existing observations (for over 900 objects) was obtained for CP stars.

2. Observational data

We list here the most obvious advantages of the above progress:

1. There is accumulated a large set of B_e measure-

ments.

2. In some cases new magnetic measurements were obtained from spectra of relatively low resolution.

3. Those data were accumulated during a long time period (over 60 years), which actually allows one to study the long-period magnetic behavior of some objects.

Table 1: Principal methods of B_e measurements:

Method	N measurements
Phot.	5375
Elc.	6991
LSD and WDLS	4083
BS	1544
FORS1/2	2540

“Phot.” stands for the photographic method (Babcock 1947a,b, 1958 and many others). This method is now obsolete and is not used.

The “Elc.” method is an analogue of the photographic method, but a CCD matrix is used as the receiver of light. Previously CCD matrix replaced a photographic plate in classical spectrometers. Currently echelle spectrometers are routinely used due to limited size of CCD matrices. This method is still sometimes applied.

“LSD and WDLS”: It is a well known method, cf. Donati et al. (1997), Wade et al. (2000) and many other papers. This is a precise method, which was actively in recent years and has yielded many new results.

“BS” denotes the average surface field of stars. Such a number of measurements does not imply that “BS” was measured for high number of stars. For some slowly rotating CP stars BS was measured many times.

FORS1/2 stands for the low-resolution spectropolarimeter at the ESO Very Large Telescope.

“H-line” denotes B_e measurements observed in hydrogen lines (Borra and Landstreet 1980, Bychkov et al, 1988 and many other papers).

3. Stars with known magnetic phase curves

There exist 218 stars with measured phase curves of their longitudinal (effective) magnetic field B_e . In that

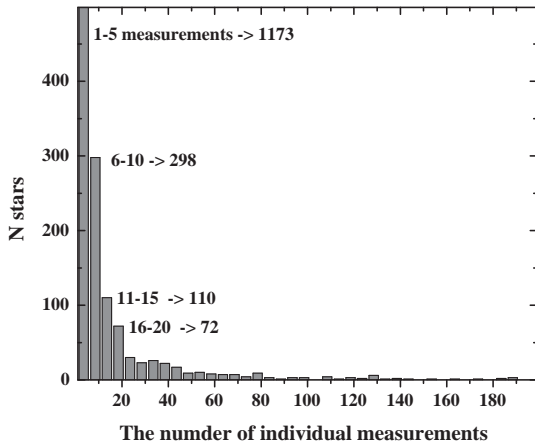


Figure 2: Number of individual B_e measurements. bychdoc

Table 2: Number of stars for which magnetic phase curves were determined vs. the most important types.

All stars with mag. phase curves	218
mCP stars	172
Ae/Be Herbig stars	7
Be stars	7
Supermassive Of?	3
Normal early B stars	5
Flare stars	3
TTS (T Tau type)	2
var. Beta Cep type	6
SPBS	3
var. BY Dra type	4
var. RS CVn type	1
Semi-regular var.	1
DA	1
var.pulsating stars	2
HPMS (high proper motions stars)	3
var.Ori type	2

group, 172 objects are classified as magnetic chemically peculiar stars. Remaining objects are stars of various spectral types, from the most massive hot Of?p supergiants to low-mass red dwarfs and stars with planets.

Some stars were simultaneously put into two different classes. For example, HD 96446 belongs to both the He-r and β Cep classes and HD 97048 belongs to both the TTS and Ae/Be Herbig classes. The binary system DT Vir consists of two companions: UV+RS (Flare + RS CVn type stars). Therefore, the distribution of stars between classes had to be arbitrary or redundant in some cases.

For example, Fig.5 shows the magnetic phase curve for mCp stars β CrB. Periodic variability of the mag-

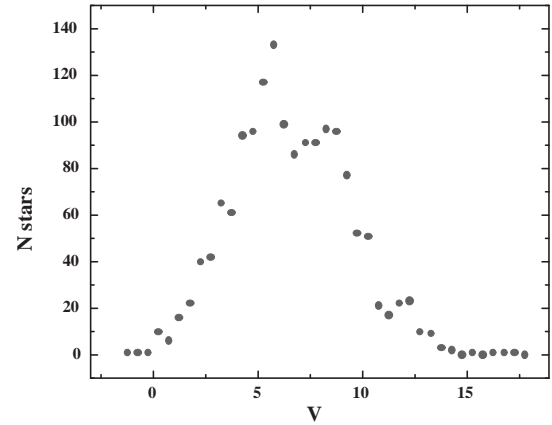


Figure 3: Distribution of magnetic stars vs. apparent stellar magnitude.

netic field of stars was described in more detail by Bychkov et al. (2005, 2013).

We selected the following most important conclusions about the magnetic activity among stars of various types.

- 1. New class of magnetised objects was recently discovered – supermassive hot stars, type Of?p?. These stars show periodic variations of the longitudinal magnetic field. Amplitudes of magnetic phase curves (MPC) reach several hundred G. Of?p stars apparently are slow rotators. Configuration of their magnetic field is represented by an oblique rotator.
- 2. Magnetic fields were found among chemically normal early B stars. MPC's were obtained for 3 stars of this type. In one object, HD 149438, MPC shows complicated double wave shape, displayed also by some mCP stars.
- 3. Magnetic field and its behaviour was best investigated in the group of mCP stars. Longitudinal magnetic fields B_e have simple dipole configuration in majority of mCP stars (in 86 % objects). Rotational magnetic phase curves often display simple harmonic shape with amplitudes reaching 10 kG. Remaining 14 % of investigated mCP stars display more complex phase curves being a superposition of two sine waves and have either dipole or more complex structure of their global magnetic fields. Amplitudes of rotational B_e variation essentially do not differ from those in “sine-wave” mCP stars.
- 4. Solar-type stars have global magnetic fields of low strength, seldom approaching few dozens of G.

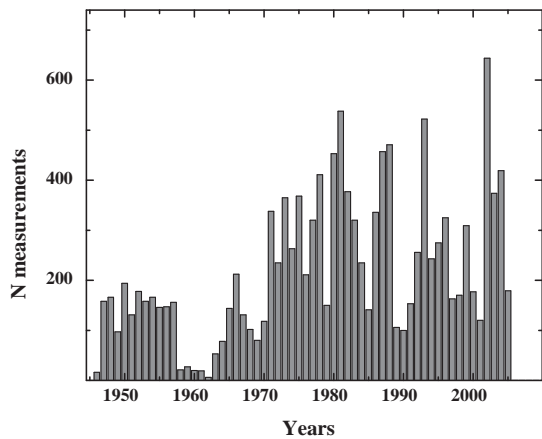


Figure 4: Number of B_e measurements obtained in various years.

Measuring of such low-intensity fields meets with many methodological difficulties. Therefore, we can only suppose, that in some investigated stars (in ξ Boo A, for example) magnetic phase curves appear as simple harmonic waves. Very significant progress in measuring of magnetic fields in stars was achieved using the ZDI method (magnetic cartography of the surface). More credible considerations require higher number of investigated stars and still higher accuracy of magnetic field observations. Moreover, it is known that magnetic properties of solar-type stars vary periodically in time scale from few years to several dozens of years.

- 5. Ae/Be Herbig stars usually exhibit magnetic rotational phase curves of a purely harmonic shape with amplitudes reaching several hundred G.
- 6. Magnetic phase curves of pulsating β Cep stars vary with the period of rotation. MPC show a complicated structure with low amplitudes of dozens G. Closely related slowly pulsating B stars (SPB) also display longitudinal magnetic field varying with the period of rotation. MPC show a simple harmonic shape with amplitudes reaching several dozens G.
- 7. T Tau stars have magnetic fields of complex structure, display also complex magnetic phase curves with amplitudes approaching several hundred G. Undoubtedly, fields of such a strength have to strongly influence accretion of matter onto stars.
- 8. Late-type stars – M dwarfs have global magnetic fields of complex structure. Magnetic rotational phase curves only roughly can be approxi-

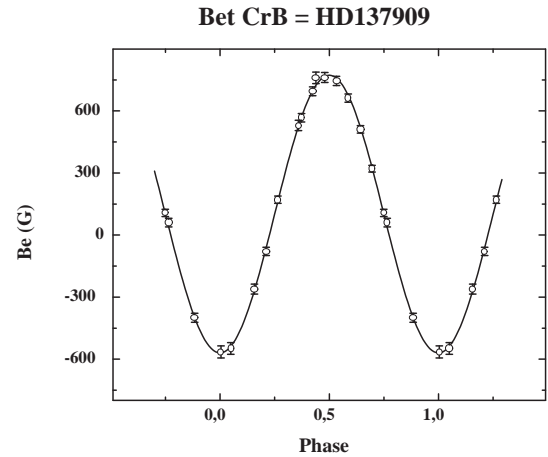


Figure 5: Magnetic rotational phase curve of the mCp star β CrB (HD 137909) for the accurate rotational period derived by Wade et al. (2000).

mated by a superposition of two waves. This was also directly confirmed by recent observations using the ZDI method. Amplitudes of variations of the integrated longitudinal magnetic fields reach several hundred G. Some stars present an amazing feature, stepwise creation or annihilation of the global magnetic field and related B_e variations.

- 9. HD 189733 – this is a typical dwarf of spectral class K2V, where a giant planet, “hot Jupiter” was found. Central star in the system is a solar-like object. The star possesses magnetic field which is typical for its spectral class, and its longitudinal component varies with the amplitude of several G.

4. mCp stars

Magnetic fields of stars are best studied for mCp stars. One of major problems for these stars is the relations between their magnetic field and the chemical composition. We proposed a way to clarify this problem (Bychkov et al. 2009). We defined relative magnetization (MA) for different types of chemical peculiarity comparing distributions of their occurrence with the observed $\langle B_e \rangle$. Example of such a distribution for stars of Si peculiarity is shown in Fig. 6. Number distribution of CP stars vs. T_{eff} for all different types of chemical peculiarity was shown in Fig. 7. Magnetization “MA” for various subclasses of CP stars vs. T_{eff} was shown in Fig. 8. Reduction of “MA” with the reduction of T_{eff} is apparent there for H-r, He-w and Si stars. Such a reduction of “MA” supports the fossil theory of the magnetic field origin in those stars. If the age of a star is high, then its mass is lower and “MA” also is lower. But we see sharp rise of

“MA” about $T_{\text{eff}} = 10000 K^{\circ}$. Therefore, we raise the assumption that the dynamo mechanism joins at this point on the T_{eff} scale.

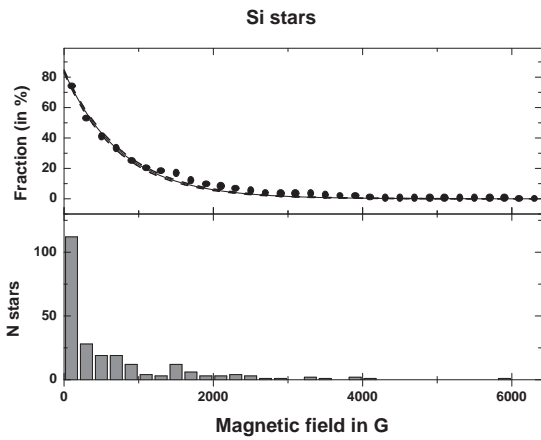


Figure 6: Integrated distribution function $N_{Int}(B)$ in percent (upper panel), and the number distribution function $N(B)$ (lower panel) for stars of Si peculiarity type.

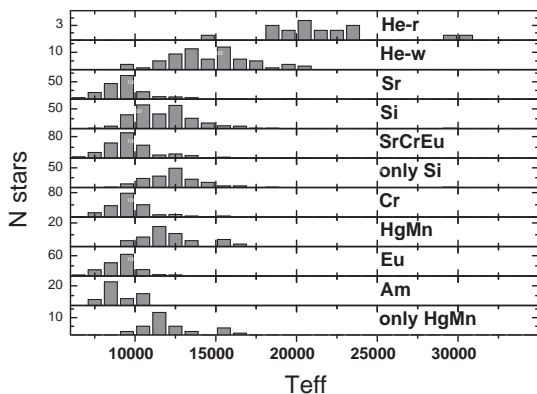


Figure 7: Number distribution of CP stars vs. T_{eff} for various types of chemical peculiarity.

Summary

In recent years significant progress was attained in the study of stellar magnetism. While previously one could measure and discuss behaviour of the stellar magnetic field only in mCP stars, white dwarfs and the Sun, currently we can measure and collect data on the magnetic field for many more types of stars ranging from supermassive hot giants to fully convective cold dwarfs of low mass. One can note significant contribution of the MiMeS collaboration which has discovered

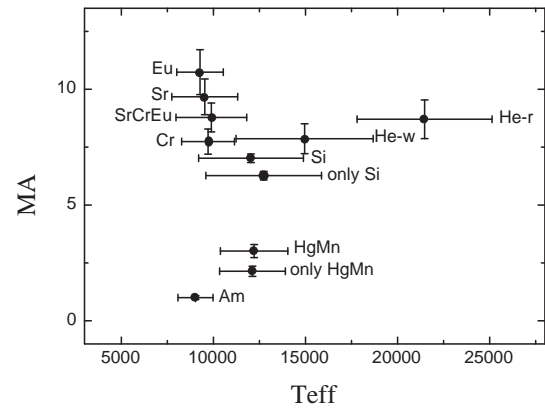


Figure 8: Magnetization (MA) for various subclasses of CP stars. Bars define the range of T_{eff} and MA occupied by a given subclass.

a new class of magnetic objects, supermassive hot giants Ofp? type and other magnetised hot stars. These discoveries significantly extended our knowledge about magnetism of hot stars and in future will give rise to our understanding of processes in stellar atmospheres and circumstellar space.

One can expect that rapid accumulation of new observational data will allow one to study in detail the variability of stellar magnetic field in stars both of different spectral types and evolutionary stages. We share the conviction that the magnetic field and its evolution is a crucial agent of stellar physics.

Acknowledgements. We acknowledge support from the Polish Ministry of Science and Higher Education grant No. N N203 511638 and the Russian grant “Leading Scientific Schools” N4308-2012.2.

References

- Babcock H.W.: 1958, *Ap.J.Suppl.Ser.*, **30**, 141.
 Borra E.F., Landstreet J.D.: 1980, *Ap.J.Suppl.Ser.*, **42**, 421.
 Donati J.F., Semel M., Carter B.D., Rees D.E., Cameron A.C.: 1997, *MNRAS*, **291**, 658.
 Wade G.A., Donati J.-F., Landstreet J.D., Shorlin S.L.S.: 2000, *MNRAS*, **313**, 823.
 Babcock H.W.: 1947a, *ApJ*, **105**, 105.
 Babcock H. W.: 1947b, *PASP*, **59**, 260.
 Bychkov V.D., Gazhur E.B., Glagolevskij Yu.V., El’kin V.G., Nazarenko A.F., Najdenov I.D., Romanyuk I.I., Chuntunov G.A., Shtol’ V.G.: 1988, *Magnetic stars*, 12.
 Bychkov V.D., Bychkova L.V., Madej J.: 2005, *A&A*, **430**, 1143.
 Bychkov V.D., Bychkova L.V., Madej J.: 2013, *AJ*, **146:74**, 10pp.

THE VARIABILITY OF GLOBAL MAGNETIC FIELDS OF STARS. THE NEW OBSERVATIONS DATA

V.D. Bychkov¹, L.V. Bychkova¹, J. Madej²

¹ Special Astronomical Observatory of RAS,
Nizhnij Arkhyz, Russia, *vbych@sao.ru*

² Warsaw University Observatory, Warsaw, Poland *jm@astroww.edu.pl*

Research on the variability of magnetic field of stars allows one to understand many aspects of the nature of this phenomenon. Variability of global magnetic field was found practically in all types of stars, beginning from hot supermassive $O\tilde{f}^?p$ stars to few cold low-mass red dwarfs (Bychkov et al. 2013). Currently the fossil theory is very popular (Braithwaite & Nordlund, 2006) and is seen in hot young stars (MiMeS collaboration). Formation of the global field is a long process, it takes time close to age of a star (not less than 10^4 years). But now there are new observational data which show, that there are mechanisms which can change magnetic status of a star much faster, in time scale 1-2 years. Ae/Be star HD190073 is the example of such a change. This star has changed the magnetic behaviour in the very short interval of time. Dependence of B_e on JD for HD190073 is shown in Fig.1 (Alecian et al. 2013). Certainly such a change in the behaviour of the longitudinal magnetic field cannot be explained by the fossil theory. Possibly convection “has included” the dynamo mechanism. Then, the generation of the global magnetic field can proceed in so short time period (leading to the configuration of inclined rotator).

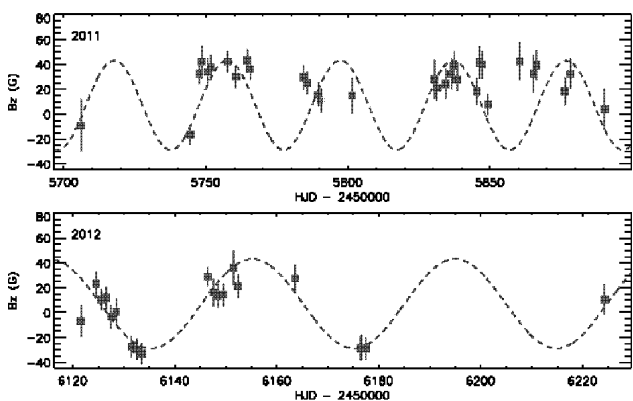


Figure 1: Measured longitudinal magnetic fields B_e vs. JD for HD190073.

OT Ser

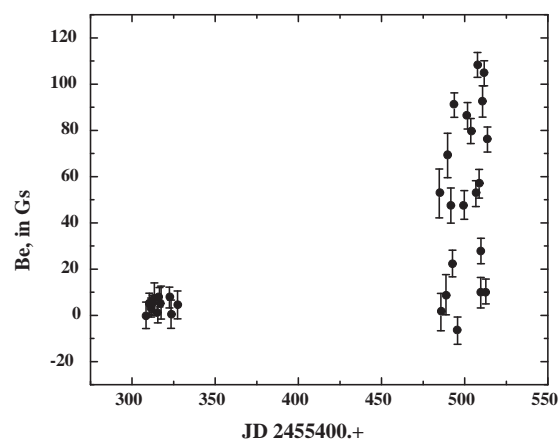


Figure 2: Measured longitudinal magnetic fields B_e vs. JD for OT Ser.

Rapid change of the magnetic status was observed in cold red dwarf OT Ser (Donati et al. 2008). Run of B_e vs. JD for OT Ser is shown in Fig.2. It is seen that the magnetic behaviour considerably changed during half a year - in the time interval between both sets of observations. Fig.3 shows the magnetic phase curve for OT Ser with the period of rotation $3^d.424$ obtained from B_e measurements of the second set.

OT Ser belongs to the class of flare stars, which are very interesting objects. These stars lose energy of rotation in flashes following the scheme: rotation - differential rotation - generation of local magnetic fields - flares (dissipation of local magnetic fields). The energy loss is dominated by radiative processes. There occurs “slight” braking. It is now clear, that sometimes (possibly seldom) local magnetic fields do not dissipate, but can built up to form the global magnetic field. It is only the most tentative assumption. Real mechanism maybe is much more complex. In stars with the global magnetic field development of flares will occur

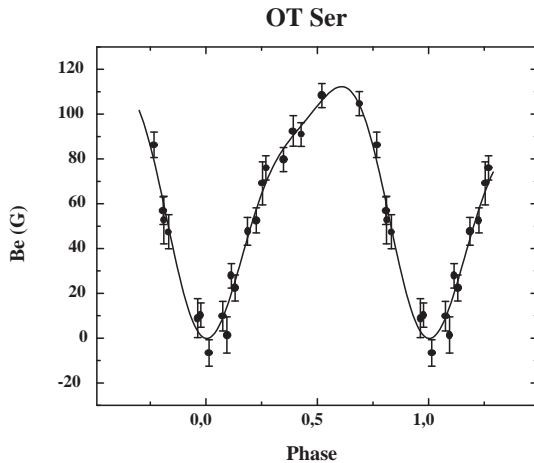


Figure 3: Magnetic rotational phase curve for the cold red dwarf OT Ser for the rotational period $3^d.424$.

in the presence of that field which will undoubtedly affect movement of matter. In any event it is necessary to reconsider the standard models of flashes, cf. Hawley et al. (1995); Katsova et al. (1999); Katsova and Livshits (2001); Shibata and Yokoyama (1999, 2002); Stepanov et al. (2005).

New observational data require review of some of the settled concepts on the mechanisms of occurrence and evolution of global magnetic fields.

Acknowledgements. We acknowledge support from the Polish Ministry of Science and Higher Education grant No. N N203 511638 and the Russian grant "Leading Scientific Schools" N4308-2012.2.

References

- Alecian E., Neiner C., Mathis S., Catala C., Kochukhov O., Landstreet J., and the MiMeS collaboration: 2013, *A&A*, **549**, id.L8, 4 pp.
- Braithwaite J., Nordlund A.: 2006, *A&A*, **450**, 1077.
- Bychkov V.D., Bychkova L.V., Madej J.: 2013, *Astron. J.*, **146**, a.id. 74, 10 pp.
- Donati J.-F., Morin J., Petit P., Delfosse X., Forveille T., Auriere M., Cabanac R., Dintrans B., Fares R., Gastine T., Jardine M.M., Lignieres F., Paletou F., Ramirez Velez J.C., Theado S.: 2008, *MNRAS*, **390**, 545.
- Hawley S.L., Fisher G.H., Simon T., Cully S.L., Deustua S.E., Jablonski M., Johns-Krull C.M., Pettersen B.R., Smith V., Spiesman W.J., Valenti J.: 1995, *Ap.J.*, **453**, 464.
- Katsova M.M., Drake J.J., Livshits M.A.: 1999, *Ap.J.*, **510**, 986.
- Katsova M.M., Livshits M.A.: 2001, *Astron. and Astrophys. Transactions*, **20**, 531.
- Shibata K., Yokoyama T.: 1999, *Ap.J.*, **526**, L49.
- Shibata K., Yokoyama T.: 2002, *Ap.J.*, **577**, 422.
- Stepanov A.V., Kopylova Yu.G., Tsap Yu.T., Kupriyanova E.G.: 2005, *Astron. Lett.*, **31**, 612.

THE DETERMINATION OF ABSOLUTE PARAMETERS AND ABUNDANCE OF COMPONENTS BINARY SYSTEMS: THE SPECIFICITY AND PROBLEMS

L. V. Glazunova^{1,2}

¹ Odessa National Academy of Telecommunications, Kuznechnaya str. 1, Odessa, 65029, Ukraine

² Department of Astronomy, Odessa National University Shevchenko Park, Odessa, 65014, Ukraine

ABSTRACT. Spectroscopic binaries remain a laboratory for testing the stellar atmosphere and the stellar evolution theories. It's considering problems determination of parameters of components and their errors for example two spectroscopic binaries with the main-sequence components BW Boo and OU Gem.

Key words: Spectroscopic: absolute parameters: spectroscopic binary; stars: individual: BW Boo, OU Gem

1. Introduction

Spectroscopic binaries, for which we can determine masses and radii of their components based on their orbiting, are still good sites to test the modern stellar atmosphere and stellar evolution theories, as well as to estimate the effect of duplicity on the variation in the internal structure of binaries and, consequently, on the divergence of the model parameters of such binaries from those of single stars of the given mass. It is difficult to determine the abundance of spectroscopic binaries as it is necessary to concordantly solve the problem of simulation of atmospheres for two stars at once. The selection of spectral lines to determine the abundance is also complicated as those lines should not be blended either with other lines of the star nor with the lines of the companion star. For two spectroscopic binaries with the main-sequence components we determined absolute parameters of the components by the radial velocity curves, the light curves of the binaries, as well as the rotational

velocities of their components, measured using the LSD-profiles. The age of binary was estimated by the presence of its components' rotation, synchronised with their orbiting, and the orbital eccentricity. Those parameters are applied to compute the models of atmospheres of the binary components, to obtain the total synthetic spectrum and to calculate the chemical abundances of elements, the lines of which are reliably identified in the observed spectrum. However, the bi-

nary parameters determined by different methods are not in good agreement.

2. Eclipsing and spectroscopic binary BW Boo

BW Boo (HD128661) is a poorly studied bright eclipsing binary ($V=7.14^m$) with the orbital period of 3.33^d . The spectral and photometric orbital elements, projected rotational velocities of the components were estimated and the absolute parameters of the binary components and the age of the binary system of $2 \cdot 10^7$ years (Table 1) were determined by two spectra, obtained with the 2.7-meter telescope of the McDonald Observatory with resolving power $R=60000$ and $S/N=300$ at the wavelength range $5000 - 6500 \text{ \AA}$, as well as by the light curves reported in the literature (Glazunova 2011). The position of the primary on the Hertzsprung–Russell diagram correlates well with the determined mass and age (Fig. 1). According to the age of a star with mass of $1.1M_{\odot}$ and high lithium abundance in its atmosphere ($\lg Li/H = 3.0 \text{ dex}$), the secondary has not yet reached the main sequence.

Table 1: The absolute parameters.

Parameters	A	B
T_{eff} (K)	8900	5550
M (M_{\odot})	2.0 ± 0.1	1.1
R (R_{\odot})	1.9 ± 0.4	1.2
a (R_{\odot})	13.67	
L (L_{\odot})	21.62	1.24
v_{spin} (/)	2 ± 0.5	17 ± 2
v_{psyn} (/)	37	24
$F(v_{psyn}/v_{spin})$	18	1.4

The atmospheric parameters of the primary (see Table 2 where the rotational velocity was measured using the LSD-profiles of the lines, and the relative contributions of the components to the total luminosity were

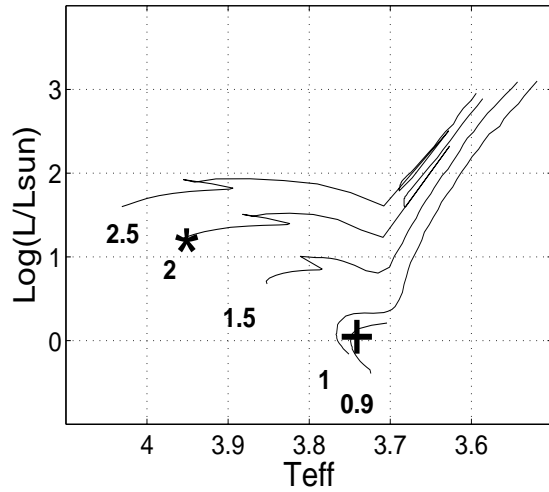


Figure 1: Evolutionary tracks for stars from 0.9 to $2.5 M_{\odot}$ (Schaller et al. 1992). The primary and the secondary are marked by asterisk.

determined from the light-curve solution) were determined by 114 neutral iron lines and 64 ionized iron lines, applying the method described by Yushchenko et al. (1999). The initial chemical composition was supposed to be similar to the solar one. The abundances of 38 chemical elements, including those with $Z > 60$ (Fig. 2) were estimated. The abundance is typical for an Am star with the iron abundance $[\text{Fe}/\text{H}] = 0.15 \pm 0.08$ dex. About 100 lines were identified for the secondary, but with the component luminosity ratio of 23 those are lines with large equivalent widths, so they are unsuitable for the abundance estimation. However, it can be said that those lines are well specified by the given model parameters (within the error of 20% for weak lines). The results of comparison of the observed lines with the synthetic spectrum of the selected model are not contrary to the solar chemical composition.

Table 2: Atmospheric parameters

Parameters	A comp	B comp
$T_{eff} K$	8900 ± 100	5500
$\lg g$	4.1 ± 0.1	4.3
v_{micr} (km/s)	1.3	2
v_{rot} (km/s)	2 ± 1	17
L_{rel}	0.96	0.04

2. Problems in estimation of the parameters of the close binary BW Boo components

Determination of effective temperature and surface gravity by different methods (by the colour indices, the neutral and ionized iron lines, the evolutionary

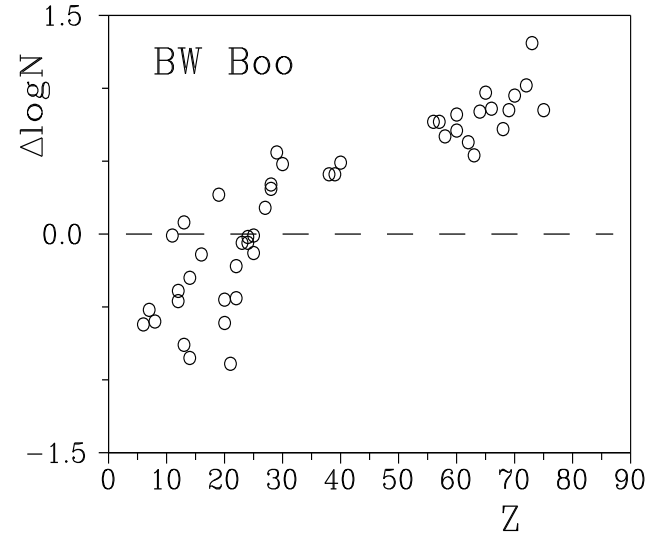


Figure 2: Elemental abundances by atomic number the primary of BW Boo.

model) results in a wide scatter of values (Table 3). As is seen in Table 3, the closer towards the red end of the spectrum region is used to estimate the temperature, the lower that temperature is. According to the binary galactic coordinates ($l = 61, b = 66$), the interstellar absorption should be very low $0.1^m - 0.15^m$. The same is confirmed by determination of the interstellar absorption by the colour excesses in $U-B=0.04$ and $B-V=0.12$ as such $A_V=0.2$. The colour indices $U-B=0.04$ (for the model with a mass of $2 M_{\odot} - 0.043$), $B-V=0.13$ (0.058), $V-J=0.34$ (0.051), $V-K=0.44$ (0.067) for red emission do not correspond to those of a star with mass $2 M_{\odot}$ and normal solar abundance. Apparently, such a wide scatter in the temperature and surface gravity determinations for the given star is associated with the metallicity of the star's atmosphere and, subsequently, the variation in energy distribution in its spectrum. With the component luminosity ratio of 23 the secondary contribution affects the composite spectrum just slightly. The absolute magnitude of the primary can be determined by the parallax and interstellar absorption: the parallax is 8.1 ± 0.6 , $M_V = m_V + 5 - 5 \lg r - A_V$, $M_V = 1.68 - 0.2 \pm 0.16$. What is the most astounding about BW Boo binary is the rotational velocity of its primary component, which is 18 times slower than the pseudo-synchronous rotational velocity for that component, and that ensures the Am star effect. It follows from the theory on circularisation and synchronisation in the close binaries that the binary components with the orbital periods less than 5 days should be synchronised as early as at the stage before the main sequence. According to that theory, the time of synchronisation for the BW Boo binary com-

ponents is $2.6 \cdot 10^5$ years (Taussol 1988), and the time of circularisation is $5 \cdot 10^8$ years. Such asynchrony can be explained by a sharp decline in the binary period that is possible only in the presence of the protostellar disc, from which the binary system was originated or a multiple system was broken down. However, both alternatives require that the binary system is located in the star-forming high-density regions in the interstellar medium with high stellar density. As can be seen from the above, more accurate definition of the absolute parameters of the binary components allowed of selecting the model parameters of their atmospheres, which are in good agreement with each other.

3. The BY Dra type spectroscopic binary OU Gem

OU Gem (HD 45088) is a BY Dra type bright spectroscopic binary with $m_v = 6.79^m$ and $P = 6.99^d$ with components of close spectral types $K3V + K5V$ that is located at a distance of 14.7 pc. OU Gem may belong to the UMa moving group, the estimated age of which is 300 Myr (Montes et al. 2000a). The binary light curve does not exhibit eclipses, but shows a smooth variation in brightness with an amplitude within the range of $0.02^m - 0.05^m$ and period, which is a little bit longer than the orbital one $P = 7.36^d$. The spectral elements of the binary orbit were redetermined by Mishenina et al. (2010). Strong emission in the CaII H&K lines is observed in both components of OU Gem binary just as in many other BY Dra type stars. With the components' contributions $L_A/L_B=0.7/0.3$ the equivalent widths of the component emission are estimated of 1.08/1.71 Å for the K line and 1.02/1.51 Å for the H line of the calcium (Montes et al. 1996, 2000b). As is seen from these estimations, the secondary, which is less massive, has higher chromospheric activity.

10 spectra with the resolving power $R=75000$ and S/N within the high signal-to-noise in the range of 71–173 were obtained by T. Mishenina with the fiber-fed echelle spectrograph SOPHIE at the 1.93-m telescope of the Observatoire de Haute-Provence (France) in 2009, 2010 and 2011. The spectra processing was performed using the DECH20 software package. The total spectrum of the binary was analysed with the URAN code by Yushchenko (1998). The component temperatures were determined by the ratio of depths of specially selected lines applying the methods, described by V. Kovtyukh (2003). The computations of the component temperatures and abundances of chemical elements in their spectra were conducted by V. Kovtyukh.

Some spectral characteristics of the binary components at different spectral and photometric orbital phase given in Table 4. The spectral elements of the binary orbit, which allow of estimating the minimum

Table 3: Determination of the temperature and surface of gravity by different methods.

Method	Magnitude	Reference	Teff K	lg g
B	7.258			
V	7.138			
J	6.788	2003yCat.2246	7850	3.5
H	6.726	OC		
K	6.692			
V	7.14	Guetter et al,		
B-V	0.12	PASP,96,44, 1984	8250	4.5
b-y	0.079	Hill et al,		
c1	1.175	Mem.R. astr. Soc.,	8500	3.65
m1	0.170	79,131,1975		
FeI/FeII as singel star		this paper	8900 8700	4.1 3.7
M_A/t_{age}		this paper	9000	4.3

masses of its components, were computed by the radial velocities of the binary components (Mishenina et al. 2010); but to estimate the absolute parameters of the binary, it is necessary to determine the orbital inclination to the plane of projection i and radii of the binary components. To do that, the luminosities of the components should be determined. To determine the absolute magnitude of the binary, we used the binary parallax value of 68.20 ± 1.10 mms that makes up $r=14.7$ pc (Hipparcos 1997).

Thus, $M_V = m_V + 5 - 5 \lg r = 5.89^m \pm 0.03$. Having made the bolometric correction for $T_{eff}=5025$ K ($\lg T_{eff}=3.70$) and $B-V=0.92$, obtained by the calibration by Flower et al. (1996), $BC=-0.295$, we get the absolute bolometric magnitude $M_{bol} = 5.595^m \pm 0.03$ and $\lg L/L_\odot = -0.306 \pm 0.002$. The binary luminosity will be equal to $0.496 L_\odot$. Assuming that the luminosity contribution averages to $0.75(\lg L_A/L_\odot=-0.429)$ for the primary component and $0.25(\lg L_B/L_\odot=-0.907)$ for the secondary component, the luminosity and then the radius of each component could be determined. Therefore, the primary component mass is $0.78 \pm 0.02 M_\odot$, and the mass of the secondary component is $0.66 \pm 0.02 M_\odot$. The orbital inclination to the plane of projection is $i=76^\circ \pm 1$. Such an angle is consistent with the absence of eclipses in the binary, which are likely to occur at $i > 85^\circ$ for the given radii of the components. That is how the absolute parameters of the OU Gem binary components were obtained (Table 5).

The pseudo-synchronous velocities of the binary components for the determined radii are $7.5 (v_{ps} \sin i = 7.3 \text{ km/s})$ and $6.3 (v_{ps} \sin i = 6.2 \text{ km/s})$. The observed rotational velocity of the primary is 22% slower than its pseudo-synchronous one; and the rotational velocity of the secondary is close to its pseudo-synchronous ve-

Table 4: Determination of the temperature and surface of gravity by different methods .

JD 24+	$T_{eff A}$	$T_{eff B}$	$Fe(L_A/L_B)$	L_A/L_B	$v_A \sin i$	$v_B \sin i$	New sp. phase	New ph. phase
54898.313 (a)	5044±22	4693±67	0.74/0.26	0.71/0.29	6.14	6.57	0.74	0.65
54899.293(b)	5013±15	4486±50	0.78±0.02/0.22	0.74/0.26	5.2	5.30	0.88	0.78
54900.280(c)	4881±13						0.02	0.91
54901.395(d)	5025±10	44538±18	0.75±0.03/0/25	0.74/0.26	6.17	6.94	0.18	0.07
55128.695	5027±13	4559±39	0.73±0.03/0.27	0.72/0.28	5.94	6.53	0.69	0.95
55130.627	4985±13	4275±29	0.75±0.02/0.25	0.73/0.27	5.97	6.14	0.96	0.21
55131.623	5036±12	4498±35	0.76/0.24	0.74/0.26	5.89	6.29	0.11	0.21
55132.622	5058±10	4578±38	0.76/0.24	0.74/0.26	5.93	6.24	0.25	0.48
55835.685	5027±14	4459±37	0.78/0.22	0.70/0.30	5.94	6.93	0.80	0.01
55836.684	5010±11	4484±30	0.72/0.28	0.71/0.29	6.48	7.43	0.95	0.14
Average values	5025±13	4508±38	0.75/0.25	0.73/0.27	5.96±0.3	6.49±0.6		

locity. If a period of 7.36^d corresponds to the rotation period of the secondary at the latitude of the existing spot, then its rotational velocity at that latitude should equal to 4.4 km/s. The difference between the rotational velocities, measured using the LSD-profile of the secondary, and that one, obtained by the photometric period, can be explained by the differential rotation of that component. The synchronization and circularization time for the binary components for the given parameters, which was calculated with the formulas by Taussol (1988), is $t_{syn A}=2 \cdot 10^5$ years, $t_{cir A}=5 \cdot 10^8$ years (with N=8); and by Zahn 1977 - $t_{syn A}=3 \cdot 10^7$ years, $t_{cir A}=3 \cdot 10^{10}$ years.

Table 5: Atmospheric parameters

Parameters	A comp	B comp
$lg L/L_{\odot}$	-0.46±0.02	-0.83
M (M_{\odot})	0.78±0.02	0.66
R (R_{\odot})	0.76±0.03	0.64
lg g	4.57±0.04	4.65

Using the URAN code the non-blended lines of the primary and secondary were identified in the spectra at different phases of the orbital period; their equivalent widths were measured and subsequently parted in relative luminosities of the components accounting for the change in their contributions at different wavelengths according to the ratio of radiation flux of the components. The abundances of different chemical elements in the atmospheres of the binary components were determined by the reduced equivalent widths. The surface gravity $lg g_A = 4.3 \pm 0.1$ and $lg g_B = 4.5$, as well as the microturbulent velocities 1.3 ± 0.2 and 1.5 km/s, which were used in the models, were determined on the base of the ionization-equilibrium neutral and ionized iron lines (220 and 9 lines, respectively). The abundances of 22 elements were estimated in the primary (with accuracy of 0.11 dex by the iron lines) and those of 14 elements were estimated in the spectrum

of the secondary (with accuracy of 0.2 dex by the iron lines). The same iron abundances in the atmospheres of the binary components are reached at the luminosities $L_A=0.78$ and $L_B=0.22$ (Fig. 3).

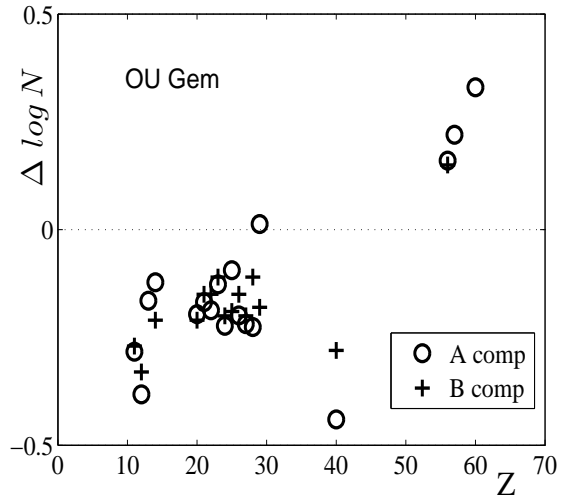


Figure 3: Elemental abundances by atomic number of components of OU Gem.

The abundances of most elements are lower relative to those solar ones (-0.18 dex for Fe). The heaviest elements are slightly overabundant. The binary age of $3 \cdot 10^8$ years is in good agreement with the absence of the Li I 6707 Å line in the spectra of both components. According to the studies of the lithium abundance in the Hyades cluster stars with age of $7 \cdot 10^8$ years (Cayrel et al. 1984), the lithium abundances in the stars with the given mass correspond to the equivalent width of the Li I 6707 Å line less than 5 mÅ, and that is consistent with our measurements.

4. Peculiarities and contradictions

The ratio of the components' luminosities (table 4) does not correspond to the main-sequence stars with the mass ratio $q=0.85$ (for the given masses the models result in the ratio of fluxes of 3.5 by 5000 Å $F_A/F_B < 2$ in the observed spectra). The surface gravity, determined in the ionization equilibrium (4.3 ± 0.1 and 4.5), does not correlate with that one, determined by the mass and radius (4.57 ± 0.04 and 4.65), as well as by the luminosity and effective temperature. An alternative explanation of such a difference is given in the paper by Tsantaki et al.(2013). The secondary component seldom exhibits sharp changes in effective temperature, which significantly exceed the method errors in its determination (see the table 4). The most common used formulae for estimation of the synchronization and circularization time in binary systems ($t_{syn A}=2 \cdot 10^5$ years, $t_{cir A}=5 \cdot 10^8$ years by Taussol 1988) do not expound the rotational velocities of the components or the orbital eccentricity.

5. Conclusion

The indicated method errors are just the technical errors as the accuracy errors of determination of effective temperature, surface gravity, metallicity and rotational velocity projection even by spectra with very high resolution are much larger ($> 2 - 3 \%$, 0.3 dex, > 0.2 dex, > 2 km/s).

References

- Cayrel R. et al.: 1984, *ApJ*, **283**, 205.
Flower P.J.: 1996, *ApJ*, **469**, 355.
Glazunava L.V.: 2011, *Astronomy Letters*, bf 37, 414.
Kovtyukh V. et al.: 2003, *A&A*, **411**, 559.
Mishenina T. et al.: 2010, *Odessa Astronomical Publication*, **23**, 83.
Montes D. et al.: 1996, *A&A*, **312**, 221.
Montes D. et al.: 2000a, *ASPC*, **198**, 203.
Montes D. et al.: 2000b, *A&AS*, **146**, 103.
Schaller D. et al.: 1992, *A&AS*, **96**, 269.
Taussol J.L.: 1988, *ApJ*, **324**, 71.
The Hipparcos and Tycho Catalogues (vol.1-17): 1997, European Space Agency SP-1200
Tsantaki M. et al.: 2013, *A&A*, **555**, 150.
Yushchenko A. et al.: 1999, *Astronomy Letters*, **25**, 453.
Yushchenko A.: 1998, *Proc. of the 29th Conf. of variable star research, Brno, Czech Republic, Nov. 5-9*, 201.
Zahn J.P.: 1977, *A&A*, **57**, 383.

THE ABUNDANCES OF HEAVY ELEMENTS IN RED SUPERGIANTS OF MAGELLANIC CLOUDS

V. Gopka¹, A. Yushchenko², V. Kovtyukh¹, A. Shavrina³, V. Yushchenko¹,
S. Vasilyeva¹, Y. Pavlenko³, S. Andrievsky¹

¹Astronomical observatory, Odessa National University, Odessa, 65014, Ukraine

²Department of Astronomy & Space Sciences, Sejong University,
Gunja-dong, Seoul, 143-747, Korea, *yua@sejong.ac.kr*

³Main Astronomical observatory, NAS of Ukraine, Kyiv, 03680, Ukraine

ABSTRACT. The spectra of Magellanic Clouds (MC) supergiants PMMR 23, PMMR 144 and RM-1-667 with resolving power $R=30,000$ and signal to noise ratio near 100 obtained at 3.6 meter telescope in Chile were analysed. We present a report on the detailed investigation of MC supergiants, with special attention to the thorium abundance in these stars. The abundance patterns of three supergiants show that r-process elements are clearly detected in the atmospheres of investigated stars, but the abundances of s-processes elements can vary from star to star.

Key words: Magellanic Clouds, supergiants, chemical abundances, heavy elements, r-process elements, s-process elements.

1. Introduction

The investigation of different types of stellar objects outside of the Galaxy (Milky Way) usually starts from LMC & SMC – the nearest irregular galaxies located at the distances 50 Kpc (e.g. Bekki, 2011) and 60.6 Kpc (Hilditch et al., 2005), respectively. Our Galaxy and the MCs constitute the most examined part of the larger formation, called the Local Group of galaxies that includes up to 50 galaxies. The comparative analysis of the stars in the Milky Way and other galaxies leads to better understanding of the evolution of Local Group.

Huge interest to the nearest MC galaxies is revealed both through the amount of multiwavelength observational studies and astrophysical theories which have been developed using the obtained information. Among the three galaxies (Milky Way, LMC and SMC), the SMC has the smallest mass which is 50 times less than that of our Galaxy (e.g. Novara et al., 2011) and 5 times less than the mass of LMC (Skilba et al., 2012).

It is known that the chemical composition of MCs

stellar population differs from that of our Galaxy, and the SMC metallicity $[Fe/H]$ is lower than that of the LMC. According to the study of F-supergiants (Russel & Bessel, 1989), $[Fe/H]=-0.65$ dex for the SMC and $[Fe/H]=-0.3$ dex for the LMC stars.

The investigations of abundances of heavy elements are usually performed only for Galactic stars. High resolution spectra of at least brightest extragalactic objects are available now. These spectra as well as the new atomic and molecular data, and the development of new theoretical methods allow to investigate the abundances of heaviest chemical elements in the members of closest of Local Group galaxies. It can be helpful for understanding the evolution of these galaxies and finding the possible differences in the history of stellar formation.

Relying on the observational data, Russel and Dopita (1992), concluded that the r-process is more efficient in the Magellanic Clouds than in our Galaxy. According to Rolleston (1991), the MC galaxies can serve as an example to test the evolutionary model of the average chemical composition of galaxies. The matter enriched by heavy elements in the interstellar space of these galaxies is the source material to form the new generation of stars. The enrichment of SMC member stars with heavy elements is the indicator of more evolved chemical composition in those stars in comparison with the stars of the same spectral class of our Galaxy.

To compare, let us consider the results of the chemical composition examination of a supergiant in our Galaxy, namely Canopus (α Car) which, according to Reynolds et al. (1988), does not show any overabundances of heavy elements. Reynolds et al. (1988) result shows that the chemical abundances of 21 heavy r- and s-processes elements are very similar to the solar ones. A numerous investigations of stellar objects, including 64 supergiants of our Galaxy from F- to M-type (Luck & Bond, 1989), can also be discussed. Luck & Bond

(1989) showed that the heavy elements abundances in these stars are very similar to solar ones. In contrast to MC supergiants there are no anomalies, found in the supergiants of our Galaxy.

This paper is the overview of heavy elements investigation in the atmospheres of MC supergiants PMMR 144 & RM.1-667. The results for PMMR 23 (Gopka et al., 2005) are also shown for comparison. The chemical composition of LMC red supergiant RM.1-667 was not investigated earlier. This star was selected for careful analysis due to peculiar H_α and sodium lines, which clearly indicated the mass loss (Gopka et al. 2013). Here after we present the determination of atmospheric parameters and the analysis of chemical composition with special attention to r - and s -processes elements.

2. Observational data and atmospheric parameters

We used the high-resolution spectra of RM.1-667 and PMMR 144 obtained in 1989 and 1993 by V. Hill at the 3.6 m telescope of ESO in La Silla, Chile. The EMMI spectrometer with spectral resolving power $R=30,000$ was used in 1989 to obtain the data in spectral range from 5900 Å to 6100 Å. The observations with CASPEC spectrometer ($R=20,000$) in the spectral range from 5900 Å to 6700 Å were made in 1993. The initial reduction of images were made by V. Hill. It is necessary to note that the visual magnitudes of RM.1-667 and PMMR 144 are $V=13.124$, and $V=12.82$ respectively (Hill, 1997). The signal to noise ratio of the spectra is only near $S/N=100$.

The parameters of atmospheric model of RM.1-667 were specified using the absorption lines of neutral and ionized iron: $T_{\text{eff}}=3750$ K, $\log g=-1.5$, $v_{\text{micro}}=2.4$ kms^{-1} , $v_{\text{macro}}=9$ kms^{-1} . The individual model atmosphere with these parameters and plane-parallel geometry was calculated using SAM12 code (Pavlenko, 2003), which is a modification of ATLAS12 code (Kurucz, 1995).

The effective temperature and other parameters of PMMR 144 were also determined using the lines of iron in the spectrum of this star. We adopted the values $T_{\text{eff}}=4100$ K, $\log g=-0.7$, $v_{\text{micro}}=4$ kms^{-1} , $v_{\text{macro}}=9$ kms^{-1} . Our values of effective temperature and surface gravity of the star are in good agreement with those determined by Hill (1997), only the microturbulent velocity is higher by 0.5 kms^{-1} .

The first approximation of abundances in PMMR 144 were used by R. E. Luck to create the individual atmosphere model with ATLAS12 code (Kurucz, 1995). The relations between iron abundances, equivalent widths and excitation energies of iron lines calculated with our individual atmosphere model support the derived parameters of PMMR 144.

3. Investigation of n-capture elements in the atmospheres of RM.1-667 and PMMR 144

Since the end of 80th of the former century we developed a method which allows to increase the reliability of identification of lines of chemical elements in stellar spectra. The main idea of this method is the comparison of observed and calculated spectra in wide spectrum region. The calculations of synthetic spectra should be made using the extended database of atomic and molecular lines and the observed spectra of different type stars should be compared. The more detailed description of the method and the examples of results can be found in Gopka et al. (2004), Yushchenko et al. (2005), Kang et al. (2012, 2013). The use of this method allowed us to find the identifications of lines of neutron-capture elements in the spectra of MCs supergiants and to calculate the abundances of these elements in the atmospheres of RM.1-667 and PMMR 144.

To increase the validity of results we used also the last version of SYNTHV code (Tsymbal, 1996), The last version of input list of atomic lines from VALD (Piskunov et al., 1995) and the model atmosphere 3750/-1.5 were used to create the synthetic spectra. The abundances of chemical derived using the equivalent widths of lines in observed spectra were applied as a first approximation for calculation of synthetic spectra. These spectra were used for comparison with observations and refining initial abundances in the next iterations.

First of all the abundances of C, N, O, Mg and Ti which define the intensity of predominant lines of TiO, CN, MgH and other molecules were specified before the analysis of other elements. The lines with maximum sensitivity to abundance changes were selected for final estimates.

PMMR 23. In 2005 we presented the investigation of this SMC supergiant (Gopka et al., 2005). One of the results was the determination of thorium abundance using the spectral lines in wavelength range from 5300 to 7100 Å in the observed spectra of several stars. Gopka et al. (2005) also derived the abundances of chemical elements in the atmosphere of PMMR 23, located in the region of low-velocity neutral hydrogen flow. It was found that the abundances of heavy ($Z>56$) elements such as La, Ce, Pr, Nd, Sm, Eu, Gd, Dy, Er, Lu, Hf, Tl, and Th in the atmosphere of PMMR 23, the star with iron abundance $[\text{Fe}/\text{H}]=-0.51$, are close to $[\text{el}/\text{Fe}]=0.8$ dex.

Fig. 1 shows one of the thorium lines in the spectrum of PMMR 23. Fig. 2 is the abundance pattern of PMMR 23, and Fig. 3 compares the abundances in the atmosphere of PMMR 23 with scaled solar r - and s -process distributions. For this and next figures the solar r - and s -processes distributions were taken from

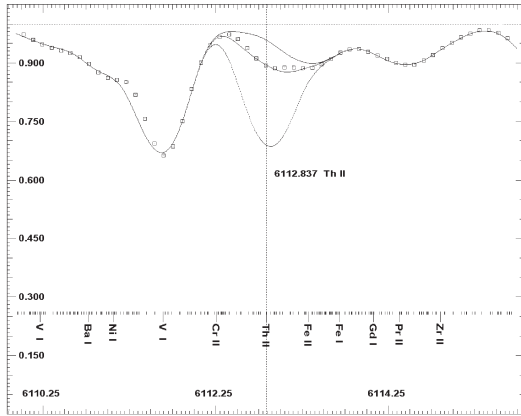


Figure 1: The fitting of observed spectrum (open squares) of PMMR 23 by synthetic spectra (lines) in the vicinity of Th II line λ 6112.837 Å. The axes are wavelength in angstroms and relative fluxes. Three synthetic spectra are shown near center of thorium line. One of these spectra fit the observations, the other two are calculated for under and overabundance of thorium by ± 0.5 dex from the best value. The position of thorium line is marked by vertical dotted line. The wavelengths of atomic and molecular lines used for calculations of synthetic spectra are shown in the bottom part of the figure. The identifications are shown for the strongest of them.

Simmerer et al. (2004).

Two subsequent triplets of figures, namely Figures 4, 5, & 6 and Figures 7, 8, & 9 exhibit the similar information for next two stars: PMMR 144 and RM_1-667 respectively.

PMMR 144. In the sample of six SMC stars investigated by Hill (1997) PMMR 144 demonstrated the most deficient iron abundance with respect to other stars. It was supposed that the object was likely to have second component with magnitude of 16-17^m. The lanthanum and europium were not overabundant relative to iron (Hill, 1997). In the present study, like in earlier works devoted to the investigation of chemical composition of MC stars, we focus our attention on the identification of the heavy elements lines.

Each line in the spectrum range from 5790 to 6835 Å was analyzed by synthetic spectrum method to determine the major contributors to line absorption coefficient. It was found that thorium, lutetium, europium, neodymium, cerium, lanthanum, zirconium, yttrium, and other heavy elements lines can be identified in the visible spectrum. The equivalent widths of these lines can be as high as 80-100 mÅ.

Using the synthetic spectrum method the abundances of 31 chemical elements, including 15 neutron-capture elements, were estimated. For most of the investigated elements, the abundance pattern of PMMR144 shows a deficiency of about 1.0 dex with

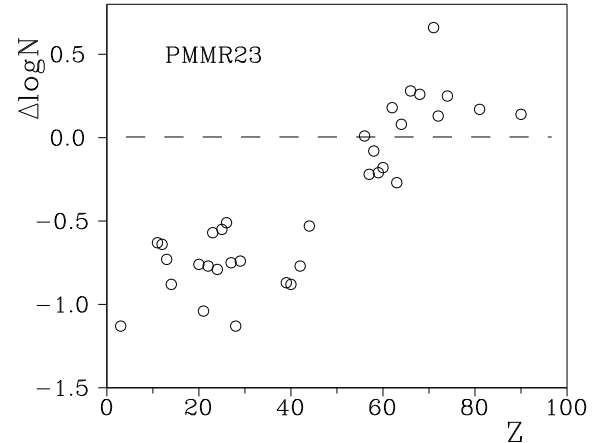


Figure 2: The plot of relative abundances of chemical elements in the atmosphere of PMMR 23 with respect to atomic numbers of these elements. Horizontal dotted line designates the solar abundances.

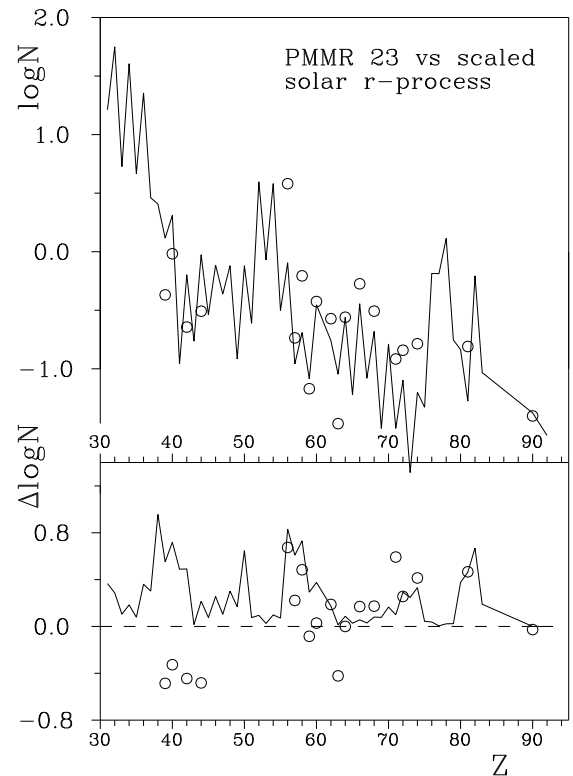


Figure 3: The upper panel shows the comparison of the surface abundances in PMMR 23 (circles) with the solar system r -process abundance distribution scaled at the observed Gd abundance (line). The bottom panel shows the differences of the observed abundances in PMMR 23 and the scaled solar system r -abundances (circles). The line is the deviations of solar photosphere abundances from solar r -process abundance distribution. The maximums of this curve are expected for the elements with highest relative s -process contributions.

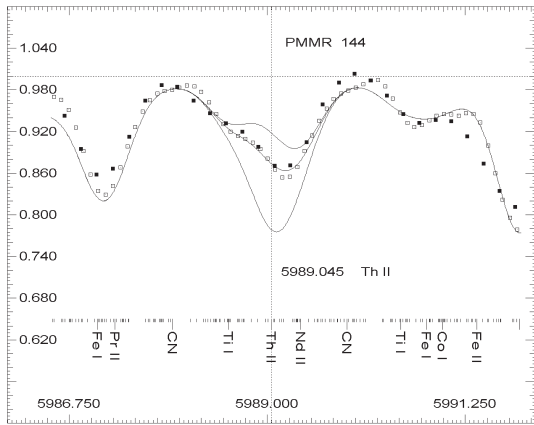


Figure 4: Similar to Fig. 1, but the star is PMMR 144, and the thorium line is λ 5989.045 Å. Open and filled squares are different observed spectra.

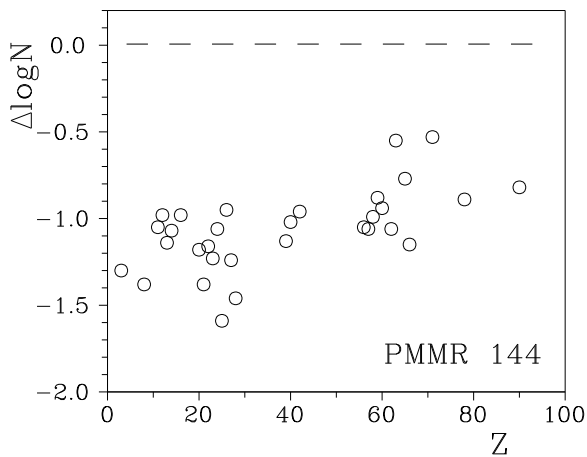


Figure 5: Similar to Fig. 2, but for PMMR 144.

respect to the solar values. Elements heavier than barium are enhanced with respect to iron by +0.5 dex.

RM.1-667. The detailed identification of the absorption lines in the RM.1-667 spectrum was carried out. It was found that the lines of several post-lanthanides, namely Hf, Pt, and Th can be detected in the visible spectrum. The identification of thorium lines in the visible spectrum of RM.1-667 is an important result of our study (Fig. 7). The coincidence of observed and laboratory wavelengths as well as the abundances derived for different lines are the undeniable proof of the presence of r-process elements in the atmosphere of this star.

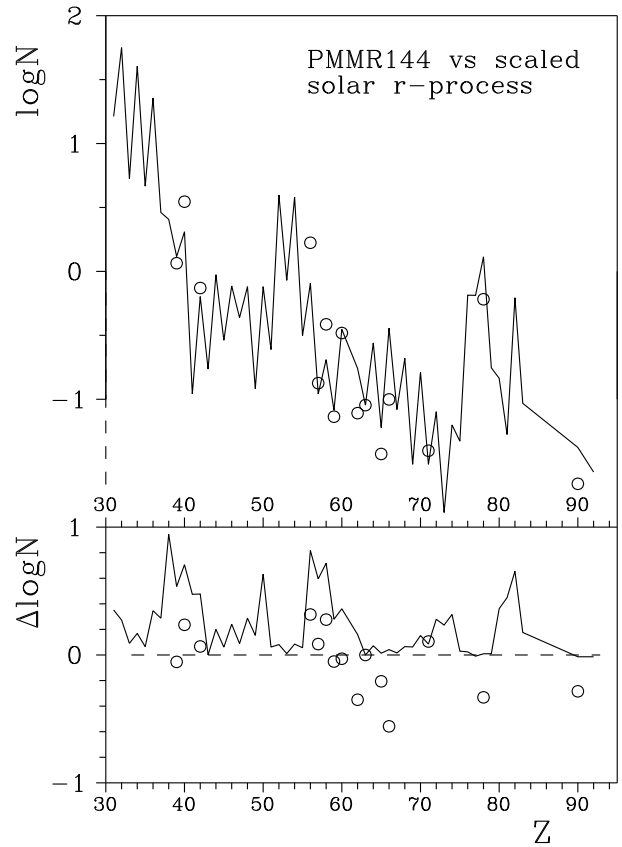


Figure 6: Similar to Fig. 3, but for PMMR 144. Solar r -process abundance distribution is scaled to the observed europium abundance.

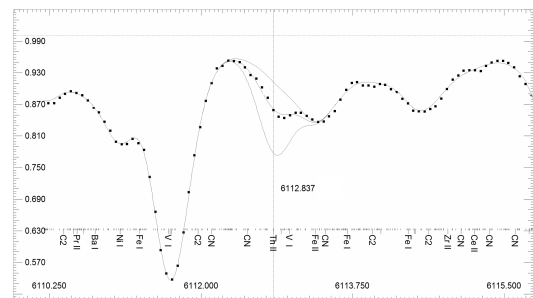


Figure 7: Similar to Fig. 1, but the star is RM.1-667. Observed spectrum is shown by filled squares.

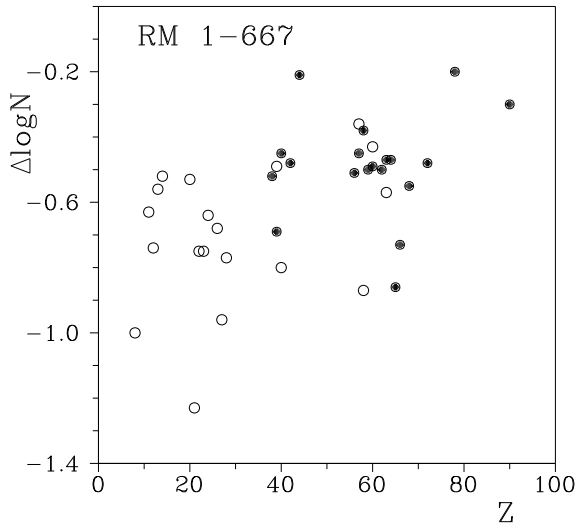


Figure 8: Similar to Fig. 2, but the star is RM_1-667. Open and filled circles are the values calculated using model atmospheres and spectrum synthesis methods respectively.

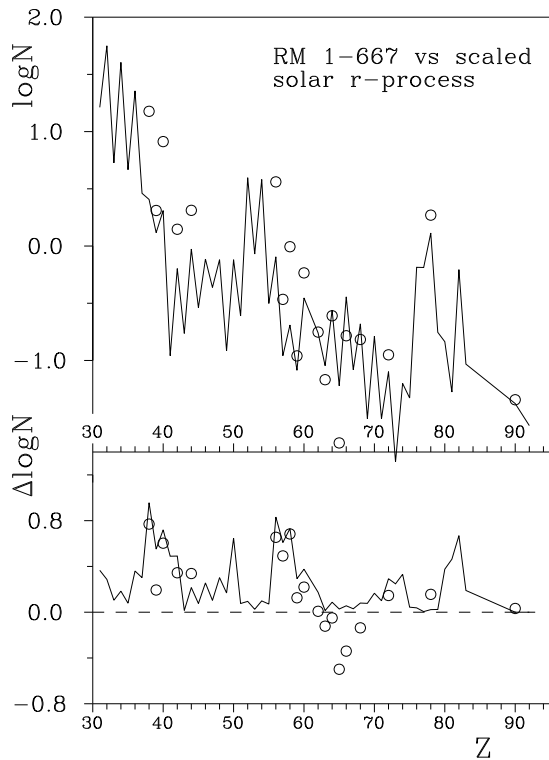


Figure 9: Similar to Fig. 3, but the star is RM_1-667. The solar system r -process abundances are scaled at the observed abundance of gadolinium.

4. Discussion

The knowledge of actinides abundances in extragalactic objects now is restricted by Local Group members. Only few papers were devoted to this observational problem. One of the first was the investigation of metal-poor red giant COS 82 in Ursa Minor dwarf galaxy (Aoki et al, 2007). The thorium abundance was found using the line Th II λ 5989.045 Å, which was first identified in stellar spectrum by Yushchenko et al. (2005).

We identified thorium lines in the spectra of three MC supergiants, find the chemical composition of these stars, and compared the abundance patterns with solar system r -, and s -processes abundance distributions. Analysis of Figures 3, 6, and 9 allows to conclude that the abundance patterns can not be explained by only r -process contribution. The influence of s -process is clearly visible at the bottom panels of these figures, but it is also clear that the input of s -process can not be easily estimated – it differs from star to star.

As it was discussed by Yushchenko et al. (2013) not only the nonuniversality of r -process, but also the accretion of interstellar gas also can be important to understand the chemical anomalies in stellar atmospheres. Kang et al. (2012, 2013) show that the signs of accretion of interstellar gas can be found not only in hot stars with radiative atmospheres, but also in cooler stars if the accretion is strong enough.

Our preliminary results shows that the possibility of accretion can not be neglected for explanation of abundance anomalies in the atmospheres of these three MC supergiants. The detection of signs of accretion can be additional confirmation of high density of interstellar gas in MC.

5. Conclusion

In present investigation we demonstrated the detectability of thorium lines in the spectra of MC supergiants.

The comparison of the theoretical curves of r -process and the abundance patterns, obtained in present study for MC supergiants, show resemblance that enables us to assume that the matter, from which the target stars were formed, was enriched by main r -process elements. But some percents of s -process elements are present in these stars. The elements with important contribution of s -process elements clearly deviate from solar system r -process abundance distribution, but the deviations are different from star to star.

It is necessary to discuss the possibility of additional scenarios to explain the chemical anomalies of these stars.

This work was supported in part by Mid-career and General Researcher Programs, and Science and Technology grants 2011-0028001 and 2011-0010696 respectively, through the National Research Foundation (NRF) funded by the Ministry of Education of Korea. One of the authors was granted by the Swiss National Science Foundation (SCOPEs project No. IZ73Z0 - 128180/1).

References

- Aoki W., Honda S., Sadakane K., Arimoto N.: 2007, *PASJ*, **59**, L15.
- Bekki K.: 2011, *MNRAS*, **416**, 2359.
- Gopka V.F., Yushchenko A.V., Mishenina T.V., Kim Chulhee, Musaev F.A., Bondar A.V.: 2004, *ARep*, **48**, 577.
- Gopka V., Yushchenko A., Andrievsky S., Goriely S., Vasileva S., Kang Y.-W.: 2005, *IAU Symp.*, **228**, 535.
- Gopka V.F., Shavrina A.V., Vasil'eva S.V., Yushchenko V.A., Yushchenko A.V., Andrievsky S.M.: 2013, *Bull. CrAO*, **109**, 41.
- Hilditch R.W., Howarth I.D., Harris T.J.: 2005, *MNRAS*, **357**, 304.
- Hill V.: 1997, *A&A*, **324**, 435.
- Kang Y.-W., Yushchenko A., Hong K., Kim S., Yushchenko V.: 2012, *AJ*, **144**, 35.
- Kang Y.-W., Yushchenko A.V., Hong K., Guinan E.F., Gopka V.F.: 2013, *AJ*, **145**, 167.
- Kurucz R.L.: 1995, CDROM No. 23 (Cambridge, MA, Smithsonian Astrophys. Obs.).
- Luck R.E., Bond H.: 1989, *ApJS*, **71**, 559.
- Novara G.N., La Palombara S., Mereghetti H.F., Coe M. et al.: 2011, *A&A*, **532**, 153.
- Pavlenko Ya.V.: 2003, *ARep*, **47**, 59.
- Piskunov N.E., Kupka F., Ryabchikova T.A., Weiss W.W., Jeffery C.S.: 1995, *A&A*, **112**, 525.
- Reynolds S.E., Hearnshaw J.B., Cotrell P.L.: 1988, *MNRAS*, **235**, 1423.
- Rolleston W.R.J.: 1991, *AJ*, **120**, 60.
- Russell S.C., Bessell M.S.: 1989, *ApJS*, **70**, 865.
- Russell S.C., Dopita M.A.: 1992, *ApJ*, **384**, 508.
- Simmerer J., Sneden C., Cowan J.J., Collier J., Woolf V.M., Lawler J.E.: 2004, *ApJ*, **617**, 1091.
- Skibba R.A., Charles W., Engelbracht C.W., Aniano G., Babler B. et al.: 2012, *ApJ*, **761**, 42.
- Tsybal V.: 1996, *ASP Conf. Ser.*, **108**, 198.
- Yushchenko A., Gopka V., Goriely S., Musaev F., Shavrina A., Kim C., Kang Y. Woon, Kuznietsova J., Yushchenko V.: 2005, *A&A*, **430**, 255.
- Yushchenko A.V., Rittipruk P., Yushchenko V.A., Kang Y.-W.: 2013, *OAP*, **This volume**.

MANGANESE ABUNDANCES IN THE ATMOSPHERE OF CLUMP GIANTS

T. I. Gorbaneva

Astronomical Observatory, Odessa National University
Shevchenko Park, 65014, Odessa, Ukraine, *clumpstars@rambler.ua*

ABSTRACT. The manganese abundances was determined in the atmospheres of clump giants stars whose selection was made earlier based on their chemical composition and evolutionary tracks. The spectra of the studied stars were obtained using the facilities of the 1.93m telescope of the Haute-Provence Observatoire (France) equipped with the échelle spectrograph ELODIE ($R = 42000$, $S/N = \sim 100-300$). The Mn abundances was determined under the LTE approximation by the synthetic spectrum approach with a detailed consideration of the superfine structure. The behaviour of manganese abundances with metallicity $[Fe/H]$ was considered.

Key words: stars: abundances

Manganese is a typical Fe-peak element. A debate is still on-going to determine the main sources and their contributors to the Mn abundances whether type II or type Ia supernovae (SNe). Wallerstein (1962) first noted that Mn is deficiency relative to Fe in low-metallicity stars unlike other elements of the iron peak. Later, Gratton (1989) showed that the behavior of manganese inverse behavior of α -elements whose content is increased with a decrease in metallicity. We studied the Mn abundances in clump giants stars whose selection and atmospheric parameters were determined earlier (Mishenina et al., 2006, Kovtyukh et al., 2006).

The Mn abundances in program stars were obtained by fitting synthetic spectra to the observational profiles. We used the STARSP LTE spectral synthesis code developed by Tymbal (1996), Kurucz models (Kurucz, 1993), and VALD atomic data (Kupka et al., 1999) while accounting for the superfine structure (Prochaska et al., 2000) (see Fig.1).

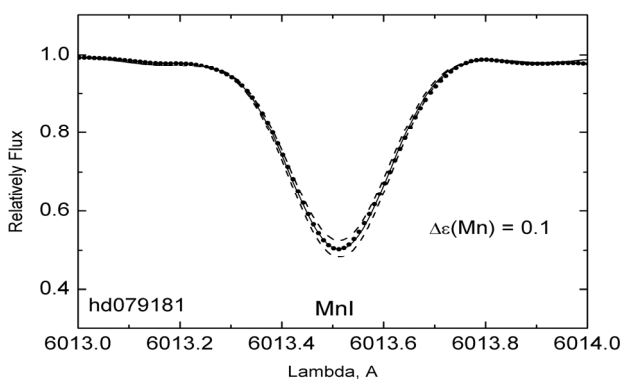


Fig.1. Spectrum synthesis fitting of observed profiles of Mn line 6113 Å.

For sixteen lines we estimated the manganese abundances in the Sun's atmosphere. The analysis resulted in the selection of three lines, viz., 5432, 6013, and 6021 Å. The abundance ratios $[Mn/Fe]$ for each star in our set are plotted against $[Fe/H]$ in Figs. 2, 3.

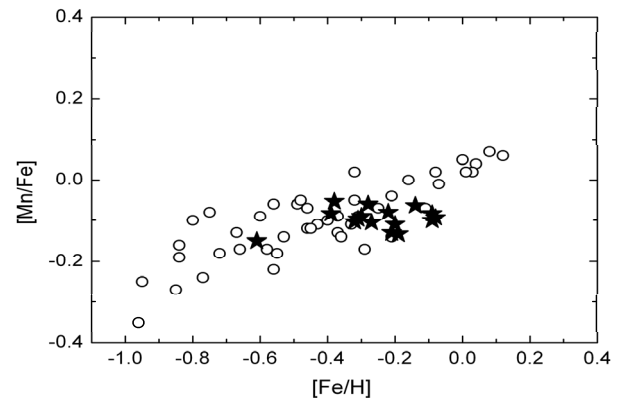


Fig.2. $[Mn/Fe]$ ratios for our giants (asterisks), and dwarfs of the disk (open circles).

We compared the obtained Mn abundances with the results of other authors (Fig. 3).

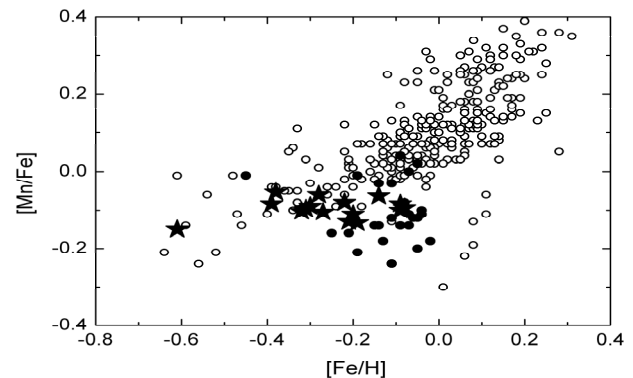


Fig.3. Comparison of our data (asterisks), with that obtained by other authors: for stars in the open clusters (Reddy, 2012, 2013) – black circles and for giants in local field (Luck, 2007) – open circles.

What is the cause of this inconsistency? We did not take the deviation from the LTE into account in the calculation of Mn content and other authors also did not account for it. Does the problem consist of the incorrect selection of lines or correct accounting for the superfine structure of the lines? To answer these and other questions, further investigations are needed.

References

- Wallerstein G.: 1962, *ApJSS*, **6**, 407.
 Gratton R.G.: 1989, *A & A*, **208**, 171.
 Kovtyukh V.V. et al.: 2006, *AZh*, **73**, 862.
 Mishenina T.V. et al.: 2006, *A&A*, **456**, 1109.
 Kurucz R.L.: 1993, CD ROM n13.
 Tymbal V.V.: 1996, *ASP Conf. Ser.*, **108**, 198.
 Prochaska J.X. et al.: 2000, *AnJ*, **120**, 2513.
 Reddy A.B.S. et al.: 2012, *MNRAS*, **419**, 1350.
 Luck R.E. et al.: 2007, *AnJ*, **133**, 2464.

THE MASSES OF THE IONIZED GAS OF PLANETARY NEBULAE ENVELOPES IN LARGE MAGELLANIC CLOUD

V.Holovatyy ¹, A.Demchyna ²

Ivan Franko National University of Lviv, Lviv, Ukraine

¹ vholovatyy@gmail.com, ² ademchyna@gmail.com

ABSTRACT. The masses of ionized gas in the shells of planetary nebulae which belong in the Large Magellanic Cloud are calculated by three different ways. The value of mass is calculated for the cases: 1) spherical, 2) elliptical forms of envelopes and 3) commonly known method based on the line ratio $F(H\beta)$ of the shell to its emissivity of $\epsilon(H\beta)$. It is shown that the values of masses M_i of nebulae envelopes differ up to 50%. The values of M_i calculated by the other methods which differ more from previous ones. We consider the dependence of M_i on the radius and the electron density in the envelopes of nebulae.

Key words: mass of ionized gas, planetary nebulae of LMC

To determine the masses of ionized gas in the shells of planetary nebulae (PN) are commonly used method based on the observed radiation flux $F(H\beta)$ from its envelopes in line $H\beta$ and its emissivity $\epsilon(H\beta)$ [2]. As a result the volume of gas emitted $V(H^+) = 4\pi r^3 \cdot F(H\beta) / \epsilon(H\beta)$ is determined by a sphere of radius r and respectively of the ionized hydrogen mass M_i with the helium atoms :

$$M_i(r) = \left(\frac{4}{3}\pi r^3\right) \cdot \epsilon \cdot n(H^+) \cdot m_H \cdot (1+4\gamma),$$

where r is radius envelopes PN (distance to PN 50,6 kpc [6]), $n(H^+)$ is concentration of H ions. Factor $(1+4\gamma)$ takes into account the contribution of the atoms He. The filling factor $\epsilon = 1$, if the sphere is completely filled of uniform density gas, and $\epsilon < 1$, if it is only partially filled.

It is known that the masses of envelopes PN founded of different authors are differ vary. One explanation for this difference is that forms of envelopes PN different from spherical, i.e. are elliptical. The values of corresponding sides of the ellipses are given in [6].

In this paper is investigated the influence of different radiuses of the ellipses, on the determination V and, corresponding, mass M_i of the envelopes PN.

The values of the corresponding parameters for determining M_i are derived in table. Col.1 contains the name of PN, col.2 and col. 3 gives the values of parties ellipses [6] col. 4 contains fluxes in line $F(H\beta)$ [5], col.5 contains the electron temperatures, col.6 contains the electron density n_e [5]. Some data of the electron density n_e were taken from [1,3,4]. To calculate the volumes of envelopes PN used the formula $V(r) = \frac{4}{3}\pi r^3$ are derived (col.7). In col. 8 are derived $V(r = a) = \frac{4}{3}\pi a^3$. Col. 9 contain $V(a, b) = \frac{4}{3}\pi (a \cdot b)^2$ and presents the volumes founded into account the shape of envelope, corresponding. These dates of the volumes of envelopes PN and the electron densities n_e , were used for calculation of the ionized gas masses:

$$M_i = V \cdot n(H^+) \cdot m_H \cdot (1+4\gamma),$$

The corresponding values of the mass of ionized gas in the envelopes PN are gives in col.10, 11, 12 table, corresponding.

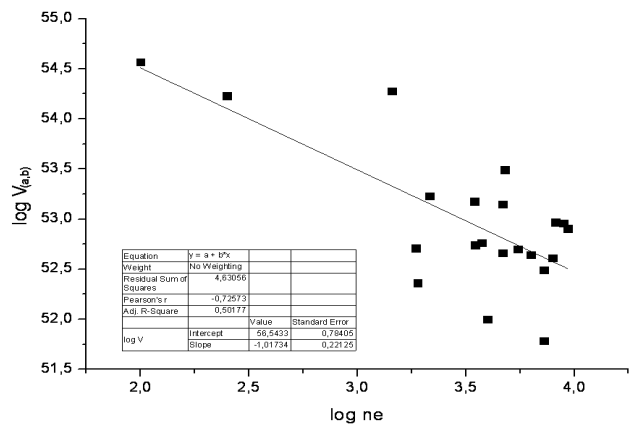


Figure 1. Dependence of the electron density from the volumes of the envelopes PN

Table : Parameters of envelopes PN

NAME PN	diameter		$F(H\beta)$ $\frac{erg}{cm^2 \cdot c}$	Te K	n_e cm^{-3}	V(r) cm^3	V(r=a) cm^3	V(a,b) cm^3	$M_i(r)$ M_\odot	$M_i(r=a)$ M_\odot	$M_i(a,b)$ M_\odot
	a	b									
	arcsec	arcsec									
1	2	3	4	5	6	7	8	9	10	11	12
SMP3	0,26	0,23	-12,19	13800	7244	5,80E+52	7,81E+51	6,10E+51	0,35	0,04	0,05
SMP5	0,46	0,5	-12,02	11700	1862	9,30E+53	4,33E+52	5,10E+52	1,45	0,08	0,07
SMP6	0,67	0,56	-12,11	13300	8202	5,00E+52	1,34E+53	9,30E+52	0,35	0,64	0,92
SMP14	2,41	1,87	-13,25	10090	100 [4]	1,40E+55	6,22E+54	3,70E+54	1,18	0,32	0,52
SMP29	0,51	0,47	-12,63	20000	5495	7,60E+52	5,89E+52	5,00E+52	0,35	0,23	0,27
SMP37	0,5	0,43	-12,52	13600	7943	2,20E+52	5,55E+52	4,10E+52	0,15	0,27	0,37
SMP45	1,66	1,62	-12,73	15900	1445	5,50E+53	2,03E+54	1,90E+54	0,67	2,35	2,47
SMP48	0,4	0,36	-12,33	13200	1900 [1]	5,50E+53	2,84E+52	2,30E+52	0,88	0,04	0,05
SMP52	0,73	0,73	-12,24	12300	2153	4,60E+53	1,73E+53	1,70E+53	0,84	0,31	0,31
SMP62	0,59	0,41	-12,1	15700	6310	1,20E+53	9,13E+52	4,40E+52	0,64	0,23	0,48
SMP63	0,63	0,57	-12,25	11200	8913	2,20E+52	1,11E+53	9,10E+52	0,16	0,68	0,83
SMP67	0,88	0,61	-12,66	12400	3467	6,90E+52	3,03E+53	1,50E+53	0,20	0,42	0,88
SMP69	1,84	1,43	-13,17	-	250 [4]	-	2,77E+54	1,70E+54	-	0,35	0,58
SMP73	0,31	0,27	-12,16	13100	3981	1,80E+53	1,32E+52	1,00E+52	0,61	0,03	0,04
SMP74	0,79	0,63	-12,11	12500	4677	1,40E+53	2,19E+53	1,40E+53	0,54	0,55	0,86
SMP84	0,57	0,48	-12,63	13300	3750 [3]	7,20E+52	8,23E+52	5,80E+52	0,23	0,18	0,26
SMP88	0,61	0,45	-12,49	25500	3500 [4]	4,20E+53	1,01E+53	5,50E+52	1,23	0,16	0,30
SMP89	0,51	0,45	-11,94	12300	4677	2,00E+53	5,89E+52	4,60E+52	0,77	0,18	0,23
SMP92	0,62	0,54	-12,07	13400	9333	4,30E+52	1,06E+53	8,00E+52	0,34	0,63	0,83
SMP98	0,41	0,41		12800	7244	-	3,06E+52	3,10E+52	-	0,19	0,19
SMP101	1,03	0,82	-12,7	15200	4786	4,90E+52	4,86E+53	3,10E+53	0,20	1,24	1,95

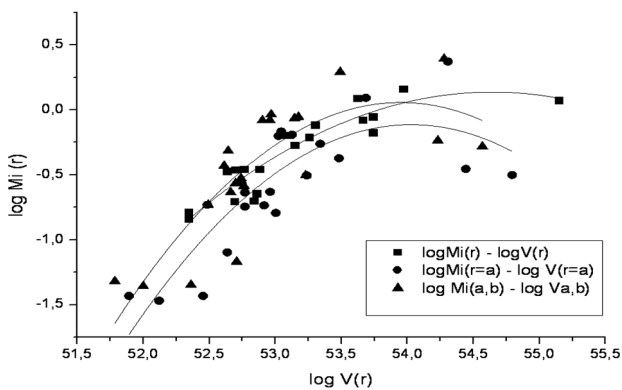
Figure 2. Dependence of the masses of ionized gas M_i from the volume of the envelopes PN V

Figure 1 shows the dependence of the electron concentration n_e from the volumes of the envelopes PN. It is clearly seen when the volume of envelopes PN are increased then electron density n_e are decreased. An approximation of this dependence $\log V(a,b)=1,017\log n_e+56,54$.

Figure 2 shows the dependence of the masses of ionized gas in the envelopes M_i from its V. It is clearly seen that the difference between acceptable forms of envelopes PN lead to a large difference in values M_i comparable to the variation of the masses found by different authors.

References

1. García-Hernández D. et al.: 2012, *ApJ*, **760**, 107.
2. Holovatyy V., Demchyna A.: 2013, *JPhSt*, **17**, 1, 1902.
3. Holovatyy V., Melekh B.: 2012, *Astron J.*, **90**, 5, 406.
4. Leisy P., Dennefeld M.: 1996, *Astron. Astrophys.*, **116**, 95.
5. Richer M.: 1993, *ApJ*, **415**, 240.
6. Villaver E., Stanghellini L.: 2007, *Astron. J.*, **656**, 831.

CHEMICAL COMPOSITIONS OF CRAB NEBULA FILAMENTS

V.V. Holovaty, B.Ya. Melekh, N.V. Havrylova

Department of Astrophysics of Ivan Franko National University,
Lviv, Ukraine, *bmelekh@gmail.com*

ABSTRACT. The chemical compositions in filaments of Crab Nebula are obtained using two methods: new Ionization Correction Factors taking into account density inhomogeneities of the nebular gas, and new 3-stages method based on the optimized photoionization modelling of the nebular gas.

Key words: Crab Nebula; nebular diagnostics; photoionization modelling.

The problem of the determination of physical characteristics and chemical compositions in filaments of Crab Nebula was considered by Woltijer (1958), Holovaty & Pronik (1973), Contini et al. (1977, 1978). It was shown by Holovaty & Pronik (1973), that the chemical abundances increase outwards nebula. For our research we used the observed spectra, obtained by Fesen & Kirshner (1982).

The electron temperatures T_e , electron densities n_e , ionic abundances and chemical compositions for individual filaments of Crab Nebula are obtained, using code FREE DIAGN (Holovaty et al., 1999) with new Ionization Correction Factors, which take into account density inhomogeneities of nebular gas (Holovaty & Havrylova, 2005).

Distances from the center of Crab nebula to the individual filaments are recalculated for the $R=1800$ pc. To the determination of distances to the observed parts of Crab Nebula the averaged over radius and weighed over electron density ionic abundances O^+/H^+ and O^{++}/H^+ . We derived the following dependence of distances to the corresponding observed filaments of Crab Nebula on oxygen ionic abundances:

$$r = 689,70 \times \left(\frac{O^{++} + O^+}{H^+} - 7,02 \times 10^{-4} \right). \quad (1)$$

The radial distribution of chemical compositions in Crab filaments are obtained. The increasing of the abundances outwards nebula were confirmed for He/H, O/H, Ne/H and were not confirmed for S/H and N/H (see Fig.1 and first two dependences in Fig.2).

Also the chemical compositions in filaments of Crab Nebula were obtained using new 3-stages method based on the optimized photoionization modelling (OPhM) of the nebular gas (Melekh B.Ya. et al.: 2012). This

method uses the diagnostic ratios between the emission line intensities. The following diagnostic ratios (DRs) between emission line intensities are used to the reproducing of the observed data (Melekh, 2009):

$\lambda 6731[\text{SII}] / \lambda 6716[\text{SII}]$, $\lambda 7323[\text{OII}] / \lambda 7332[\text{OII}]$,
 $\lambda 3727[\text{OII}] / \lambda 6300[\text{OI}]$, $\lambda 4686(\text{HeII}) / \lambda 4471(\text{HeI})$,
 $\lambda 4686(\text{HeII}) / \lambda 5876(\text{HeI})$, $\lambda 4471(\text{HeI}) / \lambda 5412(\text{HeII})$,
 $\lambda 5876(\text{HeI}) / \lambda 5412(\text{HeII})$, $\lambda 4959[\text{OIII}] / \lambda 4363[\text{OIII}]$,
 $\lambda 5007[\text{OIII}] / \lambda 4363[\text{OIII}]$, $\lambda 5007[\text{OIII}] / \lambda 3727[\text{OII}]$,
 $\lambda 6731[\text{SII}] / \lambda 6312[\text{SIII}]$.

At the first stage the ionization structure of nebula was determined, using mainly reproducing of the observed diagnostic ratios between line intensities. At the second stage the chemical elements abundances were corrected at the ionization structure obtained at previous stage. At the last third stage all free parameters were employed in optimization process to avoid the consequences due to the assumptions used for division of the optimization process into the two first stages.

The following free parameters were used for OPhM of Crab Nebula: hydrogen density, covering factor, energy distribution in ionizing spectra and chemical abundances (He/H and O/H for Stage I, all available chemical elements for Stage II and Stage III). To initialization of the chemical composition of elements the corresponding data obtained previously by diagnostic methods were used. To comparison of modelling results with observed ones the model emission line spectra, the flux in H_β line, the nebular outer radius and the DRs were used.

The ionizing Lyc-spectrum was also varied during optimization process. It allows to reproduce the optimal energy distribution in the ionizing radiation spectrum in the modelling region and, therefore, the detailed consideration of the ionizing radiation transfer from pulsar to the modelling (observed) part of nebula is not required. Peter van Hoof's optimization algorithm Phymir (<http://dissertations.ub.rug.nl/faculties/science/1997/p.a.m.van.hoof>) was used to the minimization of χ^2 -function. For OPhM of nebular gas in filaments we used Gary Ferland's code Cloudy 08.00 (<http://www.nublado.org>), upgraded by us to the including of the ionizing spectrum shape to the free parameters as well as to the comparison of the model

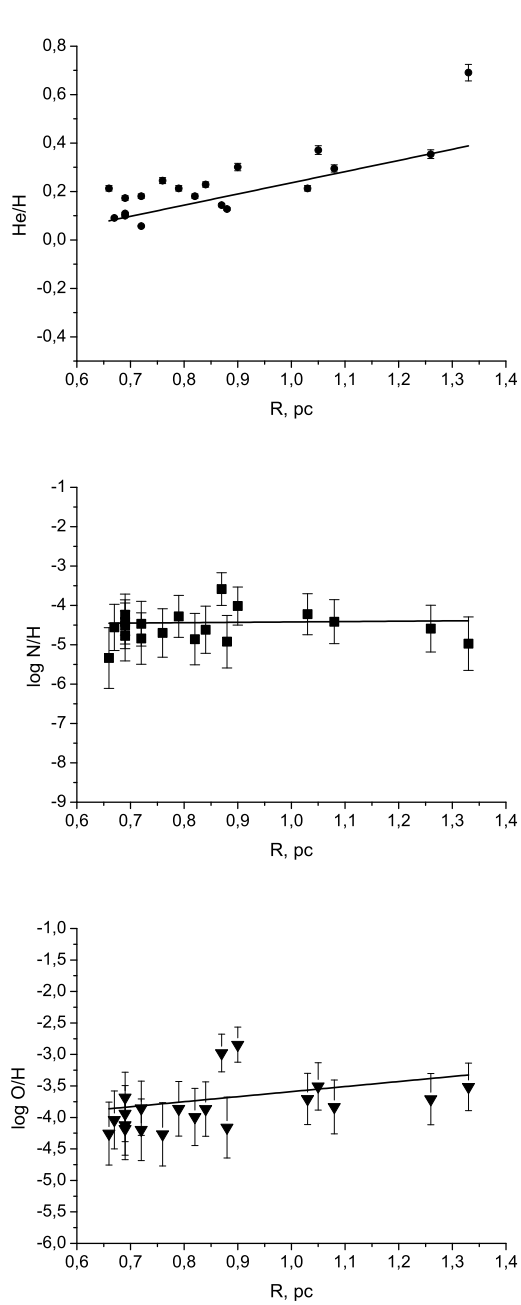


Figure 1: The radial distribution of He/H, N/H and O/H in Crab Nebula filaments.

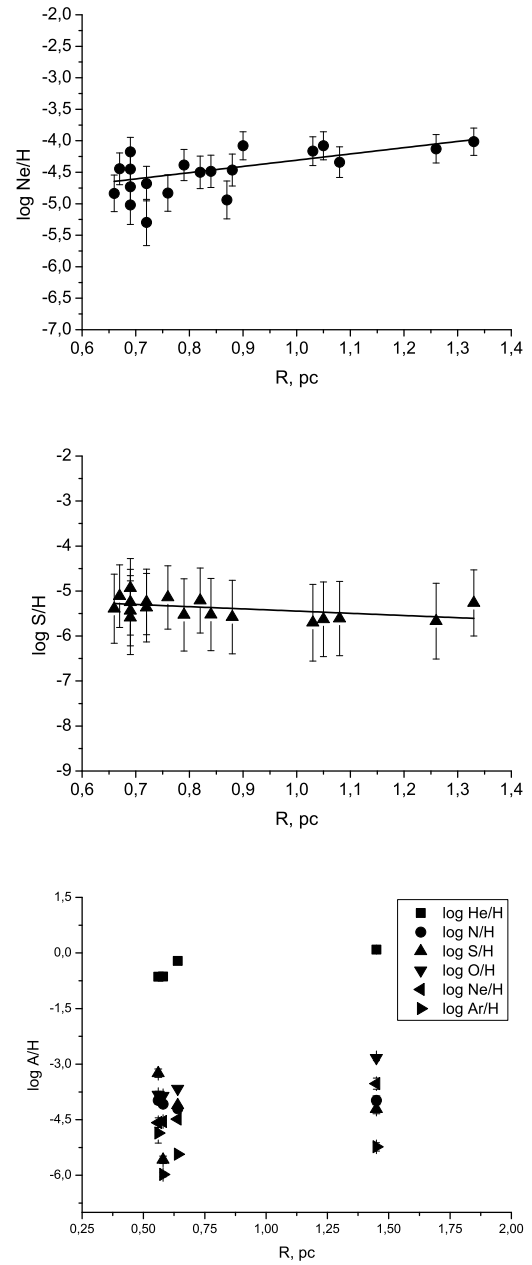


Figure 2: The radial distribution of Ne/H and S/H in Crab Nebula filaments. The bottom (last) figure shows the chemical compositions in Crab filaments obtained using OPhM.

DRs with observed ones. The sensitivity of the relative line intensities and the diagnostic ratios to the chemical abundances variations were analyzed and taken into account.

The radial distribution of the chemical compositions in Crab Nebula filaments were analyzed using OPhM results for 4 parts of Crab Nebula filaments. At present the OPhM results can not confidently confirm the increasing of the abundances outwards nebula (see last Fig.2). It is planned to calculate the OPhM of all regions of Crab Nebula observed by Fesen, Kirshner.

References

Contini M., Kozlovsky B., Shaviv G.: 1977, *Astron. Astrophys.*, **59**, 387.
Contini M., Kozlovsky B., Shaviv G.: 1978, *Astron. Astrophys.*, **68**, 443.

Fesen R.A., Kirshner R.P.: 1982, *A. J.*, **258**, 1.
Holovatyy V.V. et al.: 1999, *Izvest. Krymsk. astro-phys. observ.*, **96**, 1.
Holovatyy V.V., Havrylova N.V.: 2005, *Astron. Zh.*, **82**, **5**, 437.
Holovatyy V.V., Pronik V.I.: 1973, *Astron. Zh.*, **50**, **6**, 1147.
Melekh B.Ya.: 2009, *JPhS* **13**, **3**, 3901.
Melekh B.Ya. et al.: 2012, *Odessa Astr. Publ.*, **25/2**, 178.
Woltier L.: 1958, *Bull. Astron. Inst. Neth.*, **14**, 483.

DETERMINATION OF THE EPHEMERIS ACCURACY FOR AJISAI, LAGEOS AND ETALON SATELLITES, OBTAINED WITH A SIMPLIFIED NUMERICAL MOTION MODEL USING THE ILRS COORDINATES

I. V. Kara

Astronomical Observatory of the I. I. Mechnikov Odessa National University
Shevchenko Park, 65014, Odessa, Ukraine, *lionkiv@gmail.com*

ABSTRACT. This paper describes a simplified numerical model of passive artificial Earth satellite (AES) motion. The model accuracy is determined using the International Laser Ranging Service (ILRS) high-precision coordinates. Those data are freely available on <http://ilrs.gsfc.nasa.gov>. The differential equations of the AES motion are solved by the Everhart numerical method of 17th and 19th orders with the integration step automatic correction. The comparison between the AES coordinates computed with the motion model and the ILRS coordinates enabled to determine the accuracy of the ephemerides obtained. As a result, the discrepancy of the computed Etalon-1 ephemerides from the ILRS data is about 10'' for a one-year ephemeris.

Introduction

The development of the space industry in Ukraine demands advancement of the artificial Earth satellite (AES) tracking networks. Such networks must provide the AES tracking and safety of their motion. That is a very important task as the AES cost is very high, and loss of a satellite already put into space threatens the country with not only heavy economic losses, but also with losses of international launch contracts. So far the satellite tracking can be performed in several observatories in Ukraine. The accuracy of the obtained observation data has been continuously increasing, and the methods and instruments of observation has been modified and retrofitted. To ensure safe AES operation, numerical motion models for passive object tracking are required as the space debris (SD) poses the greatest threat to satellites.

This paper describes a simplified numerical motion model for the near-Earth space objects. The model is primarily focused on high speed of position computation for objects at altitude above 1,500 km.

AES motion equations

Equations of the near-Earth space object motion in the Earth-centred inertial coordinate system (Cartesian coordinate frame) take the following form:

$$\frac{d^2\vec{r}}{dt^2} = \frac{\partial U}{\partial \vec{r}} + \vec{a}_{MS} + \vec{a}_{Sp}. \quad (1)$$

where \vec{r} – the object position vectors in the indicated coordinate frame; t – time. Summand $\frac{\partial U}{\partial \vec{r}}$ on the right side of the equation is related to the accelerations caused by the Earth's gravitational field; \vec{a}_{MS} – the total perturbing acceleration by the Moon and the Sun; \vec{a}_{Sp} – the light pressure.

Perturbations due to the Earth gravitational potential

The geopotential value in the International Terrestrial Reference System (ITRS) is of the following form [1, pp. 24-26].

$$U = \frac{GM}{r_{\oplus}} \left\{ \sum_{n=2}^N \sum_{m=0}^n \left(\frac{r_{\oplus}}{r} \right)^{n+1} P_n^m(\sin \varphi) [C_n^m \cos(m\lambda) + S_n^m \sin(m\lambda)] \right\} \quad (2)$$

where GM_{\oplus} and r_{\oplus} – the geocentric gravitational constant and the Earth's equatorial radius; $\vec{r} = (x; y; z)$ – the object position vectors in the ITRS; $P_n^m(\sin \varphi)$ – the associated Legendre functions; φ and λ – the AES latitude and longitude in the same coordinate frame; C_n^m and S_n^m – numerical coefficients of the zonal, tesseral

and sectorial harmonic expansion of the Earth's gravitational potential.

As partial derivatives $\frac{\partial U}{\partial \vec{r}}$ are used in equation (1), the calculation of those partial derivatives of geopotential (2) presents the main complexity in practice. There are several commonly used recurrent algorithms for computation of geopotential derivatives, for instance, the algorithm suggested by L.Cunningham [3, pp. 71-74]. Simpler derivation of recurrence relations and also a method of smoothing work with imaginary values away were suggested in the algorithm by A. Drozyner and V. A. Brumberg [4]. The algorithm, developed by K. V. Kholshchikov in 2005, offers an alternate approach to calculation of geopotential derivatives [6].

In this paper the method of direct calculation of geopotential partial derivatives in the Cartesian coordinate frame with regard to recurrent properties of the Legendre polynomials is used as an alternative method of computation the geopotential perturbations. Such method of perturbation computation showed computation speed comparable with the above-described methods, and it is quite intuitive and simple.

To derive a working equation, it is necessary to accomplish a rather large amount of computations, but that eventually results in a single set of equations ready for being used in software algorithmization for any possible number of harmonics. If expansion in an arbitrary number of harmonics is used (1), a set of equations suitable for computation of geopotential partial derivatives can be obtained as a result of a series of manipulations:

$$\begin{aligned} \frac{\partial U}{\partial x} &= GM_{\oplus} \sum_{n=2}^N \sum_{m=0}^n \frac{r_{\oplus}^n}{r^{n+1}} \left[\frac{myP_n^m(\sin\varphi)}{x^2+y^2} (C_n^m \sin m\lambda - S_n^m \cos m\lambda) - \right. \\ &\quad \left. -CS \left\{ \frac{xz}{r^3} dP_n^m + \frac{(n+1)x}{r^2} P_n^m(\sin\varphi) \right\} \right] \\ \frac{\partial U}{\partial y} &= GM_{\oplus} \sum_{n=2}^N \sum_{m=0}^n \frac{r_{\oplus}^n}{r^{n+1}} \left[\frac{mxP_n^m(\sin\varphi)}{x^2+y^2} (S_n^m \cos m\lambda - C_n^m \sin m\lambda) - \right. \\ &\quad \left. -CS \left\{ \frac{yz}{r^3} dP_n^m + \frac{(n+1)y}{r^2} P_n^m(\sin\varphi) \right\} \right], (3) \\ \frac{\partial U}{\partial z} &= GM_{\oplus} \sum_{n=2}^N \sum_{m=0}^n \frac{r_{\oplus}^n}{r^{n+2}} CS \left[\frac{(x^2+y^2)}{r} dP_n^m - (n+1)zP_n^m(\sin\varphi) \right] \\ dP_n^m &= \frac{dP_n^m(\sin\varphi)}{d(\sin\varphi)}, \quad CS = (C_n^m \cos m\lambda + S_n^m \sin m\lambda). \end{aligned}$$

Although those expressions are cumbersome, it is fairly easy to arrange calculation of their values. It is important to use recurrent expressions for the Legendre polynomials.

Complete definition of instantaneous values C_2^1 and S_2^1 with regard to the inelastic Earth pole tide is performed as follows [7, pp. 57-69]:

$$C_2^1 = \bar{C}_2^1 + \frac{dC_2^1}{dt}(t - t_{J2000}), \quad S_2^1 = \bar{S}_2^1 + \frac{dS_2^1}{dt}(t - t_{J2000}),$$

where $\frac{dC_2^1}{dt} = -0,337 \cdot 10^{-11} \text{ year}^{-1}$ and

$\frac{dS_2^1}{dt} = 1,606 \cdot 10^{-11} \text{ year}^{-1}$ – derivatives, determined at epoch J2000. The standardised coefficients at epoch J2000 are

the following:

$$\bar{C}_2^1 = -2,20 \cdot 10^{-10}, \quad \bar{S}_2^1 = 14,51 \cdot 10^{-10},$$

Tidal corrections to the harmonic coefficients of the geopotential expansion are computed using the following formula:

$$\Delta C_n^m - i\Delta S_n^m = \frac{k_{nm}}{2n+1} \sum_{j=2}^3 \frac{GM_j}{GM_{\oplus}} \left(\frac{r_{\oplus}}{r_j} \right)^{n+1} P_n^m(\sin\Phi_j) e^{-im\lambda_j}$$

where k_{nm} – nominal values of the Love number; GM_j – gravitational parameter of the Moon ($j = 2$) and the Sun ($j = 3$); r_j – geocentric distance to the Moon or to the Sun; Φ_j – fixed geocentric latitude of the Moon or the Sun; λ_j – fixed West longitude (West of Greenwich) of the Moon or the Sun.

Perturbations by the Moon and the Sun

The next perturbations with the highest value, which affect the body motion in the near-Earth space, are those by the Moon and the Sun. Their perturbing accelerations were computed by formula (4):

$$\vec{a}_{MS} = GM_{Moon} \left(\frac{\vec{r}_M - \vec{r}}{|\vec{r}_M - \vec{r}|^3} - \frac{\vec{r}_M}{|\vec{r}_M|^3} \right) + GM_{Sun} \left(\frac{\vec{r}_S - \vec{r}}{|\vec{r}_S - \vec{r}|^3} - \frac{\vec{r}_S}{|\vec{r}_S|^3} \right) (4)$$

\vec{r}_M, \vec{r}_S – geocentric position vectors of the Moon and the Sun. When integrating equations of motion (1), the Moon's and the Sun's coordinates were computed using the DE405/LE405 model data [9].

Light pressure perturbations

We assume that the rate of solar radiation flux is constant, and the satellite has a spherical shape. With such assumptions the force of direct sunlight pressure on the satellite can be expressed by formula [5, pp. 617-625]:

$$\vec{a}_{sp} = kqs'\Psi \left(\frac{a_s}{\Delta_s} \right)^2 \frac{\vec{r}_s - \vec{r}}{\Delta_s} (5)$$

where \vec{r}_s – geocentric position vector of the Sun; Δ_s – distance between the satellite and the Sun; a_s – astronomical unit (the average distance from the Earth to the Sun); k – parameter that describes the reflective properties of the satellite surface (with $k = 1$ – specular reflection, with $k = 1,44$ – diffuse reflection), $q = 4,5605 \cdot 10^{-6} \frac{H}{M^2}$ – the solar constant; s' – the effective cross-sectional area of the satellite that is the

ratio between the cross-sectional area of the satellite and its mass.

When computing perturbations caused by the light pressure, the central problem was to account for the effect of a satellite's entering the Earth's shadow. The model by Ferraz-Mello is applied in this paper [5, p. 622]. He suggested eliminating the problem by introducing the so-called shadow function δ into the perturbing acceleration: with $\delta = 1$, if the satellite is sunlit, $\delta = 0$ - otherwise. In general, the shadow is cone-shaped, but it may be considered as cylindrical shaped due to far distance of the source casting the shadow.

Determination of the ephemeris accuracy using the ILRS coordinates

Integrating of the set of differential equations of the AES motion (1) was performed by the Everhart numerical method of 19th orders in the Cartesian coordinate frame with extended precision. The integration step partition coefficients were calculated independently to improve their accuracy [2]. The integrating is done using variable step [8].

To evaluate the model performance and accuracy, the ILRS (the International Laser ranging System <http://ilrs.gsfc.nasa.gov>) satellite Cartesian coordinate database is used. The coordinates are presented in the Earth-bound rotating reference frame (ITRF). More detailed information on the coordinate structure can be found in the file on the ILRS official website (http://ilrs.gsfc.nasa.gov/docs/cpf_1.01.pdf). The AES coordinate database is freely available via the ILRS open source FTP (<ftp://cddis.gsfc.nasa.gov/pub/slr/>

[cpf_predicts](#)). Using of those coordinates allows of control the satellite tracking accuracy. As those coordinates were obtained with high-precision numerical model for the AES motion, they can be used as reference to evaluate accuracy of other motion models, as well as to control the accuracy of the satellite observations collected [10]. To evaluate the model accuracy, we chose the following AES from the list of the satellites tracked by the ILRS: Etalon-1, Lageos-2 and Ajisai. The main parameters and physical characteristics of those satellites, available on the ILRS official website, are presented in Table 1.

Those are small-sized passive spherical in shape AES. As they move at different altitudes, the evaluation of the model with those satellites will enable to qualitatively assess the accuracy and amplitude of perturbations affecting AES.

According to the description of the ILRS files of the AES coordinate database, each file contains the ITRF coordinates with constant time increment. The inference step for coordinates in a file depends on a satellite as such it can be from several minutes to tens of seconds. Residuals of computed positions were determined by the method of numerical integration of motion equations (1) from the model with reference to the ILRS coordinates. The satellite coordinates and velocity components for initial conditions were determined by the Lagrange interpolation method through 12 points.

The differences between the coordinates obtained and those in the database can define quality of the developed motion model. The obtained absolute values of residuals (O-C) in altitude and computed angular geocentric residuals (O-C) at the end of the intervals of integration are given in Tables 2-4.

Table 1. Orbital parameters of the selected AES

	Diameter, m	Mass, kg	P, min	i , degrees	e	Perigee, km
Etalon-1	1.294 M	1415	676	64.9	0.00061	19120
Lageos-2	0.6 M	405.38	223	52.64	0.0135	5620
Ajisai (EGS)	2.15 M	685	116	50.0	0.001	1490

Table 2. The (O-C) prediction dynamics for Etalon-1

	6 months	9 months	12 months
Δr [m]	1239	1776	2223
$\Delta \alpha$ ["]	-6.13 \pm 2.99	-8.72 \pm 3.66	-10.86 \pm 3.65
$\Delta \delta$ ["]	-0.05 \pm 7.76	-1.74 \pm 11.08	+0.45 \pm 13.85

Table 3. The (O-C) prediction dynamics for Lageos-2

	6 months	9 months	12 months
Δr [m]	442	1064	2544
$\Delta \alpha$ ["]	-7.02 \pm 1.18	-10.34 \pm 4.36	-28.72 \pm 8.33
$\Delta \delta$ ["]	+1.04 \pm 2.48	-0.45 \pm 14.16	+0.7 \pm 31.12

Table 4. The (O-C) prediction dynamics for Ajisai (EGS)

	10 days	20 days	30 days	40 days
Δr [m]	79	437	1065	2011
$\Delta \alpha$ ["]	-0.76 \pm 1.13	-8.43 \pm 2.55	-21.18 \pm 4.81	-40.04 \pm 8.31
$\Delta \delta$ ["]	+0.54 \pm 1.71	+0.46 \pm 7.62	-0.42 \pm 17.84	-1.57 \pm 33.52

The mean value of residual O-C in angles for an interval of integration is given in the first part of the above tables, and the largest biases from that mean value are presented in the tables' second part. Thus, it can be seen that the mean value of residual and the bias values gradually increase with time. However, the residual values allow of pointing to the fact that the developed model enables to obtain retrieval ephemerides of a rather high quality online. Such accuracy in computation of the year ephemeris of the AES at altitude above that of Lageos-2 can be sufficient with the telescope field of view of about 0.5° .

Conclusions

The results show that the prediction accuracy provided by suggested simplified numerical model of the AES motion is quite applicable to plot retrieval one-year ephemerides for satellites at altitude above 1,500 km.

To improve the AES ephemeris accuracy in the motion model, it is necessary to account for weaker perturbations. At present, work is underway on modification of the motion model and accounting for the following perturbations:

- atmospheric braking of the AES with orbit of altitude up to 1000 km;
- usage of the Earth's shadow model of more complex shape when computing perturbations due to the solar radiation pressure;
- accounting for perturbations due to the ocean and atmospheric tidal bulges;
- accounting for perturbations caused by other planets.

The obtained simplified motion model with time intervals of several weeks can be used to search for close approaches of objects. But the model accuracy is not

sufficient to do that for the AES with orbit altitude lower than that of Lageos-2. Therefore, the obtained numerical model can be used to search for approaches of the high-orbit AES and geosynchronous objects only. As the geostationary region population has been increasing from year to year, provision of safety of motion of the satellites in operation demands a mechanism for online searching and tracking of space debris, as well as for predicting close approaches of objects.

References

- Aksenov E.P. *Theory of motion of artificial Earth satellites*. Moscow: Nauka, 1977, 360 p.
- Bazey A.A., Kara I.V.: 2009, *Herald of astronomical school, Kherson*, p. 155-157.
- Bordovitsyna T.V., Avdyushev V.: 2007, *Theory of motion of artificial Earth satellites*, the Tomsk State University publishing house, p. 175.
- Brumberg V.A.. *Analytical algorithms of celestial mechanics*. Moscow: Nauka, 1980, 208 p.
- Reference Guide on Celestial Mechanics and Astrodynamics* // ed. of G. N. Duboshin, Moscow: Nauka, 1971, 862 p.
- Kholshevnikov K.V., Pitiev N.V., Titov V.B.: 2005, *Attraction of celestial bodies*, the St. Petersburg University publishing house, p. 104.
- IERS Conventions, 2003 – IERS Technical Note № 32 // U.S. Naval Observatory, 2004.
- Everhart E.: 1974, *Celest. Mech.*, **10**, p. 35-55.
- Standish E.M. *JPL Planetary and Lunar Ephemerides, DE405/LE405*. Jet Propulsion Laboratory, Interoffice Memorandum, IOM 312.F-98-048, August 26, 1998.
- Kara I.V.: 2010, *Odessa Astron. Publ.*, **22**, p. 20-24.

OBSERVATIONS OF APOPHIS IN NSFCTC (YEVPATORIA) AND RI NAO (MYKOLAIV)

A.M.Kozhukhov¹, N.V.Maigurova², A.V.Pomazan², V.F.Kryuchkovskiy²

¹National Space Facilities Control and Test Center, Yevpatoria, Ukraine

²Research Institute "Nikolaev Astronomical Observatory", Mykolaiv, Ukraine

ABSTRACT. The results of observations of potentially hazardous asteroid Apophis, performed in January-February 2013 are presented. Technical characteristics of equipment and method of observation are described. The results are shown in comparison with the observations of this object by other observatories.

Introduction

History of the discovery and the first observations. The asteroid was discovered at the Kitt Peak Observatory on June 19, 2004 and received preliminary designation 2004 MN4. The analysis of the orbit calculated from the results of the first observations has found out that this object has a relatively high (2.7%) probability of collision with the Earth at close approach in April 2029. This is the highest value for all known asteroids.

New optical observations and radar measurements with the Arecibo radio telescope in 2005 have greatly clarified the parameters of orbit. New orbit has shown significant decrease in the collision probability with the Earth. Precision of the orbit was sufficient to assign this object of numbered value 99942 and own name Apophis.

The problem of "keyhole". Refined estimates of the orbit have shown that the asteroid will pass at a distance of about 37,000 km from the Earth's surface in 2029 (Chodas, 2005). The uncertainties of the orbital parameters allowed us only approximately determine the areas the closest approach of Apophis. The probability of collision with Earth in 2036 may be increase due to gravitational interaction when asteroid will pass through certain points within calculated area of closest approach in April 2029. This problem is called "keyhole" (see, e.g., Chesley et al., 2006). There are many work (Bancelin et al., 2012; Chesley et al., 2006; Farnocchia et al., 2013; Giorgini et al., 2008; Ivashkin et al., 2007; Królikowska et al., 2009; Włodarczyk, 2008; Zabolin et al., 2009) devoted to estimating of the uncertainties of the orbital parameters and modeling possible orbit of Apophis after its close approach.

Due to the nature of the orbital motion, Apophis can be observed from the Earth only in limited periods of time, usually during the close approaches (Chesley et al., 2006). Apophis was available for both optical and radar observations during the close approach in the winter 2012-2013 year. This was of particular importance to improving the accuracy determination of the orbital parameters of the

asteroid (Giorgini et al., 2008) and the main reason for carrying out the international campaign of Apophis observations by GAIA-FUN-SSO group.

RI NAO and NSFCTC have made observations of the Apophis as members of the GAIA-FUN-SSO group, as part of the observation campaign announced by coordinators of the network.

Equipment and methods of observations

Telescope Mobitel (RI NAO). The telescope Mobitel (D=0.5 m, F=3.0 m) has begun regular observations of selected asteroids and NEO objects since 2011 (Ivantsov et al., 2012). The CCD camera Alta U9000 (3056x3056 pix, 12x12 mkm²) of Apogee Imaging Systems allows us to get frames with 42.0'x42.0' field of view with 0.83"/pix of scale. The observations were carried out in time delay and integration mode with time of exposure 85 seconds using R filter close to R photometric band of Johnson-Cousins-Bessel system. The astrometric reductions of observations were made using Astrometrica software. Model of linkage of 4th order polynomial between measured and tangential CCD coordinates was chosen. The UCAC4 (Zacharias et al., 2013) catalog was used as reference catalog for processing of all data.

Telescope AZT-8 (NSFCTC). The modified telescope AZT-8 (D=0.7 m, F=2.8 m) have made Apophis observations in NSFCTC (Yevpatoria). The telescope is also equipped with CCD camera FLI PL09000 (3056x3056 pix, 12x12 mkm²) and filter R (based on the color glass OG-12). The camera was used in binning mode so the actual size of the images was 1528x1528 pix, pixel size – 24x24 mkm². Telescope field of view with this camera was 44.0'x44.0'. Time synchronization of camera work was carried out with GPS Trimble Resolution-T.

The observations of Apophis were carried out in the frame mode only when zenith distance according calculated ephemeris was less than 70 degrees for reducing the effect of refraction. Exposure time was chosen depending on the rate of apparent motion for obtaining maximal SNR for point source. The time of exposures ranged from 30 to 90 seconds.

The observations were processed with Astrometrica software. Catalogs UCAC3 (Zacharias et al., 2010) and UCAC4 were used as the reference catalog. The model of cubic polynomial was chosen as the linkage model between measured and tangential CCD-coordinates.

Table 1: Results of observations of the Apophis in RI NAO (according MPC and NeoDys centers)

Date	Number	(O-C)_RA, arcsec	RMS_RA, arcsec	(O-C)_DEC, arcsec	RMS_DEC, arcsec
24/ 01*	26	0.09	0.12	-0.43	0.21
05/ 02	29	0.02	0.11	-0.04	0.15
12/ 02	24	-0.03	0.07	-0.02	0.07
13/ 02	29	-0.04	0.08	-0.02	0.11
26/ 02*	30	0.17	0.10	0.06	0.12

* Results were obtained combined method (Shulga et al., 2007): Shulga O.V.; Sybiryakova Y.; Kozyryev Y.; Kulichenko N.; Vovk V.

Table 2: Results of observations of the Apophis in NSFCTC (according MPC and NeoDys centers)

Date	Number	(O-C)_RA, arcsec	RMS_RA, arcsec	O-C_DEC, arcsec	RMS_DEC, arcsec
22/ 01	21	0.09	0.11	-0.26	0.06
24/ 01	15	0.2	0.17	0.2	0.11
30/ 01	17	0.14	0.18	0.03	0.16
05/ 02	7	0.14	0.14	0.02	0.13
06/ 02	6	0.17	0.13	0.06	0.12
08/ 02	3	0.46	0.23	0.06	0.02
12/ 02	14	0.23	0.20	-0.1	0.20

Table 3: Top 15 observatories on results of Apophis observations (December 2012 – May 2013).

MPC Cod, Observatory	Frame number	Date number	(O-C)_RA, arcsec	RMS_RA, arcsec	(O-C)_DEC, arcsec	RMS_DEC, arcsec	Catalog
D20, Zadko Observatory, Wallingup Plain	391	14	0.05	0.10	-0.03	0.10	PPMXL, UCAC-3
071, NAO Rozhen, Smolyan	379	10	0,04	0,54	-0.03	0.31	USNO-B1.0
C40, AO Kuban State University	253	10	-0.09	0.30	0.07	0.24	UCAC-2
C20, Kislovodsk Mtn. Pulkovo Obs.	244	3	0.02	0.11	0.02	0.13	UCAC-4
A84, NO TUBITAK	241	2	-0.34	0.18	0.07	0.15	UCAC-2
H45, Arkansas Sky Obs.	125	19	0.06	0.23	-0.04	0.20	UCAC-4
B17, AZT-8 Evpatoria	83	7	0.20	0.17	0.00	0.11	UCAC-3, 4
089 1, Nikolaev	82	3	0,00	0,09	-0.03	0.12	UCAC-4
188, Majdanak	58	2	-0.02	0.17	0.05	0.09	-
089 2, Nikolaev	56	2	0.04	0.13	-0.17	0.30	UCAC-3
300, BiseiSpaceguard Center-BATTeRS	53	4	0.15	0.31	-0.15	0.20	USNO-B1.0
H21, AO Westfield	49	5	0.03	0.17	0.01	0.14	UCAC-3
F65, Haleakala-Faulkes Telescope North	48	13	0.00	0.16	0.01	0.11	PPMXL
585, Kiev comet station	33	2	0.00	0.18	0.05	0.16	UCAC-3
I47, Pierre Auger Observatory, Malargüe	32		0.10	0.09	-0.05	0.11	UCAC-3
168, Kourovskaya	30	2	-0,16	0,38	0.16	0.48	UCAC-2

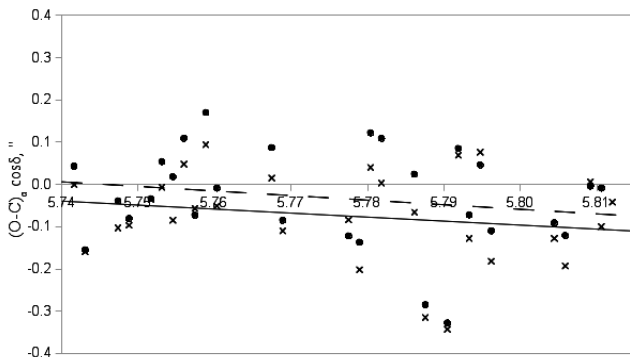


Fig. 1. The distribution of differences (O-C) in right ascension at February 5, 2013 (Mobitel, RI NAO). Points (dotted line) correspond to the positions of new ephemerid; crosses (solid line) correspond to the positions of ephemerid without observations were made in February and later.

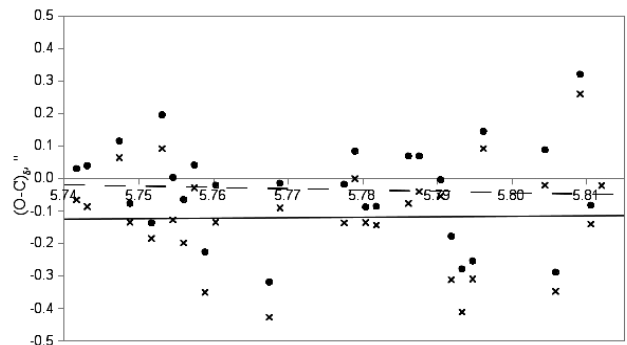


Fig. 2. The distribution of differences (O-C) in declination at February 5, 2013 (Mobitel, RI NAO). Points (dotted line) correspond to the positions of new ephemerid; crosses (solid line) correspond to the positions of ephemerid without observations were made in February and later.

Results of observations

138 astrometric positions of Apophis were obtained by two groups of observers from RI NAO for 5 nights in January-February 2013 in total. For the same period 83 positions was obtained for 7 nights in NSFCTC. Detailed results of observations according of the NeoDys data are presented in Table 1 (RI NAO) and 2 (NSFCTC). Unfortunately, the bad weather conditions are typical for this season and that is not allowed to get more observations.

The observations of Apophis were performed by 66 observatories during this period, but the 15 most productive observatories got around 80% of all positions. The Table 3 are shown the place RI NAO and NSFCTC among other observatories where observations of Apophis were performed. Underlined lines are names of observatories-members of GAIA-FUN-SSO, bold – results obtained by NSFCTC and RI NAO. Database of MPC contains 4,131 optical positions of asteroid Apophis received from 128 observatories for observations between March 15, 2004 and May 27, 2013. The 2,607 (63.1%) positions of the total number were received during last close approach with Earth (end 2012 – beginning 2013). The 63.6% (1,657) observations of the total were obtained by observatories which are member of GAIA-FUN SSO (MPC codes: 071, 089, 188, 300, 585, A84, B04, B17, C01, C20, D20).

Statistics for the 15 most productive observatories is presented in table 3. It should be noted that most productive observatories for observation of Apophis are members of the GAIA-FUN SSO. The Table 3 is given the values of (O-C) differences, where O means observed position, C – ephemeris position. It should be noted, that C values were calculated taking into account these observations. The Table 3 also contains root mean square (RMS) errors of (O-C) values as a measure of the accuracy of positions. The RMS value includes not only the measurement accuracy but the accuracy of the reference catalog because data for different dates were averaged. Data of the table shows that NSFCTC and RI NAO are quite well in comparison with other observatories. For the telescope AZT-8 RMS errors are less than 0.17" in right ascension and 0.11" in declination, for the telescope Mobitel – nearly 0.11" in both coordinates.

An analysis of the values (O-C) revealed a gradual decrease of these differences with respect to the HORIZONS ephemeris of JPL. The Fig. 1 and Fig. 2 show distribution of (O-C) differences for observations in RI NAO at February 5, 2013. Points and dotted line (trend) corresponds to (O-C) were calculated with new ephemerid which are included all observed positions during close approach in 2012-2013. Crosses and solid line (trend) corresponds to (O-C) were calculated with old ephemerid. As can be see, the values of the (O-C) differences for new ephemerid are closer to zero. This indicates that the using of the new high-precision positions allows us to refine the calculated ephemeris. According to NASA calculations, the new orbit of Apophis, calculated with using the results of observational campaign 2012–2013 yr., practically excludes the possibility of the asteroid collision with Earth in 2036.

Conclusions

The organization of special campaign of ground observations provides a sufficient number of observations for qualitative refinement of the orbits in a relatively short period of time.

It is shown, that even small telescopes with a diameter of less than 1m equipped with modern CCD cameras, can be used for observations of such NEO objects with using of high-precision catalogs for astrometric reductions.

References

- Bancelin D., Colas F., Thuillot W. et al.: 2012, *A&A*, **544**, A15.
- Chesley S.R. et al.: 2006, *Asteroids, Comets, Meteors, Proc. of IAU Symposium №229*, Rio de Janeiro, Brazil, eds.: Daniela L., Sylvio Ferraz M., Angel F. Julio, Cambridge University Press, 215.
- Chodas P.: 2005, *Radar Observations Refine the Future Motion of Asteroid 2004 MN4*, <http://neo.jpl.nasa.gov/news/news149.html>.
- Farnocchia D., Chesley S.R., Chodas P.W. et al.: 2013, *Icarus*, **224**, №1, 192.
- Giorgini J.D., Benner L.A.M., Ostro S.J.: 2008, *Icarus*, **193**, №1, 1.
- Ivantsov A., Pomazan A., Kryuchkovskiy V., Gudkova L.: 2012, *Odessa Astron. Publ.*, **25**, №1, 66.
- Ivashkin V.V., Stikhno C.A.: 2007, Planetary Defense Conference, March 5-8, Cloyd Heck Marvin Center, George Washington University, Washington, D.C., USA.
- Królikowska M., Sitarski G., Sołtan A.M.: 2009, *MNRAS*, **399**, №4, 1964-1976.
- Shulga O., Kozyryev Y., Sibiryakova Y.: 2007, *Proc. of IAU Symposium №248*, Shanghai, China, 128.
- Włodarczyk I.: 2008, *Contributions of the Astronomical Observatory Skalnaté Pleso*, **38**, №1, 21.
- Zabotin A. S., Medvedev Yu. D.: 2009, *Astron. Lett.*, **35**, №4, 278.
- Zacharias N., Finch C.T., Girard T.M. et al.: 2010, *AJ*, **139**, №6, 2184.
- Zacharias N., Finch C.T., Girard T.M.: 2013, *AJ*, **145**, №2, article id. 44, 14.
- Astrometrica, <http://www.astrometrica.at>.
- IAU Minor Planet Center. (99942) Apophis = 2004 MN4, http://www.minorplanetcenter.net/db_search/show_object?utf8=%E2%9C%93&object_id=Apophis
- NASA Rules Out Earth Impact in 2036 for Asteroid Apophis, <http://www.jpl.nasa.gov/asteroidwatch/news-features.cfm?release=2013-017>.
- NEODyS: Near Earth Objects - Dynamic Site, <http://newton.dm.unipi.it/neodys/index.php?pc=1.1.7.1&n=99942&ab=0>.
- The GAIA-FUN-SSO Collaborative space, <https://www.imcce.fr/gaia-fun-ss0/start>.

HOMOGENIZED EFFECTIVE TEMPERATURES FOR THE OPEN CLUSTER NGC 188

V. Malyuto¹, S. Zubarev²

¹ Tartu Observatory,
Tartu, Estonia, *valeri@aai.ee*

² Ural Federal University,
Yekaterinburg, Russia, *sergey.cl@gmail.com*

Key words: stars: fundamental parameters; -
Galaxy: open clusters and associations: individual
(NGC188)

We have analysed the most numerous published independent stellar catalogues of $B - V$ and V values for the open cluster NGC 188. Our analysis started with the reduction of unreddened $(B - V)_0$ indices and V_0 magnitudes from four catalogues to the system of the catalogue of Platais et al. (2003) considered as a basic catalogue. As a next step in our analysis, the reduced $(B - V)_0$ and V_0 magnitudes for the catalogues were used to calculate the variances of data differences for every pair of the catalogues for the stars in common. Then we estimated the errors of these catalogues from data intercomparisons with the technique outlined in Malyuto and Shvelidze (2011).

Then we homogenized the data by their averaging (with the weights inversely proportional to the errors squared). A recent calibration by Casagrande et al. (2010) with the $B - V$ versus effective temperatures for F-G-K dwarfs and subgiants was used to produce the homogenized effective temperatures for 227 stars. The errors of T_{eff} are between 7 and 20 K, they do not account for the uncertainty in the zero point of the temperature scale, which is of order 15 – 20 K (Casagrande et al., 2010).

The published distance modulus $V_0 - M_V = 11.24$ for NGC 188 was taken from Meibom et al. (2009) to derive the absolute magnitudes M_V from the homogenized magnitudes V_0 . The homogenized HR diagram (the relationship between the effective temperatures and the absolute magnitudes) is presented in Fig. 1. The homogenized data may be considered as a source of reliable and homogeneous T_{eff} and M_V values for selected stars for using them as classification templates in future large galactic surveys. The obtained results may be compared with the model results based on the Padova database of stellar evolutionary tracks and isochrones.

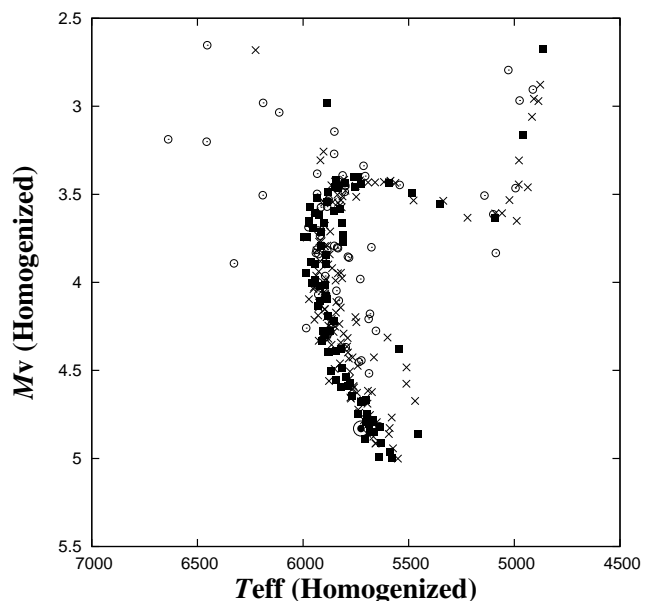


Figure 1: Homogenized HR diagram for NGC 188. Filled squares denote the most precise data with the errors of T_{eff} better 10 K, crosses denote the remaining (less precise) data, open circles denote the stars identified as binaries in the WEBDA site. The position of the Sun is denoted with the filled circle inside the larger open circle. The HRD displays a well-defined main sequence, cluster turnoff and subgiant branch, a population of blue stragglers is also clear.

References

- Casagrande, L., Ramirez, I., Melendez, et al.: 2010, *Astron. Astroph.*, **512**, 54.
 Malyuto, V., Schvelidze, T.: 2011, *Baltic Astronomy*, **20**, 91.
 Meibom, S., Frank Grundahl, F., Clausen, J.V., et al.: 2009, *AJ*, **137**, 5086.
 Platais I., Kozhurina-Platais V., Girard T.M., et al.: 2003, *AJ*, **118**, 2894.

OPEN CLUSTERS AND FIELD CEPHEIDS IN THE GALACTIC DISK – CONTRADICTIONS IN PROPERTIES

V.A. Marsakov¹, B.B. Koval¹, M.L. Gozha¹, B.B. Kovtyukh², T.V. Mishenina²

¹ Southern Federal University, Rostov-on-Don, Russia

² Astronomical Observatory of Odessa National University, Odessa, Ukraine

ABSTRACT. The comparative analysis of the abundances of α -process elements, elements of the rapid and the slow neutron capture and iron in the open stellar clusters, field Cepheids, and also in red giants and dwarfs of the thin disk has been performed. The found distinctions and the revealed regularities are attracted for clarification of the history of star formation in the thin disk of the Galaxy.

Key words: cepheids, open clusters, galactic disk

Introduction

Both classical Cepheids and the open stellar clusters are typical representatives of the thin galactic disk, therefore the chemical composition of the atmospheres of these objects can be used for the analysis of stages of formation and evolution of this subsystem. This is due to the difference of times of entering of chemical elements produced in the various processes of nuclear synthesis in previous generations of stars into the interstellar medium, out of which more young Cepheids and open clusters were later formed. To now sufficient amount of precision astrometric and spectroscopic data are collected to make statistical comparison of chemical properties of classical Cepheids and open clusters in our Galaxy for the testing of degree of homogeneity of these populations.

Initial data

We have restricted the use of the abundances of only those chemical elements which, according to modern views, have almost no changes related to the nuclear processes in the atmospheres of the studied stars. In particular such elements are α -elements (O, Mg, Si, and Ca), iron-peak elements (Fe), elements of the slow (Ba, La, and Ce) and of the rapid neutron capture (Eu) (see rationale for choosing below). We have used homogeneous data on the abundances for 221 Cepheids from the papers of one group of authors (see Andrievsky et al., 2013 and references therein to earlier papers). http://www.multitrans.ru/c/m.exe?a=110&t=3501211_2_1&sc=41 Determination accuracy of the abundances for the elements having more than 10 lines (e.g., iron) reaches 0.05-0.10 dex, whereas the error increase to 0.15-0.20 dex in case of five lines or less. We calculated the ages of these stars from the formula

$\log t = 8.50 - 0.65 \log P$, where t is the age in years, and P is the Cepheid period in days (Efremov, 2003).

The abundances of the listed chemical elements in 77 open clusters were taken from 72 papers published between 1994 and 2013. The most probable number of the measured stars in the cluster is equal to four, whereas the abundances received by one star and in one paper are defined only for four clusters. We averaged data from different sources in inverse proportion to the declared errors. External convergences of the relative abundances of all elements range within $\sigma_{[el/Fe]} = 0.08-0.15$ dex.

For comparison, we have involved data on the abundances of the same elements in 212 dwarfs and in 171 ascending-branch giants and the clump-giants which are close to the evolutionary status of Cepheids received by group of authors, using a similar technique (Mishenina et al., 2006; 2007; 2013). The errors in determining the abundances of all the elements in these stars do not exceed 0.15 dex. The uniformity of approaches to determining the abundances of chemical elements in the Cepheids, dwarfs and giants is provided by using everywhere the unified system of solar oscillator strengths, the uniform list of spectral lines and the uniform grid of the atmospheric models of Kurucz.

Dependences of the relative abundances of the various chemical elements on metallicity

According to modern views, the basic processes of nuclear synthesis, which produced isotopes of all chemical elements, take place in stars of a certain masses. In particular, the bulk of α -elements are synthesized in the interiors of massive ($M > 10M_{\odot}$) stars in the late stages of their evolution and are ejected into the interstellar medium as a result of outbursts as Type II supernovae. At that only oxygen and magnesium are produced exclusively in these stars, while the others α -elements can be synthesized in SNe Ia in small amounts. At the same time, for dwarfs of the disk, the relative abundances of two more α -elements, silicon and calcium, change with increasing metallicity like oxygen and magnesium, i.e. the contribution to their abundance from SNe Ia is insignificant (Mishenina et al., 2013). The abundances of these elements are practically unchanged in the atmospheres of stars in advanced stages of evolution too, that is, in the red giants and the red clump-

giants, in which the helium is burning in core (see Mishenina et al., 2006). The abundances in the atmospheres of Cepheids also don't undergo significant changes (Kovtyukh et al., 2005). We have used the abundances only four α -elements, namely O, Mg, Si and Ca, to study.

It is believed that the synthesis of the bulk of atoms of rapid neutron capture elements takes place directly during outbursts of SNe II with the masses $8 < M/M_{\odot} < 10$. When SNe II explode, some of the atoms of iron-peak elements are also formed. The bulk of elements of iron peak are produced in the explosions of SNe Ia which are the final stage of the evolution of close binary stars with masses $< 8M_{\odot}$.

Chemical elements, which produced in the process of nuclear synthesis in stars of different masses, are ejected into the interstellar medium in different time. So time of the evolution of massive stars (SNe II progenitors), enriching the interstellar medium with α -elements, the r-process elements, and a small amount of iron, is not more than about 30 million years, and the mass explosions of supernovae SN Ia, making the major contribution to the enrichment of the interstellar medium with iron group elements, occur $\approx 1-1.5$ Gyr later. Therefore, the relative abundances of $[\alpha/Fe]$ and $[r/Fe]$ in new generations of stars will decrease at increasing metallicity. Slow neutron capture elements are also produced in stars of different masses. The bulk of them at solar metallicity are produced in the atmospheres of asymptotic giant branch (AGB-stars) with masses $M < 4M_{\odot}$ are brought into the interstellar space through the envelope ejection. According to theoretical calculations, peak of the yield is formed near $[Fe/H] \approx -0.2$ and the ratio $[s/Fe]$ decreases at a further increasing metallicity. Some more amount of atoms of the s-process elements are produced at high temperatures in the interiors of massive stars; this is the weak component of s-process. We used three heavy s-process elements, namely Ba, La and Ce, for the analysis.

We analyze dependences of the relative abundances of four α -elements on metallicity. Dispersions of the relative abundances of oxygen and magnesium for Cepheid are substantially greater than for the other types of stars: $\Delta [O/Fe] = -0.08 \pm 0.02$ and $\Delta [Mg/Fe] = -0.07 \pm 0.02$. Both elements exhibit weak tendencies to decrease of the relative abundances with increasing metallicity ($r = 0.14 \pm 0.07$ and 0.20 ± 0.07 respectively, at $P_N < 5\%$). For dwarfs and giants, analogous dependencies are narrower; slopes are larger; and correlations are much more significant. The relative abundances of silicon and calcium in Cepheids steadily decrease with a small spread at increasing metallicity in the same way as the other two types of stars ($r = 0.4 \pm 0.1$ and 0.3 ± 0.1 respectively, at $P_N \ll 1\%$). But as well as for two previous α -elements, both relations lie on $\Delta [Si/Fe] = -0.06 \pm 0.01$ and $\Delta [Ca/Fe] = -0.07 \pm 0.01$ lower than those for giants. To compensate for slightly possible systematic deviations in determinations of the abundances for each element, further we will investigate the behavior of the average abundances of all four α -elements.

Dependences of the abundances of three heavy s-elements, viz. Ba, La and Ce, on the metallicity were investigated as well. The slopes of dependences of $[Ba/Fe]$ on $[Fe/H]$ within the error limits for Cepheids and other stars are the same, but the sequence of Cepheids lies up by $\Delta [Ba/Fe] = +0.12 \pm 0.02$. The values of the relative abundances of these s-elements also decrease at increasing

$[Fe/H]$ (in both cases, $P_N \ll 1\%$). In this case, both elements also show increased abundances in comparison with giants and dwarfs. Moreover, for Cepheids and the giants, the slopes of the dependences of $[La/Fe]$ on $[Fe/H]$ within the errors are the same, and the overabundance for Cepheids is very large ($\Delta [La/Fe] = +0.35 \pm 0.02$). The slope of the dependence of cerium abundance outside the error limits for Cepheids is larger, than for giants; and the overabundance is smaller than for the previous two s-elements on $\Delta [Ce/Fe] = +0.07 \pm 0.02$. For dwarfs, the slopes for all elements even in a limited range of metallicity differ only slightly from zero. Thus, regardless of the method used, the relative abundances of each s-process element in Cepheids always turn out to be enhanced. As all listed elements of slow neutron capture behave in Cepheids in approximately the same way relative to the giants, further we will use the average value for all three heavy elements of s-process.

Despite the difference in methods, the slopes of the dependences $\langle [Eu/Fe] - [Fe/H] \rangle$ for all three types of stars are practically the same, exhibiting, on the average, a shift ($\Delta [Eu/Fe] \approx +0.05 \pm 0.01$) in the direction of greater relative abundance in Cepheids in comparison with giants. Thus, the relative abundances of all investigated α -elements in Cepheids show in a varying degrees lower ratios of $[\alpha/Fe]$, than those in other field stars (including the Sun). Instead, the relative abundances of all studied elements of s- and r-processes in Cepheids turn out to be enhanced compared to field stars. Besides all elements show a decrease of the relative abundances with increasing metallicity.

Connection of relative abundances of chemical elements of different processes

The first three panels in Fig. 1 shows the dependence of the relative abundances of the α -elements, rapid and slow neutron capture elements on the metallicity for open clusters, Cepheids, giants and dwarfs. At first we have made the comparative analysis of the behavior of Cepheids versus field stars. For each star, the errors of different signs in the determinations of the abundances of elements produced in a single process are compensated a little at such averaging. As can be seen, the relative abundances of the elements produced in α - and r-processes decrease approximately identically for all objects with increasing metallicity. Besides the sequences for dwarfs and giants are practically the same, while the sequence of α -elements for Cepheids lies outside the 3σ limits lower ($\Delta [\alpha/Fe] = -0.07 \pm 0.01$), than for giants and dwarfs, and the sequence of r-process element lies outside the error limits higher ($\Delta [Eu/Fe] = +0.03 \pm 0.01$). The slope of the dependence of $[s/Fe]$ on $[Fe/H]$ for Cepheids is about the same as that for giants with the same metallicity (i.e. $[Fe/H] > -0.30$). But at that point Cepheids lie much higher ($\Delta [s/Fe] = +0.19 \pm 0.01$). Note that the nature of the dependence of s-elements and the other two types of elements on metallicity is different. If the yield of s-elements decreases at increasing metallicity of their parent stars, then the relative abundances of α -elements and r-process elements decrease in the next more metal-rich generations of stars due to the later onset of the epoch of mass iron ejections during SNe Ia explosions.

Existence of the correlation between the elements of the s- and r-processes surprises. The fact is that, with the solar metallicity, low-mass ($<4M_{\odot}$) AGB-stars contribute mainly to the enrichment of s-process elements. Some of these stars, being close binaries, subsequently explode as a SN Ia, enriching the interstellar medium with iron.

That is, both processes proceed successively in the same stars, and so the relative number of atoms of the s-process elements ejected by them into the interstellar medium seems to should not to depend on metallicity. The existence of correlations most likely stems from the fact that the yield of the relative amount of s-process elements decreases with increasing metallicity of AGB stars in which atmospheres their formation happens. As a result, as shown in the top panels of Fig. 1, dependences of the relative abundances of the s-elements on metallicity for all stars were very similar to the analogous dependences of the relative abundances of α - and r-elements; the reason for their appearance is related to the sequence of enrichment of the interstellar medium with these elements and iron.

The abundances of chemical elements in open clusters

In Fig. 1 dependences of the relative abundances of chemical elements of all three processes of nuclear synthesis on metallicity in the open clusters are also shown. There are notable differences in the behavior of these elements for all types of objects. So, although the average abundances of α -elements in the clusters and field giants are almost the same, but the slope of dependence for the clusters has practically absent. As a result, the relative abundances of α -elements in the clusters with metallicity less than solar value significantly lower than that for the field giants. For clusters, the slope is also absent in dependence of s-process elements on metallicity. But the sequence of clusters is far higher outside the error limits than for field giants. In Fig. 1c europium in clusters shows a very large spread, although the sequences for all objects are parallel. Unfortunately, in young clusters where there are Cepheids, there are no red giants, and it isn't possible to compare the chemical composition of these stars inside the cluster. The correct comparison is possible only after a detailed analysis of the methods for determining the abundances of chemical elements in the clusters by different authors. Therefore we will try to explain only the behavior of the abundances of chemical elements in field Cepheids.

Discussion

The change of the relative abundances of some chemical elements $[e/Fe]$ with increasing metallicity can be interpreted within the framework of chemical evolution of a stellar-gaseous system only in case if the total abundance of heavy elements in it increases on the average with time, that is, if metallicity is the statistical indicator of age. In a recent paper (Marsakov et al. 2011), we made the complete sample of F-G-dwarfs of the thin disk located within 70 pc of the Sun on the basis of the catalog (Holmberg et al. 2009); we showed in it that the interstellar matter in the thin disk demonstrated really on average approximately the same amount of heavy elements ($<[Fe/H] \approx -0.2$) and a low homogeneity within the first few billion years of the formation of the thin disk.

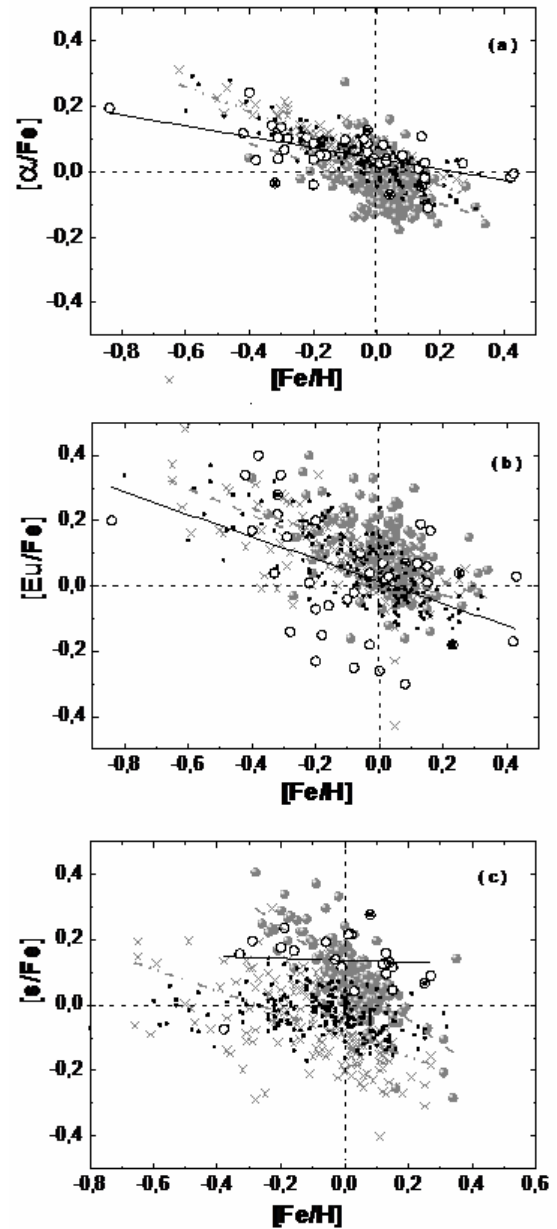


Figure 1: Dependences of the relative abundances of the chemical elements of different processes on the metallicity in open clusters (large open circles), Cepheids (gray filled circles), red giants (gray crosses), and field dwarfs (small dark gray circles). The solid, dashed and dotted inclined lines are the regression for Cepheids, open clusters and giants.

However about 4-5 Gyr ago the mean metallicity began to increase systematically. Therefore it is possible to consider metallicity in the thin disk in the last ~ 5 Gyr as a temporal parameter and to explain observed differences in the relative abundances of α - and r-elements in Cepheids in comparison with other field stars within the framework of chemical evolution of interstellar matter.

The decrease in the relative abundances of the α -elements and r-process elements with metallicity, observed in Fig. 1a,b for Cepheids and field stars, is due to the later ejection of bulk of the iron group atoms into the interstellar medium. As the metallicity in the thin disk is an age indicator and as the

range of ages for the giants and dwarfs are much greater than the evolution time of the progenitors of SN Ia, that such dependences have an evolutionary meaning for these stars. In contrast to dwarfs and giants, Cepheids are very young stars, and dependences of $[\alpha/\text{Fe}]$ on $[\text{Fe}/\text{H}]$ and of $[\text{r}/\text{Fe}]$ on $[\text{Fe}/\text{H}]$ observed for them testify not to their sequential birth, but only to the lack of homogeneity of the chemical composition of the interstellar medium in which star formation took place. From fig. 1a, it can be seen that the correlations are significant, and dependences in both panels are parallel but they are spaced from each other outside the error limits. The parallelism means that all stars were formed from the matter that experienced the same history of enrichment with chemical elements. Apparently, star formation in the past bypassed some regions of interstellar matter, and only then the young stars, which representatives are present Cepheids, were formed out of them. As a result, existence of the dependences for Cepheids testifies to a weak mixing of interstellar matter and "delayed" star formation in some regions, when the stars with different abundances of heavy elements are formed at the same time not far from each other (see also Lepine et al, 2011; Gozha and Marsakov, 2013). Note that stars with ages, typical for Cepheids, are practically absent among our near dwarfs and giants, so a significant gap in ages between the Cepheids and other stars is observed.

Thus, the systematic underabundances of α -elements and overabundances of r -process elements in Cepheids compared to field dwarfs and giants can be explained by the fact that very massive stars stopped to explode as supernovae when the interstellar medium reached about solar metallicity, and as a result the number of atoms of α -elements ejected into the interstellar medium decreased sharply. In view of the fact that high-mass supernovae also produced a significant amount of iron-group elements during their explosions, the $[\text{r}/\text{Fe}]$ ratios increased in the interstellar medium, but the final values of $[\alpha/\text{Fe}]$ nevertheless decreased. Subsequently the Cepheids observed now were formed from this medium. This assumption is supported also by the observational fact, being that all Type II supernovae progenitors investigated in other galaxies do not exceed the maximum of masses ≈ 20 solar masses (see Smartt et al, 2009; Kochanek et al, 2008).

The overabundance of s -process elements in Cepheids can also be explained by the ending of outbursts of massive SNe II, which enriched the interstellar medium also with a significant amount of iron-peak elements except α -elements. But in the atmospheres of massive stars, some amount of the s -elements is also produced in the weak component of the s -process. It is likely that these stars can eject the upper layers of their envelopes even without an explosion like AGB stars, still increasing the relative abundances of the s -elements in the next generation of stars. As a result, the $[\text{s}/\text{Fe}]$ ratios in young stars, Cepheids, could turn out to be enhanced. But the parallelism of dependencies $[\text{s}/\text{Fe}]$ on $[\text{Fe}/\text{H}]$ for the Cepheids and the giants shows that AGB stars, in which $[\text{s}/\text{Fe}]$ ratios in the output depend on their metallicity, remain the main supplier of these elements.

Certainly the expressed assumption can be true only if the discussed distinctions between the relative abundances of various chemical elements in Cepheids, dwarfs and red giants are not due to unrevealed systematic errors in the

determinations of these abundances in Cepheids. Otherwise, it is necessary to reconsider the approach to determining of the chemical element abundances in the evolutionarily advanced stars, namely Cepheids. For testing conclusions of this work, it is desirable to investigate the behavior of the abundances of the same elements in open star clusters, as young as Cepheids.

References

- Andrievsky S.M., Lepine J.R.D., Korotin S.A. et al.: 2013, *Monthly Not. Roy. Astron. Soc.*, **428**, 3252A.
- Berdnikov L.N., Rastorguev A.S., Dambis A.K. et al.: 2003, *A catalogue of data on Galactic Cepheids*, <http://www.sai.msu.su/groups/cluster/CEP/RADVEL/>
- Woolley S.E., Wilson J.R., Mathews G.J. et al.: 1994, *Astrophys. J.*, **433**, 229.
- Gallino R., Arlandini C., Busso M. et al.: 1998, *Astrophys. J.*, **497**, 388.
- Gozha M.L., Borkova T.V., Marsakov V.A.: 2012a, *Astronomy Lett.*, **38**, 506.
- Gozha M.L., Borkova T.V., Marsakov V.A.: 2012b, *Astronomy Lett.*, **38**, 519.
- Gozha M.L., Marsakov V.A.: 2013, *Astronomy Lett.*, **39**, 171.
- Efremov U.N.: 2003, *Astron. Rep.*, **80**, 1086.
- Yoshii Y., Tsujimoto T., Nomoto K.: 1996, *Astrophys. J.*, **462**, 266.
- Kovtyukh V.V., Wallerstein G., Andrievsky S.M.: 2005, *PASP*, **117**, 1173.
- Korotin C.A.: 2009, *Astron. Rep.*, **86**, 702.
- Kochanek C.S., Beacom J.F., Kistler M.D. et al.: 2008, *Astrophys. J.*, **684**, 1336.
- Cristallo S., Straniero O., Gallino R. et al.: 2009, *Astrophys. J.*, **696**, 797.
- Luck R.E., Andrievsky S.M., Kovtyukh V.V. et al.: 2011, *Astron. Astrophys. J.*, **142**, 51.
- Lepine J.R.D., Cruz P., Scariano S. et al.: 2011, *Mont. Not. Roy. Astron. Soc.*, **417**, 698.
- Marsakov V.A., Koval' V.V., Borkova T.V. et al.: 2011, *Astron. Rep.*, **88**, 726.
- Matteucci F., Greggio I.: 1986, *Astron. Astrophys.*, **154**, 279.
- Mishenina T.V., Pignatary M., Korotin S.A. et al.: 2013, *Astron. & Astrophys.*, **552A**, 128M.
- Mishenina T.V., Bienayme O., Gorbaneva T.I. et al.: 2006, *Astron. & Astrophys.*, **456**, 1109.
- Mishenina T.V., Gorbaneva T.I., Bienayme O. et al.: 2007, *Astron. Rep.*, **84**, 1.
- Pignatary M., Gallini R., Hell M. et al.: 2010, *Astrophys. J.*, **710**, 1557.
- Serminato A., Gallino R., Travaglio C. et al.: 2009, *PASA*, **6**, 153.
- Smartt S.J., Eldridge J.J., Crockett R.M., Maund J.R.: 2009, *Mont. Not. Roy. Astron. Soc.*, **395**, 1409.
- Thielemann F.-K., Arcones A., Kappeli R. et al.: 2011, *Progress in Particle and Nuclear Physics*, **66**, 346.
- Thielemann F.-K., Nomoto K., Yokoi K.: 1986, *Astron. & Astrophys.* **158**, 17.
- Timmes F.X., Woolley S.E., Weaver T.A.: 1995, *Astrophys. J. S.*, **98**, 617.
- Travaglio C., Galli D., Gallino R., et al.: 1999, *Astrophys. J.*, **521**, 691.
- Travaglio C., Gallino R., Arnone E. et al.: 2004, *Astrophys. J.*, **601**, 864.
- Holmberg J., Nordstrom B., Andersen J.: 2009, *Astron. & Astrophys.*, **501**, 941.

T CEP, U UMI, Z SCO – MIRA-TYPE VARIABLES WITH CYCLIC PERIOD CHANGES

V.I. Marsakova

Department of Astronomy, Odessa National University
Shevchenko Park, 65014, Odessa, Ukraine
vmarsakova@mail.ru

ABSTRACT. Period and amplitude changes of three Mira-type variables have been analyzed. Characteristics of long-term cyclicality were obtained.

Key words: Stars: LPVs, Mira-type, period changes, individual: T Cep, U UMi, Z Sco.

Introduction. Many Mira-type variables show period changes. They may be small cycle-to-cycle scatter or significant secular or irregular variations. Zijlstra & Bedding (2002) mark out continuously changing periods; sudden changes and meandering Miras (their periods change from one value to another and then backwards). Some representatives of the last group have smooth nearby cyclic variations with cycle length about 20000 days. Three of them are discussed in this paper. They listed in the table 1 with range of period changes (obtained by individual cycle length) and spectral classes. Some results concerning T Cep was presented in Marsakova & Andronov (2000).

Table 1

Variable	P, days	Sp. class (Samus et al., 2012)
T Cep	381-410	M5.5e-M8.8e
U UMi	300-350	M6e-M8e
Z Sco	315-380	M5.5e:-M7e

Analysis. We have analyzed light curves of these stars obtained by amateur astronomers from the AFOEV and AAVSO databases of visual observations. Our analysis process was described by Andronov & Marsakova (2006). "Running parabola" Andronov (1997) fit has been used to determine parameters of the extrema. Some details of methods have been discussed by Andronov (2005). For each extremum, the following parameters were obtained: the deviation of the moment of extremum from a linear ephemeris *O-C*, amplitudes and mean brightness for both (ascending and descending) branches, individual cycle length using successive maxima and (alternatively) minima. The range of period changes (noted in Table 1) was obtained using successive maxima. The minima show bigger range of changes and sometimes bigger amplitude

at the *O-C* diagrams (Fig 2, 5, 6). Variations of the parameters are shown in Fig 2-4 for T Cep, as the example. Variation of amplitude and mean brightness of U UMi and Z Sco are similar, but with smaller quantity of data points (the periods are close to 1 year, so the same parts of light curves are poorly observed). Mean light curves of T Cep for three seasons are shown in Fig 1. They have been obtained using a trigonometric polynomial fit. Characteristics of these approximations are listed in Table 2.

Then we have applied the periodogram analysis of *O-C* (for maxima and minima), individual amplitudes and mean brightness, taking into account the linear trend using program MCV (Andronov & Baklanov (2004)). Most statistically significant periods, which correspond to highest peaks, are listed in Table 3. The peaks are listed, if the corresponding values of the test-function exceed a limiting value of 0.1. Corresponding periodograms are shown at the Figures 7-9.

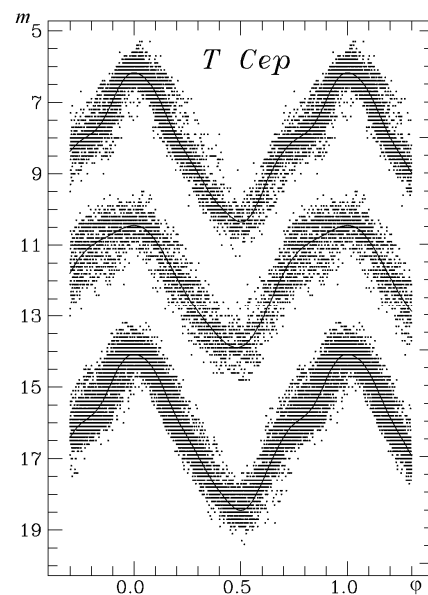


Fig.1. Phase light curves of T Cep during 3 seasons and statistically optimal trigonometric polynomial fits.

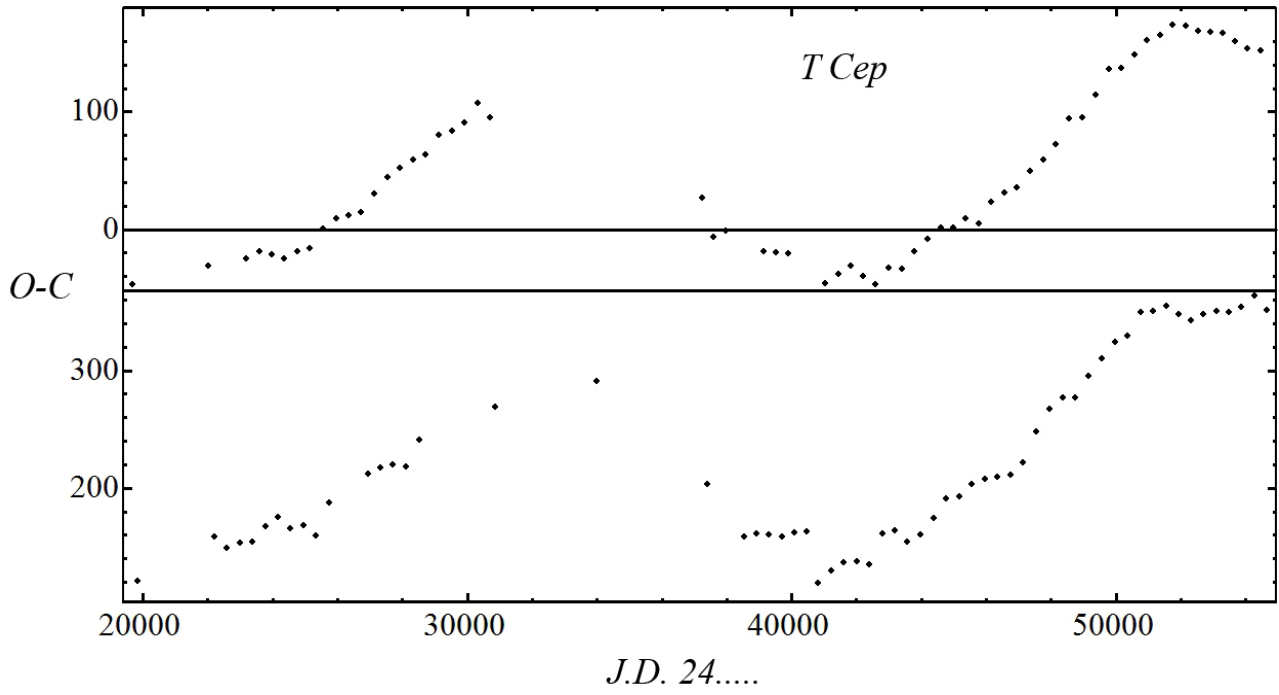


Fig. 2. O-C curves for T Cep. Top curve is O-C obtained for maxima, bottom one is O-C obtained for minima.

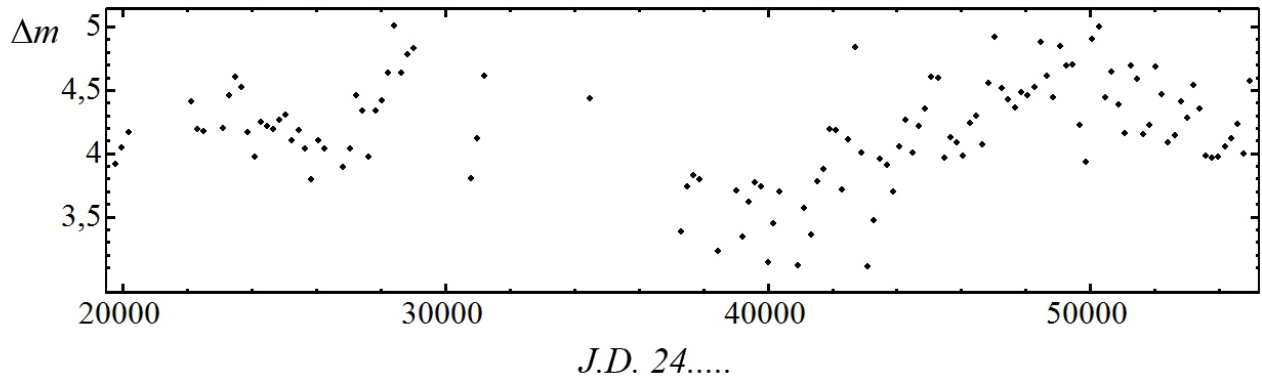


Fig. 3. Amplitude variations for T Cep.

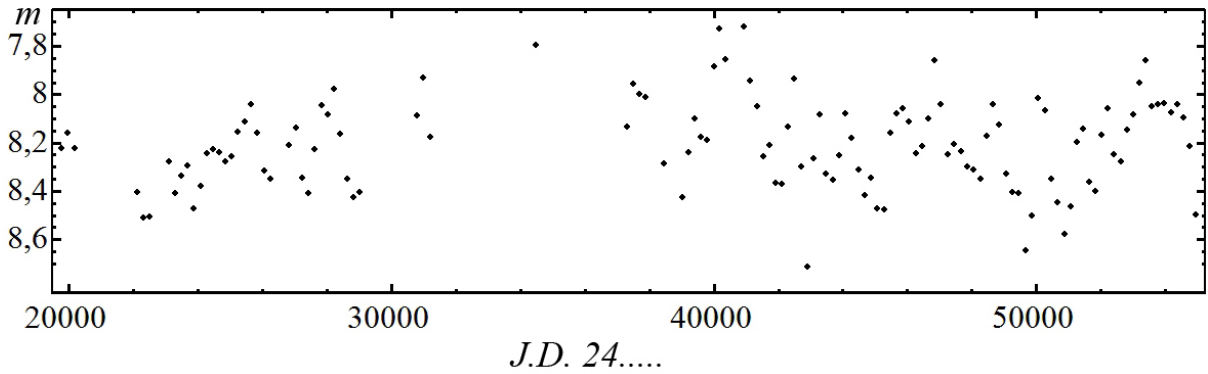


Fig. 4. Mean brightness variations for T Cep.

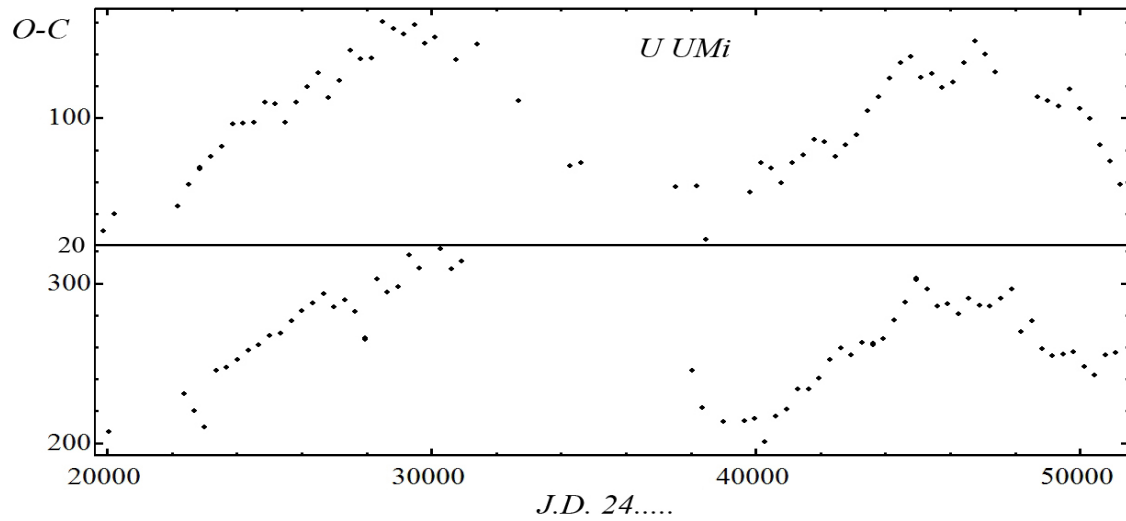


Fig. 5. O-C curves for U UMi. Top curve is O-C obtained for maxima, the bottom one is O-C obtained for minima.

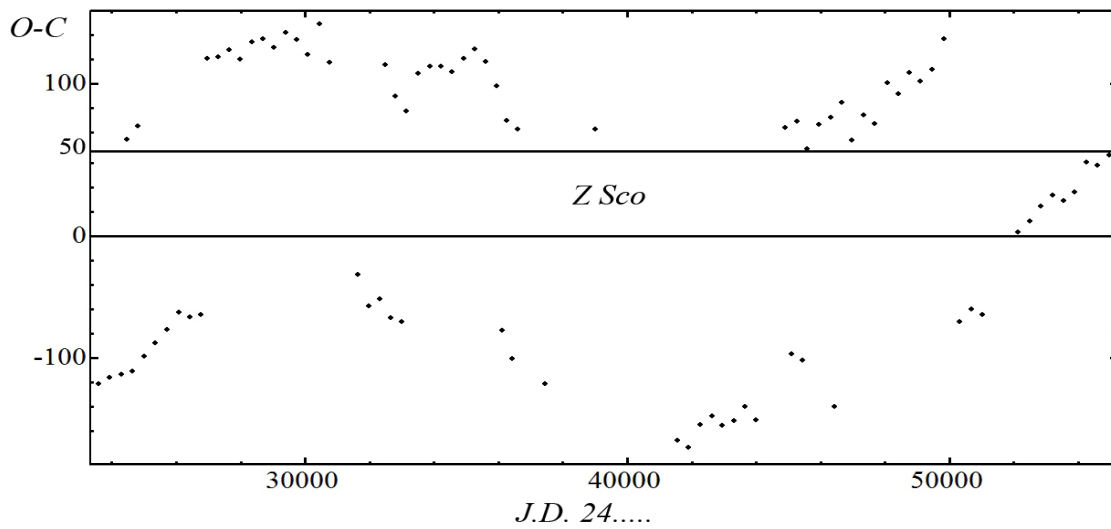


Fig. 6. O-C curves for Z Sco. Top curve is O-C obtained for maxima, the bottom one is O-C obtained for minima.

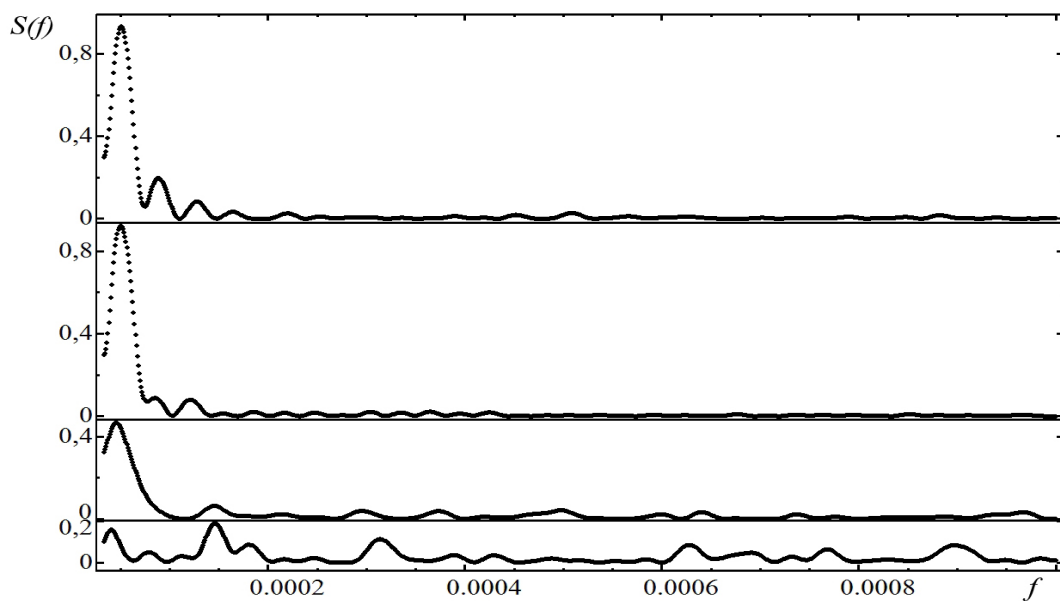


Fig. 7. Periodograms for T Cep. Top curve correspond to O-C obtained for maxima, next one correspond to O-C obtained for minima, next one correspond to amplitude variations and the bottom one corresponds to mean brightness variations.

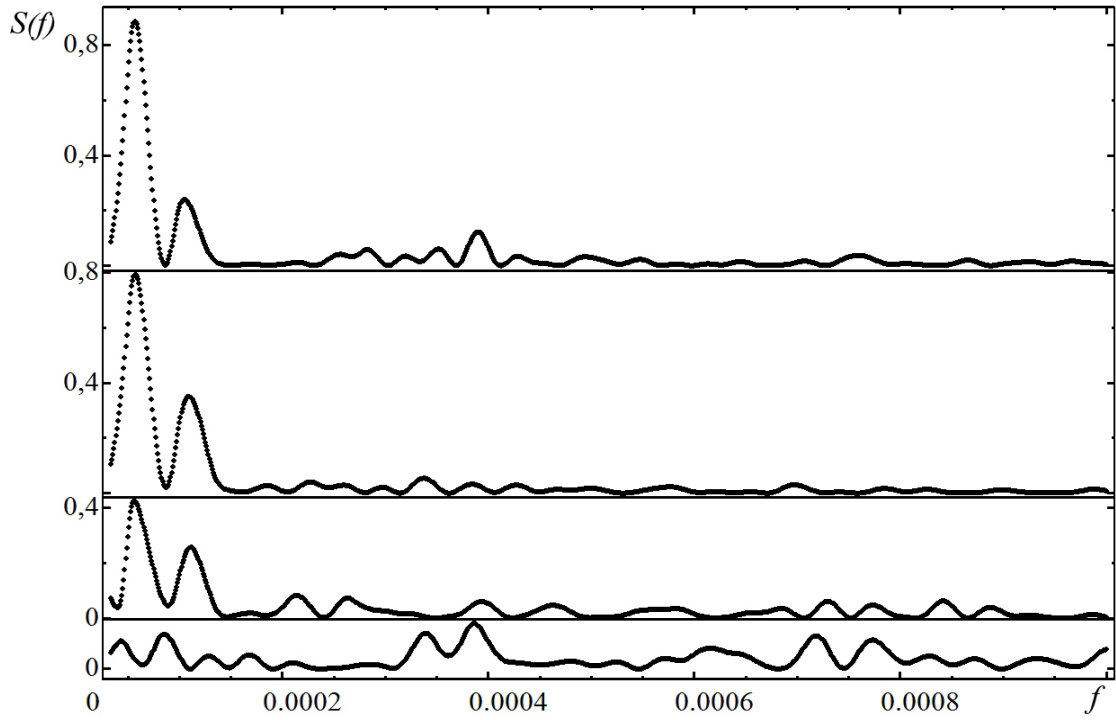


Fig. 8. Periodograms for U UMi (see explanation to Fig 7 for details).

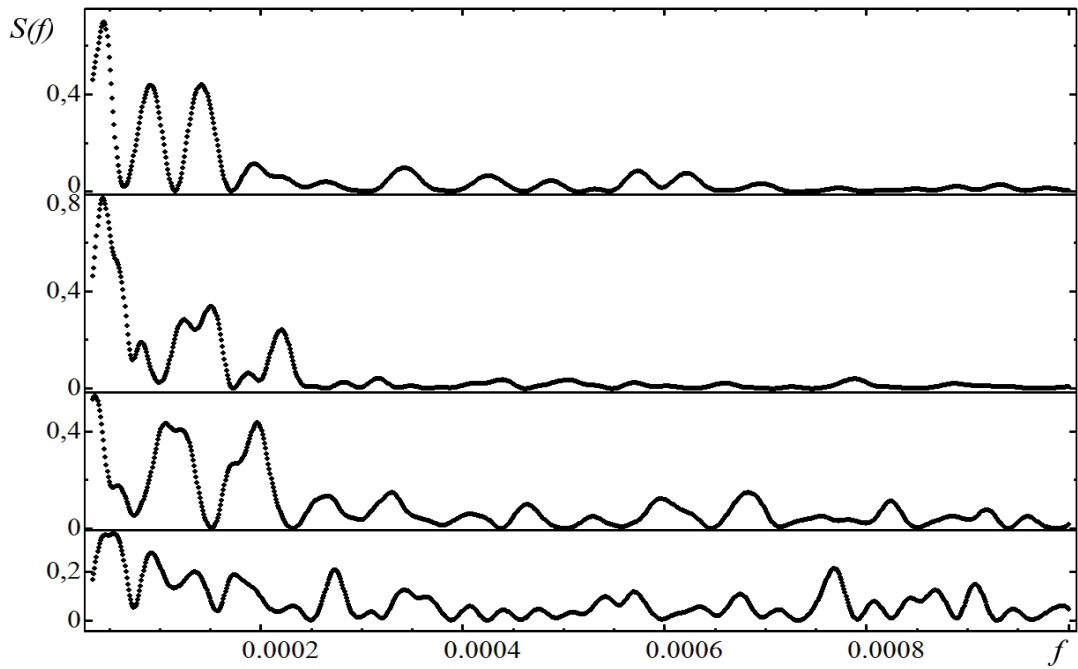


Fig. 9. Periodograms for Z Sco (see explanation to Fig 7 for details).

Table 2

Interval J.D. 24....	Period	T_0	s	As	Am
23100- 33430	394.98 ± 0.03	26331 ± 1	6	0.497 ± 0.006	4.18 ± 0.02
33430- 41820	379.94 ± 0.08	38368 ± 3	4	0.519 ± 0.004	3.44 ± 0.03
41820- 50600	398.68 ± 0.02	47354 ± 6	6	0.500 ± 0.004	4.36 ± 0.02

Here T_0 is the initial epoch, s is the degree of the statistically optimal trigonometric polynomial approximation, As is the asymmetry, Am is the amplitude of light curve.

Table 3

T Cep			
parameter	cyclicity		
	P_1	P_2	P_3
O-C (maxima)	19700	11300	
O-C (minima)	19700	11700	8250
amplitude	21800	6900	
Mean brightness	6900	24350	3200
U UMi			
parameter	cyclicity		
	P_1	P_2	P_3
O-C (maxima)	17700	9550	2550
O-C (minima)	17700	9200	
amplitude	17700	9050	
Mean brightness	2600	2950	11700
Z Sco			
parameter	cyclicity		
	P_1	P_2	P_3
O-C (maxima)	22750	7100	11050
O-C (minima)	22750	6600	8100
amplitude	28350	5100	9550
Mean brightness	18645, 21800	10950	1302

Results. As we can see from the O-C diagrams, the changes of period are not strongly cyclic. They are smooth transitions between extreme values, which are not very different. Maximal long-term cycle length is exhibited by Z Sco, the mean pulsational period of which is not the biggest among these variables. But as the period variations are not strongly periodical, and the observations cover only 2 long "periods", so we can conclude that the long "periods" are close to each other. It looks like similar variations may be present in other Mira-type variables, such as W Lyr (Marsakova & Andronov (1997).

Periods of amplitude variations are close to the O-C periods, but oscillations with smaller characteristic time are also

evident. In general, smaller period corresponds to smaller amplitude, but in Marsakova & Andronov (2000), where the cross-correlation analysis of individual cycles characteristics of T Cep were presented, it was mentioned that there is a shift for about 3 cycles between the variations of period and amplitude.

Some Mira-type variables have humps at the ascending branches of their light curves. Their general characteristics were discussed in Kudashkina & Rudnitskij (1995) and Marsakova & Andronov (2007). T Cep and U UMi also have humps. In the Fig. 1 one may see that in season with smaller period, the hump transforms into a double-peak maximum (at individual curves) or flat (at the mean phase curve) maximum. For U UMi, the variations of parameters of hump are not so clear and Z Sco has a not detectable hump at the ascending branch.

Some carbon Miras and semiregular variables have significant changes of the mean brightness (Marsakova, 1999; Marsakova & Andronov, 2006). Some of these changes are sudden or linear trends and some changes are approximately cyclic with a cyclicity from 1500 to 10000 days. Similar cyclicities one may see in the Table 3, they are often more appreciable than the period close to 20000 d. Some of these peaks are also visible (Fig. 7-8) at periodograms for amplitude variations.

Acknowledgements. We sincerely thank variable star amateur observers from AFOEV and AAVSO for their work which made such researches possible.

Author are grateful to I.L. Andronov for helpful discussions.

References

- Andronov I.L.: 1997, *Astron. Astrophys. Suppl.*, **125**, 207
 Andronov I.L., Baklanov A.V.: 2004, *Astronomy School Reports*, **5**, 264, <http://uavso.pochta.ru/mcv>
 Andronov I. L.: 2005, *ASP Conference Series*, **335**, 37°
 Andronov I.L., Marsakova V.I.: 2006, *Astrophysics*, **49**, 370.
 Kudashkina L. S., Rudnitskij G. M.: 1995, *Odessa Astron. Publ.*, **7**, 63.
 Marsakova V.I., Andronov I.L.: 1997, *Kinematics and Physics of Celestial Bodies*, **13**, № 6, 49.
 Marsakova V.I., Andronov I.L.: 2000, *ASP Conference Series*, **203**, 131.
 Marsakova V.I.: 1999, *Odessa Astronomical Publication*, **12**, 205.
 Marsakova V.I., Andronov I.L.: 2006, *Astrophysics*, **49**, 506.
 Marsakova V.I., Andronov I.L.: 2007, *Astrophysics*, **50**, 99.
 Samus N.N., Durlevich O.V., Kazarovets E. V., Kireeva N.N., Pastukhova E.N., Zharova A.V., et al.: 2012, General Catalog of Variable Stars (GCVS database, Version 2012Jan), <http://www.sai.msu.su/gcvs/gcvs/>
 Zijlstra A.A. & Bedding T.R.: 2002, *Journal AAVSO*, **31**, 2.

NON-LTE EFFECTS IN AL I LINES: CHOICE OF ATOMIC DATA

V.V. Menzhevitski¹, N.N. Shimanskaya¹, V.V. Shimansky¹,
D.O. Kudryavtsev², N.A. Sakhibullin¹

¹ Kazan (Volga region) Federal University, Kazan, Russia

² Special Astrophysical Observatory, Russian Academy of Sciences, Nizhnii Arkhyz, Russia

ABSTRACT. The analyses of deviations from the LTE in the atmospheres of *F-K* stars show that their magnitude largely depend on the ground levels photoionization cross-section of the studied elements. In particular, the *AlI* atoms with significant threshold sections are intensely ionized by the UV flux and transit to the "overionization" state with underpopulation of the ground level. Therefore, for the *AlI* atoms we should observe large deviations from the LTE (Baumuller D. and Gehren T., 1996; Menzhevitski V.S., Shimansky V.V., Shimanskaya N.N., 2012). As the photoionization of *AlI* atoms occurs exclusively from the ground state 3p, the value of this cross-sections becomes main parameter for non-LTE calculating.

We performed special test calculations for 2 different sets of atomic data: with data from *TOPbase* database (Seaton M.J., Zeippen C.J., Tully J.A. et al., 1992), and with set of sections from (Hofsaess D., 1979) to estimate the effect of adopted values of photoionization cross-sections on the value of non-LTE deviations. A comparison of the result of calculations (Menzhevitski V.S., Shimansky V.V., Shimanskaya N.N., 2012) shows that the use both sets of atomic data do not change the conclusion on the nature of the non-LTE deviations: the values of ΔX_{NLTE} remain positive and increase with increasing atmospheric temperature and with decreasing of metallicity. However, the use of a set of sections from (Hofsaess D., 1979) leads to decrease of non-LTE corrections in comparison with atomic data from *TOPbase*.

It was shown (Menzhevitski V.S., Shimansky V.V., Shimanskaya N.N., 2012) the difference in the choice of used photoionization cross-sections is most pronounced for the stars with temperatures in the range of $T_{eff} = 5500 \div 7000$ K. Therefore, in order to select the correct set of ionization cross-sections from the low levels of the Al I atom, it seems desirable to determine simultaneously the aluminum abundance in the atmospheres of such stars from the resonance and subordinate lines. The best option is the study of stars with metallicity close to $[Fe/H] = -1.0$.

On May 22, 2013 we obtained the spectrum on the range $\lambda\lambda 3900-7000$ Å for HD 201889 star with temperature $T_{eff} = 5740 \pm 10$ and the force of gravity

$\log g = 4.11 \pm 0.05$. The observations were performed by echelle-spectrograph NES (resolution $R = 60000$, signal-to-noise ratio $S/N = 150$) of BTA SAO RAS telescope. The star metallicity ($[Fe/H] = -0.92 \pm 0.09$) and value of microturbulence velocity ($\xi_{turb} = 1.2$ km/s) were redetermined using the standard analysis of the equivalent *FeII* line widths, implemented based on the *WIDTH* code, similar to the our work (Menzhevitski V.S., Shimanskaya N.N., Shimansky V.V. et al., 2013).

The comparison the theoretical and observed profiles for resonance doublet $\lambda\lambda 3944.01, 3961.52$ Å and for subordinate doublet $\lambda\lambda 6693.03, 6698.68$ Å was made for both sets of photoionization cross-sections. We show that the agreement of the theoretical and observed profiles both for resonance and subordinate doublets was achieved only with atomic data from (Hofsaess D., 1979) and with the common aluminum abundance for a both group of lines: $[Al/Fe] = 0.33$. This result demonstrates the need for to use atomic data with low values of photoionization cross-sections for a determination of non-LTE aluminium abundances. This is especially important in the study of halo stars (e.g. for the stars with low metallicity), where the aluminium abundance is determined by the resonance lines with the largest deviations from LTE.

The complete paper is to be published in "Astrophysical Bulletin" at 2014.

Key words: stars: abundances: aluminium; line: profiles; atomic data: photoionization cross-sections.

References

- Baumuller D., Gehren T.: 1996, *A&A*, **307**, 961.
Menzhevitski V.S., Shimansky V.V., Shimanskaya N.N.: 2012, *Astrophys.Bull.*, **67**, 245.
Seaton M.J., Zeippen C.J., Tully J.A. et al.: 1992, *Rev. Mex. Astron. Astrofis.*, **23**, 19.
Hofsaess D.: 1979, *Atomic Data and Nuclear Data Tables*, **24**, 285.
Menzhevitski V.S., Shimanskaya N.N., Shimansky V.V. et al.: 2013, *Astrophys.Bull.*, **68**, 243.

THE NUMERICAL THREE-DIMENSIONAL HYDRODYNAMIC SIMULATION OF THE γ -RAY BURSTERS AND X-RAY BURSTERS

V.V. Nazarenko¹, L.V. Glazunova², S.V. Nazarenko¹

¹ Astronomical Observatory of I.I.Mechnikov Odessa National University,
Odessa, Ukraine, *astro@paco.odessa.ua*

² The A.S. Popov National Academy of Telecommunications, Odessa, Ukraine

ABSTRACT. An radiative wind accretion onto the compact object in a detached close binary system (CBS) where one of the components is a supergiant with radiation stellar wind that blows from its surface, and another component is a compact object (black hole or neutron star), is simulated applying methods of three-dimensional numerical hydrodynamics. The simulation of bursts similar to the gamma-ray bursters and X-ray bursters, i.e. isolated bursts with nearly zero in time ascending and descending branches with amplitudes from $6 - 7^m$ to $15 - 18^m$, commences in the vicinity of the compact object when the precession of the donor star starts. Due to the course numerical spatial grid of 0.01 units of the orbital separation, the duration of such isolated bursts is 10-40 minutes of the orbital time. The burst simulation is as follows: when the donor stars precession starts, small grid-cell-sized regions of higher density appear in the vicinity of the compact object due to the RayleighTaylor instability. The temperature in one of those regions increases abruptly when they interact with the stellar wind from the donor star. Prior to the temperature increase, the indicated regions were radiopaque. When the temperature reaches its peak, those regions become radiolucent, and all energy contained there is momentarily illuminated, giving off a burst that appears as an isolated sharp peak. That is how the bursts similar to the γ -ray bursts and X-ray bursts are simulated.

Key words: Stars: close binary system; X-ray bursters; gamma-ray bursters.

1. Introduction

In this study an attempt was made to simulate the X-ray bursters and γ -ray bursters, i.e. to model sharp peaks of emission with very large amplitudes (of more than 10^m), using the three-dimensional numerical hydrodynamic methods. As is known, the X-ray bursters and γ -ray bursters are unique objects with sharp bursts and total radiant energy output of

approximately $10^{38} \div 10^{39}$ erg for the X-ray bursters and $10^{51} \div 10^{52}$ erg for the γ -ray bursters. It was found that some bursts exhibit optical emission along with the γ -ray bursts and X-ray bursts (McClintock et al., 1977; Grindlay et al., 1978). The presence of the optical echo allows of assuming that burster is a close binary system where the X-ray emission by one component is absorbed and re-emitted in the optical band by another component. The main objective of the presented numerical study was to simulate the radiation wind and precession of the CBS donor star.

2. Numerical simulation of a binary system, the wind from its donor star and accretion disc

We simulated the wind from the donor star based on the radiation wind model by Castor (1975), according to which the sonic point is reached close to the level of the layer near the donor stars photosphere, and 90 is attained at the outer boundary of the atmosphere. In the present study the wind from the donor star was simulated implementing the algorithm reported by Nazarenko (2005, 2006, 2008). The CBS model in this study is as follows: the Roche model is applied to calculate the gravitational fields of the CBS components, the donor star rotation is deemed to be synchronised with its orbiting.

To simulate the driven precession, we assume that the donor star is embedded, and it is the compact object that moves in the numerical grid. In the present computations the built numerical grid is rectangular and uniform with the cell size of around 0.006085 in the orbital plane and approximately 0.02 along the z-axis. The computations were made in the Cartesian coordinate system, rigidly bound to the precessing donor star.

The numerical scheme of the astrophysical version of the large particle method by Belotserkovskiy and Davydov was applied in computations. To perform those, all space in the numerical domain was divided

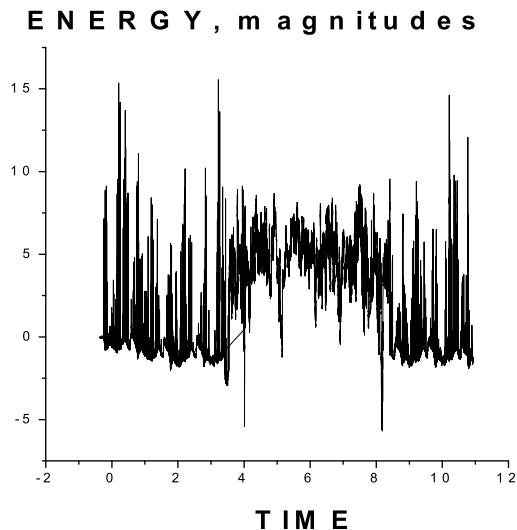


Figure 1: Radiation from the region where the burst occur for all the interval of calculation time.

into three-dimensional rectangular grid cells. All physical quantities are constant within the given cell.

The only effects that were taken into account at the first stage of computations with the given time-increment were the pressure and external fields effects; and the effect of the physical quantities transfer across the cell boundaries were the only accounted for at the second stage; that makes the numerical scheme of the large particle method absolutely stable, constant and strictly conservative on the whole.

One of the crucial aspects of this study is the radiative-cooling model. The magnitude of the radiative cooling is taken from Cox (1971) where it was computed applying the ionization-equilibrium optically-thin plasma model.

To estimate the phenomenon of the γ -ray bursters and X-ray bursters, we used several alternative sets of the CBS parameters, but in this paper we present the computations made with just one of them. The CBS parameters, used in computations, correspond to those of CYG -1: the orbital period is 5.86 days, the donor star mass is $40M_{\odot}$, and the accretor mass is $15M_{\odot}$.

3. Numerical results

The simulation of bursts proceeded during 18 precession periods, i.e. for a quite long to monitor how different physical factors affect modelling of bursts.

For the first four precession periods the simulation of bursts was performed with the precessing donor star and radiation wind that blew from its surface. For the selected CBS in that case the bursts (which are

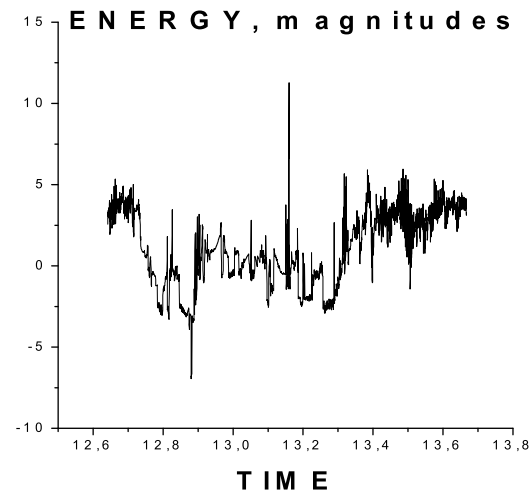


Figure 2: Radiation from the region where the burst occur for the time of 13.16.

implied to be quite rare bursts with amplitudes of more than 10m) appeared as rather small series of 4-5 bursts in each with the time separation of 1.5-2 thousand of time-increments; thus, bursts become quite a rare case.

On the time interval between the fourth and eighth precession periods we deactivated formation of the wind from the donor star. As is seen in Figure 1, as soon as the supply of matter into the vicinity of the compact object ceased, the bursts discontinued. This points to the fact that as the actual radiation wind structure is intricate and ragged, i.e. discrete, and at that it can have a shape, which is far from any symmetry, then it can affect the generating of bursts in the vicinity of the compact object.

Starting from the eighth precession period the wind from the donor star was again factored in the computations, and bursts gradually resumed and continued almost in the same order as before the wind from the donor star had been deactivated. To show how the physical conditions in the near-accretor area, i.e. the area where bursts appear, affect the characteristics of the bursts and their number, the computation of the radiation force, which acts vertically upwards from the orbital plane in the near-accretor area, was factored in simulating of bursts from the 11th to 14th precession periods. As is seen in Figure 1, the bursts ceased almost immediately.

During three precession periods while the radiation force was factored in the computations, only one burst occurred; this is indicative of the fact that with such a change in the physical conditions in the near-accretor area bursts became a very rare case in our computations that corresponds to the observations. That isolated burst is shown on a short time interval in Figure

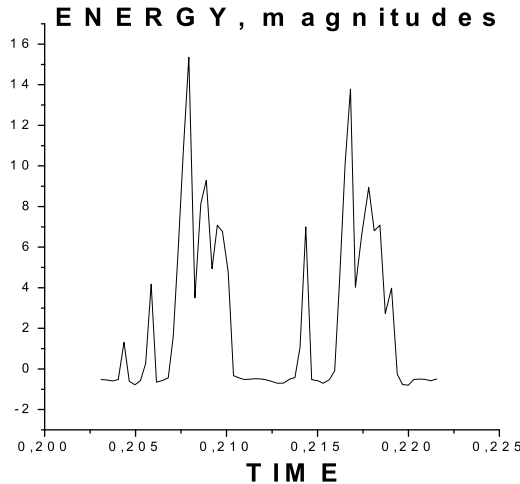


Figure 3: Radiation from the region where the burst occur. The partial bursts.

2, and as is seen the indicated burst appears as a narrow sharp peak with amplitude higher than 10^m .

Isolated bursts are shown in Figures 3 and 4. As is seen in those figures, the bursts can have intricate structure, but all of them appear as isolated sharp peaks with amplitudes of up to $14 - 15^m$.

4. Conclusions

The wind accretion and driven precession of the donor star were simulated within the frame of the CBS model applying the three-dimensional numerical hydrodynamic methods. The computations showed that when the precession starts, isolated sharp peaks of emission with amplitudes from $3 - 4^m$ to 17^m are simulated in the nearest vicinity of the accretor. The durations of those bursts are short of about 5-7 or 50 time-increments (one time-increment equals to approximately 80 seconds of the orbital time). The bursts appear as rather small series of 4-5 bursts in each with the time separation of 1.5-2 thousand of time-increments. We interpreted those bursts as the γ -ray bursts and X-ray bursts due to their ascending and descending branches, which are nearly zero in time. In so doing, numerous bursts with smaller amplitude of around $4 - 7^m$ and lower temperature at the peak are reckoned in the X-ray bursters, and bursts with amplitude of more than $10 - 17^m$ and the peak temperature of about $3.5 \cdot 10^6$ were assigned to the γ -ray bursters.

Our model of the γ -ray bursters and X-ray bursters is very simple as such it is a massive detached close binary where the precessing donor star does not fill its Roche lobe and generates radiation stellar wind onto the surface of the compact object that can be

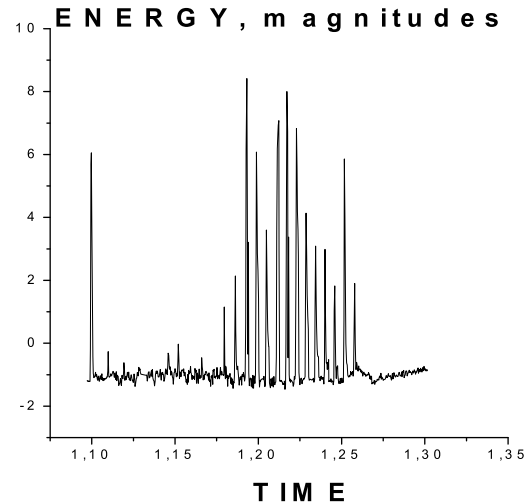


Figure 4: Radiation from the region where the burst occur for set of bursts.

either a neutron star or a black hole. At that, an radiative wind accretion onto the compact object is implemented. The size of the domain where the burst occurs is equal to its distance to the compact object. Given that, the smaller that domains size is, the shorter burst ensues, and the more energy is given off by that burst. With the smallest dimensions of the bursting domain, i.e. when the size of the bursting domain equals to that of the compact object, it will be the γ -ray burst occurred with duration of 10-4 seconds. The energy, given off by the burst, will reach up to 10^{62} erg/sec with the compact object mass of about $60 \div 80 M_{\odot}$. If the bursting domain size is about $10^{11} - 10^{12}$ cm, then, it will be the X-ray burst with duration of about several minutes.

References

- Castor J.I., Abbott D.C., Klein R.I.: 1975, *Astrophys. J.*, **195**, 157
 Cox D.P., Daltabuilt E.: 1971, *ApJ*, **167**, 113
 Grindlay J.E, McClintock J.E., Canizares C.R. et.al.: 1978, *Nature*, **274**, 567.
 McClintock J.E., Bradt H.V., Doxsey R.E. et.al.: 1977, *Nature*, **270**, 320
 Nazarenko V.V.: 2006, *Astron. Rep.*, **50**, 647
 Nazarenko V.V.: 2008, *Astron. Rep.*, **52**, 40
 Nazarenko V.V., Glazunova L.V.: 2005, *Astron. Rep.*, **49**, 826
 Nazarenko V.V., Glazunova L.V.: 2006, *Astron. Rep.*, **50**, 369
 Nazarenko V.V., Glazunova L.V.: 2006, *Astron. Rep.*, **50**, 380

THE NUMERICAL THREE-DIMENSIONAL HYDRODYNAMIC SIMULATION OF COLLIDING STELLAR WINDS IN A CLOSE BINARY SYSTEM

V.V. Nazarenko¹, L.V. Glazunova², S.V. Nazarenko¹

¹ Astronomical Observatory of I.I. Mechnikov Odessa National University,
Odessa, Ukraine, *astro@paco.odessa.ua*

² The A.S. Popov National Academy of Telecommunications, Odessa, Ukraine

ABSTRACT. In the present numerical study the stellar winds from both supergiant-components of a detached close binary system (CBS) are simulated applying methods of the three-dimensional numerical hydrodynamics. The simulated winds collide in the space between the components, forming a stationary shock wave. That shock wave has geometrically intricate shape that consists of several separate filamentary structures. The temperature in the shock wave is about 10^5K , and the temperature in the space adjacent to the shock wave is around $10^4 - 1.5 \cdot 10^4\text{K}$. Away from the line-of-centres the shock wave is curved due to the effect of the Coriolis forces and greatly expands under the gas pressure at that. At a distance of about two orbital separations from the line-of-centres the shock wave expands so much that it is practically smearing out in space.

Key words: Stars: close binary system; hydrodynamics; colliding winds.

1. Introduction

The phenomenon of colliding winds (CW) pertains to massive detached CBS consisting of supergiant stars of O and B spectral classes, which generate radiation stellar winds onto each other, forming a strong shock wave that can be a high-flux X-ray source in the space between the binary components. The CW phenomenon was first reported by Prilutskii & Usov (1976) and Cerepashchuk (1976). The observational confirmation of the CW phenomenon was made by Pollock (1987).

The numerical three-dimensional hydrodynamic model of colliding winds accounting for the Coriolis forces was presented in (Lemaster et al., 2007). In that study the geometry of the shock wave, formed in the space between the CBS components, was obtained; and it was shown that the stationary shock wave is significantly curved in space due to the effect of the Coriolis forces, being slightly expanded at that. The

only disadvantage of the above-mentioned study was that the radiative cooling was not factored in, and therefore, the temperature in the shock wave and in its surrounding space could be greatly overestimated. To correct the indicated fault, in the present study we simulate the colliding wind phenomenon accounting for the Coriolis forces and explicit radiative cooling applying the methods of numerical three-dimensional hydrodynamics.

2. Numerical methods

In this study the gas flow in the CBS was computed by the relaxation method, i.e. applying the non-stationary Euler equations, integration of which had been performed until the physical quantities within the numerical domain practically ceased to change in time. The equations of motion were integrated by the astrophysical version of the large-particle method by Belotserkovskiy and Davydov. The model of the winds from both components of the binary, as well as the algorithm, which was applied to simulate those winds, is presented in studies (Nazarenko, 2005; 2006; 2008). The indicated algorithm consists of the following: at first, a stellar atmosphere model from the Kurucz atlas (1979) is chosen according to the donor stars parameters; then, the atmosphere of the donor star is created; subsequently, the wind acceleration is introduced in each point of the atmosphere. In so doing, the absolute value of the wind acceleration should be selected to provide the required velocity in the wind. And the direction of the wind acceleration coincides with the normal to the donor stars Roche lobe. The wind, created with such an algorithm, gives the radial velocity profile similar to the model by Castor, Abbott & Klein (1975).

The gravity for the CBS components was computed according to the Roche model, in so doing, it was assumed that the components rotation was synchronized

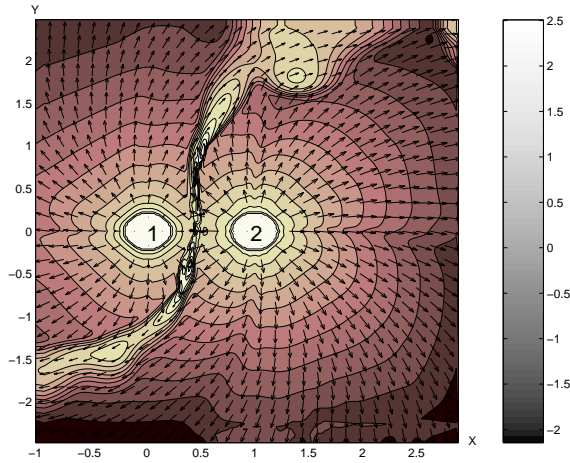


Figure 1: Concentration distribution in the orbital plane on low grid.

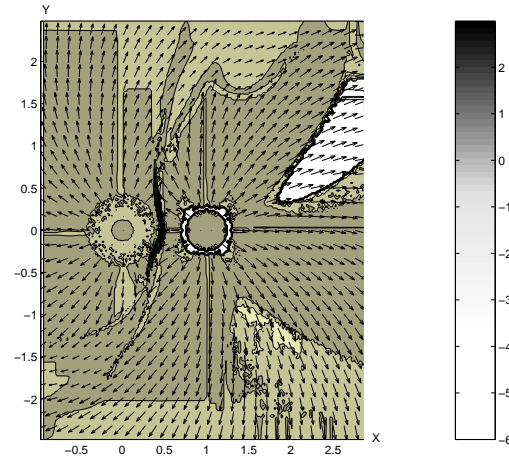


Figure 3: Temperature distribution in the orbital plane on low grid.

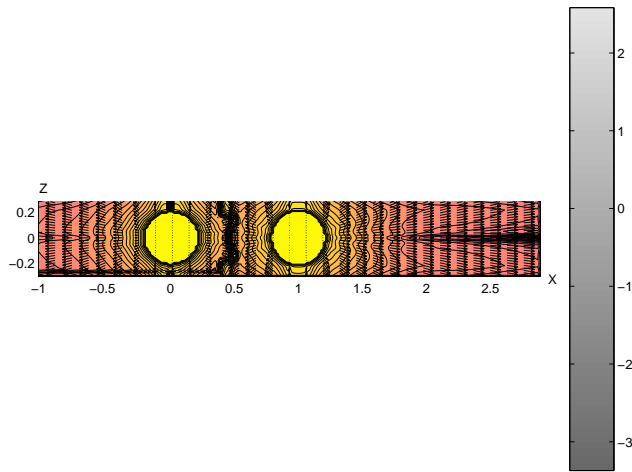


Figure 2: Concentration distribution in Z-X plane on low grid.

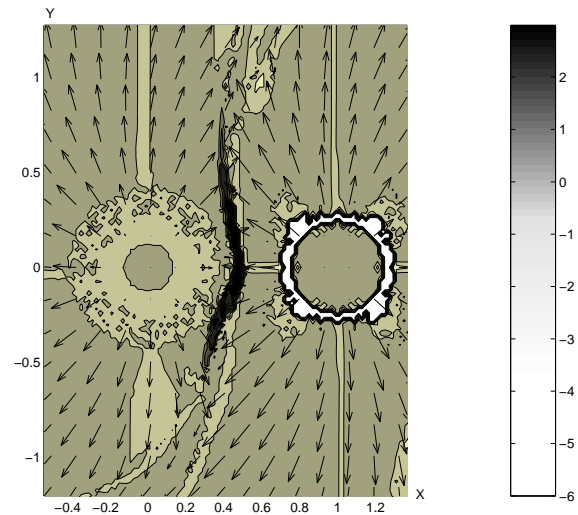


Figure 4: Temperature distribution in the orbital plane in the vicinity of shock on low grid.

with their orbiting. The masses of the components are taken to be equal to $4M_{\odot}$, and the orbital period is assumed to be 15 days.

3. Numerical results

The computations commence with simulating of the winds from both components, which are subsequently distributed over the whole numerical domain. It takes about $1/6$ of the first orbital period to form the winds from the components. As a result of interaction between the winds from both components, a stationary shock wave is formed in the space between the components, and the duration of its formation equals to approximately one orbital period. To trace the shock waves distribution in space away from the line-of-centres, the computations were made on two numerical grids.

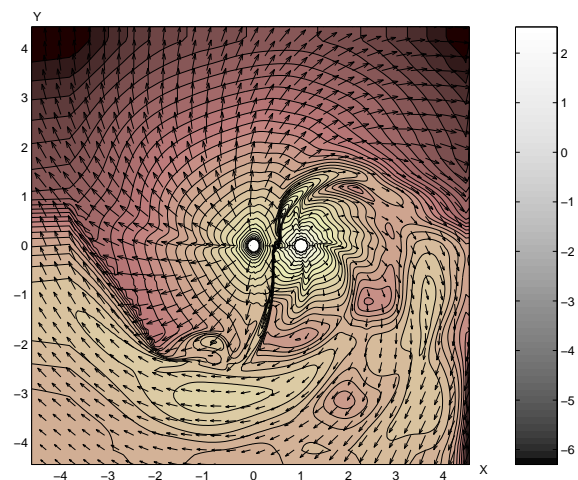


Figure 5: Concentration distribution in the orbital plane on low extended grid.

The first grid size was 1.5×2.5 units of the orbital separation, and the second grid dimensions were 4.5×4.5 (in the orbital plane). The numerical results for the first numerical grid are presented in Figure 1a-b where the distribution of the matter concentration is given in 10^{11} units of particles per cm^3 in the orbital plane and in the plane, which is perpendicular to the orbital plane and passes through the line-of-centres. As is evident from Figure 1a where the gas flow in the orbital plane is shown, the stationary shock wave, formed in the space between both components, has a rather intricate shape; and as that shock wave moves away from the line-of-centres, it is significantly curved due to the effect of the Coriolis forces and simultaneously begins to greatly expand, being rapidly mixed with the winds from both components. As is seen in Figure 1b, the indicated stationary shock wave is vertically cylindrical-symmetric and propagating quite far away from the orbital plane up to the altitude of 0.6-0.8 units of the orbital separation above or below the orbital plane.

The temperature distribution of the gas flowing in the orbital plane is presented in Figure 2a-b in $10^4 K$ units for the coarse numerical grid. It follows from the figures that the stationary shock wave takes the shape of a cord, elongated in a direction perpendicular to the line-of-centres at the distance of up to 0.5 from the line-of-centres. The temperature in that cord is about $2 \cdot 10^7 K$.

In Figure 3 the distribution of the matter concentration in the orbital plane is shown for the wide spatial numerical grid. As is seen in that figure, the gas from the stationary shock wave is twisted due to the effect of the Coriolis forces at a distance of approximately one unit of the orbital separation from the line-of-centres, and it is gradually mixed with the winds from both components (at a distance of about two units of the orbital separation from the line-of-centres), forming a wide band that spirals outwards the CBS.

4. Conclusions

A stationary shock wave, resulted from the collision of the winds from two components of a massive CBS, was simulated in the presented computations. The computations demonstrated that the indicated stationary shock wave takes the shape of a cord with the width of about 0.02-0.03 units of the orbital separation and the length of 0.5 from the line-of-centres in the perpendicular direction. The temperature in the stationary shock wave is about $2 \cdot 10^7 K$. The concentration of matter in the stationary shock wave is about 10^{11} particles per cm^3 . The above-listed parameters of the stationary shock wave indicate that the shock wave can be a high-flux X-ray source.

References

- Castor J.I., Abbott D.C., Klein R.I.: 1975, *Astrophys. J.*, **195**, 157
 Cerepashchuk A.M.: 1976, *SvAL*, **2**, 138
 Kurucz, R.L.: 1979, *ApJ.Suppl.Ser.*, **40**, 1
 Lemaster M. Nicole, Stone J.M., Gardiner T.A.: 2007, *ApJ*, **662**, 582
 Nazarenko V.V., Glazunova L.V.: 2005, *Astron. Rep.*, **49**, 826
 Nazarenko V.V., Glazunova L.V.: 2006, *Astron. Rep.*, **50**, 369
 Nazarenko V.V., Glazunova L.V.: 2006, *Astron. Rep.*, **50**, 380
 Nazarenko V.V.: 2006, *Astron. Rep.*, **50**, 647
 Nazarenko V.V.: 2008, *Astron. Rep.*, **52**, 40
 Pollock A.M.T.: 1987, *ApJ*, **320**, 283
 Prilutskii O.F., Usov V.V.: 1976, *SvA*, **20**, 2

THE CRITERIA FOR MORPHOLOGICAL CLASSIFICATION OF PF GALAXY CLUSTERS

E.A. Panko

Kalinenkov Astronomical Observatory

of the V.A. Sukhomlinsky Nikolaev National University, Nikolaev, Ukraine

Department of Astronomy of I. I. Mechnikov Odessa National University, Odessa, Ukraine

panko.elen@gmail.com

ABSTRACT. The morphological types of galaxy clusters resulting from their outward appearance is physically related to the clusters and their member galaxies. Presented here is an adopted system of morphological types of galaxy clusters based on the Zwicky, Bautz & Morgan, Rood & Sastry, and López-Cruz systems. The adopted types are suitable for automated classification of galaxy clusters from The Catalogue of Galaxy Clusters and Groups (Panko & Flin 2006). Numerical criteria describing 6 main types were distinguished: Concentrated *C*, Intermediate *I*, Open *O*, Line *L*, Flat *F*, and *cD*. The types correspond to the base divisions from regular to irregular clusters, but also note the presence of preferential direction or plane in each cluster.

Key words: clusters of galaxies: morphological types

1. Introduction

The classification of galaxy clusters at optical wavelengths is carried out using several different parameters: cluster richness (number of galaxies within a specific limiting magnitude), the central concentration, the presence of bright galaxies in the center of the cluster, the presence of peculiar galaxies, etc. Other variants of the morphological classification for galaxy clusters were developed by different authors following Abell (1958). As noted by Bachall (1997) in her review, clusters with a richness class of 30 or more members are classified in a sequence ranging from early- to late-type clusters, or equivalently, from regular to irregular groups (Abell 1958). As described by Zwicky et al. (1961–1968), regular R, intermediate (RI or IR), and irregular (I) Abell types correspond to compact, medium-compact, and open galaxy clusters, respectively. Many cluster properties (shape, concentration, dominance of brightest galaxy, galactic content, den-

sity profile, and radio and X-ray emission) are correlated with position in the sequence.

The prevalent Bautz-Morgan (BM) classification scheme (Bautz & Morgan 1970) is based on the relative contrast (dominance in extent and brightness) of the brightest galaxy to other galaxies in the cluster, ranging from type I to III in decreasing order of dominance. The Rood-Sastry (RS) system (Rood & Sastry 1971) classifies clusters based on the geometry of the distribution of the ten brightest members (from *cD*, to binary *B*, core *C*, line *L*, flat *F*, and irregular *I*). The Rood-Sastry and Bautz-Morgan schemes are in agreement and complement each other. Most Rood-Sastry *cD* clusters are of Bautz-Morgan classes I and I-II, while the majority of Bautz-Morgan class III clusters belong to Rood-Sastry types *C*, *L*, *F*, and *I*.

The Rood-Sastry scheme also adds more detail to the Bautz-Morgan classification by considering the irregularity of galaxy clusters. However, the most important contribution of the Rood-Sastry scheme is the introduction of the “*B*” class, a class originally thought to be of an intermediate type. López-Cruz (1997, 2001) introduced the definition of a *cD* cluster, where a cluster is both Bautz-Morgan class I or I-II and Rood-Sastry designation *cD*, exclusively. The complement to this class is called a non-*cD* cluster (i.e., Bautz-Morgan II, II - III, or III and Rood-Sastry *C*, *L*, *F*, *I*). Binary clusters, that is, Rood-Sastry *B* clusters, are considered a different class because of their merger nature.

BM type I *cD* clusters are a special type. van Kampen & Rhee (1990) found an alignment of *cD*-galaxies with their surroundings, based upon studies of 122 rich Abell clusters. López-Cruz (2001) has shown that *cD* clusters and non-*cD* clusters are different dynamically. Sandage & Hardy (1973) found that BM types and *BCM* (Brightest Cluster Members) absolute magnitudes were independent of cluster richness; therefore, they concluded that Bautz-Morgan types were defined by initial conditions at the onset of cluster formation rather than by later evolution. Panko, Juszczyk & Flin

(2009) analyzed the relative orientations of BCM and their parent clusters for 1056 galaxy structures from the PF Catalogue (Panko & Flin 2006). They found statistically significant alignments of *BCM* relative to the parent clusters only for BM I clusters. The Binggeli effect (Binggeli 1982) is strongest for BM type I clusters as well (Flin et al. 2011). Moreover, Struble (1990) found weak alignments for 68 clusters of type RS *B*.

The structures in the Catalogue of Galaxy Clusters and Groups (Panko & Flin 2006, PF for short) has assumed Abell and BM morphological types only for 1056 objects corresponding to ACO clusters (Abell, Corvin & Olovine 1989). Other clusters need a determination of their morphological type for future study. The main problem for such structures lies in the input data: the galaxies of the Münster Red Sky Survey have tabulated only positions, magnitudes, ellipticities, and position angles for the major axes. Thus, it is necessary to adopt the prevalent morphological systems to determine cluster classification types for the PF clusters.

2. Observational Data

The present work is based on the PF catalogue (Panko & Flin 2006). It contains information on 6188 structures containing at least 10 members in the overdense region. A total of 1746 clusters have a richness of 50 or more. The value 50 was selected as minimal for normal and rich galaxy clusters according to the study by Biernacka et al. (2007). Other structures in the PF catalogue were assumed to be poor galaxy clusters and groups of galaxies.

The 1746 clusters are distributed in richness order as: 12 have a richness of 400 or more galaxies in the cluster field, the next 27 have a richness of 301–400, 76 have a richness of 210–300, 377 have a richness of 101–200, and 1254 have a richness from 50 to 100. For all PF catalogue structures a list of galaxies in the object fields was compiled along with information about each galaxy according to the criteria of Ungrue, Seitter & Duerbeck (2003).

The analysis of the spatial orientations of galaxies in 247 rich PF clusters with assumed from ACO morphological types was executed in paper Godlowski et al. (2010). We can expand the list to 377 clusters for future study.

A specific region $11^\circ \times 16^\circ$ was selected to test our results with previous classification and to check the new criteria (Fig. 1). The region contains 55 ACO galaxy clusters (Abell, Corvin & Olovine 1989), 6 of them belong to supercluster SCL 184 (Einasto et al. 1997). Furthermore the region contains 175 clusters and groups from the PF Catalogue, 31 of them have corresponded clusters in the ACO Catalogue (Abell,

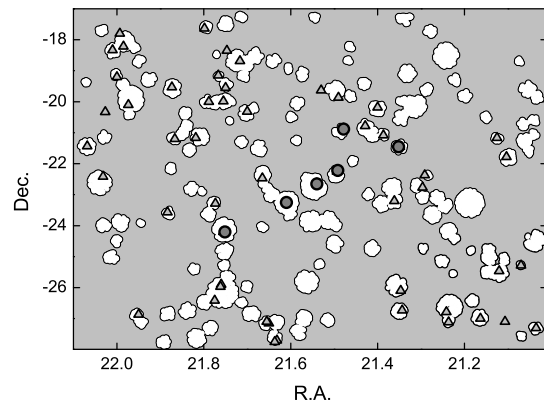


Figure 1: The distribution of large-scale structures in the test region. White symbols are PF clusters and groups, triangles are known ACO clusters, and black circles are Supercluster members.

Corvin & Olovine 1989) with assumed Abell and BM types.

In the test region all types of large-scale structures are seen: filaments and voids together with galaxy groups, clusters and superclusters. The data set permits us to check the main principles of the adopted morphological classification.

3. Determination of Morphological Types in the Test Region

Maps were constructed for 50 PF normal and rich galaxy clusters and for 14 poor ones, which have corresponded clusters in ACO catalogue in the test region using rectangular coordinates calculated in the standard manner. Four of the maps are shown in Fig. 2, where units for the axes correspond to arcseconds. The maps note the direction of each cluster's major axis according to the PF catalogue. Morphological types were determined for 31 clusters according to the Abell, Zwicky et al., Bautz-Morgan, and Rood-Sastry criteria, then compared with ACO catalogue data. Types BM I and II as well as RS *F* types can be identified confidently. However, detailed classification based on the constructed maps, particularly in automated mode, was less successful, since the maps contain only dots instead of images for the galaxies.

An automated procedure was used to distinguish 6 main types: Concentrated *N*, Intermediate *I*, Open *O*, Line *L*, Flat *F*, and *cD*. Those types correspond to the base divisions from regular to irregular, but additionally note the presence of a preferential direction or plane in the cluster.

Concentrated types can be assumed for clusters contained 20% of the galaxies within $1/3$ of the cluster's

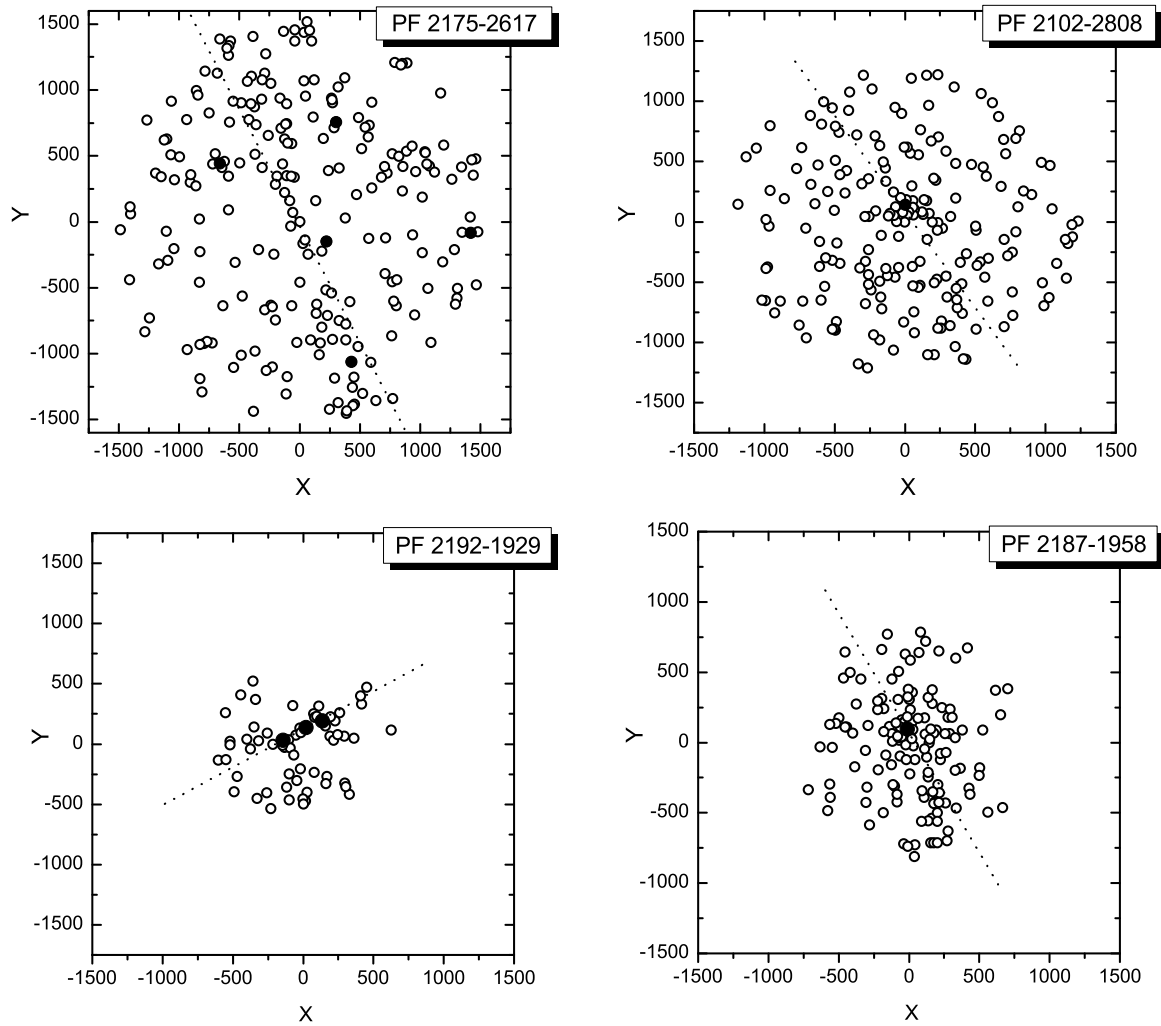


Figure 2: The positions of galaxies in 4 PF galaxy clusters (open circles). The brightest galaxies are shown as black circles. Dashed lines denote the direction of the major axes according to the PF catalogue.

equivalent radius. Intermediate types contained 50% of the galaxies within $1/2$ of the cluster's equivalent radius, and others are Dispersed types. *cD* clusters have the *BCM* in the center of a concentrated cluster, with the difference between the *BCM* and other galaxies being about 1^m . It is necessary to check the positions of 3 *BCM* for that type. Since there is no information concerning both foreground and background galaxies, one must take into consideration the possible presence of a bright foreground galaxy, making classification difficult. Line clusters must contain 25% of the galaxies in a belt along the major axis with a width corresponding to 0.1 of the cluster equivalent radius. Flat clusters must have 40% of the galaxies located in the same belt width corresponding to 0.2 of the cluster equivalent radius. Combined types, such as *CF*, *OFcD*, *IF*, *OF*, etc. are also possible.

The 4 clusters presented in Fig. 2 have the following types: PF 2175-2617 is *OF*, PF 2102-2808 is *IcD*, PF 2192-1929 is *OL*, and PF 2187-1858 is *CFcD*. In 50 galaxy clusters in the test region, 8 belong to *L* or *F*, 5 clusters have the *BCM* in the geometrical center, and 3 are *cD*.

4. Conclusion

We propose the possibility of assigning morphological types for galaxy clusters by an automated process. There are 6 adopted morphological types: Concentrated *C*, Intermediate *I*, Open *O*, Line *L*, Flat *F*, and *cD* correspond to the base divisions from regular to irregular galaxy clusters (equivalent to early-/late-type), also noting the presence of *BCM* and preferential directions or planes in each cluster. The types are based on Abell, Zwicky, BautzMorgan, Rood-Sastry, and López-Cruz criteria, but adopted to a numeric format for an automated procedure taking into consideration the properties of the analyzed data from the PF Catalogue. The most important galaxy clusters for future study are the *cD*, *L*, and *F* types.

Acknowledgements. This research has made use of NASA's Astrophysics Data System.

References

- Abell, G.O.: 1958, *ApJS*, **3**, 211.
 Abell, G.O., Corwin, H.G., Olowin, R.P.: 1989, *ApJS*, **70**, 1.
 Bahcall, N.: 1997, "Clusters and Superclusters of Galaxies," arXiv:astro-ph/9611148.
 Bautz, P., Morgan, W.W.: 1970 *ApJ*, **162**, L149.
 Biernacka, M., Flin, P., Panko, E., Juszczyk, T.: 2007, *Odessa Astr. Publ.*, **20**, 26.
 Binggeli, B.: 1982, *A&A*, **107**, 338.
 Einasto, M., Tago, E., Jaaniste, J., et al.: 1997, *A&AS*, **123**, 119.
 Flin, P., Biernacka, M., Godlowski, W., et al.: 2011, *Balt. Astr.*, **20**, 251.
 Godlowski W., Piwowarska P., Panko E., et al.: 2010, *ApJ*, **723**, 985.
 van Kampen, E., Rhee, G.: 1990, "Alignment of cD-Galaxies with their Surroundings," *I.A.U. Colloq.*, **124**, 255.
 López-Cruz, O., Yee, H.K.C., Brown, J.P., et al.: 1997, *ApJ* **475**, L97.
 Lopez-Cruz, O., Gaztanaga E.: 2001, arXiv:astro-ph/0009028).
 Panko, E., Flin, P.: 2006, *J. Astr. Data*, **12**, 1.
 Panko, E., Juszczyk, T., Flin P.: 2009, *AJ*, **138**, 1709.
 Rood, H.J., Sastry, G.N.: 1971, *PASP*, **83**, 313.
 Sandage, A., Hardy, E.: 1973, *ApJ*, **183**, 743.
 Struble, M.F.: 1990, *ApJ*, **99**, 743.
 Ungrue, R., Seitter, W.C., Duerbeck, H.W.: 2003, *J. Astr. Data*, **9**, 1.
 Zwicky, F., Herzog, E., Wild, P., et al.: 1961–1968, *Catalogue of Galaxies and of Clusters of Galaxies*, Pasadena, California Institute of Technology, Online data: <http://vizier.cfa.harvard.edu/viz-bin/VizieR?-source=VII/190>.

SULFUR ABUNDANCE IN THE GALACTIC DISC STARS

O.P.Paramonova, T.V.Mishenina, O.Chepizhko

Astronomical Observatory, Odessa National University

T.G.Shevchenko Park, Odessa 65014 Ukraine

astro@paco.odessa.ua

ABSTRACT. The sulfur abundance was determined by the synthetic spectrum method in the stars with metallicity close to that of the Sun. The comparison with the results of other authors, as well as the nucleosynthesis computations were made.

Key words: Stars: abundance – Stars: late-type

Introduction. There are several sulfur lines in the spectra of stars; those lines have hyperfine structure (HFS), and therefore, the sulfur abundance determinations are not currently available for a large sample of stars. The Type-II supernovae are the major sources of sulfur, and the knowledge of the sulfur abundance is important for the development of theories of nucleosynthesis and chemical evolution of the Galaxy. The subjects of this study are stars of the Galactic disk.

The spectra of 27 stars were obtained with S/N about 100-350 using the 1.93 m telescope at the Observatoire de Haute-Provence (OHP, France), equipped with the echelle-spectrograph ELODIE. The resolving power is $R = 42\,000$. The spectral processing was carried out by (Katz et al., 1998; Galazutdinov 1992).

The parameters of the investigated stars were taken from the studies by (Mishenina et al. 2013). The effective temperatures T_{eff} were estimated using the line depth ratio method. The surface gravities $\lg(g)$ were computed by two methods, namely the iron ionization balance and the parallax.

The abundances of sulfur were obtained under the LTE approximations upon the synthetic spectrum method, taking into account the HFS and the oscillator strengths of lines by Korotin (2009). The Kurucz model of atmospheres (Kurucz, 1993) and the new version of the STARSP code by Tsymbal (1996) were used. We used the sulfur and iron lines in the region of 6743-6762 Å. The NLTE corrections for those lines did not exceed 0.1 dex (Korotin, 2009). Fig. 1 shows the observed (as dotted) and synthetic (as line) spectra fitted for star HD108954.

Results and conclusions. The behavior of the sulfur abundance in the region of metallicity from $[\text{Fe}/\text{H}] = -2$ to $[\text{Fe}/\text{H}] = +0.3$ is presented in Fig.2 with the model predictions by Timmes et al. (1995) and the data of other authors (our data – as asterisks, Clegg et al. 1981 – as triangles, Francois 1987, 1988 – as squares and circles). The lines show the computed data with the factor of 2 variations in the iron yields from massive stars.

As is seen from the Fig.2, in the region of metallicity from $[\text{Fe}/\text{H}] = -1$ to $[\text{Fe}/\text{H}] = +0.3$ sulfur demonstrates the trend of its abundance with $[\text{Fe}/\text{H}]$ and underabundance below $[\text{Fe}/\text{H}]$

$= -0.2$. The abundance of sulfur, produced by the massive-star models with $Z > 0.1$, is balanced by the iron production from the Type-Ia supernovae, which keeps the $[\text{S}/\text{Fe}]$ ratio relatively flat in the Population I stars (Timmes et al., 1995). But the production of all stable sulfur isotopes in the massive-star models is not sufficient to explain obtained abundance trend.

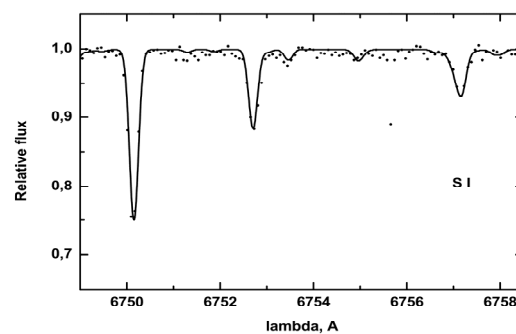


Fig.1. The observed and synthetic spectra fitting

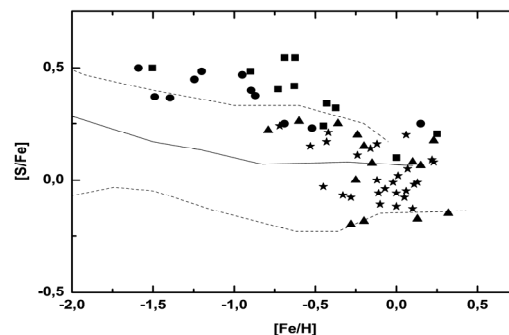


Fig.2. Dependence of $[\text{S}/\text{Fe}]$ vs. $[\text{Fe}/\text{H}]$

References

- Galazutdinov G.A.: 1992, *Prepr.SAO RAS*, **92**, 28.
 Clegg R., Lambert D., Tomkin J.: 1981, *ApJ*, **250**, 262.
 Francois P.: 1987, *Astron. and Astrophys.*, **176**, 294.
 Francois P.: 1988, *Astron. and Astrophys.*, **195**, 226.
 Katz et al.: 1998, *Astron. and Astrophys.*, **338**, 151.
 Korotin S.A.: 2009, *Asron. Rep.*, **53**, 651.
 Kurucz R.L.: 1993, CD ROM n13.
 Mishenina et al.: 2013, *Astron. and Astrophys.*, **552**, A128.
 Tsymbal V.V.: *ASP Conf. Ser.*, **108**, 198.
 Timmes et al.: 1995, *ApJS*, **98**, 617.

DETERMINATION OF THE SATELLITE'S ROTATION USING ITS LIGHT CURVE

Daniil Pavlenko

Astronomical Observatory of the I. I. Mechnikov Odessa National University
Odessa, Ukraine, *rereclon@gmail.com*

ABSTRACT. This article describes the method of determination of the Earth's artificial satellite's free (unplanned) rotation using its light curve and preliminary computed brightness charts (the spatial indicatrices of light scattering by the artificial satellite's surface), as well as provides examples of such solutions for simulated occurrences.

Introduction

In addition to the spinning with known parameters that is deliberately imparted to an artificial satellite, an unplanned rotation may occur. And generally, the characteristics of that rotation are undefined, yet the associated problems, such as inability to receive or transmit signals and energy shortage due to the failure in the satellite's positioning relative to the Sun, do not allow of estimating the parameters of such a rotation with only satellite's capabilities. In its turn, that may result in the loss of an expensive or unique satellite. However, it is possible to additionally support such an out-of-order satellite by the ground-based monitoring of changes in its light curve and interpreting them in terms of the rotation parameters. The rotation frequency can be determined by the brightness change intervals; and the orientation in space can be defined by non-uniformities in the light reflection [1]. It is natural that it is not all that simple, and there is a host of problems. For instance, the charts of characteristic features of the light reflecting off a satellite, allowing for all possible positions of that satellite and angles of the light reflection, should be created as early as the launch is performed. And it is reasonable that those charts can turn out to be useless when the specific characteristics of the brightness change later in space, for example, due to the damages caused by micrometeorites or incomplete unfolding of the solar panels. Besides, errors in both the brightness charts and the measurement of the satellite's brightness in orbit should not be neglected. With allowance for the above, the determined rotational parameters will often appear as a certain set of solutions with different probability rather than a single-valued result. Nevertheless, in most cases such investigation can provide useful and topical information on the satellite rotational parameters, not using the satellite's own capabilities at that.

Problem statement

It is required to determine the rotational parameters of the artificial satellite model by the passive remote photometric sensing method. Hence, the following will be known: two-line set of orbital elements (TLE), the model satellite light curve or curves, obtained by a single observer or by many observers - i.e., as a matter of fact, the photometric satellite model will be defined with already obtained brightness charts, which are the databases on the satellite brightness depending on its orientation relative to the light source and observer [2-3]. In the present study, the brightness charts were obtained for the model of axisymmetric satellite that allows of reduction the dimension of the four-dimensional array of brightness values; however, the artificial satellite model is planned to be replaced by a more complex one. The rotational parameters are supposed to be unaltered along the whole light curve.

Thus, the closed-loop model problem is considered: there are brightness charts available for the defined artificial satellite model, and one or several initial light curves, which act as the observed light curves, obtained either by a single or several observation sites for the real satellite orbit, are computed for that model.

The determination of the path or rotational path of, for instance, longitudinal axis of an artificial satellite (in this case – the axis of symmetry), for which the model light curve, as well as the array of the brightness values obtained by the corresponding charts will coincide with the initial observed light curve within the stipulated measurement accuracy, is deemed to be a solution of such a problem. As simple search of all possible rotational trajectories is a trivial method of solving the indicated problem, the omission of such a search to reduce the time and computer's capacity consumption to the maximum will be an additional requirement to the solution procedure.

Principle of the method

Three directions of the body's preferred axis (the axis of symmetry) in space at three different moments are necessary and sufficient to determine its rotational parameters. That allows of finding the small circle, the centre of which is the rotation pole; the small circle radius

defines the tilt angle of the rotation axis to the body's preferred axis while the angular velocity gives the rotation period. As initially we do not know the symmetry axis direction, we should determine it by ourselves; so we use the light curve and the brightness charts to do that. The brightness charts are created in such a way that two other coordinates define the symmetry axis direction in space for the fixed value of the phase angle (the angle between the satellite orientations towards the light source and observer), and the body's brightness is assigned to that direction [2-3]. Thus, having known the artificial satellite brightness and the angle between the Sun and observer for the specified instant, the corresponding symmetry axis direction in space can be determined by the brightness charts at the given moment. The problem is that equal brightness values are typically common to a large set of the symmetry axis directions. In other words, for each moment of time we will have several possible symmetry axis directions in the brightness chart reference frame, which are characterised by the same brightness (within the specified measurement accuracy). For brevity, those points on the brightness charts will be called isophots. If we try to determine the rotational parameters by the set of three different isophots, the number of alternative solutions will equal to the product of the quantity of isophots for each of three moments. For a hundred of isophots for each moment of time we will eventually obtain $100 \times 100 \times 100 = 1000000$ – a million of probable paths, and only one of them will be the true one. To find the true path, it would be necessary to plot a million of simulated light curves and compare them with the initial measured light curve for all instants. Although such operation is feasible, the computing time required would be out of proportion, the more so it is possible that the number of alternative paths is larger by an order of magnitude.

However, the number of implicit paths can be reduced. As we proceed from the assumption that the rotation frequency is constant, then such a path can be undoubtedly discarded as an infeasible one when the rotation frequency changes considerably at the time interval under test. We compute the rotation frequency within the interval between moments 1 and 2; subsequently, by a similar way we compute the frequency between moments 2 and 3, and if the frequency values differ by more than a certain value, the corresponding path is omitted. Thus, it is possible to considerably reduce the number of paths. At that, the stiffer constancy criterion of the rotation frequency is, the fewer alternative paths meet that criterion, and the higher is the probability to miss the true path.

The next step of reduction of false paths implies the consideration of alternative implicit paths determined by the above-described method, but this time for different sets of moments. Eventually, we will get several sets of alternative rotation paths. As the rotation frequency, the rotation axis direction and the initial phase (the initial direction of the symmetry axis) do not change with time, each set should contain one alternative solution with similar parameters of the path, and it is that solution that is the true rotation path.

It is clear that with a large number of false alternative paths it will become more likely that many false paths will be tested along with the true solution. That problem can be solved by statistically increasing the number of solutions;

but taking into account the finiteness of the light curve, their quantity will also be finite.

To reduce the number of false paths, it is also possible to toughen the criterion, according to which either similarity or equality of the observed satellite brightness to the values, indicated in the corresponding brightness chart grid points, is defined. Consequently, it is not always the case even for the true path that an alternative path suitable by the similarity criterion is found. Eventually, with correctly selected similarity criterion we will obtain matching distribution of alternative solutions with none of the solutions 100% matched for all sets of moments while the true rotation path has the maximum number of matches. That path can be finally tested by simulating the relevant light curve and comparing it with the observed one.

Moreover, it is worth of testing other alternative solutions that have number of matches standing out among the others. It is not improbable that there can be several alternative rotation paths that exhibit the light curve similar to the observed one. In that case, it can be concluded that a single-valued solution is not feasible under given conditions; and to obtain a single-valued result, it is necessary to collectively or individually increase the following factors: the discrete brightness chart features, the observed light curve accuracy, the number of the observed passes, and the quantity of the observers that on being geographically dispersed simultaneously measure the satellite brightness.

Measure of inaccuracy

To noticeably reduce the number of false alternative paths not accidentally rejecting the true one in so doing, it is necessary to properly choose the similarity factor stiffness and other parameters. The best result can be obtained when the similarity factor is equal to the mean photometric error. The parameters with poorer accuracy in their determination should also be excluded from the list of criteria. For instance, such a parameter as the initial position of the symmetry axis accumulates errors rapidly; therefore, it can be substituted by the angle between the symmetry axis and the rotation axis.

The total error is to be determined by two components, namely the light curve inaccuracy and the brightness chart discreteness. In our particularly simulation experiment the light curve inaccuracy was considered to be equal to zero whilst the discreteness in the brightness charts was 1 degree. Therefore, instead of actual direction of the symmetry axis with the precise phase angle the isophot determined a three-dimensional cube formed by the brightness charts, within the limits of which the corresponding brightness value fell. It is evident that all values, derived by the positions of those isophot points, have deviation from the true ones; at that it was found that such an error decreased with increasing distance between the relevant isophot points.

Figure 1 shows the errors in determination of the rotation axis pole coordinates, the angle between the rotation axis and the longitudinal axis of the model, as well as the current rotation phase depending on the angular distance between the relevant isophots expressed in terms of period's portion. It can be seen that when the

time elapsed between two measurements of isophots is close to the rotation phase 0.15, the accuracy in measurements will be optimal. Figure 2 shows the same errors in depends from the angle between the rotation axis and the axis of symmetry.

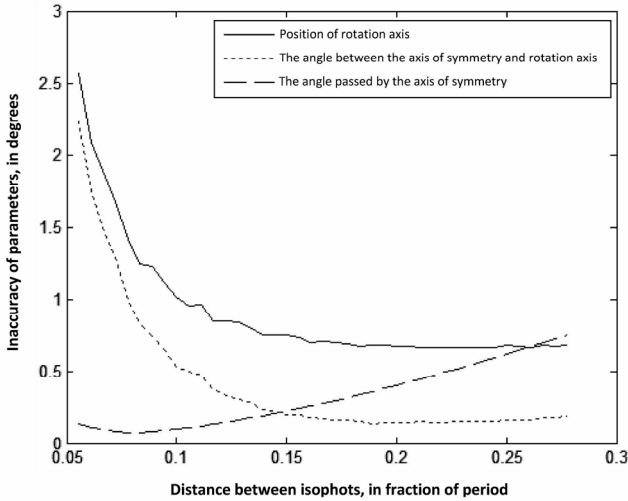


Figure 1. Errors in determination of the model rotational parameters against the angular distance between the relevant isophots.

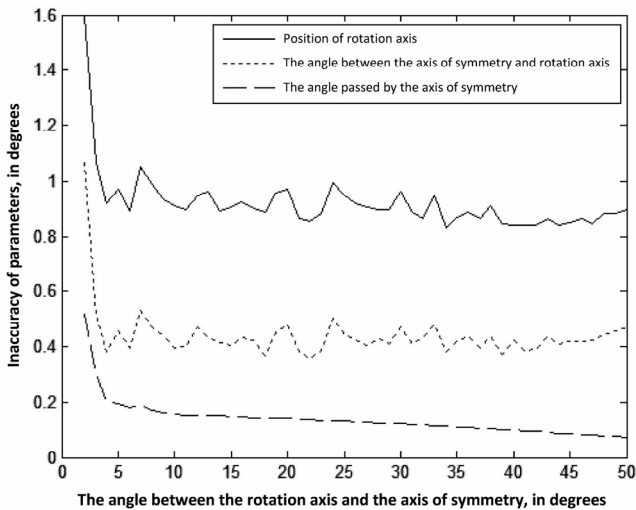


Figure 2. Errors in determination of the model rotational parameters against the angle between the rotation axis and the axis of symmetry.

One of the weaknesses of the described method of determination of rotational parameters of the artificial satellite model is that it is necessary to know an approximate value of the probable satellite angular velocity as early as at the first stage of analyzing probable rotational paths. Generally, the synodic rotation period is easily estimated when the apparent brightness change interval is available for the light curve. In case of great uncertainty, it is necessary to split up the range of probable rotation velocities into smaller ranges, for which the difference between the maximum and minimum velocities does not exceed 50%, and then, to find a general

solution (including that for the sidereal angular velocity) for each of them individually.

The description of the solution and result

1. Determination of the satellite position in orbit using its orbital data in the TLE format for each discrete time point of the observed light curve.
2. Computation of the phase angle between the light source (the Sun) and observer for each time point of the light curve.
3. Creation of the matrix for transformation of vectors from the equatorial satellite-centric coordinate system to the brightness chart reference frame at a certain instant in time. For the latter reference frame the Z-axis coincides with the direction towards the light source whilst the XOZ-plane contains the direction towards the observer (the phase angle plane).
4. Determination of the estimated range of values for the satellite rotation period based on the characteristics of its observed light curve if possible.
5. Selection of certain three moments with the interval between them close to a ninth of the rotation period and readout of the observed brightness.
6. Determination of probable symmetry axis directions in the brightness chart reference frame for each instant. The coincidence of the "chart's brightness" for a certain direction with the brightness of the observed light curve, within the specified measurement accuracy, is considered to be the grounds to designate that this direction as an "isophot".
7. Picking of all possible combinations of three isophots for different moments. Elimination of those combinations, for which the rotation frequency is essentially different for various pairs of time instants.
8. By using each three directions (isophots), converted back to the equatorial coordinate system, we derive the equation of plane, therefore the normal to that plane is the axis of rotation. The rotational velocity is determined by division of the angle between the points by the elapsed time. Then we derive other characteristics. So, the sum of those characteristics is the probable decision for rotation's kind.
9. Performance of the similar procedure for a certain number of times for other sets of moments. Comparison of the solutions resulted from each operation. Recording how many times the determined path of the longitudinal axis of the model body coincided with paths computed by other sets within the specified measurement accuracy. It is very likely that the path with maximum number of coincidences will be the true one.
10. Check-up of the obtained solution with maximum number of coincidences by plotting a corresponding light curve according to the brightness charts and comparing it with the initial one.
11. It is obvious that the light curves are very similar, and therefore, the obtained path is true or indistinguishable from that with the specified inaccuracy and discreteness in initial data.

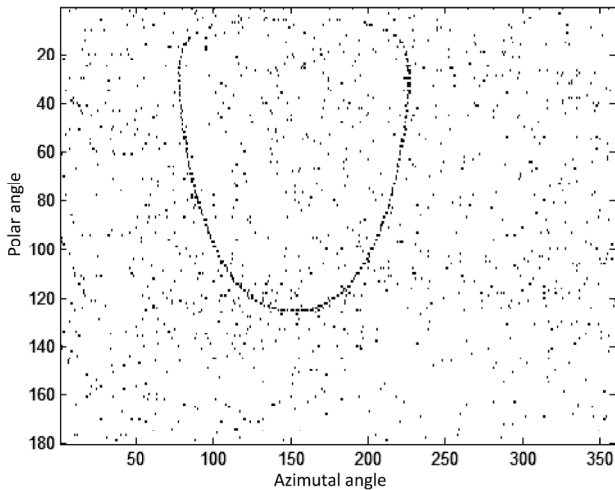


Figure 3. The summary isophots for a given time in a fixed satellite-centered coordinate system.

First we solve the direct problem – simulate the light curve low-orbit satellites. For example, consider the elements of the orbit of the Sich-2 [4].

1 37794U 11044G 12141.23295985.00000379 00000-0 88476-4 0 8582
2 37794 098.2290 218.2236 0014010 141.1597 219.0631 14.60067392 40408

Coordinates of the observer: latitude $46^{\circ}20'40.08''$ longitude $39^{\circ}45'20.32''$. We take one of the passages of the satellite and set start time of observation – May 17, 2012 in $20^{\text{h}}.1667$. We define rotation parameters – inclination of the axis of symmetry to rotation axis $nk = 60^{\circ}$, the polar angle of the rotation axis $pW = 64^{\circ}$ and the right ascension $\alpha W = 150^{\circ}$, period of the one complete revolution $T = 42$ seconds (the angular velocity is $8.57^{\circ}/\text{s}$). The error of shine values equal to 0.03% . As a result, we obtain a quasi-periodic light curve.

Inverse task. On the resulting light curve is sometimes difficult to determine the rotation period of the satellite, but as the initial value will take $T = 50$ s.

To visualize the solution of the problem look at the distribution of isophot's points for discrete moments of time in the coordinate system of brightness map (Figure 3). In this case, we can easily see the oval chain of isophots. This is the true direction in space of the longitudinal axis of body at different times, and the center of the oval - the rotation pole. The other points of isophots are false directions in the space of the longitudinal axis, but have the same shine (within the error) as in the true orientation of the body.

Now look at the result of the algorithm test. Found 34 possible paths of rotation (some are shown in Table 1).

Table 1 shows the following rotating parameters – three projection of rotation axis, the angle between the rotation axis and the longitudinal axis of the body, the rotation angular velocity. The sixth column – the number of matches (repeating solutions). The maximum number of repeating is 131 from 593, the other values are not higher than 3. Consider the rotation parameters with maximum repeatability. Translating

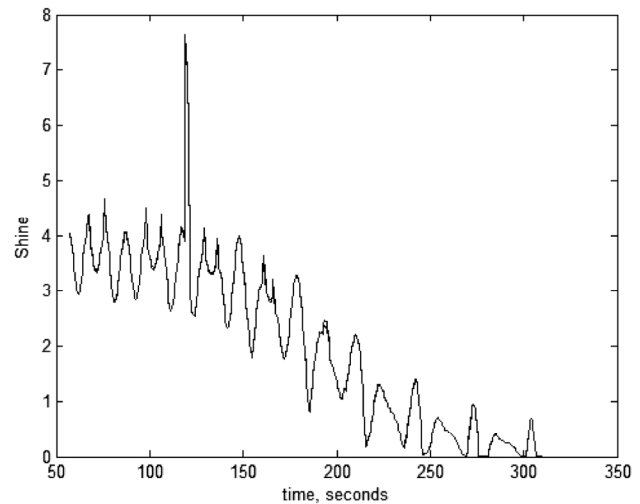


Figure 4. A comparison of the light curve, constructed for found rotation parameters, with the original light curve.

Table 1. Results of the solution to the rotation parameters.

X(W)	Y(W)	Z(W)	NK	w	N
-0,6138	-0,48301	0,624454	95,24231	-8,38806	0
-0,35448	0,32879	0,875351	147,7485	-10,9361	1
-0,31798	0,368376	0,873606	150,6086	-12,1351	0
0,362565	0,911941	0,192118	134,8943	-9,93484	0
-0,46488	-0,88232	0,073479	60,92391	-8,30496	131
-0,3791	0,404378	0,832325	157,4329	-13,2543	0
-0,41075	-0,38042	0,828595	111,5165	-10,7619	2
-0,81511	0,052696	0,5769	113,7678	8,096023	0
-0,81951	-0,26247	0,509418	96,18076	7,09923	0
-0,82469	0,10628	0,555502	117,0159	8,223101	0
-0,86196	-0,17144	0,477105	138,6802	2,952431	3

the Cartesian coordinates of the rotation axis from the coordinate system of brightness map we obtain a spherical equatorial coordinate $pW = 64^{\circ}.18$ and $aW = 149^{\circ}.9$. The period is found 43.3 seconds. The period is a relatively inaccurate, but it can be refined using the most distant in time isophots belonging to this rotation. As a result, we get the period = 42.8 seconds.

Conclusion

As a result of the algorithm is better to define the rotation axis of the satellite's model, the slope of the longitudinal axis to the rotation axis has an inaccuracy about one degree and the period - about one second. A comparison of the light curve constructed with the found rotation parameters, with the original one shows that they are extremely similar, but slightly different in extremes (Figure 4).

References

Melikyants S.M., Shakun L.S., Koshkin N.I., Dragomiretsky V.V., Strakhova S.L.: 2007, *Odessa Astron. Publ.*, **20/2**, 72.
Pavlenko D.: 2012, *Odessa Astron. Publ.*, **25/2**, 151.
The report No. 365 “The investigation of the free motion of the artificial satellites and asteroids and ecological problems of the near-Earth space”, Odessa, 2008, p. 111.
<http://www.celestrak.com/NORAD/elements/>

NUMERICAL MODELING OF GLOBULAR CLUSTERS TIDAL DISSOLUTION

M.V. Ryabova, E.G. Sendzikas, Yu.A. Shchekinov

Department of Physics, Southern Federal University
Rostov-on-Don, Russia, *mryabova@sfedu.ru*

ABSTRACT. Numerical model of dynamical evolution of globular clusters (GCs) is described, with an emphasis of the mass loss rate in tidal interactions with the Galaxy. On a set of models dependence of the tidal destruction on cluster parameters and initial conditions, such as: the initial cluster mass, its initial position in the Galaxy, the eccentricity of the orbit – are studied. An analytical description of tidal destruction of GCs and simple estimate of their lifetimes is proposed.

Key words: globular clusters – tidal perturbations: destruction.

1. Introduction

GCs have recently attracted attention of researchers (both observers and theorists) from the point of view of their origin and evolution in the Milky Way Galaxy. This interest is driven by the fact that GCs are amongst the oldest stellar population of the Galaxy, and therefore carry information about the very early evolution of the Galaxy and the Universe as a whole. Even though these circumstances is well known long time, only last several years the interest has been reanimated mostly due to recent development of observational techniques.

A principally important feature of dynamical evolution of GCs is determined by the fact that GCs throughout evolution undergo strong damaging effects from the galactic gravitational field. It is natural to assume therefore that the observed population of GCs is only a remaining part of a much larger population that existed in the earliest stages of the Galaxy evolution.

Recent observations of the GC Palomar 5 showed that the influence of the galactic tidal field can be quite substantial, so that during the evolution it could lose up to 95% of its initial mass. The problem is thus to reproduce the initial state of the huge cluster with a tiny remnant in hands.

2. The method

Numerical modeling has been performed using the

NBODY6 code. The galactic potential is accepted in the form of a three-component model that includes the bulge, Miyamoto-Nagai disk (Miyamoto & Nagai, 1975), and logarithmic halo potential.

3. Loss of stars

In the present work a set of models with different initial parameters and conditions for the clusters (the mass, radius, position, velocity) has been run. Some of their galactic orbits are shown in Fig. 1.

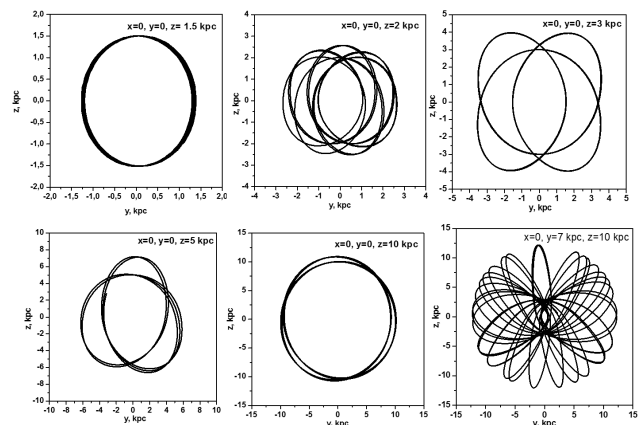


Figure 1: Examples of orbits in the $Y - Z$ plane.

To investigate the dissolution of GCs, time dependence of the number of stars gravitationally bound to their parent clusters have been calculated. Fig. 2 shows these dependencies for the clusters with orbits presented on Fig. 1. The figure demonstrates a nonmonotonic star loss rate of given GCs, with a series of well pronounced spikes.

4. Effect of the disk and the perigalacticon

Figure 3 shows time dependence of the number of stars in a GC, its position above the plane and the distance to the center of the galaxy for GC model with the initial coordinates $x = 0$, $y = 7$ kpc, $z = 10$ kpc.

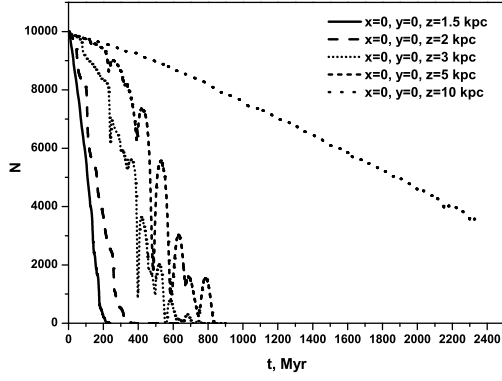


Figure 2: The dependence of the number of gravitationally bound stars vs. time for the orbits shown above in Fig. 1.

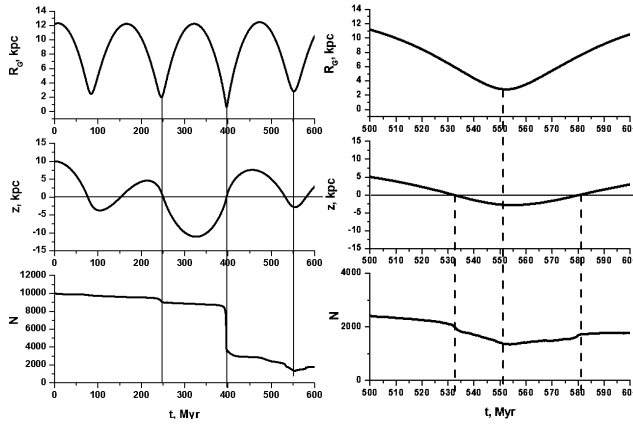


Figure 3: Time dependence of the number of stars in a GC, its position above the plane of the disk and the distance to the Galactic center (bottom to up); time interval in the range of 500 – 600 Myr is zoomed on the right panel.

Fig. 3 shows that the highest star loss occurs in moments of passing through the disk and perigalacticon. However, for most of our models these events are weakly separated in time. In order to make them seen clearer the acceleration of a GC from the Galactic gravitation $|\Phi'|$, and the magnitude of the tidal forces acting on it $|\Phi''|$ is depicted on Fig. 4. Despite the fact that the tidal force peaks when the cluster passes through the disk, its destructive action is too short, such that the dominant destructive effect comes from the perigalacticon domain.

5. GC dissolution model

Assuming that the instantaneous rate of GC dissolution depends on the current number of stars N , their mean mass m , GC radius R_c and the magnitude of the tidal forces Φ'' , one can qualitatively write the equation

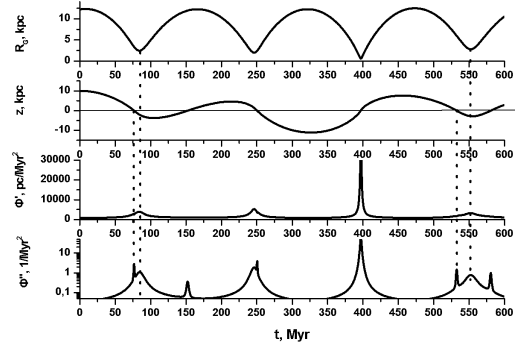


Figure 4: Time variations of the galactic acceleration and tidal force along the GC orbit.

for dN/dt as

$$\frac{dN}{dt} = -\alpha(N) \cdot \Phi'^A \cdot R_c^B \cdot G^C \cdot m^D$$

(G is gravitational constant), and dimensional analysis gives easily

$$\frac{dN}{dt} = -\alpha(N) \cdot \sqrt{\Phi''} \cdot \left(\frac{R_c^3 \Phi''}{Gm} \right)^{-C},$$

or in the general case

$$\frac{dN}{dt} = -\sqrt{\Phi''} \cdot f \left(N, \frac{R_c^3 \Phi''}{Gm} \right). \quad (1)$$

The function f can be assumed as a power law

$$f \left(N, \frac{R_c^3 \Phi''}{Gm} \right) \sim \alpha N^p \left(\frac{R_c^3 \Phi''}{Gm} \right)^q$$

for which the best approximation among the existing set of calculated models with different parameters and initial conditions (GC mass, the position in the Galaxy, the eccentricity of the orbit) is

$$\alpha \sim 25, \quad p \sim 1/6, \quad q \sim 1/3.$$

Similarly, the radius of the cluster is estimated as

$$R_c \sim R_0 (N/N_0)^{-3/2}.$$

Thus, the best agreement between the qualitative description and numerical calculations is given by the expression

$$\frac{dN}{dt} \sim -25 N^{-4/3} \Phi''^{5/6} R_0 N_0^{3/2} (Gm)^{-1/3}. \quad (2)$$

Assuming that the tidal field varies weakly along the GC orbit $\Phi'' = \text{const}$ (as, for example, for a circular orbit in the plane of the galactic disk), the equation (2) reduces to

$$dN/dt = -\beta \cdot N^{-p},$$

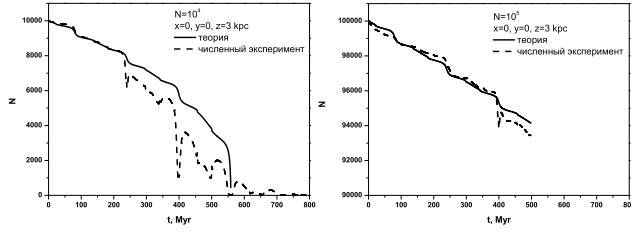


Figure 5: Comparison of numerical calculations and theoretical predictions by (2).

so

$$N(t) = N_0 \left(1 - \frac{t}{T}\right)^{1/(p+1)}$$

and GC lifetime is

$$T \sim N_0^{p+1}/[(p+1)\beta].$$

If one fixes the initial radius of the cluster $R_0 = \text{const}$, then the dependence of the lifetime on the initial mass (i.e. number of particles) is given by

$$T \sim 0.02 (Gm)^{1/3} R_0^{-1} \Phi''^{-5/6} N_0^{5/6},$$

and at a fixed density $n_0 = \text{const}$

$$T \sim 0.03 (Gmn_0)^{1/3} \Phi''^{-5/6} N_0^{1/2},$$

which is close to the relation $T \sim N_0^{0.4}$ from (Baumgardt & Makino, 2003).

6. Resistance to dissolution

To investigate GC stability, the parameter, equal to the ratio of the average value of the tidal forces to the average attractive forces within the cluster, can be introduced

$$\begin{aligned} \omega &= \frac{\Delta F_G}{F_c} = \frac{R_c \cdot dF_G/dR}{F_c} = \\ &= \frac{R_c \cdot m d^2 \Phi / dR^2}{GM_c m / R_c^2} = \frac{R_c^3 \Phi''}{GM_c}. \end{aligned}$$

In the case of the point mass potential

$$\omega = \frac{M_G}{M_c} \left(\frac{R_c}{R}\right)^3.$$

The parameter ω coincides to within a factor $1/N$ with the dimensionless parameter, being the second argument in (1).

On Fig. 6 gray circles shows the value of the stability parameter ω for the observed GCs, depending on the galactocentric distance R_G . The lines correspond to the dependence of ω on R_G for clusters with a constant density. The density increases from the bottom to the top. Under the assumption that the orbits are circular,

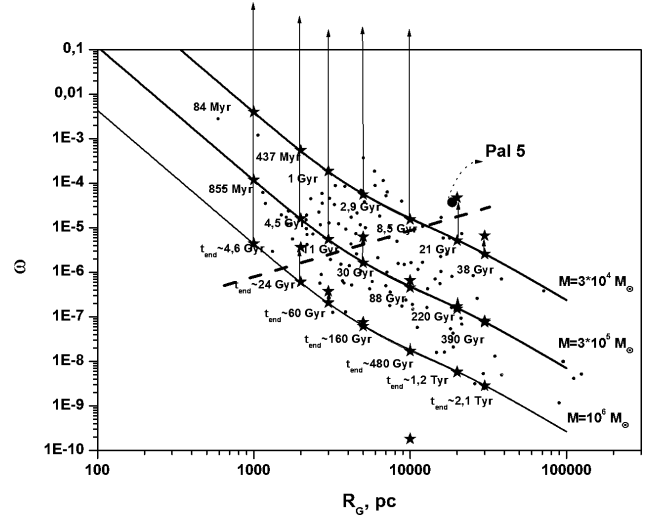


Figure 6: The parameter of GC resistance to tidal dissolution, depending on the galactocentric distance.

estimates for GCs ages (see section 5) are given on Fig. 6 for various ratios of ω and R_G at the initial time, the arrows show the direction of increase of ω in time.

7. Conclusions

We have estimated the effects of the disk and perigalacticon on destruction of GCs. For elongated orbits the effect of passing through perigalacticon is greater.

Estimates of the star loss rate of GCs and their lifetime due to the tidal field of the galaxy are given.

The evolution of the stability parameter of GC against tidal destruction, and comparison with observational data may indicate that approximately half of the Galactic GCs will be destroyed soon.

Acknowledgements. This work has been funded by grant of the Ministry of Education and Science of the Russian Federation N. 14.A18.21.1179.

References

- Baumgardt H., Makino J.: 2003, *MNRAS*, **340**, 227.
 Miyamoto M., Nagai R.: 1975, *PASJ*, **27**, 533.
 Odenkirchen M. *et al.*: 2003, *AJ*, **126**, 2385.

DETERMINATION OF PARAMETERS OF WHITE DWARF BY THE HYDROGEN SPECTRUM IN THE MODEL WITH LINEAR EQUATION OF STATE

Christian Scherbakov

Department of Astrophysics, Ivan Franko National University of Lviv
Lviv, Kyryla and Methodia str., 8, *kristian.for@gmail.com*

ABSTRACT. Solutions to Einstein's field equations, for a static spherically symmetric perfect fluid model with linear equation of state are found exactly. It is shown that space of WD can be presented as a space with deformed Heisenberg algebra so WD observational data provide powerful tool in deformed space research. Lane-Emden equation for isothermal model is considered in details.

1. Introduction

We consider in this section the spacetime of non-rotating white dwarf. Exact solutions of General Relativity are hard to come by. A great majority of those known make assumption about symmetry of spacetime, see, for instance, Delgaty & Lake (1998) and Stephani et al. (2003). Only in a few cases, they are presented as general solutions, depending on a few independent continuous parameters such as mass, charge and angular momentum. In general, the non-linearity of partial differential equations of General Relativity makes it difficult to find exact analytical solutions.

Due to the high symmetries of these objects, all non-diagonal elements in the metric vanish, and, due to the static requirements for the gravitational fields, the metric elements are mere functions of the position of a spherically symmetric shell. Static and spherically symmetric non-rotating stars therefore generate a spacetime of the following form

$$ds^2 = -c^2 \exp[2\nu(r)] dt^2 + \exp[2\lambda(r)] dr^2 + r^2 (d\theta^2 + \sin^2\theta d\varphi^2) \quad (1)$$

the two functions $\nu(r)$ and $\lambda(r)$ are uniquely given by the mass-energy distribution $\rho(r)$ in the white dwarf. As in the Newtonian stellar structure, we can define the total mass inside the radius r

$$M(r) = 4\pi \int_0^r \rho(r') r'^2 dr' \quad (2)$$

The properties of white dwarf can be obtained by solving the Einstein equations

$$R_{ab} - \frac{1}{2} g_{ab} R = \frac{8\pi G}{c^4} T_{ab} \quad (3)$$

where R_{ab} and R are Ricci tensor and Ricci scalar respectively. The energy-momentum tensor is given by

$$T_b^a = \text{diag}(-\rho c^2, P, P, P) \quad (4)$$

Equation (3) in the case of white dwarf takes the form

$$\frac{1}{r^2} - \exp(-2\lambda) \left(\frac{1}{r^2} - \frac{2\lambda'}{r} \right) = \frac{8\pi G}{c^2} \rho \quad (5)$$

$$\frac{1}{r^2} - \exp(-2\lambda) \left(\frac{1}{r^2} + \frac{2\nu'}{r} \right) = \frac{-8\pi G}{c^4} P \quad (6)$$

Using the differential energy-momentum conservation law $T_{j;i}^i = 0$ it is easy to find out Tolman-Oppenheimer-Volkoff equation

$$\frac{dP}{dr} = \frac{-GM\rho}{r^2} \left(1 + \frac{P}{\rho} \right) \left(1 + \frac{4\pi r^3 P}{Mc^2} \right) \left(1 - \frac{2GM}{c^2 r} \right)^{-1} \quad (7)$$

Specifying the equation of state is the very first step to find solutions to gravitational field equations for metrics (1). However, despite the growing number of exact static spherically symmetric perfect fluid solutions, most equations of state for known exact solutions have no physical motivation. It seems like these are chosen for specific purpose of simplifying the differential equations, and thereby allowing exact solutions to be found. Nonetheless, simplest models considered in many papers are in accordance (in conformity) with much wider class of models. The solution of the differential equa-

tion (Hartle, 1978) for $T = const$ is following

$$\rho = \frac{T}{2\pi G \left(1 + 6\frac{T}{c^2} + \left(\frac{T}{c^2}\right)^2\right)} \cdot \frac{1}{r^2} \quad (8)$$

$$M = \frac{2T}{G \left(1 + 6\frac{T}{c^2} + \left(\frac{T}{c^2}\right)^2\right)} \cdot r \quad (9)$$

and solutions of equations (5) - (6) can be written in the form

$$e^{-2\lambda} = 1 - \frac{4T}{c^2 \left(1 + 6\frac{T}{c^2} + \left(\frac{T}{c^2}\right)^2\right)} \quad (10)$$

$$\nu = 2\frac{T}{c^2}e^{2\lambda} \left(1 + \frac{T}{c^2}\right) \cdot \frac{1}{\left(1 + 6\frac{T}{c^2} + \left(\frac{T}{c^2}\right)^2\right)} \cdot \ln\left(\frac{r}{R}\right) + \nu(R) \quad (11)$$

The line element that describes 4-dimensional homogeneous and isotropic spacetime is given by

$$ds^2 = -c^2 e^{2\nu(R)} \cdot \left(\frac{r}{R}\right)^\beta dt^2 + e^{2\lambda} dr^2 + r^2 (d\theta^2 + \sin^2(\theta)d\varphi^2) \quad (12)$$

$$\dot{\beta} = 4\frac{T}{c^2}e^{2\lambda} \cdot \left(1 + \frac{T}{c^2}\right) \cdot \frac{1}{\left(1 + 6\frac{T}{c^2} + \left(\frac{T}{c^2}\right)^2\right)} \quad (13)$$

Let introduce new variable z such that

$$z = \frac{Re^\lambda}{1 - \frac{\dot{\beta}}{2}} \left(\frac{r}{R}\right)^{1 - \frac{\dot{\beta}}{2}} \quad (14)$$

Then line element of spacetime reads

$$ds^2 = \zeta^2 \left(\frac{z}{R}\right)^{2\gamma} \cdot (-\eta^2 dt^2 + dz^2 + Kz^2 (d\theta^2 + \sin^2\theta d\varphi^2)) \quad (15)$$

where

$$2\gamma = \frac{\dot{\beta}}{1 - \frac{\dot{\beta}}{2}}$$

$$\zeta^2 = \left[\left(1 - \frac{\dot{\beta}}{2}\right) e^{-\lambda} \right]^{2\gamma}$$

$$\eta^2 = c^2 e^{2\nu(R)}$$

$$K = \left(1 - \frac{\dot{\beta}}{2}\right)^2 e^{-2\lambda}$$

The line element can be written in terms of flat metric

$$ds^2 = \zeta^2 \left(\frac{z}{R}\right)^{2\gamma} \cdot (-\eta^2 dt^2 + (1 - K) dz^2 + K d\sigma^2) \quad (16)$$

where $d\sigma^2$ is the time-independent metric of the 3-dimensional flat space: $d\sigma^2 = \delta_{ij} dz^i dz^j$.

2. Deformed space of White Dwarf

A particle with mass m in space of white dwarf can be described by Dirac-Born-Infeld Lagrangian:

$$L = -\chi \cdot \left(\frac{z}{R}\right)^\gamma \sqrt{1 - \frac{K}{\eta^2} \mathbf{v}^2 - \frac{(1-K)}{\eta^2} v_z^2} \quad (17)$$

here and below a dot denotes the derivative with respect to the time, "·" $\equiv \frac{d}{dt}$ and $|\mathbf{v}| = \frac{d\sigma}{dt}$, $v_z = \frac{(\mathbf{z}, \mathbf{v})}{z} = \dot{z}$. We use the notation $\chi = m\eta\zeta$. Hamiltonian can be calculated using the usual Legendre transformations

$$H = \frac{\chi \left(\frac{z}{R}\right)^\gamma}{1 - \frac{K}{\eta^2} \mathbf{v}^2 - \frac{1-K}{\eta^2} v_z^2} \quad (18)$$

and can be written in the canonical form

$$H = \sqrt{\chi^2 \left(\frac{z}{R}\right)^{2\gamma} + \frac{\eta^2}{K} \mathbf{p}^2 + \frac{(1-K)\eta^2}{K} p_z^2} \quad (19)$$

where Hamiltonian is expressed in terms of the momenta \mathbf{p} and $p_z = \frac{(\mathbf{z}, \mathbf{p})}{z}$. From expression (14) it can be seen that in 1D space we have deformed commutation relation

$$[z, p] = i\beta \left(\frac{z}{R}\right)^{-\gamma} \quad (20)$$

where $\beta = \hbar e^\lambda \left[\left(1 - \frac{\dot{\beta}}{2}\right) e^{-\lambda} \right]^{-\gamma}$. A natural generalization of (21) which preserves the rotational symmetry is:

$$[z_i, p_j] = i\beta \left(\frac{z}{R}\right)^{-\gamma} \delta_{ij} \quad (21)$$

In the position representation p_i and z_i act as operators

$$\hat{z}_i \psi(\mathbf{z}) = z_i \psi(\mathbf{z}) \quad (22)$$

$$\hat{p}_i \psi(\mathbf{z}) = -i\beta \left(\frac{z}{R}\right)^{-\gamma} \frac{\partial}{\partial z_i} \psi(\mathbf{z}) \quad (23)$$

3. Coulomb-like problem in space with deformed Heisenberg algebra

In this section we consider Hamiltonian with well-known Coulomb-like potential $U = \frac{-\alpha}{z}$ in space of White Dwarf. From the expression for the Hamiltonian and the representation for z_i and p_i we find out

the following generalised form for the stationary state Klein-Gordon equation:

$$E^2\psi + \frac{2E\alpha}{z}\psi + \frac{\alpha^2}{z^2}\psi = \chi^2 \left(\frac{z}{R}\right)^{2\gamma} \psi - \frac{\eta^2}{K}\beta^2 \left(\frac{z}{R}\right)^{-2\gamma} \sum_{i=1}^3 \frac{\partial^2}{\partial z_i^2} \psi + \frac{\eta^2\beta^2\gamma}{KR^2} \left(\frac{z}{R}\right)^{-2\gamma-2} (\mathbf{z}, \nabla) \psi + \frac{(1-K)\eta^2}{K} \frac{(\mathbf{z}, \nabla)^2}{z^2} \psi \quad (24)$$

Note that in the spherical variables operator (\mathbf{z}, ∇) act as

$$(\mathbf{z}, \nabla) \psi = 3z \frac{\partial}{\partial z} \psi + \tan(\theta) \frac{\partial}{\partial \theta} \psi - 2 \cot(2\varphi) \frac{\partial}{\partial \varphi} \psi \quad (25)$$

In order to find the explicit solution it is useful to introduce, as usual, a new variable ξ in terms of which equation (24) takes the form

$$-k_5 \left(1 - \frac{k_3}{k_5} \xi^{-2\gamma}\right) \frac{\partial^2}{\partial \xi^2} \psi + (2k_3 - k_4) \xi^{-2\gamma-1} \frac{\partial}{\partial \xi} \psi - \frac{k_5}{\xi} \frac{\partial}{\partial \xi} \psi + \frac{k_1}{\xi} \psi + \frac{k_2}{\xi^2} \psi - \chi^2 \xi^{2\gamma} \psi + E^2 \psi = 0 \quad (26)$$

where

$$k_1 = \frac{2E\alpha}{R} \quad k_2 = \frac{\alpha^2}{R^2} \quad k_3 = \frac{\eta^2\beta^2}{KR^2} \quad k_4 = \frac{3\eta^2\beta^2\gamma}{KR^2} \quad k_5 = \frac{9(1-K)\eta^2}{KR^2}$$

4. White Dwarf with linear equation of state

As it can be seen from previous sections in general equation of state can be written as

$$P = T(\rho_0)\rho_0 \quad (27)$$

We consider in this section the simplest case with constant temperature, so we have linear equation of state. For the parametrization $\Gamma = 1$ we now introduce dimensionless variables

$$\rho_0 = \rho_c e^\theta \quad r = a\xi \quad (28)$$

whit $\rho_c = \rho_0(0)$ as the central density and a

$$a = \sqrt{\frac{T}{4\pi G\rho_c}} \quad (29)$$

The hydrostatic equilibrium therefore satisfies the following equation

$$\frac{1}{\xi^2} \frac{\partial}{\partial \xi} (\xi^2 \theta') = -e^\theta \quad (30)$$

The mass of the white dwarf can be found as

$$M(\xi) = M_0 \xi^2 |\theta'(\xi)| \quad (31)$$

where $M_0 = 4\pi \left(\frac{T}{4\pi G}\right)^{\frac{3}{2}} \frac{1}{\sqrt{\rho_c}}$.

Conclusions

In this paper we described space of White Dwarf via Lagrangian formalism and found expressions that allow us to find hydrogen atom spectra. This paper is not complicated because of it is expected to find graphical presentation for hydrogen spectra and consider relativistic Lane-Emden equation, nonethelless it can be helpful in understanding star evolution and physics of compact objects.

References

- Delgaty M. S. R. & Lake K.: 1998, *Comput. Phys. Commun.* **115**, 395.
 Stephani H., Kramer D., MacCallum M.A.H., Hoenselaers C.: 2003, *Exact Solutions of Einstein's Field Equations*, Cambridge University Press.
 Hartle J.B.: 1978, *Phys. Rep.* **46**, 201.

BELARUSIAN PROJECT “ASTROBLOKNOT” (ASTRONOMICAL NOTEBOOK) AND DATA MINING: RESULTS OBTAINED IN THE CONSTELLATION OF EQUULEUS

Ivan Sergey, Sergei Dubrouski, Igor Baluk, Alexander Pobiacha

The Regional Centre of Technical creativity of children and youth (RCTCCY)

Oktyabrya avenue, 36 A, Gomel, Belarus

seriv76@tut.by, toliman@tut.by, balig@tut.by, apobiyaha@gmail.com

ABSTRACT. Many photometric sky surveys are currently available on the open-access web-sources. The Northern Sky Variability Survey (NSVS), the All Sky Automated Survey 3 (ASAS-3) and the Catalina Real-Time Transient Survey (CRTS) are the most popular among them. In February 2013, Belarusian amateur astronomers made the decision to carry out a search for new variable stars using the CRTS dataset.

We were motivated by the following considerations: the mentioned survey is the most large-scale by many criteria, namely: the survey depth reaches up to 21 magnitudes; the photometry is available for 500 million objects (with around 300 light curves for most of them); the survey has been conducted for more than 9 years already; the photometry is high-precision.

To improve the detection efficiency, the software for data loading, filtering and processing was written. The main data filter criteria are the ratio of the amplitude of the brightness variation to the measurement error and the limiting magnitude (up to 18 magnitudes). After the

preliminary processing of the photometric arrays, at the second stage of data filtering the CSS programme for searching the period or cycle of brightness variations in the photometric sequences by the Lafler-Kinman method, which is similar to the simplified programme by Vitaliy Goranskiy.

At the final stage the physical parameters of new variable stars were specified and recorded in the VSX database.

The constellation of Equuleus (area of 71.6 square degrees) was selected as the first experimental target of the project. Before February 2013 there were about 300 variable stars recorded in that constellation.

During May-August 2013 we have processed about 700 thousand of candidate variables in the mentioned constellation, and eventually, the number of known variable stars in the constellation Equuleus increased by 371.

The irregular and semiregular variable stars detected by us have still been studied and their cycles and characteristics are specified.

Type of variability	Number of variables	The link to one of the variables of the indicated variability type that were detected by us
AGN	5	http://www.aavso.org/vsx/index.php?view=detail.top&oid=318346
BY	6	http://www.aavso.org/vsx/index.php?view=detail.top&oid=318530
CEP	1	http://www.aavso.org/vsx/index.php?view=detail.top&oid=318232
DSCT	2	http://www.aavso.org/vsx/index.php?view=detail.top&oid=318302
EA	57	http://www.aavso.org/vsx/index.php?view=detail.top&oid=318149
EB	23	http://www.aavso.org/vsx/index.php?view=detail.top&oid=318467
ELL	1	http://www.aavso.org/vsx/index.php?view=detail.top&oid=322914
EW	175	http://www.aavso.org/vsx/index.php?view=detail.top&oid=322709
GCAS	5	http://www.aavso.org/vsx/index.php?view=detail.top&oid=318345
HADS	9	http://www.aavso.org/vsx/index.php?view=detail.top&oid=318117
I	28	http://www.aavso.org/vsx/index.php?view=detail.top&oid=318480
L	1	http://www.aavso.org/vsx/index.php?view=detail.top&oid=318453
ROT	2	http://www.aavso.org/vsx/index.php?view=detail.top&oid=318406
RRAB	21	http://www.aavso.org/vsx/index.php?view=detail.top&oid=318371
RRC	26	http://www.aavso.org/vsx/index.php?view=detail.top&oid=317888
RRD	5	http://www.aavso.org/vsx/index.php?view=detail.top&oid=318375
RS	3	http://www.aavso.org/vsx/index.php?view=detail.top&oid=318383
SRD	1	http://www.aavso.org/vsx/index.php?view=detail.top&oid=317894
Total	371	

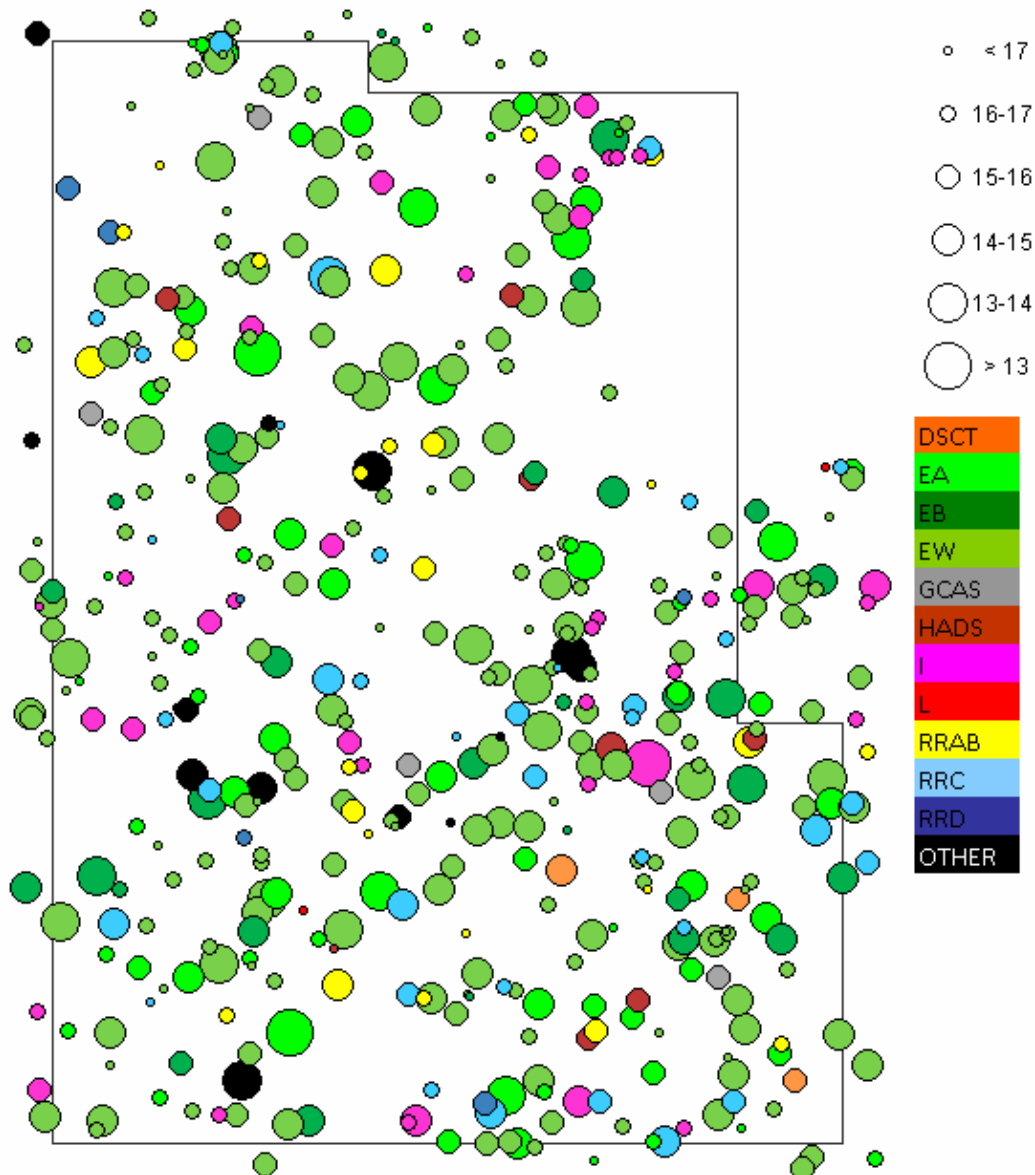


Figure 1: The chart of variable stars that have been detected during May-August 2013 within the framework of Data Mining project (“Astrobloknot” project); the colour of the stars correspond to certain variability types.

At present the investigations are proceeded in the constellation of Pegasus while alternative further studies have been discussed with the CRTS project developers (A. Drake et al., 2012)

Besides, it would be rather interesting to study a series of variables by measuring their brightness using historically valuable photographic plates from Odessa photographic glass plate archive in the B and V band.

The following specialists participated in the Data Mining project (“Astrobloknot” project), being responsible for the indicated activities:

- S. Dubrowski and A. Pobiacha were responsible for the writing of the software and the preliminary processing of data;

- I. Sergey, who initiated the search of new variable stars in the CRTS dataset, and I. Baluk, who detected the

largest number of variables within the CRTS project experiment, were responsible for searching and recording new variables.

The scientific advisers of the Data Mining project within “Astrobloknot” project were I. S. Bryukhanov and I. L. Andronov.

Acknowledgements. We express our gratitude to S.M.Andrievsky, N.N.Samus’ and S.Otero for their contribution to the project.

References

Drake A.J., Djorgovski S.G., Mahabal A. et al.: 2012, *New Horizons in Time-Domain Astronomy, IAU Symp.*, **285**, 306.

INCREASE IN THE ARRAY TELEVISION CAMERA SENSITIVITY

O. S. Shakhrukhanov

Astronomical Observatory of the I. I. Mechnikov Odessa National University

ABSTRACT. A simple adder circuit for successive television frames that enables to considerably increase the sensitivity of such radiation detectors is suggested by the example of array television camera QN902K.

Due to its high sensitivity of 0.00015 lx, the array television camera QN902K has become widespread both among amateur astronomers and professional astrophysicists. Other similar high-sensitivity cameras are popular as well. It is possible to considerably improve the sensitivity by increasing the signal storage time for the array. Due to an increase in measured thermal background, it is impossible to set the storage time of several seconds and longer for cameras without proper cooling. When the storage time is less than 1 second, the thermal background effect is not substantial.

A simple circuit of the device that regulates the storage time is presented here below. The camera sensitivity increases non-linearly with the storage time. That results from the more effective charge-packet transfer (the

charge-packet transfer losses that form a considerable part of the instrument errors decrease proportionally with the storage time).

The designed device enables to store images of up to 16 television frames. The number of frames can be set using binary code in signal inputs D1-D4 of the external control device. Array television cameras are intermediate between television cameras and cooled CCD cameras. The image processing can be performed by the methods that have been already in use in the television astronomy.

References

- Pratt W. Digital image processing, Moscow, Mir, 1982, **2**, 480 p.
- Prokofieva-Mikheylovskaya V.V., Strygin N.Z., Sukhov P.P., Karpenko G.F.: 2007, *Bull. of the Crimean Astrophysical Observatory* 103, **3**, p. 238-245.

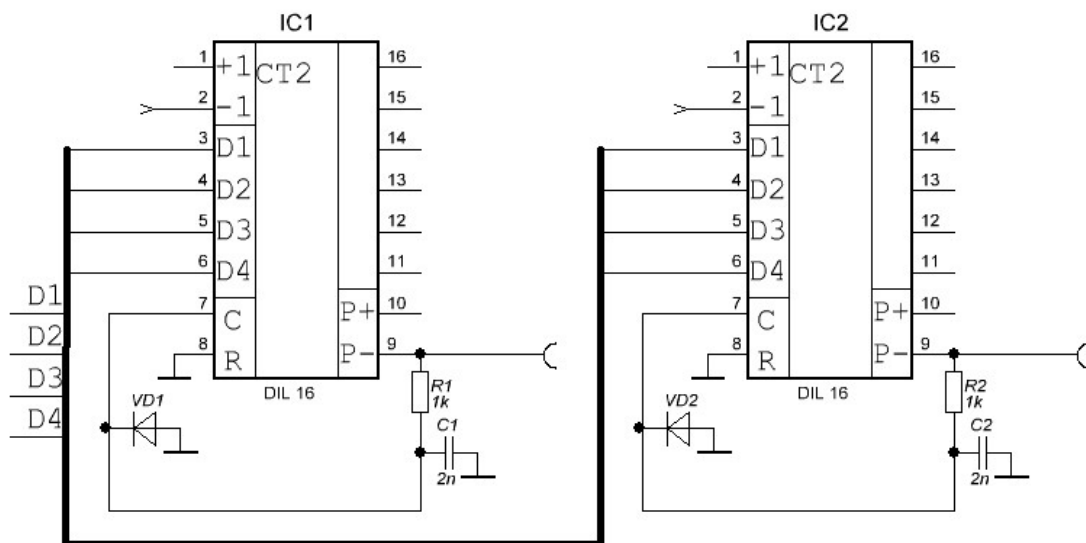


Figure 1

DETERMINATION OF THE STELLAR SCINTILLATION PROPERTIES WITH THE FAST-PHOTOMETRIC CAMERA

O.S.Shakhrukhanov

Astronomical Observatory of the I.I.Mechnikov Odessa National University,
Shevchenko Park, 65014, Odessa, Ukraine

ABSTRACT. In the present study it is shown that a television camera with adjustable signal storage time enables to measure the frequency and amplitude of the stellar scintillation. It can be used for telescopes with adaptive optics to substantially improve the image quality.

The commonly used array astrophysical observation instruments operate in the long storage time modes. At that, the scintillation effects are averaged, and only integral characteristics can be determined from the observations. The observational technique of the atmospheric research with the laser beam requires special-purpose equipment and processing. A television camera with adjustable storage time allows of measuring the frequency and amplitude of the stellar scintillation. A star's radiant image can be resulted from observations using such a camera with the storage time of several television frames. The scintillation properties can be determined by the number of rays, their length and shape. If the radiant image is steady, it means that the ratio of the storage time to the period is expressed as a multiple. And the multipleness is defined by the number of rays. For the rotating image the ratio is to be a fraction. It is even possible to measure the scintillation properties when displaying the data on a TV screen. The computer image processing is required to determine the values accurately. The described instrument can also be used for telescopes with adaptive optics. That will enable to significantly improve the image quality. For the spectral observations, the spectrograph limiting magnitude and the signal-to-noise ratio are increased.

References

- Priestley C.H.B. *Turbulent transfer in the lower atmosphere*. Leningrad: Hydrometeoizdat, 1964 (in Russian).
- Tatarskiy V.I. *Distribution of waves in the turbulent atmosphere*. Moscow: Nauka, 1967 (in Russian).
- Kolmogorov A.N.: 1941, *Proceedings of the USSR Academy of Sciences*, **32** (in Russian).
- Chukin V.V. *A study of the Earth's atmosphere by the electromagnetic radioscapy*. Russian State Hydrometeorological University, Saint-Petersburg, 2004 (in Russian).

ESTIMATIONS OF DYNAMIC PARAMETERS AND POSSIBLE HABITABLE ZONES FOR SELECTED STARS OF PULKOVO PROGRAM

N.A. Shakht¹ and L.G. Romanenko²

Central (Pulkovo) Astronomical Observation of RAS, St-Petersburg, Russia

¹shakht@gao.spb.ru , ²lrom@gao.spb.ru

ABSTRACT. We give the results of a study of selected stars located in the neighborhood of the Sun. Their observations have been made by means of Pulkovo 26-inch refractor. An interest to these objects is raised in connection with expected results of the planned space missions. We have made an estimation of habitable zones for possible planets rotating around of these stars.

Key words: binary stars, exoplanets, HZ, space projects Gaia, NEAT.

1. Introduction

Some results of observations of wide astrometric double stars on a 26-inch refractor in Pulkovo are represented.

The program of observation includes about 400 selected single and double stars located in the neighborhood of the Sun. The most part of stars of our program contain near stars of late spectral classes. Many of them are observed during some decades.

Thus we have long-term photographic and CCD-series with total duration more 50 years of relative positions with the error of 0".01 for mean annual normal place.

On the basis of Pulkovo observations more than 50 orbits of double stars were received with calculated sum of masses of components (Kiselev et al., 2009). In some cases we can estimate the individual mass of a component (Gorshanov et al., 2006, Shakht et al., 2010).

We would like to review some our stars as the possible objects for combined researches with the space and ground-based means.

2. Actuality

As examples we took stars with long series (more than 40 years) of observations: 61 Cyg, Stein 2051, ADS 7251, 16 Cyg with the parallaxes of Hipparcos which equaled 0".287, 0".180, 0".164 and 0".047 correspondingly. The more remote star ADS 8002

($\pi = 0".051 \pm 0".007$ was calculated on Pulkovo data, see, Grosheva, et al., 2013) has the precise positions during 35 years.

ADS 14636 (61 Cyg) and ADS 7251 – the nearest stars with possible planetary satellites – are selected to NASA Star and Exoplanets Database as the first targets for observations from space. 61 Cyg is also one of the main targets for observations with future NEAT (Nearby Earth Astrometric Telescope) program (Malbet et al., 2012). The component B of star ADS 12 815 (16 Cyg) has a planet with low limit of mass about 1.6 masses of Jupiter and with a period of 2.2 years (Cochran et al., 1997). The component B of double star Stein 2051 is "excellent astrometric microlensing candidate LSPM J0431+5858E" (Proft et al., 2011) and it is planned for observations with space telescope Gaia in the January, 2014. According to Agol (2011) such stars also can have planets in habitable zone.

In this connection the detailed study of dynamical properties of these stars seems very useful.

3. Results and Discussion

The information about selected stars is given in the table 1. We have calculated orbits of 61 Cyg and ADS 7251 (Gorshanov et al. 2006; Shakht et al 2010) and now we made the revision of this orbit with all Pulkovo photographic data till to 2007. Two variants of preliminary orbits of double star Stein 2051AB are calculated depending on prospective mass of component B – the white dwarf. The analysis of this star is shown, that there is a problem with determination of the curvature on a short arc of its orbit, which our observations cover, and orbital period P can be much longer.

Star 16 Cyg (ADS 12815) has been investigated by Romanenko in Pulkovo. The precise parameters of motion of this star and orbital elements have been derived. Total mass of the system has been estimated. (Kiselev et al., 1997; Kiselev & Romanenko, 2011). The

orbit of ADS 8002 is calculated by Kiselev et al. (1997) with Pulkovo parallax.

We give examples of habitable zones (HZ) of possible planets rotating around each component of a double star. HZ are calculated according to formulas of Kasting from the work of Selsis et al. (2007):

$$l_{in} = (l_{in(Sun)} - a_{in} T_* - b_{in} T_*^2) \sqrt{\frac{L_*}{L_{(Sun)}}} \quad (1)$$

$$l_{out} = (l_{out(Sun)} - a_{out} T_* - b_{out} T_*^2) \sqrt{\frac{L_*}{L_{(Sun)}}} \quad (2)$$

The internal (l_{in}) and the external (l_{out}) borders of HZ of Solar system are used in these formulas, where $l_{in(Sun)} = 0.72 \text{ a.u.}$ and $l_{out(Sun)} = 1.77 \text{ a.u.}$ Here also $T_* = T_{eff} - 5700^\circ \text{K}$, L_* = bolometric luminosity of a star and a and b are constants.

For estimation of limits of HZ by formulas (1-2) it was necessary to know the luminosity and temperature of a star. For those stars, whose effective temperatures and radii R were estimated experimentally (61 Cyg – by van Bell & von Brown (2009), for 16 Cyg – by Metcalfe et al. (2012), for ADS 7251 – by Passinetti – Fracassini et al. (2001)), bolometric luminosity has been calculated according to Stefan-Boltzmann law. The relation "spectrum - luminosity" has been used for Stein 2051A and for of ADS 8002, which are stars of the main sequence. For Stein 2051B we used the luminosity calculated accordingly to the R and T_{eff} of Liebert, 1976. The results are represented in the table 3.

For 61 Cyg in a column 3 (the top line) the radius of Jonson and Wright (1983) is given, and the radius obtained by van Bell & von Brown (2009) is placed in the low line. Two values of the luminosity and limits HZ are given correspondingly.

Masses in a column 7 for nearest stars are taken from a database RECONS.org, for 16 Cyg – from the work: Metcalfe et al. (2012). The mass of ADS 8002 is estimated according to a relation mass–luminosity (Kiselev et al., 1997). In the bottom line of a column 7 for ADS 7251 the values of masses determined in Pulkovo (Shakht et al.2010) are given. We have calculated them by means of the estimation of total mass and the mass-ratio of this binary.

Then we have calculated A – the expected astrometric signal, that is an amplitude of angular replacement of a star under the influence of planet. We used the following formula from the work of Malbet et all (2012):

$$A = 3 \left(\frac{M_p}{1M_\oplus} \right) \left(\frac{a}{\text{a.u.}} \right) \left(\frac{M_*}{1M_{Sun}} \right)^{-1} \left(\frac{D}{1\text{pc}} \right)^{-1} \quad (3)$$

Here M_p and M_* are accordingly the mass of a planet and the mass of the star. The value of a is the semimajor axis of an orbit. D – the distance from the Sun to the star with planetary system. $A1$ is the expected signal from the planet with Earth's mass, $A2$ – a signal caused by a planet with the Jupiter's mass. Results are located in table 3 depending on D .

We have chosen the distance from a star to the middle of HZ as the semimajor axis $a1$ for the Earth-like planets. And for possible Jupiter-like planets we used $a2$ that is more than $a1$ in 5.2 times by analogy with Solar system.

3. Conclusions

We represented a short description of our program with examples of stars of different spectral classes. We can see that our nearby stars are available for observations with telescope similar to NEAT with expected positional precision of $0.30 \mu\text{as}$. Our stars have precise parameters of the motions and can be useful for investigation as host-stars. In some cases for estimation of habitable zones we can use masses and parallaxes obtained with 26-inch refractor in Pulkovo.

We thank the Organizing Committee of Gamow's 2013 Conference for the possibility to take part in this meeting.

Table 1. The parameters of selected stars.

Name	$RA_{2000.0}$	$Dec_{2000.0}$	m_A m_B	Sp_A Sp_B
Stein 2051	4 ^h 31 ^m . 2	+58° 58'	12 ^m .0 13.0	M4V DC5VII
ADS 7251	9 14.4	+52 41	7.4 7.4	M0V M0V
ADS 8002	10 59.6	+25 26	8.5 8.9	K0V K5V
16 Cyg	19 41.8	+50 31	6.0 6.2	G2V G2V
61 Cyg	21 06.9	+38 45	5.4 6.1	K5V K7V

Table 2. Orbital elements of selected stars

Name	$a, a.u.$	P, yr	e	$i, ^\circ$	$\omega, ^\circ$	$\Omega, ^\circ$	Tp, yr
Stein 2051 (1)	181	2505	0.59	72	7.5	194	1788.1
Stein 2051 (2)	152	1918	0.57	70	0.5	193	1798.0
ADS 7251	136.9	1528.0	0.08	141.0	210.4	216.6	1882.8
ADS 8002	4.2	397.0	0.64	138	283	351	1767.0
16 Cyg	956	20 900	0.84	140	37	314	-7
61 Cyg	81.8	674.3	0.50	132.5	156.3	177.1	1728.5

Table 3. The estimated habitable zones and astrometric signal

Name	$T_{eff}, ^\circ K$	R/R_\odot	L/L_\odot	$l_{in}, a.u.$	$l_{out}, a.u.$	M, M_\odot	$a1, a.u.$	$a2, a.u.$	D, pc	$A1, \mu as$	$A2, \mu as$
1	2	3	4	5	6	7	8	9	10	11	12
61 Cyg A	4640	0.72	0.215	0.34	0.89	0.70	0.62	3.2	3.5	0.76	1247
	4526	0.61	0.140	0.28	0.72		0.50	2.6		0.61	1013
61 Cyg B	4400	0.67	0.151	0.29	0.76	0.63	0.52	2.7		0.71	1169
	4077	0.63	0.098	0.23	0.60		0.42	2.2		0.57	953
St 2051 A	3200	0.10	0.0008	0.02	0.06	0.22	0.04	0.21	5.6	0.10	156
St 2051 B	7050	0.01	0.0003	0.01	0.03	0.50	0.02	0.10		0.02	34
ADS 7251 A	4060	0.68	0.113	0.25	0.67	0.60	0.46	2.4	6.1	0.38	625
						0.57				0.48	803
ADS 7251 B	3850	0.65	0.083	0.22	0.58	0.60	0.40	2.1		0.32	548
						0.53				0.45	756
ADS 8002 A	5200	0.84	0.463	0.50	1.25	0.55	0.88	4.6	19.6	0.24	406
ADS 8002 B	4600	0.72	0.208	0.34	0.88	0.45	0.61	3.2		0.21	343
16 Cyg A	5825	1.24	1.57	0.90	2.21	1.11	1.56	8.1	21.3	0.19	320
16 Cyg B	5750	1.13	1.27	0.81	1.99	1.07	1.40	7.3		0.18	299

References

- Agol E.: 2011, *ApJL*, **731**, L31.
- van Bell J.T., von Brown K.: 2009, *ApJ*, **694** (2), 1085.
- Cochran W.D., Hatzes A.P., Butler R.P., Marcy G.W.: 1997, *ApJ*, **483**, 457.
- Gorshanov D.L., Shakht N.A., Kiselev A.A.: 2006, *Astrophysics*, **49**, 3, 386.
- Grosheva E.A., Izmailov I.S., Khrutskaya E.V.: 2013, *Proc. Workshop NAROO*, Paris, 93
- Kiselev A.A., Kiyayeva O.V., Romanenko L.G.: 1997, Workshop "Visual Double Stars", *ASSL* **223**, 377.
- Kiselev A.A., Romanenko L.G., Shakht N.A. et al.: 2009, *Izv. GAO*, **219**, 4, 135.
- Kiselev A.A., Romanenko L.G.: 2011, *Astron.Zh.*, **88**, 6, 530.
- Liebert J.: 1976, *ApJ*, **210**, 715.
- Malbet F., Goullioud R., Lagage P.O. et al.: 2012, *arXiv: 1207.6511 [Astro-ph.IM]*.
- Metcalfe T.S., Chaplin W.J., Appourchaux T.: 2012, *arXiv: 1201.5966 v2*, astro-ph.SR.
- Proft S., Demleitner M., Wambsganss J.: 2011, *Astron. Astrophys.*, **536**, A50.
- Selsis F., Kasting J.F., Levrard B. et al.: 2007, *A&A*, **476**, 1373.
- Shakht N.A., Grosheva E.A., Gorshanov D.L.: 2010, *Astrophysics*, **53**, 227.
- Passinetti-Frascassini L.E., Pastori L., Codino S., Pozzi A.: 2001, *A&A*, **367**, 521.

LI I 6708Å BLEND IN THE SPECTRA OF STRONGLY MAGNETIC STAR HD166473

A.V. Shavrina¹, V. Khalack², Y. Glagolevskij³, D. Lyashko⁴, J. Landstreet^{5,6}, F. Leone⁷,
N.S.Polosukhina⁸, M. Giarrusso⁷

¹ Main Astronomical Observatory, Kyiv, Ukraine, *shavrina@mao.kiev.ua*

² Université de Moncton, Moncton, N.-B., Canada

³ Special Astrophysical Observatory, Nizhnij Arkhyz, Russia

⁴ Taurian National University, Simferopol, Ukraine

⁵ University of Western Ontario, London, Canada

⁶ Armagh Observatory, Armagh, Northern Ireland – United Kingdom

⁷ Università di Catania, Catania, Italy

⁸ Crimean Astrophysical Observatory, Ukraine

ABSTRACT. The analysis of Li I 6708 Å blend in the spectra of HD166473 was performed for 6 rotational phases distributed over the whole rotational period ($P \sim 9.5$ years). The magnetic field model has been constructed based on the polarimetric measurements from Mathys et al. (2007). For each observed phase the modulus of the magnetic field has also been estimated from the modeling of Fe II 6147 Å, 6149 Å and Pr III 6706.7 Å line profiles taking into account Zeeman magnetic splitting and the angle α between the magnetic axis and the line of sight. Our measurements of the surface magnetic field agree rather well with the results of Mathys et al. (2007). The lithium abundance in each phase was obtained from the fit of the observed Li I 6708 Å line with the synthetic profile calculated assuming Paschen-Back splitting for the characteristics of magnetic field estimated from the analysis of Pr III 6706.7 Å line profile. We have also estimated the abundances of Ce II, Sm II, and Nd II, whose lines contribute to the Li 6708 Å blend.

Key words: stars: chemically peculiar, stars: individual: HD166473

Introduction

The lithium blend 6708 Å in the spectra of roAp star HD166473 with strong variable magnetic field, $B_s = 6650$ – 8850 G (Mathys et al. 2007) was studied in the work of Shavrina et al. (2006) in which ESO CAT-CES spectra with resolution $R=100000$, obtained by P. North in 1996, were used. New ESO observations (UVES and HARPS) with $R=110000$, obtained during 2001-2012 permit us to study the behavior of Li blend during the whole rotational period (phases 0.09 - 0.94, $P_{\text{rot}}=3513^{\text{d}}.64$).

Magnetic field model

The magnetic field model was constructed employing the method described by Gerth & Glagolevskij (2003) based on the measurements of mean magnetic field modulus from Mathys et al. (2007). This reconstruction results in the inclination angle of rotational axis to the line of sight $i=15^\circ$ and the angle between magnetic and rotational axis $\beta=75^\circ$ (see Fig. 1). Magnetic dipole of HD166473 is displaced from the center of this star on 0.28 stellar radii to the negative magnetic pole. This orientation permits us to see only one magnetic pole around the phase =0.0 (see Fig. 2).

Method of analysis

The Li blend 6708 Å was analyzed by the method of synthetic spectra using a Kurucz model for stellar atmosphere with $T_{\text{eff}}=7750\text{K}$ and $\log g=4.0$ (Shavrina et al. 2006). The code of synthetic spectra SYNTHM (Khan, 2004) was used with the line lists calculated taking into account magnetic

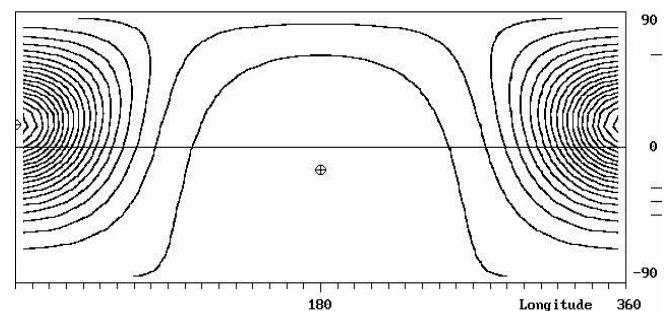


Fig.1: Magnetic dipole of HD166473 is displaced from the stellar center on 0.28R to the negative magnetic pole.

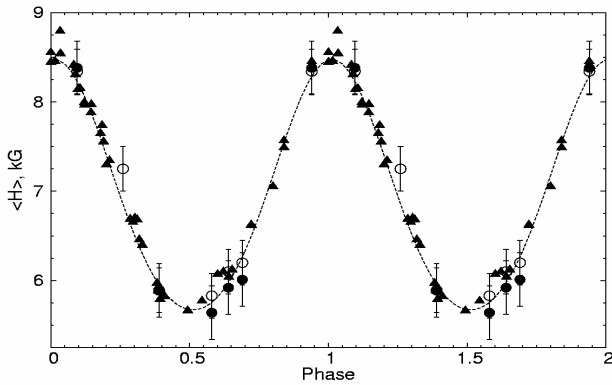


Fig.2: shows the variations of the mean magnetic field modulus (triangles) with rotational phase (Mathys et al. 2007) for HD166473 and its approximation (solid curve) in the frame of Gerth & Glagolevskij (2003) model. Magnetic field intensity estimated from the analysis of Fe II 6147 Å, 6749 Å lines (open circles), and of Pr III 6706 Å line (filled circles) accords rather well with the Mathys' data almost for all phases studied by us.

splitting for the specified values of magnetic field B and angles α between the magnetic axis of modeled dipole and the line of sight. For each observed phase the values B , α and the modulus of the magnetic field ($B \cdot \sin \alpha$) was estimated in the frame of the aforementioned dipole model from simulation of the Pr III 6706.7 Å and the Fe II 6147 Å, 6149 Å line profiles taking into account their Zeeman magnetic splitting. To perform this simulation we have used atomic data from VALD (Kupka et al. 2000) and NIST (Ralchenko et al. 2011). Note, that the angle α was accepted to be equal to 65° for the phases 0.94-0.39 and to 70° for the phases 0.58-0.69.

The lithium abundance in each phase has been obtained from fitting the observed Li I 6708 Å line with the synthetic profile calculated assuming its Paschen-Back splitting and the magnetic field characteristics estimated from analysis of Pr III 6706.7 Å line profile (Fig. 3). We have also derived the abundances of Ce II, Nd II and Sm II whose lines contribute to the Li blend (see Table 1).

The procedure for calculation of the Paschen-Back splitting takes into account the magnetically perturbed energy levels and determines the respective air wavelength and oscillator strength of components, based on the term configurations and the total strength of all lines in the multiplet under consideration (Khalack & Landstreet, 2012, Stift, Leone, Landi Degl'Innocenti, 2008). The perturbed part of the analyzed Hamiltonian includes only the contribution from the magnetic field and is nil when the field vanishes. For the condition of zero magnetic field the relative intensity of each line in a multiplet is determined through the sum of its components assuming the Russel-Saunders (or L-S) coupling scheme for the energy levels (Landi Degl'Innocenti & Landolfi 2004). The oscillator strengths derived from L-S coupling for the Li I 6708 Å resonance doublet show good agreement with the NIST data (Ralchenko et al. 2011). The pattern of the split components obtained for this particular line in the Paschen-Back regime is consistent with the results of Khochukhov et al. (2008).

Conclusions

- The Pr III 6706.7 Å line profile can be successfully used to determine magnetic field modulus B_s and angle α between magnetic axis and line of sight (with the errors 200 G and 5° respectively).
- All phases show higher than “cosmic” (-8.7 dex) abundance of lithium. Usually, diffusion theory and reactions of “spallation” are employed to explain high lithium abundance in the atmospheres of magnetic CP stars (Shavrina et al. 2001, 2006).
- Some differences in the abundance of Li I, the isotopic ratio ${}^6\text{Li}/{}^7\text{Li}$, and REE abundances for different phases, and rather different values of the magnetic field strength obtained from the Pr III 6706.7 Å profile, can be explained by the different location of lithium and REE spots, and by their different stratification with optical depth.

Table 1. Abundance of chemical species at different rotational phases of HD166473.

Phase	0.095	0.26	0.39	0.58	0.64	0.69	0.94	0.00 ¹	solar ²
$\log(N_{\text{Li}}/N_{\text{H}})$	-8.20		-8.42	-8.23	-8.20	-8.24	-8.23		-10.95
${}^6\text{Li}/{}^7\text{Li}$	0.0		0.5	0.5	0.5	0.5	0.0		<0.03 ³
$\log(N_{\text{CeII}}/N_{\text{H}})$	-7.78		-7.73	-7.60	-7.63	-7.64	-7.78	-7.55	-10.42
$\log(N_{\text{PrIII}}/N_{\text{H}})$	-7.76		-7.86	-7.82	-7.80	-7.80	-7.76	-7.60	-11.28
$\log(N_{\text{NdII}}/N_{\text{H}})$	-8.00		-8.10	-8.22	-8.10	-8.10	-8.30	-7.97	-10.58
$\log(N_{\text{SmII}}/N_{\text{H}})$	-8.45		-8.05	-7.68	-7.68	-7.75	-8.65	-8.25	-11.04
$\log(N_{\text{FeII}}/N_{\text{H}})$	-4.37	-4.42	-4.45	-4.35	-4.35	-4.30	-4.45	-4.31	-4.50

Notes:

¹Results of Gelbmann et al. (2000),

²solar data are taken from Grevesse et al. (2010),

³Baranovskii, Tarashchuk (2012).

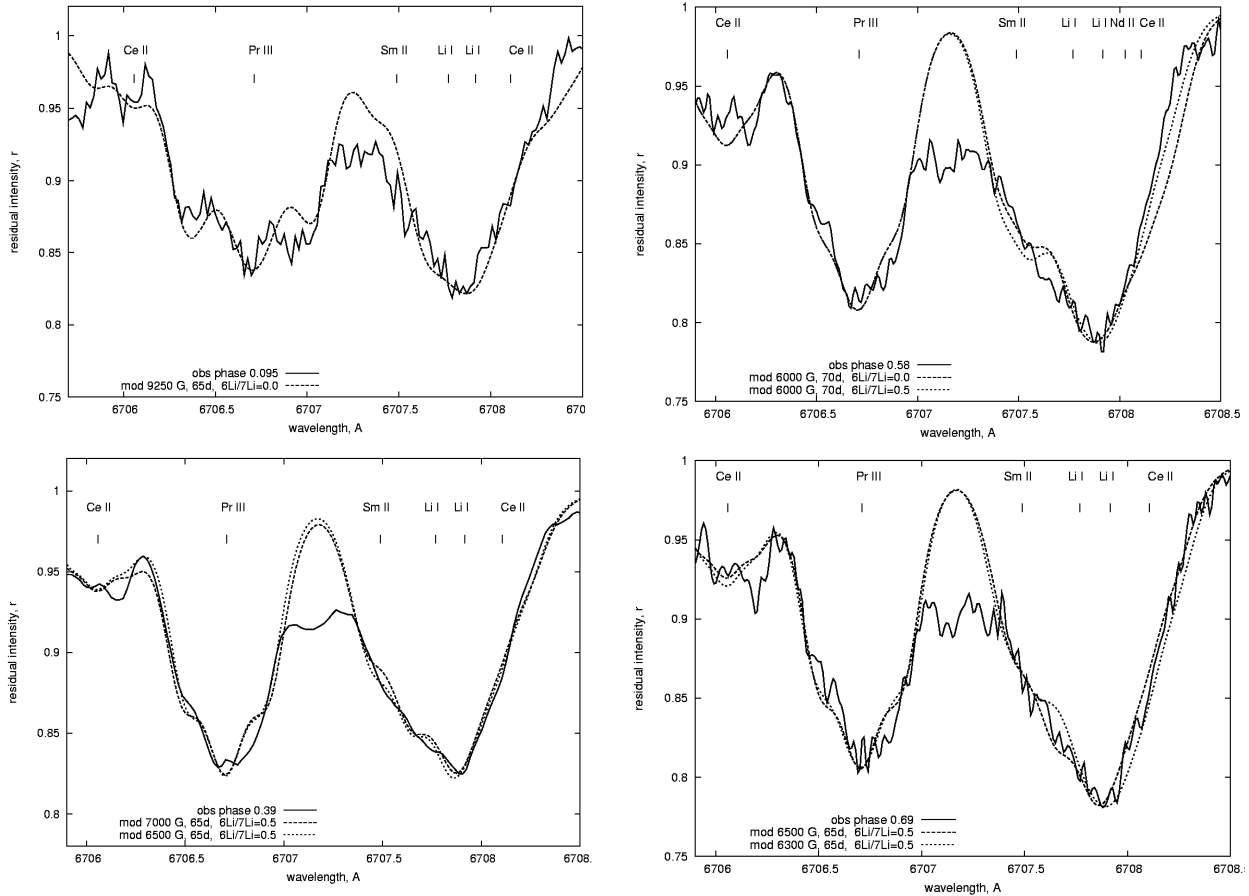


Fig.3: The observed spectrum (solid line) of HD166473 and the synthetic line profile (dotted line) calculated assuming $T_{\text{eff}}=7750\text{K}$, $\log(g)=4.0$, and the specified magnetic field parameters for the phases 0.095 (top left), 0.39 (bottom left), 0.58 (top right), and 0.69 (bottom right). The inclusion of ${}^6\text{Li}$ lines in calculations permits us to fit the synthetic spectrum better to the observed one in the phases 0.39 – 0.69. In other case we are forced to increase Nd abundance to fit a central part of the profile that results in worse red wing.

- As it seems the value of ${}^6\text{Li}/{}^7\text{Li}$ ratio correlates with the phases and magnetic field values, it is equal 0.0 (no ${}^6\text{Li}$) in the phases of magnetic maximum and 0.5 at minimum of magnetic field (see Table 1, Fig.3). On the other hand, it can be consider here as a parameter (or measure) of disagreement between the synthetic and observed profiles of Li I 6708 Å resonance doublet in HD166473.
- In this study we have imposed that Li and REE lines are formed in the spots near the magnetic poles (see Shavrina et al. 2001, 2006). Nevertheless, we have to admit that the location of Li and REE spots near the magnetic poles has not been proven yet for this slowly rotating star ($P_{\text{rot}}=3513^{\text{d}}.64$). A relatively low precision of the estimates of abundance variability with the rotational phase can be caused by the complex structure of magnetic field in HD166473 (see Fig. 1). The strong shift (0.28R) of the magnetic dipole from the stellar center leads to a large difference in the magnetic field at the magnetic poles: $B_p = -26384\text{ G}$ and 4956 G respectively. Nevertheless, the distribution of Li, Ce, Pr, Nd, Sm, Fe seems to be fairly uniform (see Table 1), which is highly unusual for a star with the relatively strong magnetic field of complex structure (see Alecian & Stift (2010) for details). Therefore, HD166473 should be studied further in detail.
- Additional spectral and spectropolarimetric observations (with high resolution and high S/N) of HD166473 are required to thoroughly cover the whole rotational period in order to proceed with abundance mapping and detailed reconstruction of the magnetic field geometry.

Acknowledgements. The authors thank S. Khan for providing the SYNTHM code, and administration of the ESO Spectral Archive for the spectra of HD166473.

References

- Alecian G., Stift M.J.: 2010, *A&A*, **516**, 53
 Baranovskii, E.A., Tarashchuk, V.P.: 2012 *Kinematics and Physics of Celestial Bodies*, **28**, iss. 5, 239
 Gelbmann M., Ryabchikova T., Weiss W.W., Piskunov N., Kupka F., Mathys G.: 2000, *A&A*, **356**, 200
 Gerth E., Glagolevskij Y.: 2003, *Bulletin of SAO*, **56**, 25
 Grevesse N., Asplund M., Sauval A.J., Scott P.: 2010, *Ap&SS*, **328**, 179
 Khalack V., Landstreet J.: 2012, *MNRAS*, **427**, 569
 Khochukhov O.: 2008, *A&A*, **483**, 557
 Khan S.: 2004, *J.Q.S.R.T.*, **88**, N1-3, 71
 Kupka F., Ryabchikova T.A., Piskunov N.E. et al.: 2000, *Baltic Astronomy*, **9**, 590
 Landi Degl'Innocenti E., Landolfi M.: 2004, *Kluwer Academic Publishers*, Dordrecht, The Netherlands, 890p.
 Mathys G., Kurtz D.W., Elkin V.G.: 2007, *MNRAS*, **380**, 181
 Ralchenko Yu., Kramida A., Reader J., and NIST ASD Team: 2011, *NIST Atomic Spectra Database* (ver. 4.1)
 Shavrina A.V., Polosukhina N.S., Khan S. et al.: 2006, *Astron. Rep.*, **50**, N6, 500
 Shavrina A.V., Polosukhina N.S., Zverko J., Khalack V., Tsymbal V.V., Žižňovský J.: 2001, *A&A*, **372**, 571
 Stift M.J., Leone F., Landi Degl'Innocenti E.: 2008, *MNRAS*, **385**, 1813

TOWARDS A DETERMINATION OF DEFINITIVE PARAMETERS FOR THE LONG PERIOD CEPHEID S VULPECULAE

D. G. Turner

Department of Astronomy and Physics, Saint Mary's University
Halifax, Nova Scotia B3H 3C3, Canada, *turner@ap.smu.ca*

ABSTRACT. A new compilation of *UBV* data for stars near the Cepheid S Vul incorporates *BV* observations from APASS and NOMAD to augment *UBV* observations published previously. A reddening analysis yields mean colour excesses and distance moduli for two main groups of stars in the field: the sparse cluster Turner 1 and an anonymous background group of BA stars. The former appears to be 1.07 ± 0.12 kpc distant and reddened by $E_{B-V} = 0.45 \pm 0.05$, with an age of 10^9 yrs. The previously overlooked latter group is 3.48 ± 0.19 kpc distant and reddened by $E_{B-V} = 0.78 \pm 0.02$, with an age of 1.3×10^7 yrs. Parameters inferred for S Vul under the assumption that it belongs to the distant group, as also argued by 2MASS data, are all consistent with similar results for other cluster Cepheids and Cepheid-like supergiants.

Key words: stars: variables: Cepheids — stars: fundamental parameters — Galaxy: open clusters and associations: individual.

1. Introduction

The variability of S Vulpeculae was first recognized in 1836-37 with an estimated cycle length of ~ 68 days. The star was at times classified as either semi-regular or RV Tauri-type (e.g., Joy 1952). A study by Nassau & Ashbrook (1943) appears to be the first to identify the variations as those of a long-period Cepheid. Photoelectric studies by Fernie (1970) and others (Berdnikov 1993, 1994; Heiser 1996) subsequently confirmed the Cepheid nature of S Vul, making it the longest period classical Cepheid recognized in the Galaxy. A few other Cepheid-like supergiants (e.g., V810 Cen, HD 18391) have periods in excess of 100 days. Like S Vul, they have small light amplitudes.

In the 1970s the possibility was raised that S Vul might be a member of the association Vul OB2 (Tsarevskii 1971; Turner 1980), a link that would provide a means of establishing both the luminosity and intrinsic colour of S Vul from the distance and reddening of association stars. Circa 1980 the author

noticed that S Vul lies in an anonymous open cluster (Fig. 1), now catalogued as Turner 1 (Turner 1985). A photometric study of the cluster was subsequently performed using photoelectric and photographic photometry (Turner et al. 1986), the latter calibrated using stars in the photoelectric sequence and secondary images offset by $\sim 4^m.6$ from the primary images using a Racine-Pickering wedge on the 3.6-m Canada-France-Hawaii Telescope. Interpreting the photometry was complicated, but it was possible to isolate an old cluster of FG dwarfs ~ 650 pc distant reddened by $E_{B-V} \simeq 0.50$, as well as possible background B stars of larger reddening. The presence of the background group of B dwarfs was later confirmed from 2MASS infrared photometry (Turner 2011), but has not yet been studied using optical photometry. This paper attempts to rectify that omission.

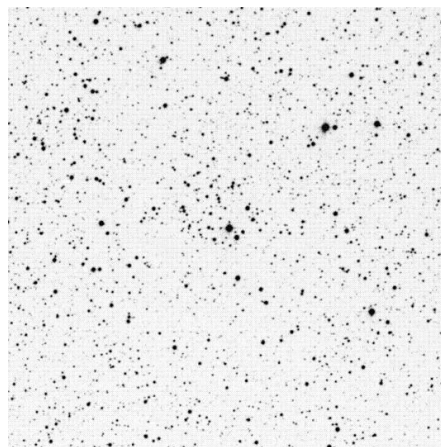


Figure 1: The $15' \times 15'$ field of S Vul from the Palomar Observatory Sky Survey blue image.

2. Data Analysis

Optical studies of reddening in Galactic star fields are best done using Johnson system *UBV* photome-

try, for which interstellar reddening is readily separated from other effects (temperature, metallicity, etc.). New U -band observations are not yet available for the S Vul field, but the availability of $BVg'r'i'$ observations for the field from the AAVSO Photometric All-Sky Survey (APASS) provides a useful beginning. A comparison of previous photoelectric and photographic V -band and B -band data for the S Vul field with APASS data is provided in the upper portion of Fig. 2. A similar comparison with BV data from the Naval Observatory Merged Astrometric Dataset (NOMAD, Zacharias et al. 2005) is shown in the lower portion of Fig. 2. NOMAD data are derived from scans of plates in the Palomar Observatory Sky Survey.

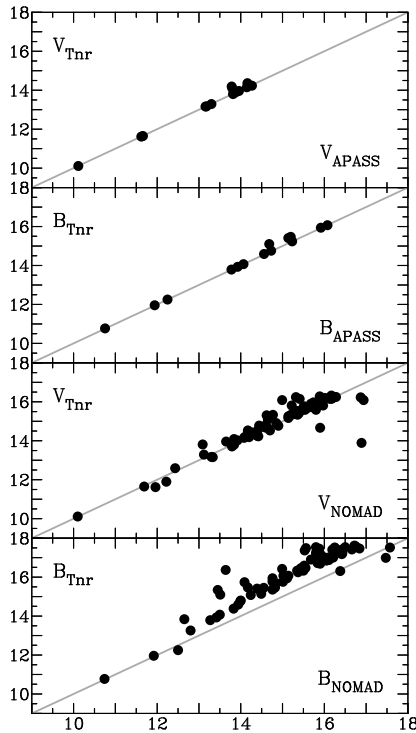


Figure 2: A comparison of BV magnitudes from Turner et al. (1986) with data from the APASS (upper) and NOMAD (lower) surveys. Gray lines represent the situation for exact coincidence.

The APASS photometry is in excellent agreement with the Turner et al. (1986) photometry, except for three stars in the APASS survey that may be affected by crowding. There is also a lack of APASS data for many stars near S Vul within the APASS limits, which may also be a result of image crowding. The next release of APASS for the S Vul field may overcome such problems.

The comparison of previous photoelectric and photographic V -band and B -band data for the S Vul field with NOMAD data reveals sizable systematic offsets, particularly in B . Such offsets appear occasionally in

other NOMAD fields and may be linked to the choice of calibration stars. It is possible to infer from the plots the main trend in the data in order to correct the NOMAD results for S Vul stars for the calibration error. But correcting the resulting NOMAD $B-V$ colours to the photoelectric system is rather complicated. Fig. 3 is a comparison of the adjusted NOMAD $B-V$ colours with the photoelectric and photographic colours in the survey of Turner et al. (1986). The adopted trend relation (not shown) depends significantly upon how many of the most discrepant stars are omitted from the fit.

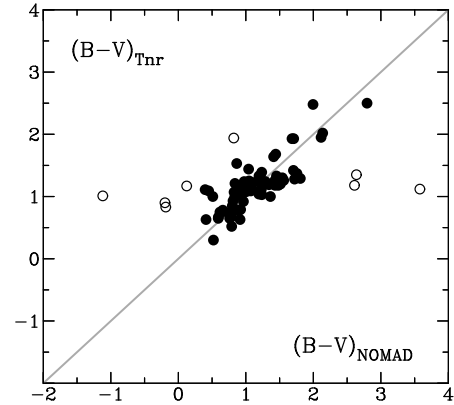


Figure 3: A comparison of $B-V$ colours from Turner et al. (1986) with colours resulting from the adjusted NOMAD photometry. A gray line represents exact coincidence, while open circles indicate discrepant points not used for the best fit.

Analysis of the combined photoelectric and photographic UBV , APASS BV CCD, and NOMAD BV observations is involved, but a solution was found. Data from the various sources were assigned weights depending upon the expected precision, with highest weights for the photoelectric observations, medium weights for the CCD and photographic BV observations, and low weights for the NOMAD BV data. The U -band data from the Turner et al. (1986) study were adopted as given. In other words, the APASS and NOMAD data were used to improve the V -magnitudes and $B-V$ colours for stars in the Turner et al. (1986) study, as well as to add BV data for faint stars lying beyond its spatial and magnitude limits. The UBV colours for the resulting sample of stars are plotted in the colour-colour diagram of Fig. 4.

The reddening relation for the field of S Vul is well established from previous studies (Turner 1980, 1989) to be described by the relation $E_{U-B}/E_{B-V} = 0.74 + 0.02 E_{B-V}$, which has been approximated by $E_{U-B}/E_{B-V} \simeq 0.75$ in Fig. 4. As found previously (Turner et al. 1986), most stars in Turner 1 are FG dwarfs reddened by $E_{B-V} \simeq 0.48$. A best fit by eye to the data of Fig. 4 yields a mean reddening of $E_{B-V} = 0.45 \pm 0.05$ for the FG dwarfs, where the

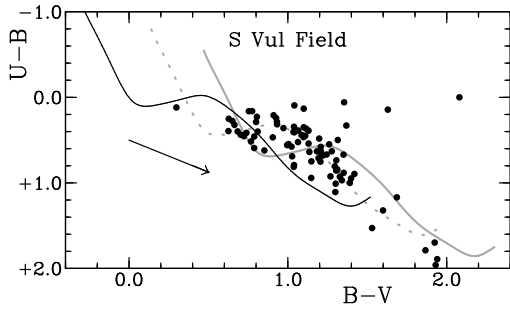


Figure 4: Colour-colour diagram for stars near S Vul with full UBV data. The intrinsic relation for dwarfs is the black polynomial, while the dotted gray relation and the solid gray relation represent the intrinsic relation reddened by $E_{B-V} = 0.45$ and $E_{B-V} = 0.78$, respectively. An arrow denotes the reddening relation for the field (Turner 1980, 1989).

uncertainty represents scatter arising from differential reddening in the field (Turner 1980), uncertainties in the observations, and unknown corrections for ultraviolet excesses in the G dwarfs resulting from line blanketing (Wildey et al. 1962). There is also a relatively clear sequence of B dwarfs reddened by $E_{B-V} = 0.78 \pm 0.02$ that represents background stars detected beyond the foreground cluster. Since the stars are dispersed across the field, the scatter in their reddenings may also arise from the small amount of differential reddening in the field.

The colour-magnitude diagram for the stars in Turner 1 can be interpreted with the established reddenings of Fig. 4. Fig. 5 presents the colour-magnitude diagram for the analyzed stars using a zero-age main sequence (ZAMS) for the smaller reddening of $E_{B-V} = 0.45$. The ZAMS matches the lower envelope of FG stars at $V - M_V \simeq 11.50 \pm 0.20$. With the adopted reddening, the intrinsic distance modulus is $V_0 - M_V = 10.15 \pm 0.25$, corresponding to a distance of 1.07 ± 0.12 kpc. That is larger than the value of 643 pc found in the study by Turner et al. (1986), the difference being accounted for by the fainter stars added here to the ZAMS for the cluster. An age isochrone for $\log t = 9.0$ also provides a good fit to the evolved portion of the main sequence, as well as to a putative group of G giant members in Fig. 5. The eye fit to the data is limited by the mixed quality of the photometry. A deeper CCD study is in progress to confirm the present results.

A colour-magnitude diagram for the same stars is presented in Fig. 6 for the established reddening of the B stars, namely $E_{B-V} = 0.78$. Here a reasonable match of the ZAMS to faint B and A stars can be made for $V - M_V \simeq 15.05 \pm 0.10$. With the adopted reddening, the intrinsic distance modulus is $V_0 - M_V = 12.71 \pm 0.12$, corresponding to a distance of 3.48 ± 0.19 kpc. That is less than the distance of 4.41

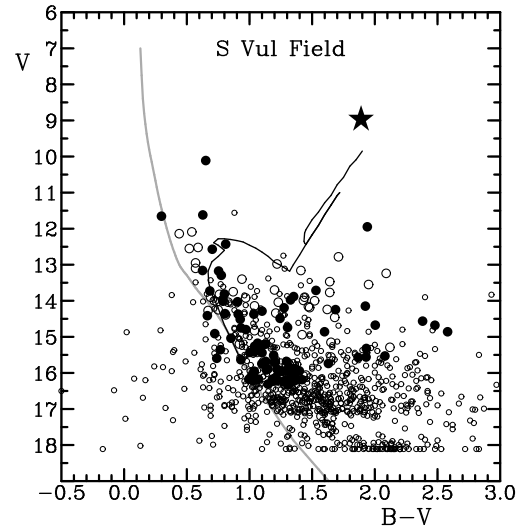


Figure 5: Colour-magnitude diagram for Turner 1 with $E_{B-V} = 0.45$ and stars from the Turner et al. (1986) survey (filled circles), APASS (open circles), and NOMAD (small open circles). S Vul is plotted as a star symbol, the gray curve is the ZAMS for $V - M_V = 11.50$, and a black curve is an isochrone for $\log t = 9.0$.

kpc found by Turner (1980) for Vul OB2, and the stars are also somewhat older than is the case for the luminous OB stars populating Vul OB2. An age isochrone for $\log t = 7.1$ provides a good fit to the evolved portion of the main sequence, as well as for S Vul. Again, a deeper CCD study is in progress to confirm the results.

The sequence of faint, reddened B dwarfs displays no degree of concentration towards the centre of Turner 1, so must represent a sparse clumping of young stars along the line of sight to the Cepheid. Similar conclusions were reached in a study of the field that made use of 2MASS observations (Turner 2011). The average reddening of $E_{B-V} = 0.78 \pm 0.02$ for these stars must also apply to the Cepheid, in which case its stellar reddening becomes $E_{B-V} = 0.695$ according to the relationship of Fernie (1970). If S Vul is a member of the same group, as seems likely, it has an inferred luminosity of $\langle M_V \rangle = -6.08 \pm 0.12$. Other properties of S Vul as a likely member of the background group of B stars are summarized in Table 1.

The consistency of the derived luminosity of S Vul with those of other calibrating Cepheids is seen in its absolute Spitzer $3.6\mu\text{m}$ magnitude ($[3.6]$) in Fig. 7, where the observations for cluster and parallax Cepheids are taken from Monson et al. (2012), but modified to the system of field reddenings for the calibrators. Similar results apply to the Spitzer $4.5\mu\text{m}$ magnitude.

Similar conclusions are reached if one compares the implied mass and age of S Vul with empirical values derived for cluster Cepheids. A preliminary study of

Table 1: Intrinsic Parameters for S Vulpeculae.

Parameter	Value	Reference
Period, P	$68^d.0194$	Berdnikov (1994)
$\log P$	1.8326	Berdnikov (1994)
$\langle V \rangle$	8.974	Berdnikov (2007)
$\langle B \rangle - \langle V \rangle$	1.890	Berdnikov (2007)
$E_{B-V}(B0)$	0.78	This Paper
$E_{B-V}(C\delta)$	0.695	This Paper
$(\langle B \rangle - \langle V \rangle)_0$	1.195	This Paper
$\log T_{\text{eff}}$	3.651	This Paper
Distance, d	3.48 ± 0.19 kpc	This Paper
$\log t$	7.1	This Paper
$\langle M_V \rangle$	-6.08 ± 0.12	This Paper
$\langle M_{\text{bol}} \rangle$	-6.40 ± 0.12	This Paper
$\langle M[3.6] \rangle$	-8.51 ± 0.12	This Paper
$\langle M[4.5] \rangle$	-8.42 ± 0.12	This Paper

such characteristics by Turner (1996) has been updated in Table 2 using new results for Cepheids and Cepheid-like supergiants associated with open clusters (Turner 2010; Turner et al. 2009, 2012a, 2012b; Majaess et al. 2013). Included are results for two red supergiant variables associated with open clusters: BC Cyg in Berkeley 87 and μ Cep in Trumpler 37.

Dynamical masses have been derived for three Cepheids in binary systems (Evans et al. 2009, 2011; Pietrzyński et al. 2010), while evolutionary masses have been deduced for Cepheids and Cepheid-like objects in clusters using M_{RTO} , the mass of stars at the red edge of the tip of the evolved main sequence, i.e., stars in the terminal stages of core hydrogen burning prior to the first crossing of the instability strip, as inferred from the models of Meynet et al. (1993). In the study by Turner (1996) the evolutionary masses of cluster Cepheids were assumed to be roughly 10% larger than values of M_{RTO} , but the close coincidence in Fig. 8 of M_{RTO} evolutionary masses with dynamical masses for binary Cepheids suggests that the two estimates may be almost identical (see also Turner 2012). The evolutionary stages of shell hydrogen burning and core helium burning therefore occur on significantly shorter time scales than is the case for core hydrogen burning in stars. The implied evolutionary mass of S Vul from its association with BA stars in its vicinity closely agrees with evolutionary masses deduced for other cluster Cepheids (Fig. 8).

A similar result is found for the empirical Cepheid period-age relation, as deduced for cluster Cepheids and pulsating red supergiants in Table 2 and plotted in Fig. 9. The pulsation periods used in Table 2 and plotted in Figs. 7, 8, and 9 are those for fundamental mode pulsation. The review by Turner (2012) and other studies of the Cepheid period-age correlation assume that the relationship is linear, but the results of Fig. 9 suggest that the relationship may be non-linear

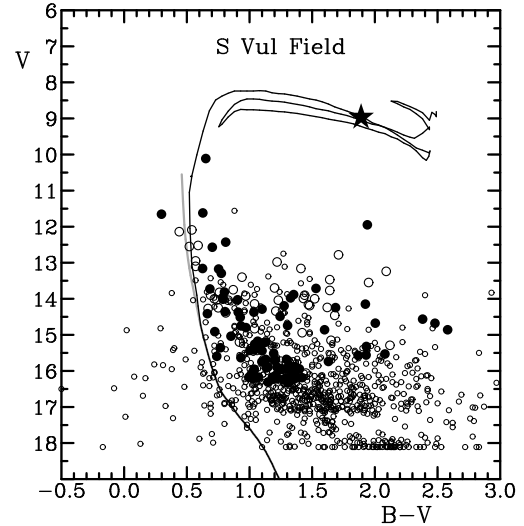


Figure 6: A repeat of Fig. 5 for the same data, with the ZAMS (gray relation) plotted using $E_{B-V} = 0.78$ and $V - M_V \simeq 15.05$. An isochrone for $\log t = 7.1$ is plotted as a black curve.

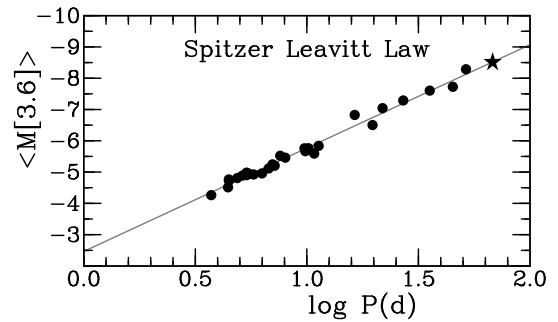


Figure 7: Absolute Spitzer $3.6\mu\text{m}$ magnitudes for parallax and cluster Cepheids tied to field reddenings for the calibrators. S Vul is depicted by a star symbol.

for high-mass pulsators. Such non-linearity depends upon how closely red supergiant pulsators resemble normal Cepheids.

3. Summary

Fundamental properties have been deduced for S Vul from its likely association with a group of B stars in its immediate vicinity. All derived parameters for the Cepheid are consistent with its membership in the loose group of B stars, but confirmation must await a deeper UBV study of stars surrounding the Cepheid and measurement of radial velocities for brighter association members. Preliminary measurements have already been made of potential candidates using the Plaskett telescope at the Dominion Astrophysical Observatory: older measurements from the 1980s by Doug

Table 2: Properties of Clusters Containing Pulsating Supergiants.

Cluster	Cepheid	$\log P$	$\log t$	M_{RTO}
Alessi 95	SU Cas	0.443	8.20	$4.1M_{\odot}$
Harrington 1	α UMi	0.599	7.90	$5.4M_{\odot}$
Platais 1	V1726 Cyg	0.627	8.00	$4.9M_{\odot}$
Berkeley 58	CG Cas	0.640	8.00	$4.9M_{\odot}$
NGC 7790	CEb Cas	0.651	8.00	$4.9M_{\odot}$
NGC 1647	SZ Tau	0.652	8.10	$4.2M_{\odot}$
NGC 7790	CF Cas	0.688	8.00	$4.9M_{\odot}$
NGC 7790	CEa Cas	0.711	8.00	$4.9M_{\odot}$
van den Bergh 1	CV Mon	0.731	7.90	$5.4M_{\odot}$
NGC 6067	QZ Nor	0.733	7.80	$5.9M_{\odot}$
NGC 6649	V367 Sct	0.799	7.85	$5.7M_{\odot}$
Collinder 394	BB Sgr	0.822	7.85	$5.7M_{\odot}$
NGC 129	DL Cas	0.903	7.85	$5.7M_{\odot}$
NGC 6087	S Nor	0.989	7.80	$5.9M_{\odot}$
Lyngå 6	TW Nor	1.033	7.80	$5.9M_{\odot}$
NGC 6067	V340 Nor	1.053	7.80	$5.9M_{\odot}$
Teutsch 106	GT Car	1.119	7.70	$6.5M_{\odot}$
Trumpler 35	RU Sct	1.295	7.55	$7.9M_{\odot}$
Turner 2	WZ Sgr	1.339	7.55	$7.9M_{\odot}$
Anon Vel OB	SW Vel	1.370	7.50	$8.3M_{\odot}$
Turner 14	AQ Pup	1.477	7.50	$8.3M_{\odot}$
Turner 8	SV Vul	1.653	7.20	$12.2M_{\odot}$
Turner 1b	S Vul	1.837	7.10	$14.2M_{\odot}$
Stock 14	V810 Cen	2.184	6.90	$20.4M_{\odot}$
Anon	HD 18391	2.250	6.90	$20.4M_{\odot}$
Berkeley 87	BC Cyg	2.841	6.70	$31.3M_{\odot}$
Trumpler 37	μ Cep	3.002	6.60	$39.7M_{\odot}$

Welch (unpublished), and more recent CCD observations. Results will be presented elsewhere. The location of S Vul at the extreme long-period end of the Leavitt relation for classical Cepheids makes it extremely valuable for anchoring the slope of the relationship, so further study is essential.

The present study expands upon results described in an oral paper given at the spring meeting of the AAVSO held in Boone, North Carolina, May 17–18, 2013.

References

Berdnikov, L.N.: 1993, *AstL*, **19**, 84.
 Berdnikov, L.N.: 1994, *AstL*, **20**, 232.
 Berdnikov, L.N.: 2007, <http://www.sai.msu.ru/groups/cluster/CEP/PHE>.
 Evans, N.R., Massa, D., Proffitt, C.: 2009, *AJ*, **137**, 3700.
 Evans, N.R., et al.: 2011, *AJ*, **142**, 87.
 Fernie, J.D.: 1970, *AJ*, **75**, 244.
 Heiser, A.H.: 1996, *PASP*, **108**, 603.
 Joy, A.H.: 1952, *ApJ*, **115**, 25.
 Mahmoud, F., Szabados, L.: 1980, *IBVS*, **1895**, 1.

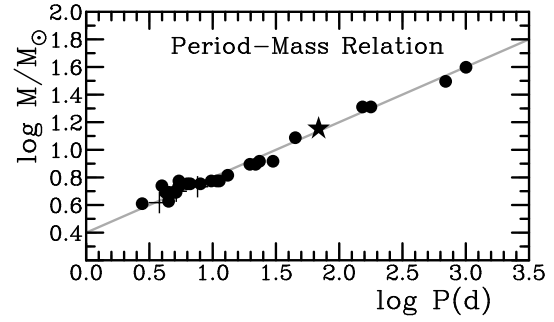


Figure 8: Evolutionary (points) and dynamical (plus signs) masses for Cepheids and Cepheid-like supergiants. S Vul is plotted as a star symbol, and the linear relation is from Turner (2012).

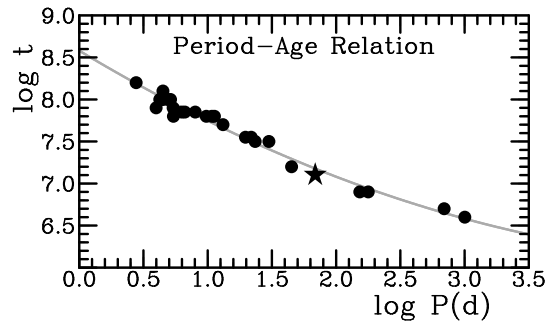


Figure 9: Empirical period-age relationship for Cepheids and Cepheid-like supergiants in open clusters (points), including S Vul (star symbol). The gray polynomial is the best-fitting relationship to the data.

Majaess, D., et al.: 2013, *Ap&SS*, in press.
 Meynet, G., Mermilliod, J.-C., Maeder, A.: 1993, *A&AS*, **98**, 477.
 Monson, A.J., et al.: 2012, *ApJ*, **759**, 146.
 Nassau, J.J., Ashbrook, J.: 1943, *AJ*, **50**, 97.
 Pietrzyński, G., et al.: 2010, *Nature*, **468**, 542.
 Turner, D.G.: 1976, *AJ*, **81**, 97.
 Turner, D.G.: 1980, *ApJ*, **235**, 146.
 Turner, D.G.: 1985, *JRASC*, **79**, 175.
 Turner, D.G.: 1989, *AJ*, **98**, 2300.
 Turner, D.G.: 1996, *JRASC*, **90**, 82.
 Turner, D.G.: 2010, *Ap&SS*, **326**, 219.
 Turner, D.G.: 2011, *RMxAA*, **47**, 127.
 Turner, D.G.: 2012, *JAASO*, **40**, 502.
 Turner, D.G., Leonard, P.J.T., Madore, B.F.: 1986, *JRASC*, **80**, 166.
 Turner, D.G., et al.: 2009, *AN*, **330**, 807.
 Turner, D.G., et al.: 2012a, *MNRAS*, **422**, 2501.
 Turner, D.G., et al.: 2012b, *AJ*, **144**, 187.
 Tsarevskii, G.S.: 1971, *SvA*, **15**, 169.
 Wildey, R.L., et al.: 1962, *ApJ*, **135**, 94.
 Zacharias N., et al.: 2005, *BAAS*, **36**, 1418.

HQ CAR IS A NEW W VIR TYPE STAR

S. N. Udovichenko¹, V. V. Kovtyukh¹, I. A. Egorova², and S. I. Belik¹

¹ Astronomical Observatory, Odessa National University,
Shevchenko Park, Odessa 65014, Ukraine, *udovich222@ukr.net*

² European Southern Observatory, Chile

ABSTRACT. HQ Car is listed as an δ Cep star (DCEP) in the GCVS. High-resolution spectra of HQ Car showed the presence of the Balmer and He I 5876Å emissions. The light curve shows steeper rise than decline, and there is evidence for the presence of a bump in the descending branch around the phase of 0.4. From considerations of the period, spectral type, presence of the bump, Helium and Balmer emissions we conclude that HQ Car belongs to the W Vir class of Type II Cepheids.

Key words: W Vir type Cepheids – stars: individual: HQ Car

1. Introduction

The type II Cepheids are low-mass, high-luminosity pulsators, with periods from 1 to 40 days. These evolved stars have a He core surrounded by an outer H shell. Type II Cepheids are population II stars and are thus old, typically metal-poor, and low mass objects.

Type II Cepheids are divided into three subclasses: BL Her, W Vir, and RV Tau. All three classes are characterized by the presence of Balmer emission, especially H α , during some parts of their pulsation cycle. Evolutionary scheme of these classes is suggested by Gingold (1985). In this scheme the BL Her stars are evolving from horizontal branch towards the lower asymptotic giant branch (AGB). However, the W Vir variables exhibit a blueshift from the AGB. The RV Tau stars exhibit a blueshift in the post-AGB phase. Now there is a consensus that Type II Cepheids are fundamental pulsators with masses below 0.8 M $_{\odot}$.

W Vir stars are typically 1.5 magnitudes fainter than their related Type I stars and have a mass of less than 1 solar mass, so that they are clearly at a different evolutionary stage. They also have a distinctive light curve with a variation of 0.3 to 1.2 magnitude and a bump on the decline branch.

The reliable identification of field type II Cepheids is important for several reasons. Achieving a firm understanding of the population to which they belong is hampered by our inability to reliably identify individ-

ual stars in the field. This limits our understanding of their origin and evolution. In turn, any potential application of these stars as tracers of older populations and possibly the structure of the halo is compromised.

Various observable parameters which have been proposed to distinguish between type I and type II Cepheids include the form of the light curve, the stability of the pulsation, spectral features, metallicity, space motions, and location.

Schmidt et al. (2004) obtained H α line profiles of Cepheids with periods longer than 8 days. The authors found that emission in H α was a good discriminator between population I and II Cepheids.

The light curves of those monoperoiodic Population II pulsators are not like those of classical Cepheids, at least regarding the usually steeper rising branch as compared to the slower brightness decline. The shorter-period W Vir stars, with say 8 to about 12 days period, can have rather smooth sinusoidal light curves, i.e. light curves, which are much more harmonic than, for example, classical Cepheids with comparable periods. On the other hand, the longer-period representers often show a well expressed secondary bump on the descending branch; that bump can be so strong that there is almost a plateau formed after the peak brightness, or the secondary maximum can even dominate over the peak light after the steep rising branch of the light curve. Spectroscopic variability is reminiscent of radial pulsations with pulsation-velocity amplitudes between 10 and 50 km/s. The velocity curves can be discontinuous, Balmer lines can pick up emission components, and metal lines can double, all indicating the propagation of strong shocks in the atmospheres of the corresponding W Vir stars.

2. The photometry

To study a behavior of the period change of HQ Car, the photometric observations were taken from ASAS (Pojmanski, 2002), VizieR On-line Data Catalog (Berdnikov, 2008) and paper (Madore, 1975). We have determined 34 times of maxima from the individual

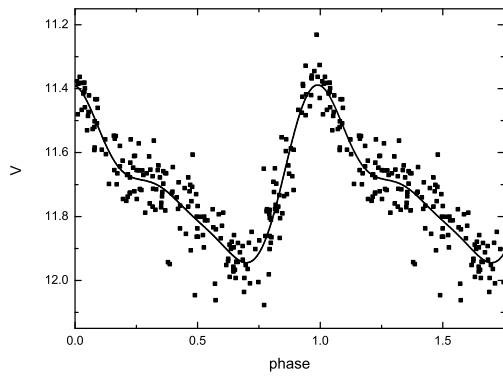


Figure 1: Light curve of HQ Car using ASAS photometry from JD2444500 through 2445168.

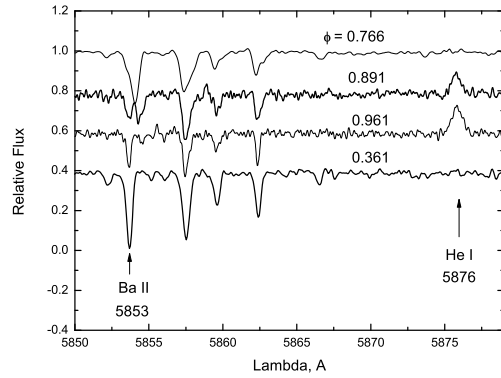


Figure 3: The behavior of the 5876 Å He I line profile.

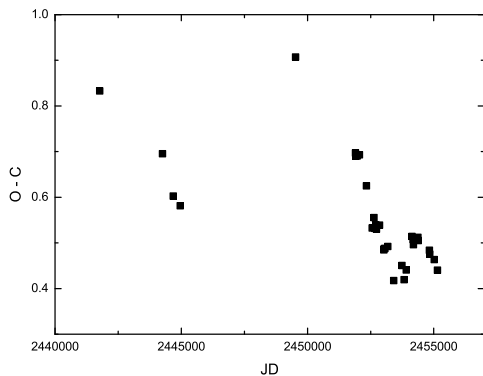


Figure 2: O-C diagram of HQ Car.

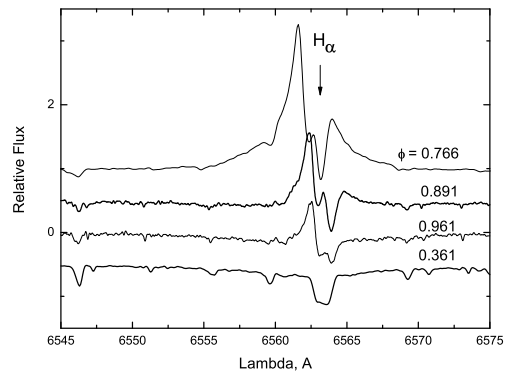


Figure 4: H α profile variation.

light curves. For calculation O-C diagram and phases of spectra we have used the elements of GSVS (Samus et al., 2011): $HJD_{max} = 2420326.03 + 14.0722 E$, and elements, which were calculated from ASAS date, respectively: $HJD_{max} = 2452784.603 + 14.06378 E$.

In Fig. 1, we have plotted the photometric phase curve of HQ Car based on the data obtained during the ASAS project (Pojmanski, 2002). It has been known for many years that there is a tendency for type II Cepheids to exhibit more scatter in their light curves than is the case for classical Cepheids.

In Fig. 2 we plot O-C, the difference between the fitted dates of maximum and dates calculated from a mean period versus the Julian Date. O-C diagram of HQ Car is typical for W Vir type stars.

3. The spectral observations

HQ Car was observed using the echelle spectrographs on the 4 m telescopes at the Cerro Tololo Inter-American Observatory (CTIO). Long red cam-

eras were used with the 31.6 lines mm^{-1} echelle gratings. Second-order blue light was blocked using GG495 filters. The wavelength coverage was 5500–8000 Å. A 1.0" slit provided a spectral resolution of 28 000 (2 pixels per resolution element) and a dispersion of 0.07 pixel at 5800 Å. The signal-to-noise ratio $S/N=57$ per pixel in the order containing H α (see Yong et al. 2006).

One spectrum was obtained using the 2.2m MPG telescope and FEROS spectrograph at ESO La Silla. The spectrum cover a continuous wavelength range from 4000 to 7850 Å with a resolving power of about 48 000. Typical maximum S/N values (per pixel) for the spectra are in excess of 150 (see Luck et al 2011).

Two spectra were obtained with the High Accuracy Radial velocity Planet Searcher (HARPS; Mayor et al. 2003) spectrograph mounted at the 3.6 m telescope at the La Silla ESO observatory. HARPS is a fibre-fed, cross-dispersed echelle spectrograph, which provides a resolution $R=115.000$ with a fixed format covering the 3800–6900 Å spectral range. The HARPS pipeline delivers science-quality products. In particular, master calibrations are created (master-bias and master-flat

Table 1: O-C residuals for HQ Car

JD	O-C	JD	O-C	JD	O-C
2441769.712	0.83295	24452657.356	0.53173	24453908.499	0.44057
2444258.555	0.69534	24452699.686	0.53979	24454134.693	0.51439
2444679.419	0.60282	24452713.687	0.53473	24454176.811	0.50738
2444960.560	0.58129	24452727.699	0.53045	24454190.726	0.49621
2449524.539	0.90719	24452854.469	0.53899	24454373.890	0.51223
2451899.783	0.69701	24453022.573	0.48481	24454387.864	0.50525
2451913.753	0.68974	24453036.682	0.48743	24454823.804	0.48406
2451970.056	0.69075	24453064.831	0.48776	24454837.755	0.47545
2452054.520	0.69294	24453177.471	0.49219	24455020.527	0.46361
2452335.006	0.62486	24453415.646	0.41740	24455146.849	0.44031
2452558.865	0.53275	24453739.773	0.45055		
2452629.546	0.55549	24453823.769	0.41948		

fields), and data are bias subtracted and divided by the flat field by using the calibrations closest in time to the science observations. Spectral orders are located and extracted, and the wavelength solution obtained using a Thorium-Argon calibration lamp is then applied.

Table 2 contains details concerning our program Cepheid observations.

4. Emission features in spectra of HQ Car

Fig. 3 give the picture of the He I 5875 line variation. As expected, this line appears as a quite strong emission on phase about 1.0, when the shock wave front passes through the photosphere, and then fades away towards the phase 0.3. Since the radiation in 5876 He I line is caused by the electron captures by ionized helium, the gas producing He line emission should be located behind the shock-wave front.

Emission in the hydrogen lines has been noted and detailed examined by many authors. Our Fig. 4 shows the behaviour of the profiles of H α line. Qualitatively, the behaviour of the H α profile is similar to that reported by Lebre & Gillet (1992) for W Vir (P = 17.277 d, see also Luck et al. 2011). As it was mentioned above, these authors assumed that this emission component is a single one at all the phases but distorted by two narrow absorptions.

HQ Car with an estimated $|z|$ of 0.3 kpc was listed as a type II Cepheid by Harris (1985).

3. Conclusion

Founded that HQ Car is a type II Cepheid according to the distance from the Galactic plane (Harris 1985), light curve, He I 5876 Å and Balmer lines emission.

Acknowledgements. The authors thank Drs. D.Yong and B.W.Carney for the CCD spectrum of HQ Car.

Table 2: Spectral observations of HQ Car

JD	phase	Remarks
2450834.86370	0.361	CTIO
2455284.65800	0.766	FEROS
2456411.53798	0.891	HARPS
2456412.51417	0.961	HARPS

For HARPS spectra:

JD_{max}=2452784.603+14.06378

References

- Berdnikov L.N.: 2008, **VizieR On-line Data Catalog**, UBVRIC-observations
- Galazutdinov G.A.: 1992, *Preprint SAO RAS*, **92**, 2
- Gingold R.A.: 1985, *Mem.Soc.Astr. Italy*, **56**, 169
- Harris H.C.: 1985, *AJ*, **90**, 756
- Lébre A. & Gillet D.: 1992, *A&A*, **255**, 221
- Luck R.E., Andrievsky S.M., Kovtyukh V.V., Gieren W., Graczyk D.: 2011, *AnJ*, **142**, 51
- Mayor M., Pepe F., Queloz D. et al.: 2003, *Messenger*, **114**, 20
- Pojmanski G.: 2002, *Acta Astronomica*, **52**, 397
- Madore B.F.: 1975, *ApJSS*, **29**, 219
- Samus N.N., Durlevich O.V., Kazarovets E.V., Kireeva N.N., Pastukhova E.N., Zharova A.V. et al.: 2011, *General Catalogue of Variable Stars* (GCVS database, Version 2011Jan)
- Schmidt E.G., Johnston D., Lee K.M., Langan S., Newman P.R., Snedden S.A.: 2004, *AJ*, **128**, 2988
- Yong D., Carney B.W., de Almeida M.L.T., Pohl B.L.: 2006, *AnJ*, **131**, 2256

MULTIPHASE SPECTROSCOPIC OBSERVATIONS OF THE LONG-PERIOD CEPHEIDS 1 CARINAE

I.A. Usenko ¹, V.V. Kravtsov ^{2 3}, V.V. Kovtyukh ¹, L.N. Berdnikov ², A.Yu. Knyazev ⁴,
R. Chini ^{5 3}, A.B. Fokin ⁶

¹ Astronomical Observatory, Odessa National University, Shevchenko Park,
Odessa 65014, Ukraine, *igus99@ukr.net*

² Sternberg Astronomical Institute, Moscow University, Moscow 119899, Russia,
lberdnikov@yandex.ru

³ Universidad Católica del Norte, Avenida Angamos 0610, Autofagasta, Chile,
vkravtsov@ucn.cl

⁴ South African Large Telescope, P.O. Box 9, Observatory, Cape Town 7935,
South Africa, *aknyazev@sao.ac.za*

⁵ Astronomisches Institut, Ruhr-Universität Bochum, Bohum 44780, Germany,
chini@astro.rub.de vhoff@astro.rub.de hdrass@astro.rub.de

⁶ Institute of Astronomy, Russian Academy of Sciences, Moscow 11907, Russia,
fokin@inasan.ru

ABSTRACT. Thirty three spectra (one spectrum for the each of 33 observational nights) have been performed to cover all pulsational period of the 35.5-days Cepheid 1 Car. Due to these data we have obtained for the first time the detailed curves of effective temperature, gravity and turbulent velocity. Curves of gravity and turbulent velocity show complicated changes, connected probably with dynamics of extensive Cepheid's atmosphere. The mean atmosphere parameters of 1 Car are: $T_{eff} = 4984 \pm 15$ K; $\log g = 1.13$; $V_t = 6.67$ km s⁻¹. Having a solar metallicity $[Fe/H] = +0.02$ dex, this Cepheid demonstrate sudden results for the "key" elements abundances of yellow supergiants evolution, – all they are close to the solar ones. In this case 1 Car resembles to SV Vul, – Cepheid with 45-days pulsational period and nearly like spectral type. It is possible that 1 Car is an object crossing the Cepheids instability strip for the first time. The content of other elements is close to solar one too.

Key words: Stars: Cepheids; stars: individual: 1 Car.

1. Introduction

1 Car is the famous Cepheid due to the some aspects. It is one of the brightest Cepheids ($\langle V \rangle = 3.^m724$) having the long period ($P = 35.^d5$), and been as a calibration object for the "period-luminosity" relation. Having a *G3Ib* spectral type it has attracted attention of observers by the presence of extensive hydrogen

envelope around the star (Kervella et al. 2006). At the same time, the results of mean atmosphere parameters and chemical composition were rather discrepant. Therefore we have set a problem to obtain as soon as possible spectra of this Cepheid during its pulsational period and to obtain its atmosphere parameters and chemical composition.

2. Observations

Observations of these objects have been realized using 0.8 m telescope of Joint Observatory of Northern Catholic University (Antofagasta, Chile) and Ruhr University (Bohum, Germany), equipped by echelle spectrograph IRIS: $\lambda\lambda$ 4300–8300 Å in 45 orders, and resolving power $R=50\,000$, and S/N ratio =100. The exposition time consists 1800 s for the each spectrum. Observational set have been carried out from 21 April to 11 June 2012. As a result we have obtained 33 spectra one at a time for one night, – see Table 1. The phases have been calculated according to Berdnikov (2013)

$$HJD_{max} = 2455134.5312 + 35.544719E \quad (1)$$

The reduction was made using IRAF software, the MIDAS context ECHELLE modified for extraction of echelle spectra obtained with an image slicer (Yushkin & Klochkova 2005), DECH20 software (Galazutdinov, 1992).

3. Atmosphere parameters and chemical composition

Atmosphere parameters were determined:

1. T_{eff} : line depth ratio (Kovtyukh & Gorlova, 2000).
2. $\log g$: by adopting the same iron abundance for Fe I and Fe II lines (accuracy: 0.15 dex).
3. V_t – by assuming abundances of the Fe II lines independent of the W_λ (accuracy: 0.25 km/s).

The atmosphere parameters for each spectrum are given in Table 1.

Table 1: Observations and atmosphere parameters

HJD 2450000+	Phase	T_{eff} (K)	$\log g$	V_t (km s ⁻¹)
6039.0455	0.477	4732±15	0.95	6.00
6048.4517	0.712	4793±20	1.05	6.80
6049.4611	0.740	4741±18	1.05	7.00
6051.4761	0.797	4896±22	1.10	7.40
6052.4825	0.825	4989±16	1.10	7.40
6054.4507	0.881	5273±14	1.20	7.00
6055.4679	0.909	5413±12	1.45	7.40
6056.4524	0.937	5516±12	1.50	6.60
6057.4634	0.965	5550±17	1.50	6.60
6058.4599	0.993	5530±13	1.40	6.30
6059.4528	0.021	5460±12	1.40	6.50
6062.0745	0.095	5296±13	1.35	6.30
6062.4561	0.106	5237±12	1.10	5.30
6063.4754	0.135	5159±12	1.10	5.40
6064.4595	0.162	5110±10	1.10	5.20
6065.4599	0.190	5027±11	1.10	5.10
6066.4611	0.219	4997±11	1.05	5.20
6067.4473	0.246	4982±12	1.00	5.40
6068.4492	0.275	4945±12	1.00	5.70
6069.4540	0.303	4884±13	1.00	5.90
6071.0368	0.347	4861±12	0.95	5.00
6073.4499	0.415	4779±13	0.90	5.00
6074.4660	0.444	4757±13	1.05	7.90
6075.4424	0.471	4720±11	1.05	7.90
6078.0265	0.544	4673±15	1.00	8.00
6079.0058	0.572	4624±13	1.10	8.80
6082.4535	0.668	4677±22	1.10	8.50
6083.4653	0.697	4727±23	1.05	7.00
6085.0270	0.741	4765±21	1.05	7.20
6085.4566	0.753	4803±23	1.15	7.70
6087.4568	0.809	4891±20	1.15	7.90
6088.4488	0.837	4994±22	1.20	7.50
6089.4536	0.865	5132±17	1.15	7.00

The effective temperature, gravity and turbulent velocity curves are given in Figure 1.

The mean effective temperature obtained by the integration of effective temperature curve area and its di-

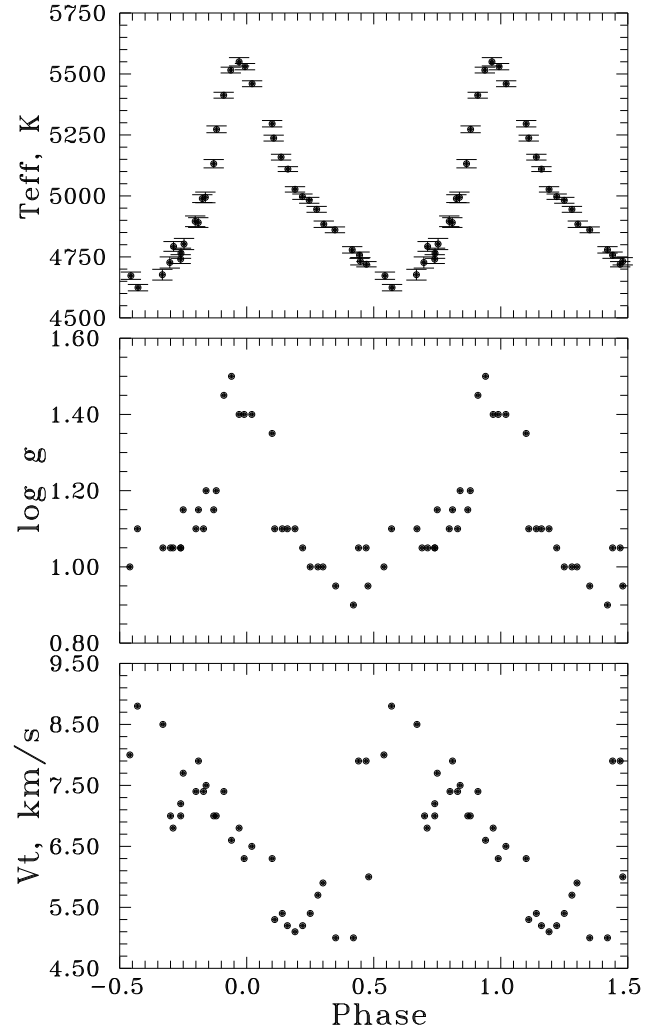


Figure 1: Effective temperature, gravity and turbulent velocity curves for l Car.

Table 2: Elemental abundance for l Car

Element	[El/H]	σ	NL	Element	[El/H]	σ	NL	Element	[El/H]	σ	NL
C I	-0.01	0.23	564	Ti I	-0.09	0.17	1613	Sr I	+0.07	0.37	53
N I	-0.00	0.22	67	Ti II	-0.10	0.16	98	Y I	-0.09	0.40	44
O I	+0.11	0.18	175	V I	-0.14	0.15	588	Y II	+0.06	0.17	144
Na I	-0.01	0.16	128	V II	-0.15	0.05	120	Zr II	+0.01	0.15	119
Mg I	+0.05	0.17	215	Cr I	-0.08	0.19	1239	Ru I	-0.01	0.33	128
Al I	+0.15	0.17	225	Cr II	-0.15	0.17	204	La II	+0.04	0.21	97
Si I	-0.04	0.13	1371	Mn I	-0.27	0.20	324	Ce II	-0.06	0.18	43
Si II	+0.26	0.27	45	Fe I	+0.02	0.14	7105	Pr II	-0.12	0.26	103
S I	+0.11	0.23	218	Fe II	+0.02	0.12	1046	Nd II	-0.07	0.14	336
K I	+0.28	0.21	31	Co I	-0.12	0.16	962	Sm II	-0.08	0.21	107
Ca I	-0.02	0.25	232	Ni I	-0.12	0.17	2445	Eu II	+0.02	0.16	98
Sc I	-0.19	0.22	159	Cu I	-0.25	0.21	67	Gd II	+0.09	0.14	28
Sc II	-0.12	0.11	130	Zn I	+0.15	0.41	39				

NL - number of lines

Table 3: Abundances of the "key" elements for l Car and Cepheids with closed pulsational periods

Object	Period (days)	Sp. type	C scI	N I	O I	Na I	Mg I	Al I	Authors
l Car	35.545	<i>G3Ib</i>	-0.01	-0.00	+0.11	-0.01	+0.05	+0.15	1
U Car	38.768	<i>G0Ib</i>	-0.38	-	-0.01	+0.30	-0.13	-0.03	2
RS Pup	41.390	<i>F8Iab</i>	+0.03	+0.73	+0.10	+0.42	-	+0.17	3
SV Vul	44.995	<i>G2.5Iab</i>	-0.02	+0.17	-0.01	+0.05	-0.17	+0.12	4

1 - This paper 2 - Usenko et al. (2011) 3 - Luck et al. (2003) 4 - Luck et al. (2001)

vision for equal parts. The mean atmosphere parameters are such:

$$T_{eff} = 4984 \pm 15 \text{ K}; \log g = 1.13; V_t = 6.67 \text{ km s}^{-1}.$$

As seen from Figure 1, the minimum of gravity curve mismatched with the one in effective temperature curve and has a left shift by 0.2 phase. But the minimum of effective temperature curve agrees with the small crest on the ascending branch of gravity curve. Turbulent velocity data formed two curves with different amplitudes and shift by 0.2 phase too.

4. Chemical composition

All the atmosphere models and chemical composition for each spectrum were calculated using our version of the WIDTH9 code on the basis of the Kurucz (1992) grid with the "solar" log gf values, adopted from Kovtyukh & Andrievsky (1999). All the data about the element abundances for this Cepheid are given in Table 2.

As seen from Table 2, l Car has not only solar metallicity but also "key" elements of yellow supergiants evolution (CNO, Na, Mg, Al) show its content, close to the solar one. Abundances of α -, Fe-group, "light" and "heavy" - s-process and r-process elements close to the solar ones. It is interesting that among the Cepheids with closed pulsational periods the most similar content of these elements exists for SV Vul (Luck

et al. 2001). These authors provided this object as a crossing the Cepheids instability strip for the *first time*.

5. Conclusions

1. Firstly we obtained the very careful effective temperature curve for l Car, and these data allows us to estimate the precise mean T_{eff} value near 4984 ± 15 K.
2. In contrast to smooth effective temperature curve the gravity and turbulent velocity ones show the presence of small crest on the ascending branch in the first case and division into two curves in the second one. The maximum of this crest agrees with the minimum of the effective temperature curve.
3. The mean atmosphere parameters, estimated by us ($T_{eff} = 4984 \pm 15$ K; $\log g = 1.13$; $V_t = 6.67$ km s⁻¹), are some lower, than in the models of Nardetto et al. (2006): $T_{eff} = 5091$ K; $\log g = 1.5$.
4. In comparison with the results of hydrodynamical models of Simon & Kanbur (1995) we can estimate the Cepheid mass near $9 M_{\odot}$.
5. l Car has metallicity, close to solar one: $[Fe/H] = +0.02$ dex.

6. Judging from the CNO-, odd elements, and Mg content, their abundances are close to solar one too. This fact is very unusual, because according to Berdnikov et al.(2003) 1 Car has a velocity of pulsational period growth in the O–C diagram $dP/dt = +16.39 \text{ c yr}^{-1}$, and this result corresponds (according to authors) to the *third crossing* of the Cepheids instability.
7. From the our results, 1 Car did not still passed through the stage after the first dredge-up and probably, crossing it for the *first time*.
8. α -elements abundances for 1 Car are close to solar ones, just as we can say about the content of Fe-group, "light" and "heavy" – s- process and r-process elements.
9. "Key" elements abundances for 1 Car are very close with SV Vul ones.

References

- Berdnikov L.N.: 2013, private communication.
 Berdnikov L.N., Mattei J.A., Beck S.J.: 2003, *JAAVSO*, **31**, 146.
 Galazutdinov G.A.: 1992, *Preprint SAO RAS*, **No.92**
 Kervella P., Mérand A., Perrin G., Coudé du Foresto V.: 2006, *A&A*, **448**, 623.
 Kovtyukh V.V. & Andrievsky S.M.: 1999, *A&A*, **351**, 597.
 Kovtyukh V.V., Gorlova N.I.: 2000, *A&A*, **358**, 587.
 Kurucz R.: 1992, *In: The Stellar Populations of Galaxies, (eds) B.Barbuy and A.Renzini, IAU Symp.*, **149**, 225.
 Luck R.E., Kovtyukh V.V., Andrievsky S.M.: 2001, *A&A*, **373**, 589.
 Luck R.E., Gieren W.P., Andrievsky S.M., Kovtyukh V.V., Fouqué P., Pont F. & Kienzle F.: 2003, *A&A*, **401**, 939.
 Nardetto N., Mourad D., Kervella P., Mathias Ph., Mérand A., Bersier D.: 2006, *A&A*, **453**, 309.
 Simon N.R. & Kanbur S.M.: 1995, *ApJ*, **451**, 703.
 Usenko I.A., Kniazev A.Yu., Berdnikov L.N., Kravtsov V.V.: 2011, *AstL*, **37**, 499.

CHEMICAL COMPOSITION AND ATMOSPHERE PARAMETERS OF THE DOUBLE-MODE CEPHEID U TRA

I.A. Usenko ¹, A.Yu. Knyazev ², L.N. Berdnikov ³, V.V. Kravtsov ^{3,4}

¹ Department of Astronomy, Odessa National University

T.G.Shevchenko Park, Odessa 65014 Ukraine, *igus99@ukr.net*

² South African Large Telescope, P.O. Box 9, Observatory, Cape Town, 7935

South Africa, *aknyazev@saa.ac.za*

³ Sternberg Astronomical Institute, Lomonosov Moscow State University

Moscow, 119899 Russia, *lberdnikov@yandex.ru*

⁴ Instituto de Astronomía, Universidad Católica del Norte, Avenida Angamos 0610

Autofagasta, Chile, *vkravtsov@ucn.cl*

ABSTRACT. Four high-resolution spectra of the double-mode Cepheid U TrA have been obtained during its pulsational period. For the first time, we obtained accurate atmosphere parameters and the chemical abundance of a number of elements, in particular of sodium, magnesium, and aluminium. We estimated the mean $T_{\text{eff}} = 6085 \pm 29$ K, $\log g = 2.00 \pm 0.15$, and $V_t = 3.90 \pm 0.25$ km s⁻¹. A deficit of carbon ($[C/H] = -0.35 \pm 0.23$ dex), overabundance of both sodium ($[Na/H] = +0.15 \pm 0.25$ dex) and aluminium ($[Al/H] = +0.30 \pm 0.32$ dex) are typical for Cepheids passing through the first dredge-up phase. The abundance of iron ($[Fe/H] = +0.01 \pm 0.15$ dex) is very close to the solar one. Moreover, we find that α -elements, those of Fe-group, as well as "light"- and "heavy"-, s- and r-process elements, all of them have abundances close to solar values, too, excepting maybe several elements with slight enhance or deficit.

1. Introduction

U TrA (*F8Ib/II*) is one of the double-mode Cepheids variables. Being 2.57 days pulsational period's variable in the fundamental mode, it has a beat period of 6.304 days. According to Jansen (1962) the $P_1/P_0 = 0.7105$, therefore its first overtone period is equal to 1.825 day.

Spectroscopic investigations of U TrA were realized by Rodgers & Gingold (1973) and Barrell (1981, 1982). The first authors determined the mean $T_{\text{eff}} = 6146$ K; and $\log g = 2.1 \pm 0.6$, using the curve-of-growth method. Some years later Barrell (1981), using 17 H_α line spectra determined the mean effective temperature as 5957 K, but using the curve-of-growth method, she determined such mean atmosphere parameters: $T_{\text{eff}} = 6215$ K, $\log g = 2.35 \pm 0.5$, $V_t = 4.8 \pm 0.1$ km s⁻¹, and

$[Fe/H] = -0.02$ dex. After that any more detailed spectroscopic investigations of this double-mode Cepheid did not carried out.

Therefore, the main aim of this work was to determine the atmosphere parameters and chemical composition using four spectra of U TrA, obtained in different phases of its pulsational period.

2. Observations and primary reduction

The observations were performed in August 2011 with GIRAFFE (Grating Instrument for Radiation Analysis with a Fibre Fed Echelle) spectrograph mounted at the Coudé focus of the 1.9m telescope at the South African Astronomical Observatory (SAAO), South Africa. Four spectra of this Cepheid have been obtained during weekly observational set. Information about U TrA spectroscopic observations and heliocentric radial velocity measurements are given in Table 1. Phases were calculated according to Berdnikov (2013) ephemeris:

$$HJD_{max} = 2455122.8479 + 2.56844306E \quad (1)$$

Since spectrum 1080030 was obtained with low S/N ratio estimation we have leaved out it from further investigations.

GIRAFFE allows to obtain high-resolution CCD echelle spectra ($R = 39000$) due to two dispersional prisms optimized for the blue (3770–5560 Å) and red (5200–10400 Å) spectral ranges. For our observations we used the red prism and a fiber with a projection diameter of 2". The detector was a 1024 × 1024 pixel TEK6 CCD camera. The total recorded spectral range (4300–6750 Å) contained 48 spectral orders.

Table 1: Observations log and radial velocity measurements.

Spectrum	HJD 2450000+	Phase	Exp. (min.)	RV (km s^{-1})
1080030	5784.3244	0.540	20	$+0.31 \pm 0.11$
1080101	5785.2752	0.910	20	-13.05 ± 0.10
1080155	5787.3440	0.716	20	$+3.80 \pm 0.09$
1080177	5788.2297	0.060	20	-37.42 ± 0.16

At the beginning of each night and before each exposure, we observed the spectra of a hollow-cathode (Th+Ar) lamp, which allowed us to take into account all temperature trends by cross-correlating the 2D images of comparison spectra during the reduction. On each night, we also observed CAMERA FLATS to correct the pixel sensitivity and FIBER FLATS to find the position of spectral orders and to apply a correction for the spectral sensitivity effect along each order (blaze correction).

We performed the primary reduction of CCD images using the standard XSPEC2 software (Balona 1999). It included: (1) background subtraction; (2) search for and extraction of the 1D fragments corresponding to individual orders from the 2D images; (3) blaze correction; (4) construction of the dispersion curves from hollow-cathode lamp spectra; (5) conversion to the wavelength scale; (6) applying the heliocentric correction; (7) determining the radial velocity by cross-correlation.

The subsequent work with the spectra, including such procedures as the continuum placement, the wavelength calibration of lines, and the measurements of line equivalent widths was performed with the DECH20 software package (Galazutdinov 1992).

3. Atmosphere parameters and chemical composition

We have estimated the following atmosphere parameters.

1. Effective temperatures, T_{eff} ; they were determined using spectroscopic criteria based on the depth ratio of selected pairs of the spectral lines most sensitive to the temperature (Kovtyukh & Gorlova, 2000). This method provides an internal accuracy in determining T_{eff} of the order of ~ 10 –30 K.
2. Surface gravity, $\log g$; it was derived from the ionization equilibrium condition for Fe I and Fe II atoms with accuracy of ~ 0.15 dex).

Table 2: Atmosphere parameters of U TrA

Spectrum	Phase	T_{eff} (K)	$\log g$	V_t (km s^{-1})
1080030	0.540	—	—	—
1080101	0.910	6101 ± 24	2.0	3.8
1080155	0.716	5577 ± 36	1.7	3.7
1080177	0.060	6576 ± 27	2.3	4.1
Mean		6085 ± 29	2.0	3.9

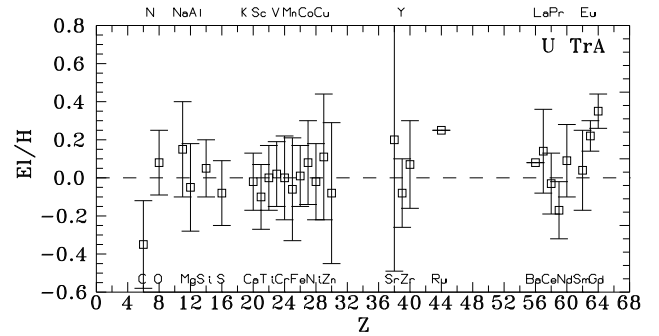


Figure 1: Averaged elemental abundances obtained for U TrA using our observations.

3. Microturbulent velocity, V_t , was deduced (with accuracy of 0.25 km s^{-1}) from the condition that the abundance of ionized iron Fe II, determined from a set of lines, should be independent of their equivalent widths (Kovtyukh & Andrievsky 1999).

The mean atmosphere parameters are given in Table 2.

4. Chemical composition

All the atmosphere models and chemical abundances were calculated for each spectrum using our version of the WIDTH9 code on the basis of the Kurucz (1992) grid with the “solar” $\log gf$ values adopted from Kovtyukh & Andrievsky (1999). The data on the elemental abundances derived from each individual spectrum and averaged abundances of U TrA are given in Tables 3. Figure 1 shows the data of Table 3.

5. Conclusions

As seen from Table 2, the mean value of the effective temperature, 6085 ± 29 K, is some smaller in comparison with 6146 K and 6215 K determined by Rodgers & Gingold (1973) and Barrell (1982), respectively. Our surface gravity value of 2.00 formally coincides with Rodgers & Gingold (1973) estimate, but some smaller of Barrell’s (1982) result. The same we can note about for the our estimate of microturbulent velocity.

Table 3: Elemental abundances in U TrA

Element	1080101			1080155			1080177			Mean		
	[El/H]	σ	NL	[El/H]	σ	NL	[El/H]	σ	NL	[El/H]	σ	NL
C I	-0.30	0.23	11	-0.36	0.23	12	-0.39	0.35	11	-0.35	0.23	34
O I	+0.00	0.05	2	-0.18	-	1	+0.21	0.06	3	+0.08	0.17	6
Na I	+0.29	0.28	6	+0.11	0.11	3	+0.02	0.21	6	+0.15	0.25	15
Mg I	+0.09	0.04	4	-0.04	0.33	5	-0.21	0.04	4	-0.05	0.23	13
Al I	-0.16	0.04	2	+0.23	0.02	2	+0.38	0.13	2	+0.30	0.32	6
Si I	+0.07	0.17	16	+0.07	0.22	16	-0.00	0.13	17	+0.05	0.16	49
Si II	-	-	-	-0.17	0.14	2	-	-	1	-0.17	0.14	2
S I	-0.04	0.29	4	-0.06	0.05	3	-0.04	0.24	5	-0.08	0.17	12
Ca I	+0.11	0.24	10	-0.00	0.15	10	-0.05	0.13	16	-0.02	0.15	36
Sc I	+0.19	0.02	2	-	0.07	3	+0.29	0.09	2	+0.24	0.08	4
Sc II	-0.06	0.19	6	-0.17	0.21	9	-0.14	0.16	8	-0.12	0.17	23
Ti I	+0.07	0.20	29	+0.02	0.16	34	+0.01	0.21	36	+0.04	0.18	99
Ti II	-0.08	0.25	9	-0.11	0.11	8	-0.11	0.16	16	-0.10	0.15	33
V I	+0.13	0.24	9	+0.08	0.22	13	+0.03	0.21	7	+0.07	0.20	29
V II	-0.09	0.16	4	-0.02	0.08	4	-0.13	0.11	5	-0.08	0.12	13
Cr I	+0.09	0.20	37	-0.03	0.26	16	-0.09	0.23	42	-0.00	0.23	95
Cr II	-0.05	0.20	16	+0.01	0.23	13	-0.00	0.22	17	-0.01	0.21	46
Mn I	-0.07	0.26	13	-0.10	0.32	13	+0.06	0.25	12	-0.06	0.27	38
Fe I	+0.02	0.15	139	+0.01	0.19	153	+0.00	0.16	162	+0.01	0.17	454
Fe II	+0.02	0.14	29	+0.01	0.16	33	-0.00	0.12	33	+0.01	0.14	95
Co I	+0.11	0.25	14	-0.01	0.27	12	+0.10	0.17	14	+0.08	0.22	40
Ni I	+0.06	0.19	71	-0.04	0.21	52	-0.05	0.20	75	-0.02	0.20	198
Cu I	+0.17	0.26	3	-0.31	0.12	2	+0.27	0.28	4	+0.11	0.33	9
Zn I	-0.08	0.35	3	-0.05	-	1	-0.08	0.66	2	-0.08	0.37	6
Sr I	-	-	1	+0.17	0.76	2	+0.23	0.93	2	+0.20	0.69	4
Y II	+0.07	0.18	7	-0.12	0.24	8	-0.13	0.08	8	-0.08	0.18	23
Zr II	+0.01	0.23	5	-0.01	0.08	3	+0.15	0.26	7	+0.07	0.23	15
Ru I	-	-	1	+0.25	-	1	-	-	-	+0.25	-	1
Ba II	-	-	-	-	-	-	+0.08	-	1	+0.08	-	1
La II	+0.23	0.20	6	+0.17	0.18	3	+0.05	0.25	7	+0.14	0.22	16
Ce II	+0.03	0.21	8	-0.07	0.15	8	+0.04	0.23	10	-0.03	0.16	26
Pr II	-0.26	0.19	2	+0.01	-	1	-0.17	0.08	2	-0.17	0.15	5
Nd II	+0.16	0.14	19	+0.01	0.20	16	+0.05	0.24	13	+0.09	0.19	48
Sm II	-0.06	0.06	4	+0.08	0.47	2	+0.15	0.11	3	+0.04	0.21	9
Eu II	+0.17	-	1	-	-	-	+0.24	0.10	2	+0.22	0.08	3
Gd II	+0.41	-	1	-	-	-	+0.28	-	1	+0.35	0.09	2

With respect to the elemental abundances obtained in the present study, we would like to summarize the following points.

1. The iron abundance is very close to solar one and is in good agreement with the results of Barrell (1982).
2. We estimated for the first time the abundances of the "key elements" of yellow supergiants evolution. Carbon is surely in deficit, and the abundance of oxygen is close to the solar one.
3. Sodium is obviously overabundant, whereas the abundances of magnesium and aluminium are close to solar ones.
4. α - element abundances are close to the solar ones.
5. The same can be noted for the element of Fe-group, as well as for "light"- and "heavy"-, s-process and r-process elements: their abundances demonstrate either slight enhance or slight deficit in comparison with the solar values. The abundances of these elements were obtained for the first time for U TrA, as well.

Taken at face value, these results suggest that U TrA is probably a Cepheid after first dredge-up phase.

References

- Balona L.A.: 1999, *Internal SAAO Report SAAO*, CapeTown, 1.
- Barrell S.L.: 1981, *MNRAS*, **196**, 357.
- Barrell S.L.: 1982, *MNRAS*, **200**, 177.
- Berdnikov L.N., 2013, *private communication*
- Galazutdinov G.A.: 1992, *Preprint SAO RAS*, **No.92**
- Jansen A.G.: 1962, *Bull. Inst. Astr. Neth.*, **16**, 141.
- Kovtyukh V.V., Andrievsky S.M.: 1999, *A&A*, **351**, 597.
- Kovtyukh V.V., Gorlova N.I.: 2000, *A&A*, **358**, 587.
- Kurucz R.: 1992, *In: The Stellar Populations of Galaxies*, (eds) B.Barbuy & A.Renzini, *IAU Symp.*, **149**, 225.
- Rodgers A.W., Gingold R.A.: 1973, *MNRAS*, **161**, 23.

THE PLANETARY HOST RED GIANT HD47536 – CHEMICAL COMPOSITION AND SIGNS OF ACCRETION

A.V. Yushchenko¹, P. Rittipruk¹, V.A. Yushchenko², Y.-W. Kang¹

¹Department of Astronomy & Space Sciences, Sejong University,
Gunja-dong, Seoul, 143-747, Korea, *yua@sejong.ac.kr*

²Astronomical observatory, Odessa National University, Odessa, 65014, Ukraine

ABSTRACT. The spectra of HD47536 with resolving power $R=30,000$ and signal to noise ratio near 100 was obtained at 1.5 meter SMART telescope of CTIO, Chile. The analysis of chemical composition allowed to find the abundances of 33 chemical elements including thorium. The star belongs to halo or intermediate population, its metallicity is $[Fe/H]=-0.58\pm 0.11$, the r - and s -processes elements are overabundant with respect to iron. The overabundance of thorium with respect to iron is $+0.72$ dex. The abundance pattern exhibits the clear signs of accretion. The star is a host of two planets, that is why it can be the result of the accretion in planetary system or the accretion of interstellar gas. The signs of accretion are clearly detected and prevent the determination of stellar age.

Key words: stars: late-type - stars: individual: HD 47536 – stars: abundances – stars: planetary systems

1. Introduction

HD47536 is a bright ($V=5.25$) halo or intermediate population K-type giant. The metallicity of HD47536 was found by different investigators in the range from $[Fe/H]=-0.54\pm 0.10$ (Sadakane et al. 2005) to $[Fe/H]=-0.68$ (da Silva et al. 2006). It hosts two planets, the first of them was discovered by Setiawan et al. (2003). The mass of this planet exceeds 5 mass of Jupiter, the semimajor axis of orbit can be more than 1.6 astronomical units, the excentricity of orbit is 0.2. Note that the radius of the star is $21.36\pm 1.47 R_{\odot}$ (van Belle & von Braun, 2009). It means that the closest distance between the planet and the host star can be as small as only 1.3 astronomical units or 13 radiuses of the host star.

The chemical composition of HD47536 was analysed earlier, the metallicity (Sadakane et al., 2005) and the abundances of few chemical elements were found, namely the upper limits of lithium and beryllium by Galvez-Ortiz et al. (2011), the abundances of oxygen by Ecuivillon et al. (2006), of sodium, magnesium, and

aluminium by Beirao et al. (2005), of sulphur by Caffau et al. (2005), and of Si, Ca, Sc, Ti, V, Cr, Mn, Co, and Ni by Gilli et al. (2006).

That is why HD47536 was included in our program of investigating the chemical composition of stars with planets. The abundances of planetary hosts were compared with the abundances of stars without planets in numerous researches.

As an example it is possible to notice that the survey of 1111 FGK stars (Adibekyan et al., 2012) shows for the stars with giant planets up to 0.5 dex higher abundances of N, Mg, Al, Si, Ca and iron group elements than for the stars without planets or with Neptunian and super-Earth planets. In accordance with this investigation the stars without planets and stars with non-giant planets have similar abundances of above pointed chemical elements.

Is it possible to predict the existence of planets having the information about the abundance pattern only? Is it possible to distinguish the stars with non-giant planets and the stars without planets? To answer these questions it is necessary to find the reliable abundance patterns of different stars and to analyze the derived abundances.

In the next sections of this paper we will show the abundances of 33 chemical elements in the atmosphere of HD47536 derived by model atmospheres method and discuss the features of this abundance pattern possibly derived by the accretion from planetary system.

2. Observations

Four spectra of HD47536 were observed with Chiron spectrograph installed at 1.5 meter SMART telescope of CTIO, Chile in 2012. The spectral resolving power was $R=30,000$, the wavelength range – 4105-8170 Å, the signal to noise ratio exceeds $S/N=100$ at the centers of echelle orders.

The initial reduction of spectra was made using standard IRAF package, the final spectra process-

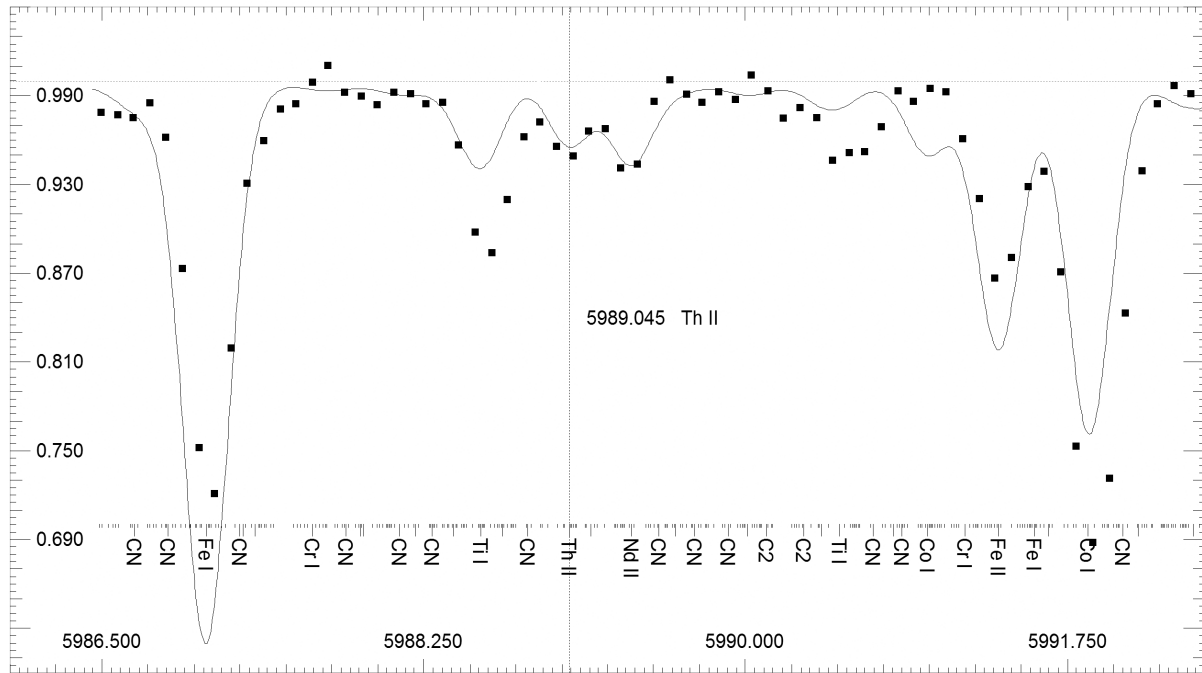


Figure 1: The spectrum of HD47536 in the vicinity of thorium line λ 5989.045 Å. The axes are the wavelength in angstroms and the relative intensities. One of the observed spectra is shown by filled squares. The solid line indicates the synthetic spectrum. The abundances of chemical elements with $Z < 38$ are accepted to be deficient by -0.5 dex with respect to the Sun. The solar abundances of heavier elements were selected for this calculation. The wavelengths of used atomic and molecular lines are indicated in the bottom part of the plot. The identifications of strongest lines are shown.

ing, including continuum placement, coadding of the spectra, identification of spectral lines, and equivalent widths measurements was made using URAN program (Yushchenko, 1998).

The example of spectrum in the vicinity of thorium line 5989.045 Å is shown in Fig. 1. Note that the synthetic spectrum of HD47536 was calculated for the whole observed wavelength region. It was taken into account in continuum placement and identification of spectral lines.

3. Atmospheric parameters

To find the values of effective temperature, surface gravity, microturbulence and metallicity of the host star we calculated the iron abundances for a grid of atmosphere models taken from Castelli & Kurucz (2003). The grid was interpolated in the ranges of $4000 \text{ K} \leq T_{\text{eff}} \leq 4000 \text{ K}$, $1.0 \leq \log g \leq 3.0$ by steps 50 K in T_{eff} and 0.05 in $\log g$ respectively.

The equivalent widths of 90 and 18 clean lines of neutral and singly ionized iron respectively were measured in the observed spectrum of HD47536. Using these lines the iron abundances were calculated for grids of models described here before with nine values of microturbulent velocity distributed in the range from 0.1

to 6 km s^{-1} .

The obtained abundances were analyzed to find the values of atmosphere parameters which satisfy several conditions, namely the zero correlations of abundances with equivalent width, energies of low levels, and wavelengths of used lines, as well as the equality of mean iron abundances calculated for neutral and ionized species.

After several iterations the values of 4400 K, 1.80, 1.5 km s^{-1} , and -0.58 were found for effective temperature, surface gravity, microturbulent velocity and metallicity respectively. More detailed description of used method can be found in recent papers by Kang et al. (2012, 2013) and our earlier publications.

The obtained results coincide with previous determinations of these parameters. For example Chezzi et al. (2010) found for the above listed parameters the values of 4588 K, 2.17, 2.03, and -0.61 respectively. The values of effective temperature of HD47536 published by different researches ranged from $4352 \pm 70 \text{ K}$ (da Silva et al. 2006) to $4853 \pm 130 \text{ K}$ (van Belle & von Braun 2009).

4. Chemical composition

The identification of spectral lines in observed spec-

Table 1: Chemical composition of HD47536

Z	Ion	$\Delta\log N$	σ	n
6	C I	-0.32		1
11	Na I	-0.14	0.34	8
12	Mg I	-0.34	0.18	8
13	Al I	-0.41	0.31	8
14	Si I	-0.32	0.19	11
16	S I	-0.19		1
19	K I	-0.06		1
20	Ca I	-0.32	0.20	11
21	Sc I	-0.56	0.07	4
	Sc II	-0.29	0.27	8
22	Ti I	-0.31	0.29	18
	Ti II	-0.76	0.24	2
23	V I	-0.15	0.26	17
24	Cr I	-0.40	0.29	15
	Cr II	-0.49		1
25	Mn I	-0.31	0.34	10
26	Fe I	-0.58	0.11	90
	Fe II	-0.59	0.14	18
27	Co I	-0.21	0.36	18
28	Ni I	-0.42	0.24	25
30	Zn I	-0.17	0.22	3
37	Rb I	0.07	0.10	2
38	Sr I	-0.16	0.25	2
39	Y I	-0.55		1
	Y II	-0.46	0.22	10
40	Zr I	-0.30	0.30	10
	Zr II	0.00	0.06	2
41	Nb I	-0.19		1
42	Mo I	-0.08	0.26	4
44	Ru I	-0.17	0.11	3
57	La II	-0.19	0.21	14
58	Ce II	-0.48	0.16	6
59	Pr II	-0.21	0.27	4
60	Nd II	-0.04	0.38	12
62	Sm II	0.11	0.23	9
64	Gd II	0.34	0.20	4
68	Er II	-0.07		1
74	W I	-0.32	0.12	2
90	Th II	0.14		1

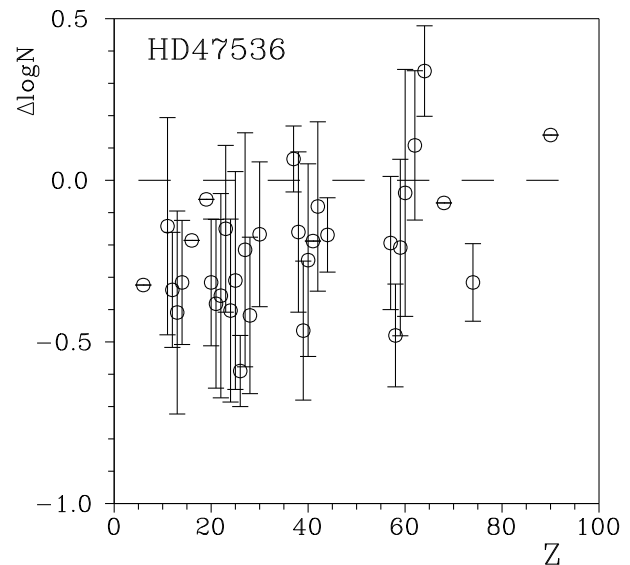


Figure 2: The abundances of chemical elements in the atmosphere of HD47536 with respect to the solar abundances (horizontal dashed line). The axes are the atomic numbers and the relative abundances.

trum of HD47536 was based on the comparison with synthetic spectrum calculated for the whole wavelength region of observed spectra. After several iterations we selected the atmosphere model (parameters were pointed in previous section) with the enhanced abundances of heavy neutron captured elements, namely the abundances of elements with atomic numbers $Z \geq 38$ were accepted to be solar, while all lighter elements were underabundant by 0.5 dex with respect to the solar values. It allowed to reach the better fit of observed spectrum by calculated one.

To find more precise result the equivalent widths of identified lines were measured and the abundances for individual lines were calculated using Kurucz's program WIDTH9. Table 1 contains the mean values of abundances of 33 chemical elements with respect to the solar or solar system values (Grevesse et al. 2010), the errors, and the number of used lines.

Fig. 2 shows the abundance pattern of HD47536. The *r*- and *s*-processes elements are slightly overabundant with respect to iron. It resembles the usual case of halo star with enhanced abundances of heavy elements.

Note that the overabundance of thorium is found using the line λ 5989.045 Å. This line was identified for the first time in stellar spectra by Yushchenko et al. (2005).

5. Discussion

Usually the low abundances of chemical elements in metal-poor stars were explained by formation of these stars at the early evolutionary stages of the Universe,

when the synthesis of elements heavier than helium in stellar interiors took place and the abundances of these elements were lower than those at present time.

If the mass of star is low enough to exist up to the present time the abundance pattern of such star can reflect the chemical composition of the Galaxy at the birth time of the star. That is why one can try to estimate the stellar age using the abundance ratio of radioactive and stable or of two radioactive elements. Usually the ratio of Th and Eu abundances is used.

To calculate the age one should know the initial abundance ratio and to find the present value of this ratio from observations. The application of this method allowed to find the ages of metal-poor stars with enhanced abundances of heavy elements.

The necessary conditions to determine the reliable age are:

- 1) the information about the initial abundance ratio, usually it is taken from the standard cosmology; that is why it is necessary to believe the validity of this theory;
- 2) the universality of r -process, more exactly it is the hypothesis that the abundance ratios in the products of different supernova explosions are equal;
- 3) the changes of abundance ratios mainly due to natural radioactive decay; the influence of other factors should be neglected or estimated.

To make the result independent on the validity of any theory it was proposed to find not the age but the age difference between different halo type stars, in this case the knowledge of initial abundance ratio is not necessary. Yushchenko et al. (2005) showed that the age difference between HD115444 and GS31082-001 can be as high as 48 ± 14 billions years. To explain this result in the frames of standard cosmology it is necessary to reject the universality of r -process or to suppose the changes of abundance ratios not only due to natural radioactive decay.

The latest provement of nonuniversality of r -process was made by Ren et al. (2012), but the validity of the third condition (the changes of abundance ratios mainly due to natural radioactive decay) seems to be not doubted before. The abundance pattern of HD47536 allow us to discuss this item.

Fig. 3 shows the abundances of heavy elements in the atmosphere of HD47536 in comparison with solar system r -process abundances. The coincidence of abundances in the top panel seems to be satisfactory, but the bottom panel indicates that the deviations are as high as 0.3-0.5 dex.

Note that the metallicity of the star is only -0.58 dex and the heavy elements (except Rb, Sm, Gd, and Th) are overabundant with respect to iron by less than this

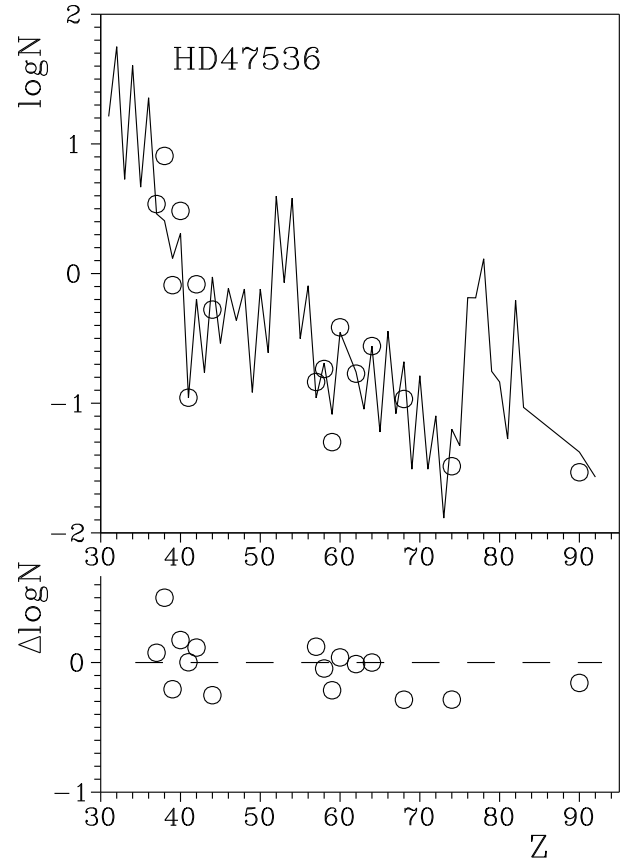


Figure 3: The top panel: the comparison of surface abundances in HD47536 (circles) with solar system r -process abundance distribution (line) taken from Simmerer et al. (2004). and scaled to the observed abundance of gadolinium. The bottom panel: the deviations of observed abundances in HD47536 from scaled solar system r -process abundance distribution.

value. That is why it seems desirable to find additional scenario which can influence the surface abundances in HD47536. Maybe the interaction of several physical phenomena produce the observed abundance pattern.

Fig. 4 plots the relative abundance of chemical elements in the atmosphere of HD47536 against the condensation temperatures of these elements. The elements with condensation temperatures above 500 K exhibit the negative correlation of relative abundance and condensation temperatures. Similar correlations are observed also in λ Boo type stars, as it was discussed, for example, by Venn & Lambert (1990, 2008). It was explained by dust-gas separation mechanism in circumstellar envelopes.

HD47536 has a planetary system, that is why it is natural to expect the existence of circumstellar envelope. It is worth to note that the star shows the detectable IRAS fluxes. The observed values are higher than it can be predicted using the visual magnitude

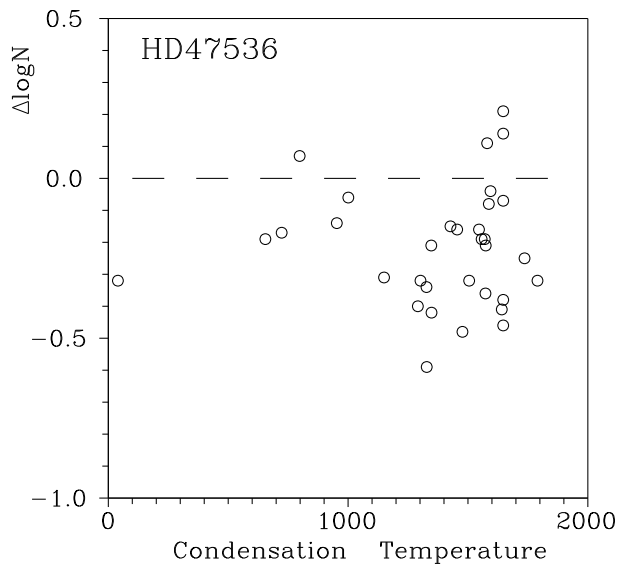


Figure 4: The plot of relative surface abundances of chemical elements in HD47536 as a function of the condensation temperature of these elements. The values of condensation temperatures for a solar-photosphere composition gas are taken from Lodders (2003).

and effective temperature, that is why it is possible to claim the existence of infrared excess, which is usually explained by dust envelope.

Note that the star hosts two planets, one of them has the mass not less than 5 masses of Jupiter. Taking into account the parameters of orbital motion published by Setiawan et al. (2003) it is easy to estimate that the closest distance between the host star and the planet is only 13 radiuses of the host star. The discovery of two planets allow to suppose the existence of smaller planets at closer orbits. The accretion of matter from the planetary system can explain the λ Boo type features in the abundance pattern of HD47536.

We also tried to find the possible dependence between the relative abundances of chemical elements and the second ionization potentials of these elements (Fig. 5). It was first noticed by Greenstein (1949), one of the latest investigations of this effect was published by Böhm-Vitense (2006). Greenstein (1949) investigated Am stars and found that the relative abundances of elements with second ionization potentials close to the ionization potential of hydrogen are lower than relative abundances of other elements.

It was explained by the accretion of interstellar gas and the charge-exchange reactions between the atoms of interstellar gas (mainly hydrogen) and the target atoms in radiative stellar atmosphere. Kang et al. (2012, 2013) showed that in the case of strong accretion this effect can be detected in the atmospheres of cooler stars with convective atmospheres.

Fig. 5 allows to point the deficiency of elements

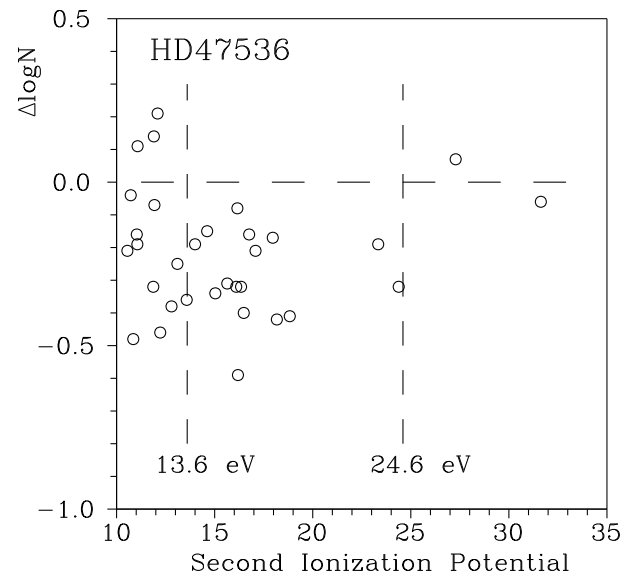


Figure 5: The plot of relative surface abundances of chemical elements in HD47536 as a function of second ionization potentials of these elements. The positions of the ionizations energies of hydrogen (13.6 eV) and helium (24.6 eV) atoms are marked by vertical dotted lines.

with ionization potentials close to 13.6 eV (the ionization potential of hydrogen) and also the positive correlation of relative abundance and ionization potentials for chemical elements with second ionization potentials higher than 13.6 eV. Similar correlations was found by Kang et al. (2013) for both components of RS CVn type eclipsing binary LX Per.

Unfortunately the theory of charge-exchange reactions in stellar atmospheres was not developed in details. Recent observations shows that the results of this reactions can be detected not only is stars with radiative atmospheres but also in stars with effective temperatures as low as 5000 K (Kang et al. 2013). HD47536 has even lower effective temperature.

Figures 4 and 5 prove that the atmosphere of HD47536 is influenced by accretion from the outer space, and the relative abundances of chemical elements are changed due to accretion.

We found the abundance of thorium and it seems possible to determine the age of the star. But the clear signs of accretion prevent it. It is impossible to accept that the abundance ratios in the atmosphere of HD47536 were changed only due to natural radioactive decay.

It is hard to expect that the atmospheres of all metal-poor stars are influenced by the accretion of dust or gas. For example Kim et al. (2012) found no signs of dust accretion in the abundance pattern of BE Lyn. This halo star can be SX Phe type pulsating variable. But the accretion of interstellar gas should influence

all galactic stars as any object should cross the plane of the Galaxy where the density of interstellar gas is enhanced. Even if the signs of this type accretion will be destroyed by convection or other effects it is not possible to neglect the importance of charge-exchange reactions on stellar and Galactic evolution.

As an example it is necessary to note that Havnes (1971) discussed the charge-exchange reactions as the effective mechanism of braking the rotation of magnetic stars and generating the cosmic rays.

6. Conclusion

The high resolution spectra of bright ($V=5.25$) planetary host star HD47536 was used to find the abundances of 33 chemical elements including thorium. HD47536 is a halo or intermediate population star. The heavy elements are enhanced with respect to iron. The relative overabundance of thorium with respect to iron is +0.72 dex. The signs of accretion are clearly detected in the atmosphere of this object. The IRAS fluxes of HD47536 allow to point the existence of infrared excess.

It is impossible to accept that the abundance ratios of thorium and stable chemical elements in the atmosphere of HD47536 were changed mainly due to natural radioactive decay. It makes impossible the calculation of stellar age.

The results of this investigation will be used as the first iteration to determine the more accurate abundance pattern of this star by spectrum synthesis method.

Acknowledgements. This work was supported in part by Mid-career and General Research Programs, and Science and Technology grants 2011-0028001 and 2011-0010696 respectively, through the National Research Foundation (NRF) funded by the Ministry of Education of Korea. One of the authors was granted by the Swiss National Science Foundation (SCOPE project No. IZ73Z0 -128180/1).

References

- Adibekyan V.Zh., Sousa S.G., Santos N.C., Delgado Mena E., Gonzalez Hernandez J.I., Israelian G., Mayor M., Khachatryan G.: 2012, *A&A*, **545**, A32.
- Beirao P., Santos N.C., Israelian G., Mayor M.: 2005, *A&A*, **438**, 251.
- Böhm-Vitense E.: 2006, *PASP*, **118**, 419.
- Chezzi L., Cunha K., Schuler S.C., Smith V.V.: 2010, *ApJ*, **725**, 721.
- Castelli F., Kurucz R.: 2003, it IAU Symp. 210, Poster contributions, A20, <http://wwwuser.oat.ts.astro.it/castelli/grids.html>.
- Caffau E., Bonifacio P., Faraggiana R., Francois P., Gratton R.G., Barbieri M.: 2005, *A&A*, **441**, 533.
- da Silva L., Girardi L., Pasquini L., Setiawan J., von der Luhe O., de Medeiros J.R., Hatzes A., Dollinger M.P., Weiss A.: 2006, *A&A*, **458**, 609.
- Ecuivillon A., Israelian G., Santos N.C., Shchukina N.G., Mayor M., Rebolo R.: 2006, *A&A*, **445**, 633.
- Galvez-Ortiz M.C., Delgado-Mena E., Gonzalez Hernandez J.I., Israelian G., Santos N.C., Rebolo R., Ecuivillon A.: 2011, *A&A*, **530**, A66.
- Gilli G., Israelian G., Ecuivillon A., Santos N.C., Mayor M.: 2006, *A&A*, **449**, 723.
- Greenstein J.L.: 1949, *ApJ*, **109**, 121.
- Grevesse N., Asplund M., Sauval A.J., Scott P.: 2010, *As & SpSci*, **328**, 179.
- Havnes O.: 1971, *A&A*, **13**, 52.
- Kang Y.-W., Yushchenko A., Hong K., Kim S., Yushchenko V.: 2012, *AJ*, **144**, 35.
- Kang Y.-W., Yushchenko A.V., Hong K., Guinan E.F., Gopka V.F.: 2013, *AJ*, **145**, 167.
- Kim Chulhee, Yushchenko A.V., Hong K., Kim S.-L., Jeon Y.-B., Kim Chun-Hwey: 2012, *PASP*, **124**, 401.
- Lodders K.: 2003, *ApJ*, **591**, 1220.
- Ren J., Christlib N., Zhao G.: 2012, *A&A*, **537**, A118.
- Setiawan J., Hatzes A.P., von der Luhe O., Pasquini L., Naef D., da Silva L., Udry S., Queloz D., Girardi L.: 2003, *A&A*, **398**, L19.
- Sadakane K., Ohnishi T., Ohkubo M., Takeda Y.: 2005, *PASJ*, **57**, 127.
- Simmerer J., Sneden C., Cowan J.J., Collier J., Woolf V.M., Lawler J.E.: 2004, *ApJ*, **617**, 1091.
- van Belle G.T., von Braun T.: 2009, *ApJ*, **694**, 1085.
- Venn K.A., Lambert D.L.: 1990, *ApJ*, **363**, 234.
- Venn K.A., Lambert D.L.: 2008, *ApJ*, **677**, 572.
- Yushchenko A.V.: 1998, in *Proceedings of the 20th Stellar Conference of the Czech and Slovak Astronomical Institutes*, Ed. by J. Dusek (ISBN 80-85882-08-6, Brno), p. 201.
- Yushchenko A., Gopka V., Goriely S., Musaev F., Shavrina A., Kim C., Kang Y.W., Kuznietsova J., Yushchenko V.: 2005, *A&A*, **430**, 255.